The Interaction Point Collision Feedback System at the International Linear Collider and its Sensitivity to Expected Electromagnetic Backgrounds

C. I. Clarke
Wolfson College

Thesis submitted in fulfilment of the requirements for the degree of Doctor of Philosophy at the University of Oxford

Hilary Term, 2008

Abstract

An Interaction Point Collision Feedback System is necessary to achieve design luminosity at the future International Linear Collider (ILC). This is proposed to include a stripline beam position monitor (BPM) positioned ∼3 m from the Interaction Point (IP). The BPM is required to be able to measure the position of the outgoing electron or positron beam with a resolution of ∼1 μm.

Prototype feedback systems have been built and tested at the Next Linear Collider Test Accelerator (NLCTA) at the Stanford Linear Accelerator Center in the USA (SLAC) and also at the Accelerator Test Facility (ATF) at the High Energy Research Laboratory in Japan (KEK). The successful correction of position offsets is demonstrated with the lowest latency achieved 24 ns, the best position resolution 4 μm and the best correction ratio 23:1.

To make the feedback system a more powerful tool, a digital processor is added. It raises the total latency of the feedback system to ∼140 ns. Its ability to perform algorithms is demonstrated with charge normalisation. Preliminary results indicate a resolution of ∼8 μm and correction ratio 7:1.

Backgrounds at the ILC comprise mainly electron-positron pairs from the beam-beam interaction. For the high luminosity 1TeV accelerator parameters, 10^5 pairs are produced per bunch crossing. This is the worst case for ILC pair backgrounds. These pairs produce $\sim 5 \times 10^5$ particle hits on a stripline of the IP feedback BPM.

In two experiments at End Station A (ESA) at SLAC, a stripline BPM was exposed to secondary particle backgrounds to determine if the particle hits degraded the ability of the stripline BPM to resolve micron-level position offsets. The experiments agree that the worst ILC pair backgrounds degrade the resolution by less than 8.5 nm (95% confidence level). It is concluded that micron-level resolution will not be affected by the ILC pair backgrounds.

Studies of stripline signals caused by backgrounds led to the development of a GEANT3-based tool that could predict the signals. The prediction tool was tested against one of the experiments at ESA and used to predict the signals on the ILC feedback BPM striplines. The results confirm that the ILC pair backgrounds do not produce micron-level errors in position measurement, indicating that the degradation in resolution by the worst pair backgrounds expected was under 13 nm.

For Clifford E Jones (1915-2007)

Acknowledgements

I would like to thank the many people that made these studies not just possible but also a fulfilling experience, some of whom are mentioned by name on this page. Those that are not, know that I greatly appreciate the help, insight and/or friendship you gave.

My PhD began at Queen Mary and I thank the head of the particle physics department Tony Carter and my supervisor Phil Burrows for getting me there. Everyone I met at Queen Mary and in the University of London lectures made the experience enjoyable (including the ones that brewed the tea).

Some of my work was done in support of the main FONT project of developing the IP feedback system. Steve Molloy was an excellent teacher and provided a lot of support and friendship over the years even after he left the project. Glenn Christian, Colin Perry, Hamid Dabiri Khah and Ben Constance were invaluable, building and testing the FONT prototypes. The beam tests were performed at KEK in Japan and I thank Junji Urakawa and the rest of the ATF scientists and staff for being our hosts. I also thank the other visitors at ATF that offered their technical expertise and, importantly, advice on what to eat. These vital people include Marc Ross, Doug McCormick, Stewart Boogert, Steve Smith and all of those I think of as the NLCTA crowd.

The rest of my thesis owes thanks in particular to Tony Hartin for his simulation work and fantastic support. The experiments at ESA could not have happened without all the hard work from Mike Woods, Ray Arnold and many other people at SLAC. I thank them all. I also thank Brian Todd and engineers at Daresbury for the construction of the FONT module.

Extra special mention needs to go to Glen White and Alexander Kalinin, both of whom helped in every part of my thesis by imparting a slither of their vast knowledge and expertise. Also, for her services in every part of my work and travel and for her friendship, I thank Christina Swinson.

I am very grateful to TMD Technologies who sponsored this work, in particular Howard Smith who paid a friendly interest in his investment.

Of course the biggest thanks goes once again to Phil Burrows: there at the start and there at the end.

On a personal note, the family and friends that stood by me for the past three years were just as important as those that worked by me. Most thanks go to my Mum and Dad and also the friends that kept me sane in America: Mary-Rose, Joe Frisch, RianSeeking and skittledog.

Contents

1 Introduction **1**
1.1 Particle physics and future colliders . . . 1
1.1.1 The Standard Model . . . 1
1.1.2 Why look towards the Terascale? . . . 2
1.1.3 What is the ILC? . . . 4
1.1.4 Why a linear collider? . . . 5
1.1.5 Why an electron-positron collider? . . . 7
1.2 Backgrounds at the ILC Interaction Point . . . 8
1.2.1 Principal sources of IP backgrounds . . . 8
1.3 The Beam-Beam Effect on Luminosity . . . 10
1.3.1 GUINEA PIG simulation of the beam-beam interaction . . . 11
1.4 Feedback in the ILC Beam Delivery System . . . 12
1.4.1 Ground Motion and Cultural Noise Issues for Stabilisation . . . 12
1.4.2 Intra-train Feedbacks at the ILC . . . 15
1.5 Beam Position Monitors . . . 18
1.5.1 Button BPMs . . . 19
1.5.2 Stripline BPMs . . . 20
1.5.3 Cavity BPMs . . . 26
1.6 Summary . . . 27

2 FONT Fast Feedback Systems **28**
2.1 FONT1 . . . 28
2.2 FONT2 . . . 30
2.3 FONT3 . . . 34
2.3.1 Moving to ATF . . . 34
2.3.2 FONT3 Processor . . . 35
2.3.3 FONT3 Feedback Results . . . 41
2.3.4 Simulations of FONT3 feedback . . . 42
2.4 FONT 4 . . . 45
2.4.1 Analogue Processor . . . 48
2.4.2 Digital Processor . . . 53
2.4.3 Amplifier . . . 55
2.4.4 Method . . . 55
2.4.5 Results . . . 56
2.5 Summary . . . 57

3 The Interaction Region at the International Linear Collider (ILC) 60
3.1 Stripline susceptibility to backgrounds . . . 60
3.1.1 Particle-matter interactions . . . 60
3.1.2 Signals of charges hitting and being emitted from striplines . . . 65
3.2 The Interaction Region Components . . . 67
3.2.1 The IR for the Silicon Detector . . . 68
3.2.2 Other Detector Concepts . . . 70
3.2.3 DID and anti-DID . . . 72
3.3 Simulation Tools . . . 74
3.3.1 GEANT Modifications . . . 75
3.4 Simulations of ILC IR conditions . . . 76
3.4.1 Number of charged particle hits . . . 76
3.4.2 Distribution of charged particles . . . 81
3.4.3 Distribution of charged particle energies . . . 84
3.4.4 14 mrad crossing angle simulations . . . 84
3.5 Summary . . . 85

4 Recreating the ILC Interaction Region at End Station A 87
4.1 End Station A . . . 87
4.2 The FONT Module . . . 88
4.2.1 The Low-Z Mask . . . 88
4.2.2 The BeamCal . . . 88
4.2.3 The Stripline BPM . . . 91
4.2.4 The Quadrupole . . . 91
4.2.5 Module simulations . . . 93
4.3 Summary . . . 95

5 Methods for recreating ILC backgrounds: Introduction and Method A 96
5.1 Introduction to the methods for recreating ILC backgrounds . . . 96
5.2 Methods for creating spray: A . . . 97
5.2.1 Overview . . . 97
5.2.2 Simulating the experiment: Method A . . . 97
5.2.3 Instrumenting the experiment: Method A . . . 100
5.2.4 Performing the experiment: Method A . . . 104
5.3 Results: Method A . . . 105
5.3.1 Raw stripline response . . . 105
5.3.2 Processed difference signals . . . 108
5.4 ILC Prediction based on Method A . . . 110
5.5 Summary to Method A . . . 113

6 Methods for recreating ILC backgrounds: Method B 115
6.1 Methods for creating spray: B . . . 115
6.1.1 Overview . . . 115
6.1.2 Designing the experiment . . . 116
6.1.3 Performing the experiment: Method B . . . 118

6.2 Results: Method B . . . 120
6.2.1 Raw stripline data . . . 120
6.2.2 The processed signals . . . 123
6.3 Simulating the experiment: Method B . . . 125
6.3.1 Using GEANT3 Simulations to scale from ESA to ILC . . . 126
6.4 Summary to Method B . . . 130

7 Methods for recreating ILC backgrounds: Method C 131
7.1 Methods for creating spray: C . . . 131
7.1.1 Overview . . . 131
7.1.2 Thick Target Simulations . . . 131
7.1.3 Tracking in the A-line . . . 132
7.2 Simulating the experiment: Method C . . . 135
7.3 Summary to Method C . . . 137

8 GEANT3-based simulations of stripline signals 139
8.1 Simulating stripline signals . . . 139
8.1.1 Overview . . . 139
8.1.2 Using GEANT3 results to produce the normal stripline response . . . 139
8.1.3 Response from emission . . . 140
8.1.4 Response from impaction . . . 143
8.2 Simulation of Method A Results . . . 144
8.3 Prediction for the ILC . . . 150
8.4 Summary . . . 152

9 Summary and Conclusions 153
9.1 Summary . . . 153
9.1.1 Feedback tests of the full FONT system . . . 153
9.1.2 Background tests of a stripline BPM . . . 155
9.2 Outlook . . . 156

Bibliography 159

List of Figures

1.1 Potential terascale discoveries of the Higgs boson and dark matter 3
1.2 The ILC layout 4
1.3 The output of a GUINEA PIG simulation of the beam-beam interaction for the ILC at a centre of mass energy of 500 GeV. 12
1.4 The luminosity normalised to its maximum vs vertical position offset as a fraction of the RMS beam size in y 13
1.5 The luminosity normalised to its maximum vs vertical angle offset as a fraction of the RMS beam divergence in y 13
1.6 The integrated amplitude of the ground motion versus frequency for various sites at SLAC 14
1.7 The correlation in ground movement at two points 100 m apart with frequency 15
1.8 The luminosity vs time in the presence of ground motion 16
1.9 Block diagram of IP position feedback 16
1.10 The angle that the beam-beam interaction gives to the beams versus the normalised vertical position offset 17
1.11 The luminosity versus bunch number with intra-train feedback in the presence of ground motion 18
1.12 The luminosity normalised to the maximum luminosity versus RMS jitter on the main linac quadrupoles 19
1.13 The button BPM response to a passing beam of charged particles 20
1.14 The production of a signal from an electron on a stripline with the downstream end shorted 21
1.15 The production of a signal from an electron on a stripline with the downstream end terminated through matched impedance with the stripline 22
1.16 The production of a signal from an electron on a stripline with the downstream end open 23
1.17 The signal from an electron hitting the upstream end of a stripline 24
1.18 Cross-section of a beampipe (radius b) with striplines mounted on the side and a beam a distance r from the centre of the beampipe 25
1.19 The frequency response of a 15 cm stripline normalised to its maximum value 26

2.1 Schematic of FONT tests on a single beam showing the three necessary beam-line components 29
2.2 Feedback operation for FONT1 showing (a) without feedback, (b) feedback main loop on and (c) both the feedback main loop and delay loop on 31

2.3 Feedback operation for FONT2 showing (a) without feedback, (b) no feedback, beam flattener on, (c) feedback main loop on plus beam flattener on and (c) the feedback main loop, the delay loop and the beam flattener all on 33
2.4 ATF extraction line and beamline components used in FONT3 35
2.5 A block diagram of the FONT3 processor 36
2.6 A block diagram showing the setup used to correctly phase the LO with the RF 37
2.7 Calibration curves for three BPMs instrumented with the FONT3 analogue processor 39
2.8 The distribution of the residuals for three BPMs instrumented with the FONT3 analogue processor 40
2.9 Feedback operation for FONT3 showing the signal from the difference processor on BPM11. (a) No feedback. (b) Feedback main loop on. (c) Feedback main loop plus the delay loop on 41
2.10 The FONT3 feedback as simulated in Simulink 43
2.11 The feedback simulation results with ideal gains and delay loop setting . . . 44
2.12 A function derived from empirical observation describing the non-linearity of the amplifier 44
2.13 A comparison of simulated results and real results from ATF 46
2.14 The feedback simulation results with ideal gain, non-linear amplifier and a delay loop setting 2 ns below the system latency 47
2.15 Simulation results of having multiple gains depending on the offset compared to one single gain for the IP position offset feedback 48
2.16 A System View simulation of the FONT3 processor output and the FONT4 processor output with the revised filter values 49
2.17 Photograph of the FONT4 analogue processor 50
2.18 Block diagram of the FONT4 analogue processor components 50
2.19 Calibration curves for three BPMs instrumented with the FONT4 analogue processor 51
2.20 The distribution of the residuals for three BPMs instrumented with the FONT4 analogue processor 52
2.21 Measurement of the FONT4 analogue processor latency 53
2.22 The latency of the FONT digital processor 55
2.23 FONT4 feedback without charge normalisation 56
2.24 FONT4 feedback with online charge normalisation 57
2.25 The latency measurement of the FONT4 feedback 58

3.1 Fractional energy loss per radiation length as a function of energy for passage of electrons and positrons through lead 61
3.2 The photon total cross sections as a function of energy for passage through lead 62
3.3 The yield of secondary electrons from lead versus incident electron energy . . 63
3.4 Yield of secondary electrons from a TiN/Al alloy versus energy for different angles of the incident beam of electrons 64
3.5 The polarities of the voltage signals caused by the addition and subtraction of electrons and positrons from a stripline 66
3.6 The form factor for the signal caused by charges being ejected from the striplines 67

3.7 A generalised Interaction Region plan view . . . 68
3.8 Plan view SiD IR for the 2 mrad case . . . 69
3.9 Plan view SiD IR for the 20 mrad case . . . 69
3.10 The IR of the GLD 2 mrad case . . . 71
3.11 The IR of the LDC for the 20 mrad case . . . 71
3.12 The transverse B-field experienced by the incoming beams at an IP with a crossing angle of 20 mrad . . . 73
3.13 The transverse B-field experienced by the incoming beams at an IP with a crossing angle of 20 mrad with the detector solenoid, the DID and quadrupoles and the total transverse B-field . . . 73
3.14 The effect of DID on backgrounds at the LDC . . . 74
3.15 The total energy of the beamstrahlung pairs hitting the BeamCal with beampipe radius for the SiD . . . 75
3.16 The bremsstrahlung cross-section for copper versus incident electron energy . 76
3.17 The total number of electron, positron and photon hits per stripline of a stripline BPM were counted for each parameter set at both the 2 mrad and 20 mrad crossing angles . . . 77
3.18 The origin of the particles hitting the striplines for the 20 mrad crossing angle case . . . 78
3.19 Number and energy density results from a GEANT3 simulation of background pairs interacting with the 20 mrad crossing angle for SiD (without DID) . . . 79
3.20 The kinetic energies of the particles that hit the low-Z mask and the kinetic energies of those that cause spray on the striplines . . . 79
3.21 The number of hits per stripline versus the z position of the stripline BPM . 80
3.22 The number of hits per stripline versus the radius of the striplines of the BPM from the centre of the beampipe . . . 80
3.23 DID effects on the energy density of those particles that go on to cause hits on the BPM striplines . . . 81
3.24 (a) The stripline labels used in this thesis for the IP feedback BPM. (b) The distribution of the particles at the location and radius of the FONT BPM striplines . . . 82
3.25 Energy and number density distributions for electrons and positrons that hit the low-Z mask . . . 83
3.26 Energy and number density distributions for electrons and positrons near the z location of the low-Z mask that go on to cause hits on the BPM striplines . 83
3.27 Particle distributions near the location of the low-Z mask . . . 84
3.28 Comparison of energies of all charged particles at a position in front of the low-Z mask and the charged particles that cause hits on the striplines . . . 85

4.1 Plan view of the SiD 20 mrad IR and an engineering drawing of the FONT BPM Module (side view) . . . 89
4.2 The FONT module location in ESA . . . 89
4.3 Engineering drawing showing the FONT module (angled view) . . . 90
4.4 The FONT module BPM . . . 91
4.5 The end cross section view of the extraction line quadrupole . . . 92

4.6 Side view of the FONT module showing sources for particles that hit the striplines . . . 93
4.7 Histogram of the z location of the source of the particles that hit the striplines 94

5.1 The positions of the electron beam in Method A and labelling convention for FONT module BPM striplines . . . 99
5.2 Histograms for the energy distribution of charged particle hits on the striplines 99
5.3 Photographs of the CCD camera images . . . 101
5.4 Photograph of the signal from the low current toroid with the calibration current and the ADC window positioned at the second trough . . . 103
5.5 The calibration of the low current toroid against toroid 4140 . . . 103
5.6 The calibration curve for paired/opposing striplines without charge normalisation . . . 105
5.7 Stripline signals in volts from stripline C at three positions on the x axis (x = -0.5 cm, x = 0 cm, x = 0.5 cm) . . . 106
5.8 Stripline signals in volts from stripline C at three positions on the x axis (x = 1.25 cm, x = 1.5 cm, x = 1.75 cm) . . . 107
5.9 Stripline signals in volts from stripline B at three positions on the x axis (x = 1.25 cm, x = 1.5 cm, x = 1.75 cm) . . . 107
5.10 The stripline signals for two offsets at two different beam charges, showing the scaling of the signals with charge . . . 108
5.11 The stripline responses for all four striplines before and after the beam hits the low-Z mask as it is moved along x = -y . . . 109
5.12 Response of two striplines with the beam at x = -1 cm, y = 1 cm (on the low-Z mask) and two striplines with the beam at x = -1.25 cm, y = 1.25 cm 110
5.13 The response from the FONT4 analogue processor with input signals from striplines B and D . . . 111
5.14 Two positions of the beam in Method A . . . 111
5.15 Two positions of the beam that were recorded during Method A data taking, extended to cover the entire front face of the module . . . 112
5.16 Prediction for the stripline signals for the ILC IP feedback BPM (due to beam-beam pairs) based on a weighted sum of Method A stripline signal results 113

6.1 The number density of electrons, photons and positrons that hit the front face of the low-Z mask in a simulation of Method B using the 5% foil . . . 116
6.2 The three possible upstream foil positions shown schematically with the front end of the FONT module . . . 117
6.3 Calibration for the raw stripline signals with position (normalised) . . . 119
6.4 Calibration for the processed BPM signals with position . . . 120
6.5 The results for 1000 pulses taken with no foil in the beamline and the 5% foil in the beamline . . . 121
6.6 Definition of Q, P and R to be used in Method B analysis . . . 122
6.7 The normalised difference signal from the FONT4 analogue processors averaged over 1000 pulses with foils and without foils . . . 124
6.8 The FONT module with a thin target upstream . . . 126

6.9 The energy spectra of the electrons in the beam halo after being passed through foils and the energy spectrum of the pairs from the ILC IP that hit the low-Z mask . . . 126
6.10 The energy distribution of the GEANT3 ILC simulation hits on the striplines and the energy distribution to the hits on the striplines with the 5% foil at ESA 127
6.11 Cross sections for particle interactions for iron . . . 129

7.1 Layout of the Beam Switch Yard (BSY) and A-line . . . 133
7.2 The electron energy distribution before and after the beryllium target . . . 134
7.3 The x-y distribution of the incident beam of electrons and the spray generated from the target in Method C . . . 134
7.4 The number density of the spray at the position of the FONT module . . . 135
7.5 The number of electrons per electron incident on the beryllium target that reach the FONT module depending on the momentum setting of the A-line (x axis) for different linac energies . . . 136
7.6 The energy distribution of particles that hit the striplines for the 14 mrad crossing angle ILC case and Method C . . . 136
7.7 The average energy and number density of the particles versus radius . . . 137

8.1 The stripline response to charges passing its upstream end created through simulation . . . 140
8.2 The signal caused on a shorted stripline by an electron emitted from the stripline 142
8.3 The signal caused by charged particles leaving the striplines from a simulation shown as a histogram . . . 143
8.4 The signal caused by charged particles leaving the striplines based on simulations 144
8.5 The angle of approach of electrons that hit the striplines . . . 145
8.6 Diagram describing a particle hitting a stripline in terms of three stages . . . 145
8.7 The signal caused by charged particles hitting the striplines based on simulations 146
8.8 The signal caused by charged particles passing the upstream end of the striplines, leaving the striplines and hitting the striplines . . . 147
8.9 The simulated stripline signals for three positions of the beam in Method A using the method in the text . . . 148
8.10 The stripline responses for all four striplines before and after the beam hits the low-Z mask as it is moved along x = -y . . . 149
8.11 Stripline B signals with the beam at x = -1 cm, y = 1 cm (simulated and experimental data) . . . 150
8.12 The signal predicted for four striplines of the IP BPM through simulation . . . 151

List of Tables

1.1 The Standard Model . . . 2
1.2 ILC 500 GeV Beam Parameters . . . 5
1.3 ILC 1 TeV Beam Parameters . . . 6

2.1 NLCTA Beam Parameters . . . 29
2.2 FONT1 Latency Prediction . . . 30
2.3 FONT2 Latency Prediction . . . 32
2.4 ATF Beam Parameters . . . 34
2.5 FONT3 Latency Prediction . . . 34
2.6 FONT3 results . . . 42
2.7 FONT4 Latency Prediction . . . 49

3.1 A table comparing the main z locations and radii of beamline elements in the IR extraction line. . . . 72
3.2 Number of hits per stripline for Scheme 14, 14 mrad crossing (anti-DID). . . . 85

4.1 SLAC ESA beam parameters . . . 88
4.2 BeamCal mock-up in lead . . . 90
4.3 Extraction line quadrupole mock-up in stainless steel. . . . 92

5.1 A summary of methods to create backgrounds at ESA. . . . 98
5.2 Breakdown of hits on striplines between types of particles for ILC (14 mrad crossing angle IR) and Method A. . . . 100
5.3 Number of hits broken down by stripline for Method A. . . . 100

6.1 An estimate of fluxes at the low-Z mask with upstream aluminium foils. . . . 117
6.2 Estimates for Method B based on Method A results . . . 118
6.3 Parameters m and n for Method B results . . . 123
6.4 Parameter $\bar{D}$ for the foils experiment with processors with a beam near the centre of the beampipe . . . 125
6.5 Parameter $\bar{D}$ for the foils experiment with processors at a small offset . . . 125
6.6 Breakdown of hits on striplines between types of particles for ILC and Method B. . . . 127
6.7 Number of hits per stripline for Method B. . . . 128

9.1 A summary of FONT test beam results from NLCTA and ATF . . . 154
9.2 A summary of EM background methods and results for stripline tests . . . 157

Chapter 1

Introduction

1.1 Particle physics and future colliders

Particle physics is on the verge of extending knowledge to the terascale, energies of tera-electronvolts. The Large Hadron Collider (LHC) will collide protons up to a centre of mass energy of 14 TeV and make discoveries. Predicted particles such as the Higgs, weakly interacting massive particles (WIMPs) and supersymmetric (SUSY) particles may be found. But it is up to the International Linear Collider (ILC) to measure the properties of the LHC discoveries, the precision masses and the couplings, without assuming models in the process, to determine whether the particles discovered are parts of larger families, to differentiate between the theories and to delve into CP-violation. Both machines working together should be able to shed light on undiscovered principles of nature, dark matter, extra dimensions, unification at energies around 10^{15} GeV, the families of particles, the origin of the universe and the dominance of matter over anti-matter.

1.1.1 The Standard Model

The current theory of fundamental particles and their interactions, known as the Standard Model (SM) [1], has been hugely successful. The SM contains (table 1.1) twelve fermions and four vector bosons mediating three elementary forces: strong, weak and electromagnetic. Seven of these particles (the charm quarks, bottom quarks, top quarks, tau neutrinos, gluons and the W and Z bosons) were predicted by the SM before they were discovered. There is also the scalar boson known as the Higgs that gives the fermions mass within the SM and breaks the electroweak symmetry. This Higgs boson is yet to be discovered.

There is a force not included in the SM: gravity. Plus, there are at least 19 parameters that need to be measured and put in by hand, not fundamentally derived. Despite its success to date, the SM is an incomplete description of the particles and forces in the universe.

Fermions					
Leptons			Quarks		
ν_e	ν_μ	ν_τ	u	s	t
e	μ	τ	d	c	b

Force	Mediating Boson
Weak	$W^{\pm}$, Z^0
Electromagnetic	γ
Strong	gluons
Higgs	H^0

Table 1.1: The Standard Model [2].

1.1.2 Why look towards the Terascale?

Particle physics knowledge, as summarised in the SM, is missing some vital parts. There is much more to be discovered and there are various hints that the place to look next is in the region from 100 GeV to the TeV scale.

Higgs Boson

The Higgs mechanism [3] specifies a potential for the vacuum state leading to spontaneous symmetry breaking of the electroweak force. The Higgs boson and the W and Z bosons acquire masses. The Higgs mass, however, is not predicted and until it is found, the Standard Model is not complete.

The Higgs mechanism introduces longitudinal polarisation to the bosons which mediate electroweak processes at high energy. This breaks unitarity *unless* the Higgs is light and couples to the fermions and bosons as predicted in the SM, thereby cancelling processes and leading to finite cross-sections [4]. In order to satisfy unitarity in the scattering of longitudinal W and Z bosons ($2W_L^+W_L^- + Z_LZ_L$), the Higgs mass must be < 780 GeV [5]. Otherwise, the Standard Model fails around 1 TeV. New physics around 1 TeV could also solve this unitarity problem but there is no theory that generates the necessary cancellations as naturally as the "light" Higgs. Therefore, SM theory requires a Higgs under 1 TeV or, failing that, there **must** be new physics around 1 TeV.

However, the Higgs in the SM is allowed to have an infinite mass in the absence of fine tuning [4]. The "Hierarchy Problem" creates an infinite Higgs mass via fermion loops, where the fermions can have any momenta and give infinite and diverging mass corrections. It becomes necessary to impose an energy cut-off after which the SM fails and new physics exists. Using the Planck mass as the point where the SM fails produces a Higgs mass nearly as high as the Planck mass, much larger than the light Higgs required to satisfy unitarity. Therefore there must be new physics to stabilise the light Higgs mass and it is expected around 1 TeV.

Experimental searches for the SM Higgs have narrowed the range of its mass as depicted in figure 1.1(a). Direct searches at the Large Electron-Positron Collider (LEP) showed a lower limit (95% confidence level) of 114 GeV [6]. Precise measurements of electroweak observables with recent measurements of the top mass and W boson mass at the Tevatron [7] have suggested an upper limit of 144 GeV (also at the 95% confidence level).

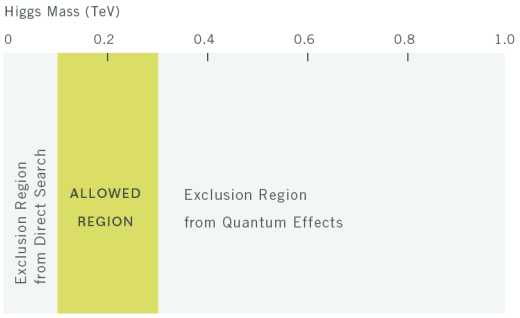

(a) The mass range of the SM Higgs is shown as the coloured region bounded by direct Higgs searches at the lower limit and precision measurements of electroweak observables at the higher limit. Recent data has narrowed the window further to 114 - 144 GeV [7].

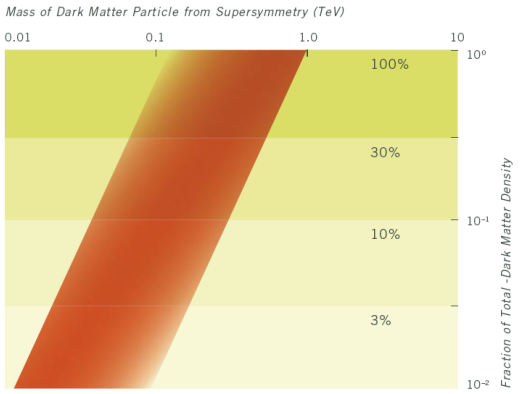

(b) The mass of SUSY dark matter candidates versus the amount of observed dark matter in the universe that they can account for. The shaded region roughly indicates the theoretically allowed values for the amount of each SUSY mass left over from the Big Bang as a fraction of the experimentally observed dark matter.

Figure 1.1: The terascale is predicted to contain the Higgs and dark matter candidates [8].

Supersymmetry

The hierarchy problem can be solved with Supersymmetry [4] (SUSY) which, in the minimal supersymmetric model, introduces two scalars for every fermion with matching couplings to cancel the diverging mass terms. Five physical Higgs are predicted: H^+, H^-, A°, h° and H° (other supersymmetry theories can predict more). In general SUSY theories, the lightest Higgs (h°) is predicted to be under 200 GeV and other supersymmetric partners are predicted to be under 1 TeV [6].

If this is the new physics required to stabilise the Higgs mass, the terascale is the place to look.

Dark Matter

Astrophysical observations indicate that not only is dark (non-luminous and non-absorbing) matter present in the universe but it is more than five times more common than baryonic matter [9]. By measuring the density of the dark matter particles (the thermal relic density) and invoking theories independent of particle physics, astrophysics studies suggest that dark matter masses lie under 1 TeV [10]. Dark matter candidates that arise from particle physics theories include weakly interacting massive particles with masses between 10 GeV and 1 TeV. The most likely candidate is the lightest supersymmetric particle with proposed mass below 1 TeV [6]. As shown in figure 1.1(b), SUSY particles with terascale masses could account for the vast proportion of observed dark matter. Other dark matter candidates include Kaluza-Klein particles (also with a predicted mass below 1 TeV) [8].

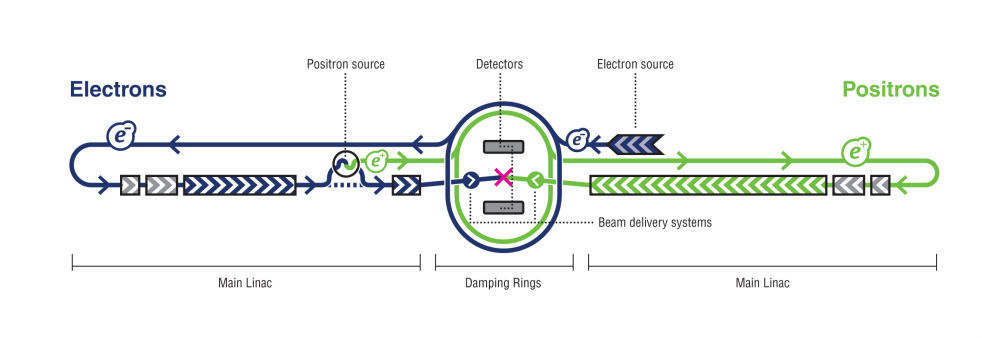

Figure 1.2: A schematic of the ILC layout [13].

The convergence of astrophysics and particle physics predictions points to the terascale as an extremely promising area to search for dark matter.

Grand Unified Theories

Precise measurements of the SM couplings demonstrated that the strong, electromagnetic and weak forces did not unify at one point at very high energies [6]. The coupling constants do meet, however, in many Grand Unified Theories (GUTs) such as supersymmetry and other models that introduce new physics around 1 TeV.

The discovery of terascale physics could lead neatly to unification of forces at higher energy scales or hold new surprises.

1.1.3 What is the ILC?

The International Linear Collider (ILC) is a proposed high energy electron-positron collider with centre of mass energies $\sqrt{s}$ from 200 to 500 GeV or 1 TeV with the proposed future upgrade. The $\sqrt{s}$ and polarisation of the electron beam (if required) will be controllable at the 0.1% level [11].

The ILC uses 11 km linear accelerators (linacs) to accelerate the electrons and positrons. It was decided to use superconducting radio frequency (RF) accelerating cavities following the recommendation of the International Technology Recommendation Panel in 2004 [12].

Figure 1.2 shows a schematic of the ILC. A photocathode DC gun is used as the electron source (with greater than 80% polarisation) and the positrons are produced from an undulator. The electrons and positrons enter damping rings of 6.7 km circumference. There is beam transport to the linac which comprises of 31.5 MV/m superconducting cavities. There is 4.5 km of beam delivery system bringing the two beams to the interaction point (IP).

The ILC has been designed to deliver 500 fb^{-1} of integrated luminosity within four years. Its pulse rate is 5 Hz and each pulse is $\sim$1 ms long, comprising 1000-6000 bunches each of $(1-2)\times10^{10}$ electrons or positrons. A plane of accelerator parameters has been defined over which the ILC can operate. These accelerator parameter schemes are shown in tables 1.2

Parameter	1.TESLA	2.USSC
N	2×10^{10}	2×10^{10}
N bunches	2820	2820
Bunch spacing (ns)	336.9	336.9
IP σ_x (nm)	554	543
IP σ_y (nm)	5.0	5.7
IP σ_z (μm)	300	300
Luminosity ($m^{-2}s^{-1}$)	2.94×10^{38}	2.57×10^{38}

Parameter	3.Nominal	4.Low Q	5.Large Y	6.Low P	7.High Lum
N particles	2×10^{10}	1×10^{10}	2×10^{10}	2×10^{10}	2×10^{10}
N bunches	2820	5640	2820	1330	2820
Bunch spacing (ns)	307.7	153.8	307.7	461.5	307.7
IP σ_x (nm)	655	495	495	452	452
IP σ_y (nm)	5.7	3.5	8.1	3.8	3.5
IP σ_z (μm)	300	150	500	200	150
Luminosity ($m^{-2}s^{-1}$)	2.03×10^{38}	2.01×10^{38}	2.00×10^{38}	2.05×10^{38}	4.92×10^{38}

Table 1.2: Shown are a few parameters of interest for the seven schemes proposed for the 500 GeV operation of the ILC with 31.5 MV/m gradient [14]. Two schemes are historical parameter sets described in preliminary documentation (the TESLA Technical Design Report [15], TESLA, and the US Technology Options Study [16], USSC). The remaining five schemes describe a "plane" that allows for flexibility when the accelerator is in operation. For each parameter in this plane, the lowest value has been highlighted (dark grey) and the highest value has been highlighted (light grey).

(for the 500 GeV centre of mass ILC) and 1.3 (for the proposed 1 TeV upgrade).

1.1.4 Why a linear collider?

The electron-positron collider has to be a linear accelerator and not a circular one at these energies. In a circular accelerator, such as the LHC, the collision particles are accelerated in a circle losing energy through synchrotron radiation due to the transverse acceleration[1] at a rate proportional to γ^4 (where γ is the Lorentz factor E/m_0c^2) as shown in equation 1.1 [17]. P_γ is the power lost to the synchrotron radiation, e is the particle charge, β is the particle velocity as a fraction of the speed of light and ρ is the bending radius. Since the rate is inversely proportional to the mass to the power of four and directly proportional to the energy to the power of four, it poses a limit on the energy of light particles such as electrons and positrons that can be accelerated in a circular accelerator. Low mass and high energy particles such as 250 GeV electrons or positrons will lose a lot of energy through synchrotron radiation, which is deposited into the vacuum components of the collider and needs to be replaced in the beam by the accelerating cavities. For the LEP ring (with circumference 27 km [18]), a 250 GeV electron (or positron) beam loses 80 GeV through synchrotron

[1]Energy is also lost due to acceleration parallel to the direction of the particle (as in a linear accelerator) but it only depends on the acceleration force. For the same acceleration force, transverse acceleration leads to more power in synchrotron radiation by a factor of γ^2, which is very large for these relativistic machines. The loss of energy due to synchrotron radiation from parallel acceleration is not significant [17].

Parameter	8.TESLA	9.USSC
N particles	1.4×10^{10}	2×10^{10}
N bunches	4886	2820
Bunch spacing (ns)	175.4	336.9
IP σ_x (nm)	392	489
IP σ_y (nm)	2.8	4.0
IP σ_z (μm)	300	300
Luminosity ($m^{-2}s^{-1}$)	5.07×10^{38}	3.81×10^{38}

Parameter	10.Nominal	11.Low Q	12.Large Y	13.Low P	14.High Lum
N particles	2×10^{10}	1×10^{10}	2×10^{10}	2×10^{10}	2×10^{10}
N bunches	2820	5640	2820	1330	2820
Bunch spacing (ns)	307.7	153.8	307.7	461.5	307.7
IP σ_x (nm)	554	392	367	350	320
IP σ_y (nm)	3.5	2.5	7.0	2.7	2.5
IP σ_z (μm)	300	150	600	200	150
Luminosity ($m^{-2}s^{-1}$)	2.82×10^{38}	2.84×10^{38}	2.92×10^{38}	2.92×10^{38}	7.88×10^{38}

Table 1.3: Shown are a few parameters of interest for the seven schemes proposed for the energy upgraded operation of the ILC with 31.5 MV/m gradient [14]. Two schemes are historical parameter sets described in preliminary documentation (the TESLA Technical Design Report [15], TESLA, and the US Technology Options Study [16], USSC). The TESLA scheme is for 800 GeV and all other schemes are for 1 TeV centre of mass energy. The remaining five schemes describe a "plane" that allows for flexibility when the accelerator is in operation. For each parameter in this plane, the lowest value has been highlighted (dark grey) and the highest value has been highlighted (light grey).

radiation per turn and a 365 GeV beam would need to have its full beam energy replaced by accelerating cavities in every turn. However, the amount of power deposited in the collider components creates the strictest limit to how much synchrotron radiation can be tolerated. LEP was running at the limit of the hardware constituents with 100 GeV beam energy by depositing 18 MW through synchrotron radiation [18]. With 250 GeV beams forty times this power would be dumped.

$$P_\gamma = \frac{2}{3} e^2 \frac{c\beta^4\gamma^4}{\rho^2} \tag{1.1}$$

1.1.5 Why an electron-positron collider?

The LHC at CERN is a discovery machine capable of finding the evidence for the Higgs, dark matter candidates, extra dimensions, supersymmetric particles and other new physics. However, proton on proton colliders do not have great sensitivity. The nominal centre of mass energy of the collider is 14 TeV but the actual interactions involve the particles within the proton, the quarks and gluons, whose momenta are not precisely known in each event. Although the mass of the Higgs can be measured to 0.1% [19] and the couplings to gauge bosons and fermions measured to 10-40% [20], the Higgs self-coupling cannot be measured and theoretical assumptions have to be made. It would also be difficult to tell a SM Higgs from a Higgs from another model such as the h^0 of MSSM.

Electron-positron colliders are measuring machines with greater sensitivity. The collisions are of a known energy and polarisation. There are also lower event rates, less background and lower radiation doses, allowing precision measurements, tracking and particle identification. It is required to take the LHC discoveries a step further, to complement the LHC and to understand the physics behind the discoveries.

The ILC measures properties to greater accuracy plus properties that the LHC cannot measure such as the Higgs trilinear self-coupling, Higgs decay branching ratios and total decay width and absolute values of coupling constants without assuming models [11]. Subtle effects in the measurements below 1 TeV could hold clues for physics at even higher energies and these would be apparent with the precision ILC measurements. For example, some models that include extra dimension predict a particle called the radion which mixes with the Higgs and reduces the strength of the interaction between the Higgs and SM particles [11]. Therefore, precision ILC measurements of the interactions can indicate the presence of extra dimensions.

The ILC is better equipped than the LHC to answer the cosmological questions of how many dimensions there are. The LHC is able to detect Kaluza-Klein gravitons, which are one signature that indicates extra dimensions, but it cannot extract information about them since the fundamental particles involved in the collision could have energies above the scale where this new physics comes into play. The ILC, however, with its e^+e^- collision of known energy, can measure the number of extra dimensions and their shape and size [21].

Likewise, the ILC can answer the question of the observed dark matter in the universe.

The LHC can only find dark matter candidates and derive information from the discoveries assuming theoretical models; the ILC would be needed to provide the model-independent measurements that reveal how much the dark matter candidates contribute to the dark matter in the universe and so whether they account fully for the astrophysics observations of dark matter [21].

SUSY decays are complicated and their cascade decay products hide the properties of the supersymmetric particles. The ILC can focus on one supersymmetric partner at a time by tuning the beam energy to scan the energies where they are produced [8]. It can then make precision measurements of the superparticle's mass, spin and couplings to confirm that it is the partner to a SM particle and also gather information on how the symmetry is broken. The LHC lacks the resolving power to measure superparticle interactions to the level of precision required to test the symmetry of the SUSY theory, due to the complicated decays and high SUSY backgrounds [21].

Greater sources of CP violation need to be found to explain why there is more matter than anti-matter in the universe, such as a family of Higgs or Higgs-like particles or SUSY. It will be hard to extract CP properties from particle decays and interactions in the Higgs sector or with SUSY sectors without precisely knowing the initial conditions. The ILC could be the only collider able to extract information about CP violation this way [8].

The ILC is more than just the second act though; running alongside the LHC it can feed back analyses to improve the LHC's identification and measurement of particles (or sparticles) and their properties [22].

1.2 Backgrounds at the ILC Interaction Point

Backgrounds are unavoidable. These unwanted particles and signals in detectors come from sources including off-orbit particles in the beam tails interacting near the IP, muons from beam tail collimation and synchrotron radiation photons; but the greatest contribution to IP backgrounds comes from the beam-beam interaction producing beamstrahlung and e^+e^- pairs. These are mainly forward and background going particles with little transverse momentum. This results in a "dead cone" in the very forward region of a detector where instrumentation is difficult.

1.2.1 Principal sources of IP backgrounds

Close to the IP the most important backgrounds are from the beam-beam interaction, which includes the processes beamstrahlung, pair generation, hadron production and bremsstrahlung.

Beamstrahlung

During an e^+e^- collision, each bunch is deformed under the high electromagnetic field of the other, radiating photons in a process termed beamstrahlung. Beamstrahlung is a stochas-

tic process where the probability that a particle radiates a photon of a certain energy is dependent on the field density of an oncoming beam of charged particles. The amount of beamstrahlung increases with more charged particles in the oncoming bunch and the bunch dimensions (equation 1.2) where B is the magnetic field strength of the oncoming (Gaussian) bunch, N_b the number of electrons (or positrons) in it and $\sigma_{x,y,z}$, its dimensions [23].

$$B \simeq \frac{1}{4\pi\varepsilon_0 c}\frac{5eN_b}{6\sigma_z(\sigma_x+\sigma_y)} \tag{1.2}$$

Beamstrahlung results in a beam energy spread which would be carried down to analysis as a lack of precision in measurement of masses. To suppress beamstrahlung without changing the luminosity ($\sim \frac{1}{\sigma_x\sigma_y}$), flat beams are used so that $\sigma_y << \sigma_x$.

The majority of beamstrahlung photons form a narrow cone that follows the beam straight down the extraction line, away from the IP [11].

Pair Generation

The beamstrahlung photons can exchange energy-momentum with electromagnetic fields producing e^+e^- pairs. This is called coherent pair production. Calculations show that this is in fact negligible for centre of mass energies under 1 TeV.

Incoherent pair production processes dominate in beam-beam interactions at ILC energies. Approximately 10^5 e^+e^- pairs [24] are produced through individual scattering events such as two real beamstrahlung photons (the Breit-Wheeler process, equation 1.3), one real photon and one virtual photon (the Bethe-Heitler process, equation 1.4) and two virtual photons (the Landau-Lifshitz process, equation 1.5) [23].

$$\gamma\gamma \rightarrow e^+e^- \tag{1.3}$$

$$e^{\pm}\gamma \rightarrow e^{\pm}e^+e^- \tag{1.4}$$

$$e^+e^- \rightarrow e^+e^-e^+e^- \tag{1.5}$$

Simulations of the beam-beam interaction at the ILC have shown the Bethe-Heitler process to account for over 70% of the pairs [25].

After production, the pairs experience the electromagnetic fields of the oncoming bunch. The particle that is the same charge as the oncoming bunch oscillates in its field. The particle that is the opposite charge as the oncoming bunch is deflected and so has slightly higher transverse momentum [26].

Hadron and Minijet Production

Beamstrahlung photons interact to produce hadrons or jets that are of low energies ("minijets") compared to jets from the e^+e^- interaction at the IP [24]. The hadrons are mostly produced with small transverse momentum and low energies and they continue along the

beam direction. Minijets have large transverse momentum. Both are produced at low rates: one hadronic event only occurs every few bunch crossings in simulations with TESLA parameters [24].

Bremsstrahlung

Bremsstrahlung, literally braking radiation, occurs when an individual particle scatters off the field of another particle and emits a photon. In the beam-beam interaction, electrons and positrons can scatter with either the initial or final states emitting a photon and hence losing energy through bremsstrahlung ($e^+e^- \rightarrow e^+e^-\gamma$). This results in a spent beam with particles in a low energy tail [24] plus bremsstrahlung photons.

This process are sometimes be referred to as Compton scattering of an electron with a virtual photon [24] or radiative Bhabha scattering [27]. The electrons and positrons that have lost energy through bremsstrahlung are referred to as bremsstrahlung leptons in this thesis.

1.3 The Beam-Beam Effect on Luminosity

The beam-beam interaction causes backgrounds and also affects the luminosity.

The field of the oncoming beam is transverse due to Lorentz contraction of the associated EM fields. The longitudinal coordinates of the two beams therefore need to be essentially the same for the charged particles in one beam to experience the electromagnetic field of the another. The beam-beam effect therefore occurs at the IP and depends greatly on the field created by the colliding bunches which, as in equation 1.2, depends on the dimensions of the beam and number of charged particles in it.

A useful parameter to describe the beam-beam interaction is the disruption factor $D_{x(y)}$ defined in equation 1.6, where r_e is the classical electron radius and the other variables as defined before [28]. For the ILC Nominal 500 GeV accelerator parameter set, D_x is 0.16 and D_y 18.5 [14].

$$D_{x(y)} \equiv \frac{2N_b r_e}{\gamma} \frac{\sigma_z}{\sigma_{x(y)}(\sigma_x + \sigma_y)} \tag{1.6}$$

If $D << 1$ (as is the case with D_x) and the beams are oppositely charged, the beam acts like a thin lens, focusing the beam, due to the mutual attraction of opposite charges. This is the "pinch effect" and it enhances the luminosity by about a factor of two.

If $1 < D \leq 10$, the force between the attracted beams is large enough that the kick it produces brings the beam centres closer and small offsets in their incoming trajectories do not result in a significant loss in luminosity.

However, at the ILC, $D_y = 18.5$ and the beam-beam effects lead to an instability known as the kink instability. Internal beam distortions are resonantly amplified and the beams

oscillate in the vertical plane. This leads to a situation where even a small offset in position or angle at the IP results in a large luminosity loss [29].

The outgoing angle of the full energy particles (Θ_y) after this beam-beam kick is related to the initial offset of the two beams in position (Δ_y) as shown in equation 1.7 [30].

$$\Theta_y = \frac{1}{2} D_y F \frac{\Delta_y}{\sigma_z} \tag{1.7}$$

For small position offsets, F is a constant and the relationship between position offset and angle kick is linear. F is empirically found through simulations to depend on the disruption factor such that the larger D_y, the larger the region where the kick is proportional to the position offset. This is a useful way of measuring the position offset at the IP given the position downstream as discussed in section 1.4.2.

1.3.1 GUINEA PIG simulation of the beam-beam interaction

GUINEA PIG [27] simulates the beam-beam interaction of e^+ and e^- bunches with a given set of input parameters. This simulation tool includes the pinch effect, beam-beam kick, beamstrahlung, pair creation, bremsstrahlung, minijets and hadronic backgrounds [24]. The pairs are tracked through the fields of the beams.

The output includes luminosity information, the disrupted outgoing beams and backgrounds. The output for the backgrounds is divided into separate files: pairs, bremsstrahlung leptons, hadrons, minijets and photons. The energy distribution for these outputs is shown in figure 1.3(a) for the ILC with 500 GeV centre of mass energy. Here, 0.005% of the disrupted beam (black) is shown, where energy loss has been due to beamstrahlung. The backgrounds are for a full bunch crossing of 2×10^{10} electrons and 2×10^{10} positrons. Bremsstrahlung leptons (red) follow the exiting beam. The highest backgrounds are beamstrahlung and bremsstrahlung photons (light blue) and electron and positron pairs (dark blue). Hadron and minijet backgrounds (green) are low.

Figure 1.3(b) shows the angle distribution of the pairs and photons with respect to the outgoing angle of the beam. The photons are in a narrow cone that exits with the beam whereas the pairs have transverse momentum. The pairs from the beam-beam interaction are therefore a concern in terms of producing secondary backgrounds by interacting with materials in the interaction region.

There are some limitations to GUINEA PIG. Approximations are used to physical processes with many second order non-linear processes not included [25]. Polarisation of the beams is not considered. Work done with a similar beam-beam interaction simulation tool, CAIN [31], has indicated that including polarisation would reduce the pair backgrounds by 10-20% [25]. The reduction is seen as fewer low energy and low transverse momentum pairs.

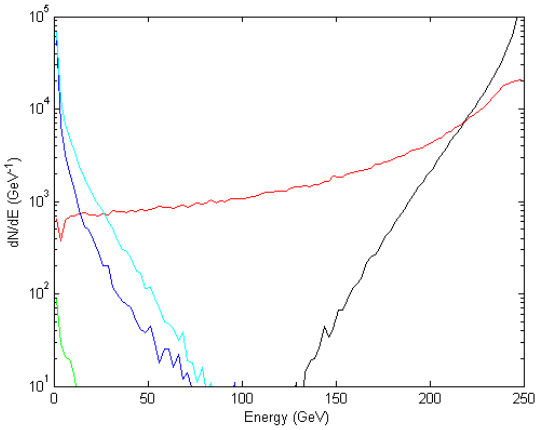

(a) Number versus Energy for GUINEA PIG simulation outputs of a simulation of the ILC with 500 GeV centre of mass energy. Black: 0.005% of the spent beam. Red: Bremsstrahlung leptons. Light Blue/Cyan: Photons. Blue: Pairs. Green: Hadrons and minijets.

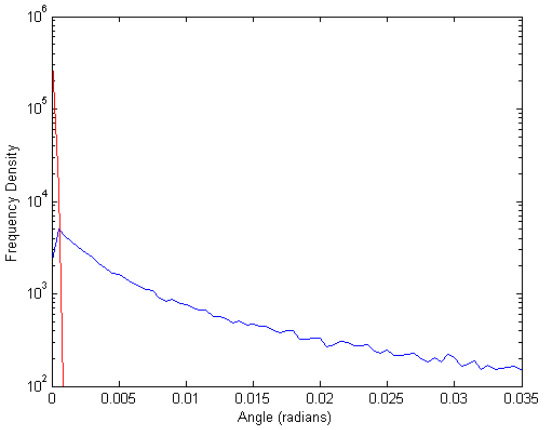

(b) The distribution of angle with respect to the outgoing beam of pairs (blue) and photons (red).

Figure 1.3: The output of a GUINEA PIG simulation of the beam-beam interaction for the ILC with 500 GeV centre of mass energy.

1.4 Feedback in the ILC Beam Delivery System

The beams at the ILC can be as small as 2.5 nm in σ_y (see table 1.3) so to achieve design luminosity, the beams must be stable in y at the IP at the sub-nanometre level. As shown in figure 1.4, the luminosity loss with a 0.5 σ_y offset is 10% according to beam-beam simulations with GUINEA PIG [27]. Keeping the beam stable within 0.1 σ_y would preserve most of the luminosity. The angle offset of the colliding beams also affects luminosity as shown in figure 1.5 which shows data from GUINEA PIG beam-beam simulations. Angle stability is therefore also required with the target stability being 0.1 σ'_y [32].

These stability goals are possible with multiple feedbacks in the beam delivery system (BDS) as described in 1.4.2.

1.4.1 Ground Motion and Cultural Noise Issues for Stabilisation

Stability must be maintained in the presence of component jitter, particularly in the BDS region where the optics are strong and magnet jitter has a large effect on the beam. Beamline components jitter due to ground motion (with wavelengths that are short compared to the distances between components) and noise from hardware both in and near the tunnel. This noise can be amplified by supports and common girders. Ground motion studies have been performed at various sites including the Stanford Linear Accelerator Center (SLAC) [34] to understand the extent of the problem for linear colliders.

Studies of the combined cultural noise and ground motion at SLAC show that natural ground motion and motion from the facilities tends to decrease in amplitude as frequency

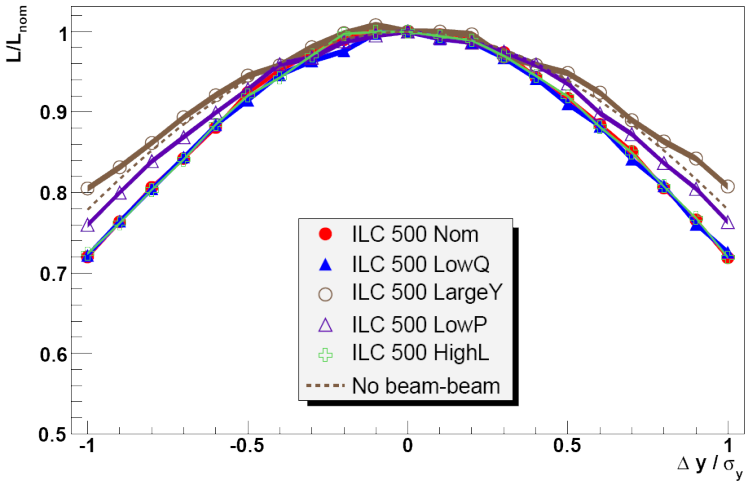

Figure 1.4: The luminosity normalised to its maximum vs vertical position offset as a fraction of the RMS beam size in y [33]. The five parameter sets for the 500 GeV centre of mass ILC are shown (as described in table 1.2) along with the calculation for luminosity ignoring the beam-beam effect.

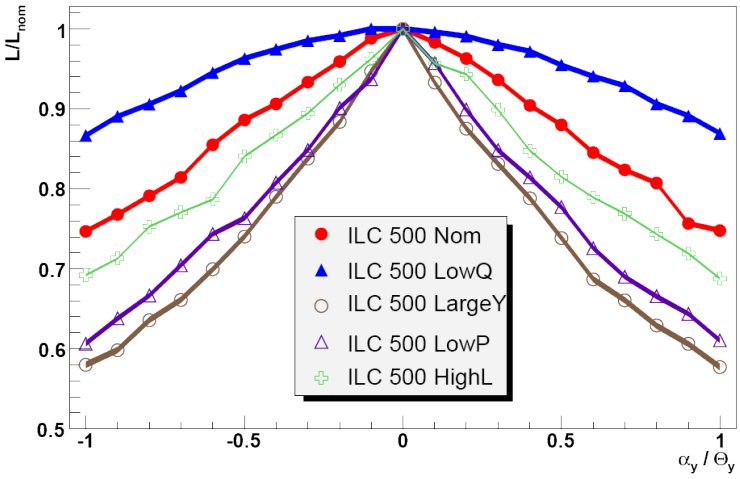

Figure 1.5: The luminosity normalised to its maximum vs vertical angle offset as a fraction of the RMS beam divergence in y [33]. The five parameter sets for the 500 GeV centre of mass ILC are shown (schemes 3-7 as described in table 1.2).

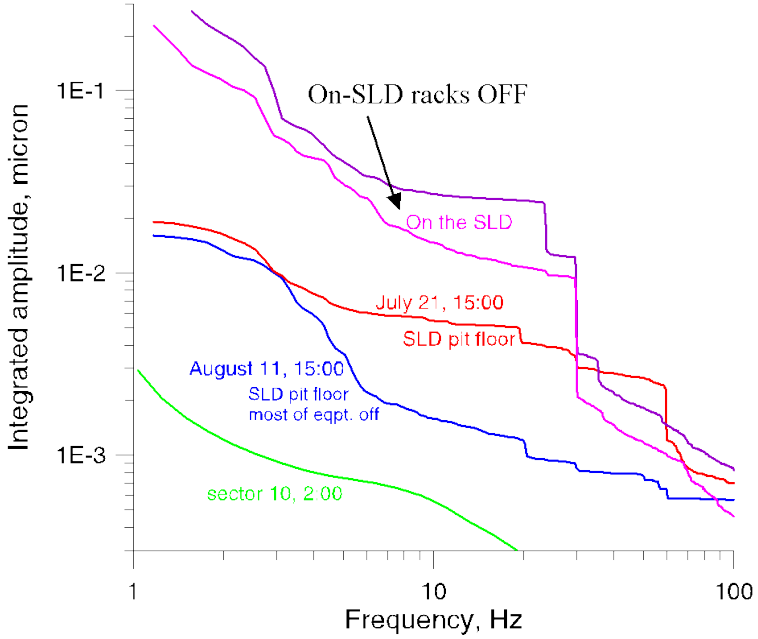

Figure 1.6: The integrated amplitude of the ground motion versus frequency is shown for various sites at SLAC [34]. The green "sector 10" curve is from data recorded at a very quiet location and so is more representative of the natural ground motion. The other curves are from data recorded on the SLAC Large Detector (SLD) with the electronics on (purple) and off (pink) and on the SLD pit floor with equipment on (red) and off (blue).

increases, as shown in figure 1.6. Most of the noise is local; the location with the least human activity (sector 10 of the SLAC linac, shown in green) has motion two orders of magnitude less than at the busiest location (the SLD detector, shown in purple), so careful design of the detector and facilities at the ILC should reduce vibrations. Further studies looking at the correlation between two points 100 m apart indicate that above 1 Hz, the wavelength of the vibrations is short enough that the effect on the beamline components is noise-like, figure 1.7. Below 1 Hz, the wavelength tends to be long so the correlation is very strong.

Being a dynamic effect, this component jitter requires a dynamic correction that steers the beam orbit within the timescale of the effect. Figure 1.6 indicates that the timescale of the nanometre-level displacement from cultural noise can be faster than the ILC (pulse) repetition rate of 5 Hz but much slower than the bunch frequency, nominally 3.25 MHz. The orbit of one bunch is therefore correlated with the next. However, successive pulse trains will be slightly uncorrelated due to this noise. A bunch-to-bunch dynamic correction based on feedback is therefore possible to maintain stability during the pulse train in the presence of noise from hardware and a 5 Hz feedback will be able to correct for the slow ground motion.

Figure 1.8 shows the luminosity (relative to the maximum) over time from simulations of the TESLA machine in the presence of ground motion and cultural noise. Luminosity is quickly lost without any feedback correction. The bunch-to-bunch correction (labeled IP FFBK) does not maintain the luminosity for long as the noise that is introduced between pulses alters the beam orbit in the BDS. Together the bunch-to-bunch feedback and a slow orbit correction can maintain stability and hence luminosity for a day before dispersion from

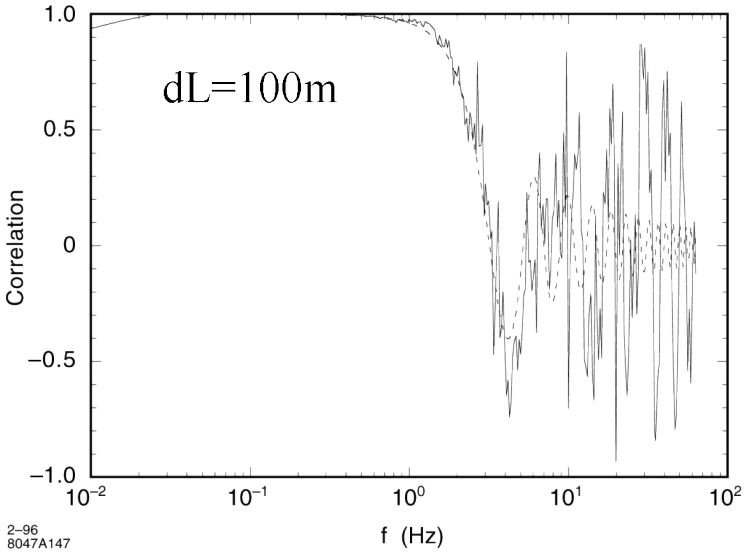

Figure 1.7: The correlation in ground movement at two points 100 m apart vs frequency [34]. The study was done in the Stanford Linear Collider tunnel.

the corrector kicks causes it to drop [15].

1.4.2 Intra-train Feedbacks at the ILC

The IP offset-correction feedback and IP angle-correction feedback are beam-based intra-(bunch)train feedbacks. They use a beam position monitor (BPM) to measure the position offset of the beam and deliver a kick to later bunches.

The hardware for IP offset-correction feedback consists of a BPM near the IP that measures the position of the outgoing bunches and a stripline kicker situated in the Final Focus Section that steers incoming bunches. This is shown schematically in figure 1.9 with an outgoing beam measured by a BPM, the signal processed and sent to a kicker on the incoming beam. The feedback BPM needs to be close to the IP to reduce latency, that is to provide fast corrections before too many bunches are lost. Having the BPM before any optics also helps to keep the correction simple as the position at the BPM is directly related to the position at the IP. Simulations of the beam-beam interaction with GUINEA-PIG have shown that an offset at the nanometre level at the IP produces a beam-beam kick that changes the angle of the exiting beam by tens of micro-radians [11]. With a BPM approximately three metres downstream, this nanometre offset is an offset of tens of microns in the BPM. Therefore, sub-nanometre stability at the IP (target stability is the 0.1 σ level) can be achieved with micron-level resolution in a BPM. The beams need to be within a certain range of each other for the fast position feedback to be effective. Simulations in GUINEA-PIG for each of the seven parameter sets at the 500 GeV ILC (see table 1.2) produced the amount of beam-beam kick expected for offsets of the beams in y as shown in figure 1.10. The feedbacks work most efficiently where angle kick increases with offset which is up to a 30 nm offset for the Low-Q set (shown in cyan) and up to a 170 nm offset in the Large Y set (shown in magenta) [32].

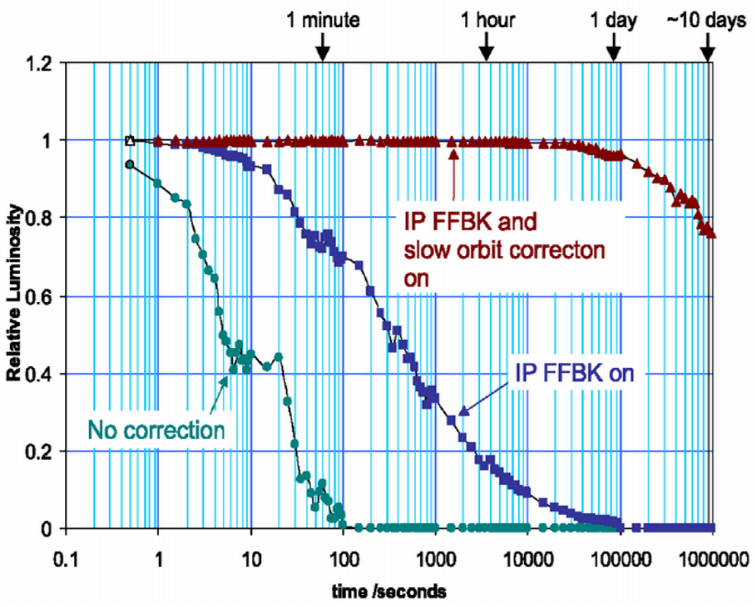

Figure 1.8: The luminosity vs time in the presence of ground motion [15]. Three cases are shown: without correction, with fast feedback correction of IP position and angle offset, and both fast feedback and slow feedback.

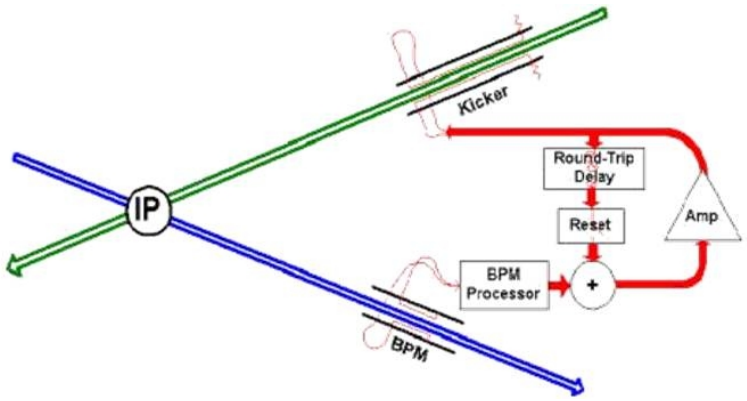

Figure 1.9: Block diagram of IP position feedback with the BPM on the extraction line and the kicker on the incoming beamline [35].

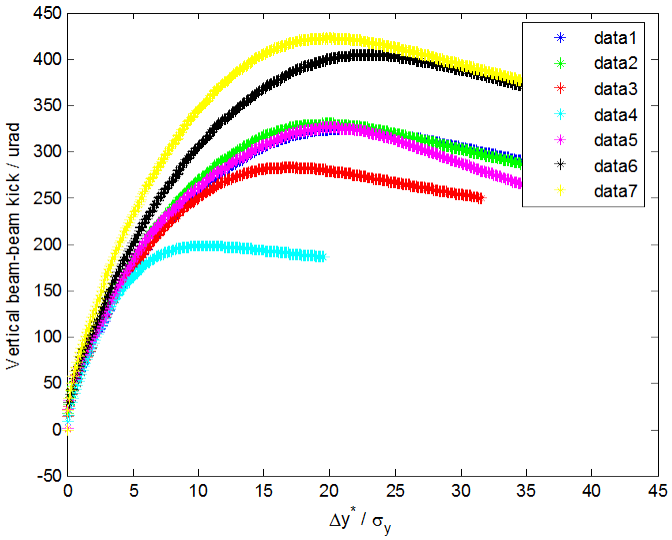

Figure 1.10: The angle that the beam-beam interaction gives to the beams versus the normalised vertical position offset [32]. The seven parameter sets as described in table 1.2 are shown. 1. TESLA (blue), 2. USSC (green), 3. Nominal (red), 4. Low Q (cyan), 5. Large Y (magenta), 6. Low P (black) and 7. High Luminosity (yellow).

The IP angle-correction feedback uses a stripline kicker at the same phase as the IP so that changes in angle given at the kicker relate to those given at the IP. The BPM needs to be downstream of the kicker and at a phase 90 degrees out of phase with the kicker and the IP. The angle offset will appear as a position offset in the BPM at that phase advance, so by zeroing the position in the BPM the angle at the IP is zeroed. This system will be placed at the entrance to the Final Focus System 1800 m upstream of the IP [32]. This is to take advantage of the large beta functions and hence the large position offset in the BPM, so that it is only required to have micron-level resolution for 0.1σ stability.

The capture range in which the IP offset-correction feedback works defines the performance requirements of the slow 5 Hz feedbacks. The 5 Hz feedbacks need to be able to recover the orbit to within this range. Once the slow feedbacks have converged within the range required by the fast feedbacks, the fast feedbacks will work.

Simulations have shown the effectiveness of the IP offset and angle corrections at recovering luminosity [36]. PLACET [37] was used to simulate beam dynamics with wakefields in the ILC linac in the presence of ground motion, injection jitter and alignment errors of the accelerating cavities, quadrupoles and BPMs up to 300 μm. Then the beam dynamics through the BDS was simulated, also with PLACET, with optics as for the ILC at a 14 mrad crossing angle. Finally the beam-beam interaction at the IP was simulated with GUINEA-PIG. The feedbacks were written in Matlab and Simulink [38].

Figure 1.11 shows how, bunch by bunch, the beam is steered until luminosity is at its maximum. The initial offsets of the beam in position and angle are removed by bunch 100. After the beam has been steered to zero position and angle offset, there are scans in position and angle (around bunch 160 and 180 respectively) in case any more luminosity can be recovered. Previous simulations [32] have shown that some luminosity is recovered this way

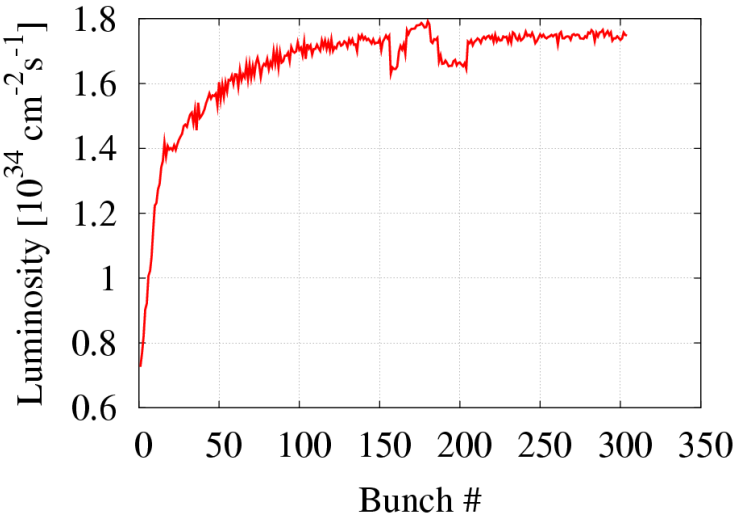

Figure 1.11: The luminosity versus bunch number with intra-train feedback in the presence of ground motion [36].

because wakefield effects in the TESLA accelerating cavities cause a y-z correlation within each bunch (the "banana effect"). With the beams no longer being Gaussian, the offset and angle at the IP for maximum luminosity is non-zero and scanning in the two dimensions of position and angle can optimise luminosity with the aid of a luminosity monitor. However, in the ILC linac simulation, wakefield effects appear not to be as strong [36].

It is not possible to achieve the luminosity calculated with perfect head-on collisions of Gaussian beams; the feedbacks require time to work and any bunch-to-bunch jitter will be magnified by the feedback.

The recovery of luminosity using these two fast feedbacks is less effective with greater jitter on the main linac quadrupoles. Simulations were done in PLACET for the beam dynamics in the TESLA linac (with wakefields) and the TESLA IR, and the beam-beam interaction was simulated with GUINEA-PIG [29]. Figure 1.12 shows that the luminosity decreases with increased jitter on the main linac quadrupoles (shown in red). Some luminosity (around 5%) is recovered with an offset-correction feedback (shown in green) and some more is gained through the angle-correction (blue). Scans in y (magenta) and y' (cyan) recover more luminosity but 13% is still lost at 100 nm of quadrupole jitter. The remainder can be recovered with intra-pulse feedback before the BDS (shown in black). This correction at the end of the linac and before the BDS is in both y and y' to the 0.1 σ level and is referred to as the "train straightener" [11].

1.5 Beam Position Monitors

Beam position monitors (BPMs) are a vital part of the feedback systems as well as being essential for machine diagnostics. There are many different BPMs, the most common being button, stripline and cavity.

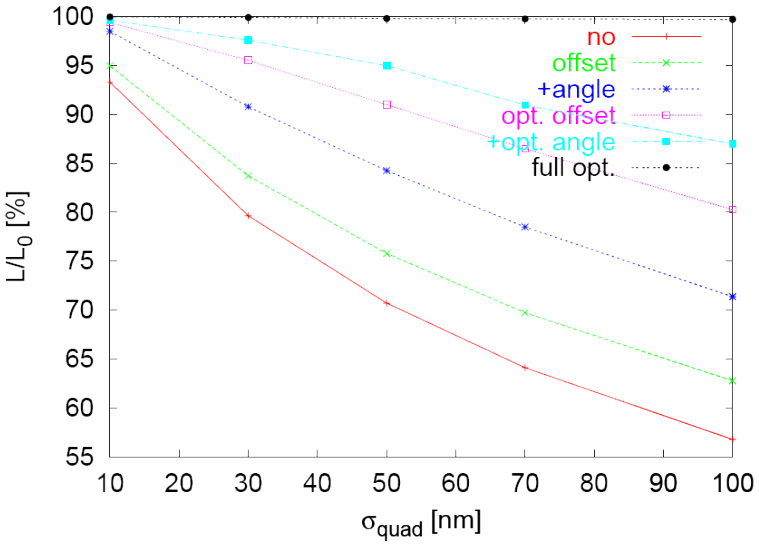

Figure 1.12: The luminosity normalised to the maximum luminosity versus RMS jitter on the main linac quadrupoles [29]. The luminosity can be recovered (from red) using feedbacks in IP y offset (green), feedbacks in IP y' offset (blue), luminosity optimisation with y (magenta), luminosity optimisation with y' (cyan) and a train straightener at the end of the linac (black).

1.5.1 Button BPMs

Button BPMs are essentially electrodes that break the continuity of the beampipe wall. As the name implies, this BPM looks like a button.

As a charged beam travels down the beampipe, associated electric and magnetic fields travel with it. The electric field is Lorentz contracted at relativistic velocities such that the electric and magnetic fields are transverse to the direction of motion [39]. This "pancake" shaped electric field intersects with the beampipe with the beam causing an induced current to travel on the wall of the beampipe. This induced current moves at the same speed as the beam. The integral of the induced current around the circumference of the beampipe is equal to the beam current but it is not distributed evenly if the particle is off-centre. The induced current can be used to monitor the position of the beam as the closer to the beampipe the beam is, the more dense the electric field and the greater the current density at that point.

The beam's induced current, travelling along the wall of the beampipe, meets a discontinuity at the button BPM and jumps the gap onto the button. The button is not grounded so the net charge on the button must be zero. A current is set up on the button BPM with one polarity when the charge hops onto the BPM and the reverse polarity when it hops off and onto the beampipe wall (as shown in figure 1.13(a) for a bunch with an approximately Gaussian longitudinal distribution) [40]. As the button BPM is very small, this bipolar current is very fast.

The signal voltage on the button BPM is affected by the capacitance of the button BPM and the signal from the BPM pickoff, usually transported far from the beampipe to the processing electrons via a cable with losses at high frequencies, does not appear as a perfect bipolar voltage signal [40]. Instead, it appears as a sharp peak followed by a small and broad

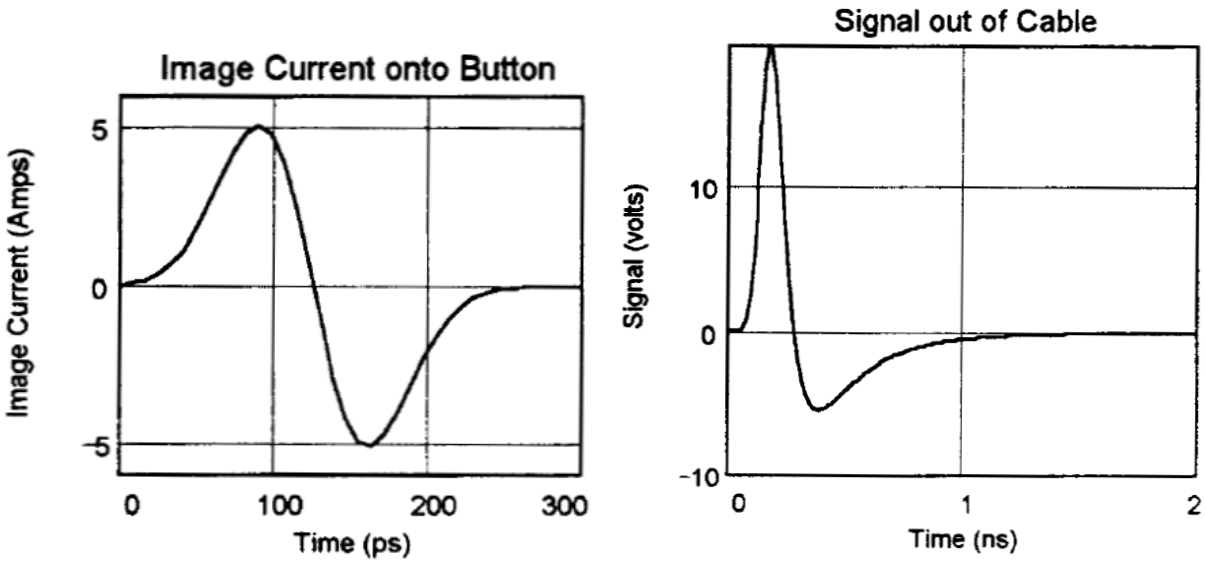

(a) The current on the button BPM with time.

(b) The signal from the button BPM after it is passed through a long cable.

Figure 1.13: The button BPM response to a passing beam of charged particles [40].

peak with the opposite polarity as shown in figure 1.13(b).

As described above, the image charge intercepted depends on the position of the beam. Therefore, the voltage signal from the button BPM can be used to monitor the beam position. The change in voltage signal at a button BPM due to a change in position is a small amount on top of a large voltage signal. Therefore the usual method of extracting the change in signal is to use two electrodes diametrically opposite each other. The difference of the signals from the two electrodes is dependent on the magnitude of the beam charge and the position offset. To remove the dependence on the beam charge, the sum of the signals (which is charge dependent only) can be used to normalise the difference signal [41].

The difference (or normalised difference) needs to be processed to near DC frequencies to be used as an indicator of position. Matlab was used to simulate a perfect processing scheme (without noise or losses) in order to find the intrinsic resolution[2] of a button BPM. It was found to be $\sim 0.5\mu$m [40] for this perfect case. Practically, this is not attainable not only due to losses and noise in the processor electronics but also due to imperfections in the construction of the button BPM and impedance mismatches.

The advantage of a button BPM is its compact size. As space is at a premium at the ILC, the button BPM is considered for the feedback BPM should a stripline BPM not fit.

1.5.2 Stripline BPMs

A stripline BPM interrupts the beampipe and intercepts the induced current similar to the button BPM. As the beam passes the stripline, the induced current moves from the beampipe to the stripline. Once the beam has passed the stripline, the induced current moves back to

[2]The resolution is the smallest deflection of the beam a BPM can measure.

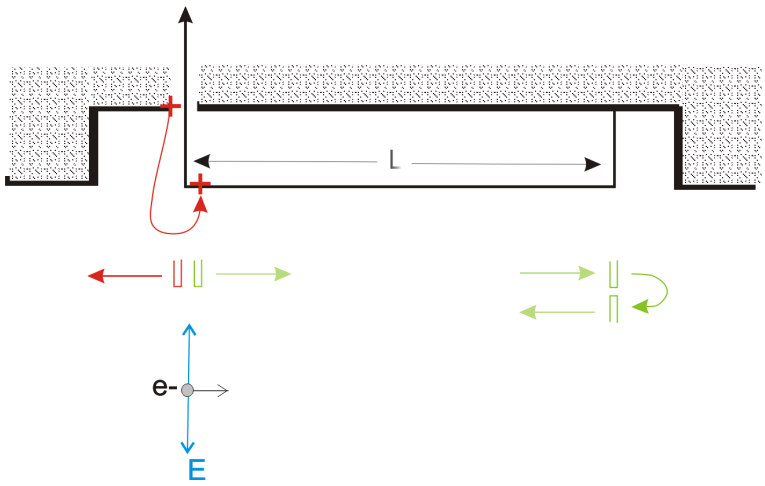

Figure 1.14: The production of a signal from an electron on a stripline with the downstream end shorted.

the beampipe.

From one stripline BPM to the next, the strips can differ in length, width and distance of the stripline from the beampipe wall. The length of the stripline affects the frequency response of the BPM as discussed in section 1.5.2. The width is often large as it is preferable to cover as much of the beampipe inner surface as possible to maximise the amount of induced charge that is on the stripline. To keep the impedance of the stripline high (standard is 50 Ω), the height of the stripline is raised from the ground plane [39]. High impedance results in good sensitivity as induced voltages are high.

Stripline designs also differ at their ends in terms of the upstream and downstream termination. The end of a stripline can be, as any transmission line, shorted, left open or terminated through a resistance (across which the voltage can be measured to extract a signal). The method of production of the stripline signal varies slightly depending on the termination [42].

Stripline BPMs have a better intrinsic resolution (∼0.05 nm) than button BPMs [35]. They are not as compact length-wise (being obviously a longer device) but are just as compact in the transverse direction making it the most likely candidate for the IP feedback BPM.

Stripline signal production

Figure 1.14 shows an electron with its "pancake" electric field (blue) approaching the upstream end of a stripline with a shorted downstream end. The induced charge (positive in charge and, when integrated over the circumference of the beampipe, equal in magnitude to the electron) follows the electron on the wall of the beampipe. The upstream end of the stripline as shown is a gap in the beampipe. Part of the induced charge (since the stripline only covers part of the beampipe) must cross the gap (as a displacement current) and continue on the stripline. The jump from wall to stripline induces a voltage of negative polarity in the stripline. The magnitude is related to the amount of induced charge intercepted by

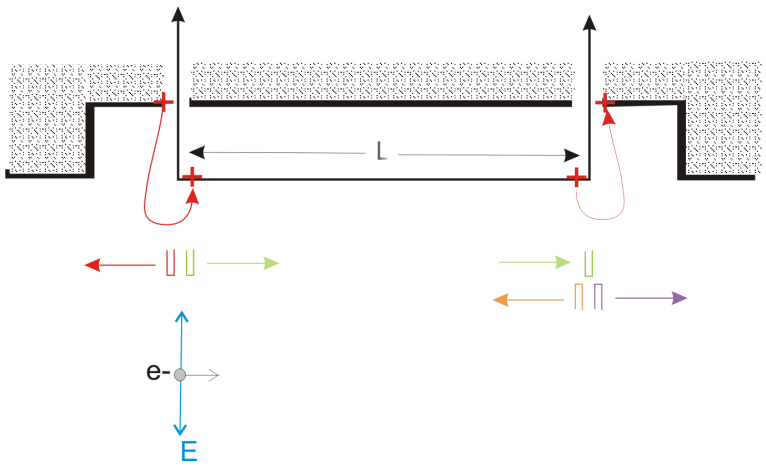

Figure 1.15: The production of a signal from an electron on a stripline with the downstream end terminated through matched impedance with the stripline.

the stripline. The voltage pulse splits into two, one travelling upstream (red) and the other downstream (green). Here the upstream end of the stripline is passed outside the beampipe to be terminated with an impedance matching that of the stripline (preventing reflections). The downstream travelling signal is reflected when it reaches the shorted downstream end and its polarity is reversed (the reflection coefficient of a shorted transmission line is -1). The reversed signal travels upstream and arrives at the upstream end at a time approximately $2L/c$ later than the initial signal (red). Thus the output of the stripline is a negative voltage pulse followed by a positive one of the same magnitude $2L/c$ later.

Figure 1.15 shows an electron approaching the upstream end of a stripline with the downstream end terminated through an impedance matched with that of the stripline. The scenario is the same at the upstream end of the stripline. However, the downstream travelling signal is not reflected. With relativistic beams, the velocity of the beam particle and the phase velocity of the stripline match. The electron will arrive at the downstream end of the stripline at the same time as the downstream travelling signal arrives. The induced charge crosses from the stripline to the beampipe wall, the reverse of the action at the upstream end. This induces a voltage signal with the reverse polarity. The voltage signal splits with half travelling upstream (orange) and a half travelling downstream (purple). This downstream travelling signal is equal in magnitude but opposite in polarity to the downstream travelling signal from the upstream end (green) and so the two signals cancel resulting in no signal at the downstream pick-off. The upstream travelling pulse (orange) arrives at the upstream end at a time approximately $2L/c$ later than the initial signal (red). Thus the output of the stripline is a negative voltage pulse followed by a positive one of the same magnitude $2L/c$ later, identical to the previous description.

Figure 1.16 shows an electron approaching the upstream end of a stripline with the downstream end open. The scenario is, again, the same at the upstream end of the stripline. The downstream travelling signal is reflected when it reaches the downstream end but its polarity is not reversed (the reflection coefficient of an open transmission line is +1). The induced charge crosses from the stripline to the beampipe wall inducing a voltage signal with the reverse polarity. The voltage signal splits with half travelling upstream (orange) and a half

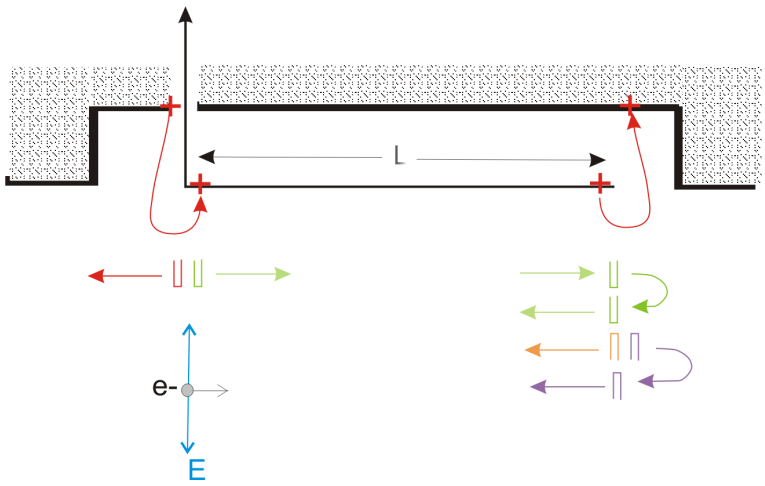

Figure 1.16: The production of a signal from an electron on a stripline with the downstream end open.

travelling downstream (purple). This upstream travelling signal (orange) is equal in magnitude but opposite in polarity to the downstream travelling signal from the upstream end (green) and so the two signals cancel. The downstream travelling signal from the downstream end (purple) is reflected and arrives at the upstream end at a time approximately $2L/c$ later than the initial signal (red). Thus the output of the stripline is a negative voltage pulse followed by a positive one of the same magnitude $2L/c$ later, identical to the two previous descriptions.

These striplines result in identical signals from a passing beam but would treat other sources of signal differently. A signal from a particle hit, for example, would not result in identical signals for these three types. Here, there would not be an induced charge jumping from beampipe to stripline back to beampipe. Instead there is one voltage pulse that is split, half upstream travelling and half downstream travelling, and the downstream travelling pulse is either reflected or transmitted depending on the end load to the transmission line. Figure 1.17 shows a voltage signal being created by an electron hit (red, the upstream-going pulse and green, the downstream-going pulse) on each stripline type as described. The differences come from the different ways the downstream end is terminated. With a shorted end, the signal from the electron hit is reflected and inverted. With an open end, the signal from the electron hit is reflected but not inverted. With the end terminated through a matched impedance, the signal is not reflected at all and can be seen as a signal on the downstream pick-off.

The striplines with shorted and open ends could be reversed with the downstream end being used as the pickup. The signal from the shorted case with the downstream end as the pick-off has a positive voltage pulse followed by a negative voltage pulse for a negatively charged beam. The stripline where the downstream end is terminated through matching impedance does not have any signal at the downstream end which makes it ideal for use in a circular machine with two beams in opposite direction as both pick-offs can be used, one receiving the signal from the beam travelling in one direction and the other receiving the signal from the beam travelling in the other direction.

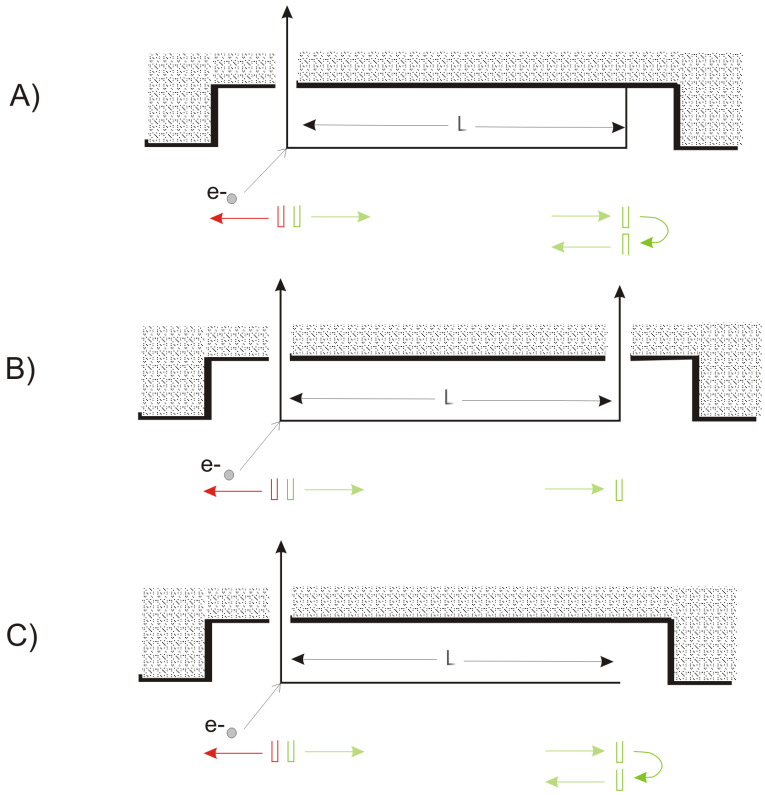

Figure 1.17: The signal from an electron hitting the upstream end of a stripline with A) the downstream end shorted, B) the downstream end terminated and C) the downstream end open.

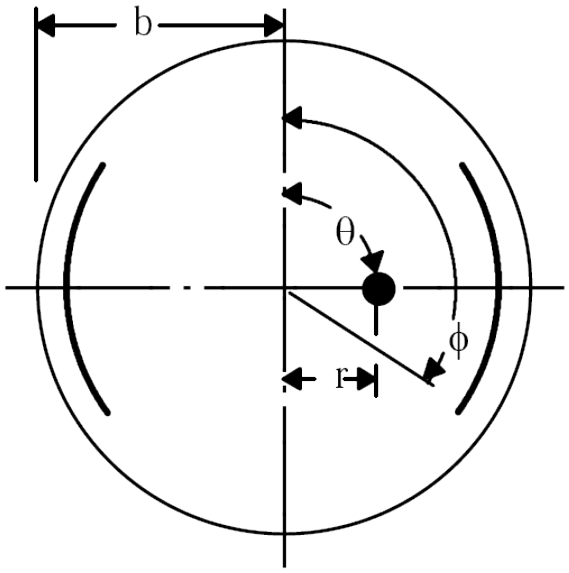

Figure 1.18: Cross-section of a beampipe (radius b) with striplines mounted on the side (as marked by dark lines) and a beam a distance r from the centre of the beampipe [39]. The striplines subtend an angle $\alpha = 2(\phi - \theta)$.

The response of the stripline to offset beams

The beam current (I_{beam}) can be approximated as a Dirac impulse in longitudinal distance z for short enough bunches of bunch charge q:

$$I_{\text{beam}} = qc\delta(z) \tag{1.8}$$

The current in the stripline has the magnitude of the fraction of induced current intercepted by the stripline subtending an angle $\alpha = 2(\phi - \theta)$ with the angles defined in figure 1.18. For a beam that goes down the centre of the beampipe this is simply $\frac{I_{\text{beam}}\alpha}{2\pi}$ but for an offset beam as shown in figure 1.18, the stripline current is given by [43]:

$$I_{\text{stripline}}(r) = \frac{I_{\text{beam}}}{2\pi}(b^2 - r^2)\int_{-\frac{\alpha}{2}}^{\frac{\alpha}{2}} \frac{d(\frac{\alpha}{2})}{b^2 + r^2 - 2br\cos(\frac{\alpha}{2})} \tag{1.9}$$

If r << b, this can be approximated:

$$\begin{aligned} I_{\text{stripline}}(r) &\approx \frac{I_{\text{beam}}}{2\pi}\int_{-\frac{\alpha}{2}}^{\frac{\alpha}{2}} 1 + 2\frac{r}{b}\cos\left(\frac{\alpha}{2}\right) d\left(\frac{\alpha}{2}\right) \\ &= \frac{I_{\text{beam}}}{2\pi}\left(\alpha + \frac{4r}{b}\sin\left(\frac{\alpha}{2}\right)\right) \end{aligned} \tag{1.10}$$

The second term in equation 1.10 is the change in current due to an offset beam. By multiplying the current change with the characteristic impedance of the stripline (Z_0), the change in voltage from the pickoff can be expressed as in equation 1.11. Taking the case of the stripline shorted at the downstream end, I_{beam} has been expanded as two Dirac impulses

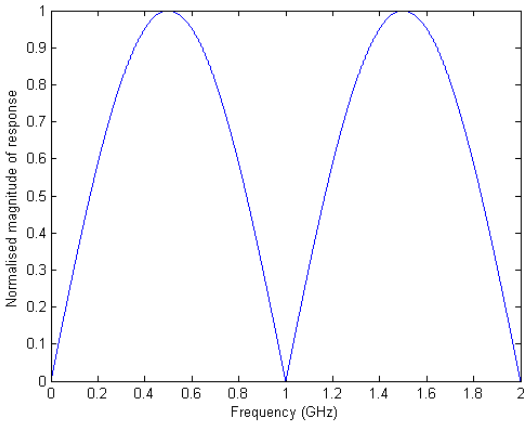

Figure 1.19: The frequency response of a 15 cm stripline normalised to its maximum value (see equation 1.12).

for the signal at the upstream end and the signal with the opposite polarity 2L/c later. The voltage signal is also divided by two as it splits into two equal pulses.

$$\Delta V(z,r) = \frac{Z_0 qcr}{\pi b} \sin\left(\frac{\alpha}{2}\right) \left(\delta(z) - \delta\left(z - 2L\right)\right) \tag{1.11}$$

The Fourier transformation of equation 1.11 is shown in equation 1.12 and figure 1.19. A stripline BPM is usually operated near the frequency that contains the most power (500 MHz is the best operating frequency of a 15 cm stripline as shown in figure 1.19).

$$\Delta V(k,r) = \frac{1}{2\pi} \frac{2Z_0 qcr}{\pi b} \sin\left(\frac{\alpha}{2}\right) \exp\left(i\frac{\pi}{2}\right) \exp(-ikL) \sin\left(kL\right) \tag{1.12}$$

1.5.3 Cavity BPMs

Cavity BPMs work on a different principle from stripline and button BPMs and are capable of much better position resolution [43].

When a bunch of charged particles passes through a RF cavity, EM fields are generated that set up standing waves. Since the charges are relativistic, the fields are transverse. The modes depend on the shape of the cavity as well as the beam charge, beam position offset, the bunch length, the bunch shape and the bunch spacing [41]. The modes that are set up in the resonant cavity are mainly TM010 (the monopole or fundamental mode) with some TM110 (the dipole mode). The monopole mode has an amplitude that is dependent on charge and needs to be suppressed in the processing electronics to extract the smaller dipole mode. The dipole mode has an amplitude that is dependent on charge and relative beam position from zero. The phase of the dipole mode relative to the monopole mode can measure the polarity of the position offset. The amplitudes and phases can be measured with antennae resonant at the appropriate frequencies to pick off the modes.

Cavity BPMs have recorded resolutions down to 20 nm [44] for single bunch extractions. For use with bunch trains, the excited signal of the cavity BPM needs to decay sufficiently in the time between bunches to allow the bunches to be resolved. Reentrant cavity BPMs are better suited to resolve individual bunches. The geometry of reentrant cavities is similar to a stripline BPM and the fields generated are below the resonant frequency of the cavity. The mode that is detected is the evanescent mode TE011 [41].

Cavity or reentrant cavity BPMs would not be appropriate as the ILC feedback BPM in terms of physical size; they are less compact than striplines or button BPMs.

1.6 Summary

The ILC is a proposed electron-positron collider with a centre of mass energy of 500 GeV with the possibility of an upgrade to 1 TeV. It will take the discoveries of the LHC further, making precise measurements of terascale physics.

The beam-beam interaction when the beams interact creates backgrounds through beamstrahlung and subsequent pair generation from the beamstrahlung photons. It also produces a beam-beam kick that is linearly dependent on the relative offset of the beams for small offsets (figure 1.10). This relation between offset and angle allows the use of a micron-resolution beam position monitor (BPM) a few metres away from the IP to infer the offset at the IP.

The flat beams of the ILC will be affected by ground motion and cultural noise at low frequencies as shown in figure 1.6 resulting in a loss of luminosity in a few seconds (figure 1.8). To restore luminosity, intra-train feedback is required.

The IP position feedback, illustrated in figure 1.9, uses a BPM to measure the position of an outgoing beam, related to its offset at the IP due to the beam-beam kick. The position is then used to kick the incoming beam, correcting the offset. Simulations have demonstrated that luminosity can be restored within a hundred bunches through this method (figure 1.11).

There are many BPM devices. Button BPMs are compact and well suited for the space-restricted ILC interaction region in that sense but micron-level resolution is technically hard to achieve. Stripline BPMs have better resolution and are still relatively compact. Cavity BPMs are capable of much better resolution than the feedback BPM requires and are larger so are not considered for this purpose.

Chapter 2

FONT Fast Feedback Systems

The IP fast offset-correction feedback as described in the Reference Design Report for the ILC [11] is being developed under the heading of FONT (Feedback on Nanosecond Timescales). Since the formation of the FONT project, the work has progressed from super-fast analogue electronics suitable for a warm machine to a digital processor suitable for a machine with superconducting technology (such as the ILC). Testing was completed for the analogue electronics at NLCTA (at SLAC) [45] and ATF (at KEK) [46]. The digital electronic tests are ongoing at ATF and, in 2008, ATF2 [47].

The tests are performed on a single beam, not two colliding beams. This is due to the fact that no available test beams have collision points and the R&D nature of the FONT tests requires test facilities rather than physics facilities as regular accesses to the beamline are needed to adjust the electronics. The principle of beam position measurement and correction can be demonstrated with a single beam as illustrated in figure 2.1. An offset ($\sim$100μm) can be given to the test beam from an upstream dipole magnet that kicks the beam off axis. The BPM instrumented with FONT electronics can measure this offset and produce a position signal to be amplified and sent to a kicker positioned between the dipole magnet and the BPM. The kicker kicks the beam such that the position of later bunches is zero in the BPM assuming the gain on the amplifier is set correctly so the correct kick is given. This demonstrates the ability to perform feedback allowing for measurements of its latency and accuracy.

Once the correction is successfully applied, the BPM reads no position offset and so no signal is passed to the amplifier from the BPM processor and the position correction is lost. This is unless part of the signal from the amplifier is delayed and applied to later bunches, thus retaining the correction even when no position offset is seen in the BPM. This delay loop can also tested in the scenario illustrated in figure 2.1.

2.1 FONT1

The first generation of FONT was designed to meet the challenges of the proposed warm machine, the Next Linear Collider (NLC) [48]. This represented the most challenging IP

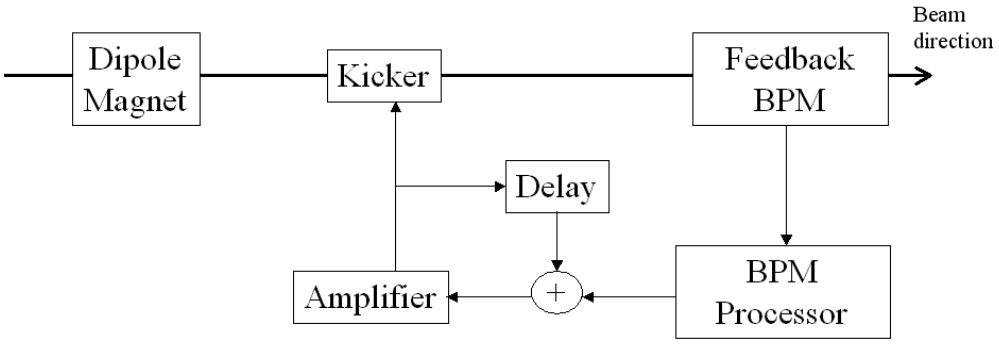

Figure 2.1: Schematic of FONT tests on a single beam showing the three necessary beamline components (the upstream dipole magnet, the kicker and the BPM for feedback) and the components of the feedback system (the BPM processor, the amplifier and the delay loop).

Parameter	NLCTA
Beam energy (GeV)	0.062
Electrons per bunch	1×10^8
Bunches per train	$\sim$2000
Bunch spacing (ps)	88
Train length (ns)	177
σ_x (μm)	500
σ_y (μm)	1000

Table 2.1: Beam parameters at NLCTA [49]

feedback for a potential future linear collider at the time due to the short bunch trains of a mere 270 ns.

Testing for the feedback electronics took place at the NLC Test Accelerator (NLCTA) at SLAC. Here the bunch trains were 177 ns long (see NLCTA parameters in table 2.1). To demonstrate the principle of FONT, it was necessary to show a feedback correction applied to the beam and then retained due to the action of the delay loop. Therefore the goal was to produce a feedback system with a latency[1] of a few tens of nanoseconds. It was predicted to be 67 ns as shown in table 2.2. Most of the latency was irreducible and came from the physical setup at NLCTA. These are the "time of flight" which is the time for the bunch to travel from the kicker to the BPM, and the "signal return delay" which is the time for the signal from the BPM to travel through the cables upstream to the kicker. The only way to reduce this is to move the BPM and the kicker closer together as was done for FONT2. The rest of the latency is from the BPM processor, the feedback circuit (where the delayed position signal was added to the current position signal), the rise-time of the amplifier and the fill-time of the kicker.

The experimental setup was as described in figure 2.1 with 4.19 m between the kicker and the feedback BPM [50]. The FONT BPM was a button BPM as described in section 1.5.1. The BPM processor worked by taking the difference between the signals from the top and

[1]The latency is defined here as the time between the position measurement of the first bunch and the position measurement of the first correction.

		Time (ns)
Irreducible	Time of flight of bunches	14
	Cable delay	18.5
Reducible	Processor	5
	Feedback circuit	10.5
	Pre-Amplifier	5
	Kicker Amplifier	12
	Kicker fill-time	2
	Total	67

Table 2.2: Latency prediction for FONT1 [50].

bottom electrodes and then dividing by the sum (for charge normalisation). However, inverting the sum took a lot of time since it was digitised, inverted and then reproduced as an analogue signal using an Arbitrary Waveform Generator (AWG). Therefore the inverted sum signal was applied to the difference signal for the next pulse.

The upstream dipole magnet was used to give the beam an offset from zero. Five beam positions were used as shown in figure 2.2(a). The red and blue lines show the position signal for the entire bunch train at the largest position offsets given to the beam, the magenta and cyan lines show bunch trains at small position offsets and the green line shows a bunch train close to the centre of the beam pipe (zero position offset). The separation between the bunches was 88 ps which is too fast for the processor to resolve.

The feedback was turned on (without the delay loop) and the measured beam position from the start of the train was used to correct later bunches as shown in figure 2.2(b). From around 140 ns, the beams start to show the effects of a kick that brings them to the same position. This position is not zero due to a static shape to the bunch train that is evident in figure 2.2(a) but the offset beams do all converge on one trajectory demonstrating successful feedback and position correction. The beams return to their original offsets around 210 ns as the correction is lost; the BPM is reading the "corrected" bunches that are near zero and so no longer provides the position signal required.

In figure 2.2(c) the delay loop is on and the correction is retained until the end of the bunch train.

The latency was 75 ns measured as the time between the start of the pulse and the start of the correction and 70 ns measured as the time during which the correction acts (from the data in figure 2.2(b), with the delay loop off) [50].

2.2 FONT2

The second generation of FONT aimed to improve the latency to 53 ns to observe more correction periods. This was achieved by moving the kicker closer to the feedback BPM, from 4 m as in FONT1 to a distance of 2 m. As shown in table 2.3, the expected lower

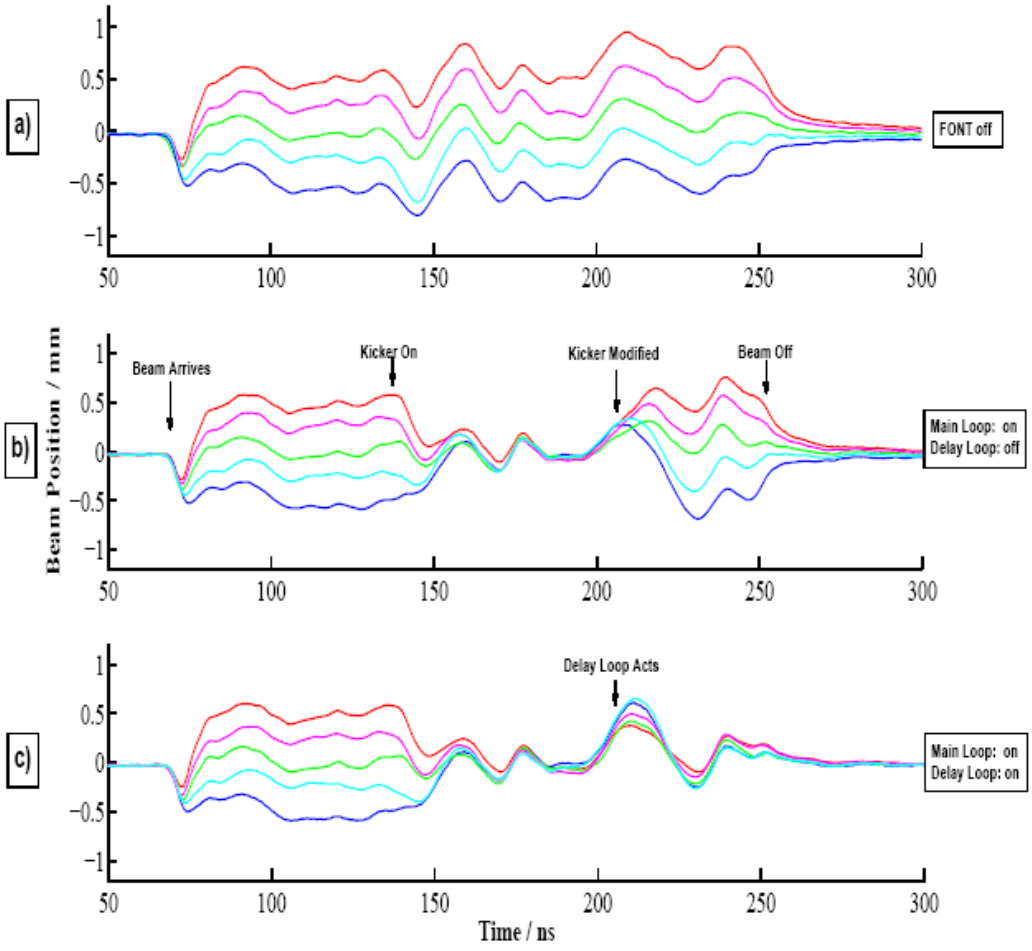

Figure 2.2: Feedback operation for FONT1 showing (a) without feedback, (b) feedback main loop on and (c) both the feedback main loop and delay loop on [49]. Each line is the average of ten pulses, showing the entire bunch train at five different position offsets.

		Time (ns)
Irreducible	Time of flight of bunches	6
	Signal return delay	10
Reducible	Processor	18
	Feedback circuit	4
	Amplifier	12
	Kicker fill-time	3
	Total	53

Table 2.3: Latency prediction for FONT2 [49].

latency comes from the lower "irreducible" part of the latency estimate.

FONT2 also included the introduction of independent witness BPMs downstream from the feedback BPM. The three BPMs were instrumented with the same design of processor and calibrated against known NLCTA beamline BPMs.

The processor designed for FONT2 shifted the 11.424 GHz button BPM response to 400 MHz by mixing it with a 11.024 GHz reference (known as "downmixing"). The sum signal was split and one output signal was passed through a limiting amplifier, producing a square wave reference at 400 MHz. Using this, the sum and difference signals were downmixed to frequencies near DC ("baseband"). Instead of normalising a pulse using the sum signal from the previous pulse, a new scheme was introduced using logarithmic amplifiers in the processor which avoided the long process of digitising and inverting the sum signal. Logarithmic amplifiers were used with the signal from the bottom electrode being subtracted from the signal from the top giving a normalised position output. The resolution for the BPM processor was calculated using two of the instrumented BPMs to predict the position in the third from a consideration of the geometry. The residual was defined as the difference between the predicted position in the third BPM and the actual position in the third BPM from the calibrated output signals. The standard deviation of the residuals was found. This contained information about the resolutions of the three BPM processors. With the assumption that the noise in each BPM was uncorrelated and the resolution for each BPM was the same, the resolution was calculated from the standard deviation of the residuals to be 10.9 μm [49].

The amplifier for FONT2 was improved on the amplifier used in FONT1 by being more compact and therefore more appropriate for use in the space-restricted ILC beamline. It had the same drive as the FONT1 amplifier. However, since the distance between the kicker and the feedback BPM was greatly reduced, more kick was needed to bring the beam to zero offset. For that reason, two kickers were used.

The static bunch position profile visible in figure 2.2 was removed using an AWG. This "beam flattener" generated a signal that was the negative of position variations around the mean position of the bunches in the train as calculated over many pulses. The signal was added to the signal from the BPM processor before the amplifier but after the delay loop.

For the feedback demonstration, the beam was given eight offsets using an upstream dipole magnet. This is shown in figure 2.3(a). The signal from the feedback BPM was split

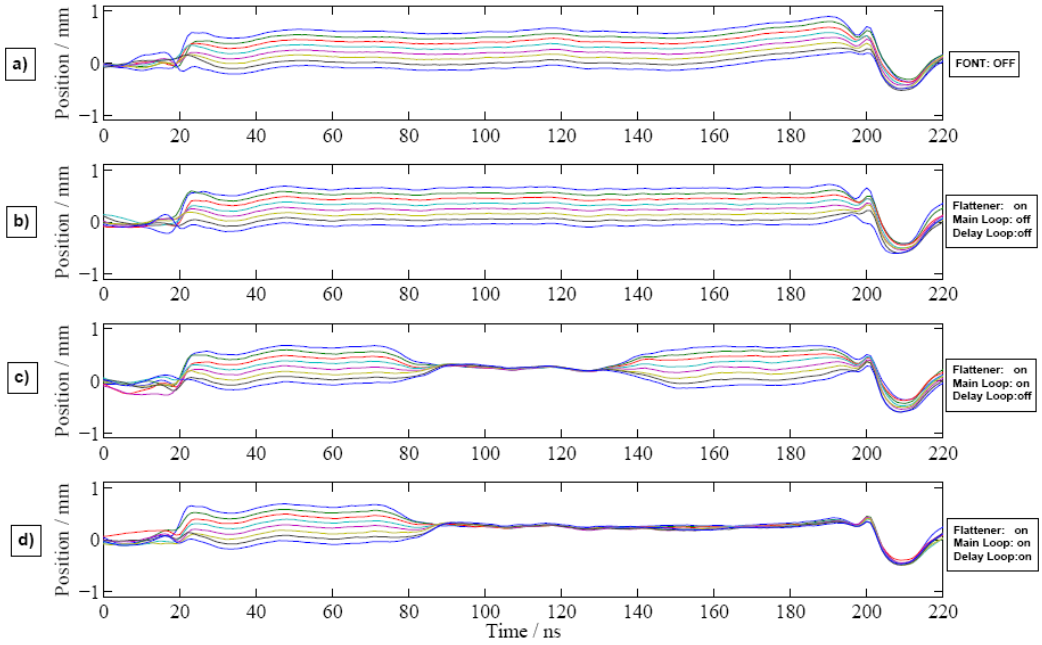

Figure 2.3: Feedback operation for FONT2 showing (a) without feedback, (b) no feedback, beam flattener on, (c) feedback main loop on plus beam flattener on and (c) the feedback main loop, the delay loop and the beam flattener all on [49]. Each line shows the bunch train at a different position offset.

to in-tunnel electronics for the feedback and out-of-tunnel electronics to be recorded on the FONT DAQ [51]. These position signals are from the out-of-tunnel electronics and show a positive "zero" offset compared to the in-tunnel electronics, the central magenta and cyan curves being around zero in the in-tunnel electronics.

Figure 2.3(b) shows the bunch train for the eight offsets and the beam flattener turned on. It successfully improved the beam profile, removing the upwards slope in position in the last 40 ns of each bunch train.

The feedback was turned on with the delay loop off. Figure 2.3(c) shows each offset beam being kicked around 80 ns to a common position, zero as measured in the feedback electronics. The latency of the feedback was found to be 57 ns, measured as the time between the onset of the kicker and the return to the original offset. After one latency period, the correction is lost as the feedback BPM sees a beam at zero position.

The delay loop was turned on showing that the correction to zero was retained after the second latency period, shown in figure 2.3(d).

This feedback test demonstrated that with beams initially spread in a range of positions spanning ∼0.7 mm, the feedback could kick them all to a common position with a spread of ∼0.05 mm. That is a 14:1 correction [49].

Parameter	ATF
Beam energy E (GeV)	1.28
ΔE/E	0.08%
Electrons per bunch	$(0.2 - 1.0) \times 10^{10}$ single bunch
	$(0.3 - 0.5) \times 10^{10}$ multi-bunch
Bunches per train	20
Bunch spacing (ns)	2.8
Train length (ns)	56
σ_x (μm)	70
σ_y (μm)	7
σ_z (mm)	8

Table 2.4: Beam parameters at ATF [52].

		Time (ns)
Irreducible	Time of flight of bunches	3
	Signal return delay	5
Reducible	Processor	5
	Amplifier	5
	Kicker fill-time	2
	Total	20

Table 2.5: Latency prediction for FONT3 [49].

2.3 FONT3

2.3.1 Moving to ATF

After two successful stages at NLCTA, FONT moved tests to the Accelerator Test Facility (ATF) at KEK.

As shown in table 2.4, the beam energy is 1.28 GeV at ATF. A feedback system that can correct at the micron level at ATF can also correct at the nanometre level at the ILC where the beams are up to 250 GeV (or 500 GeV with the 1 TeV centre of mass upgrade). Therefore, demonstrating micron-level feedback at ATF is a test of a system that can be taken to the ILC.

The beam at ATF is small and flat (shown in table 2.4) and has smaller beta functions than the beam at NLCTA. This results in smaller beam jitter and the chance at a much better correction.

However, beam tests at ATF put pressure on the feedback to be even faster as the entire bunch train at ATF was only 56 ns long. To get more than two latency periods and clearly demonstrate both the feedback and the delay loop behaviour, the new goal for latency was 20 ns, the budget for which is shown in table 2.5.

A similar setup was used at ATF as at NLCTA. The layout of the ATF extraction line

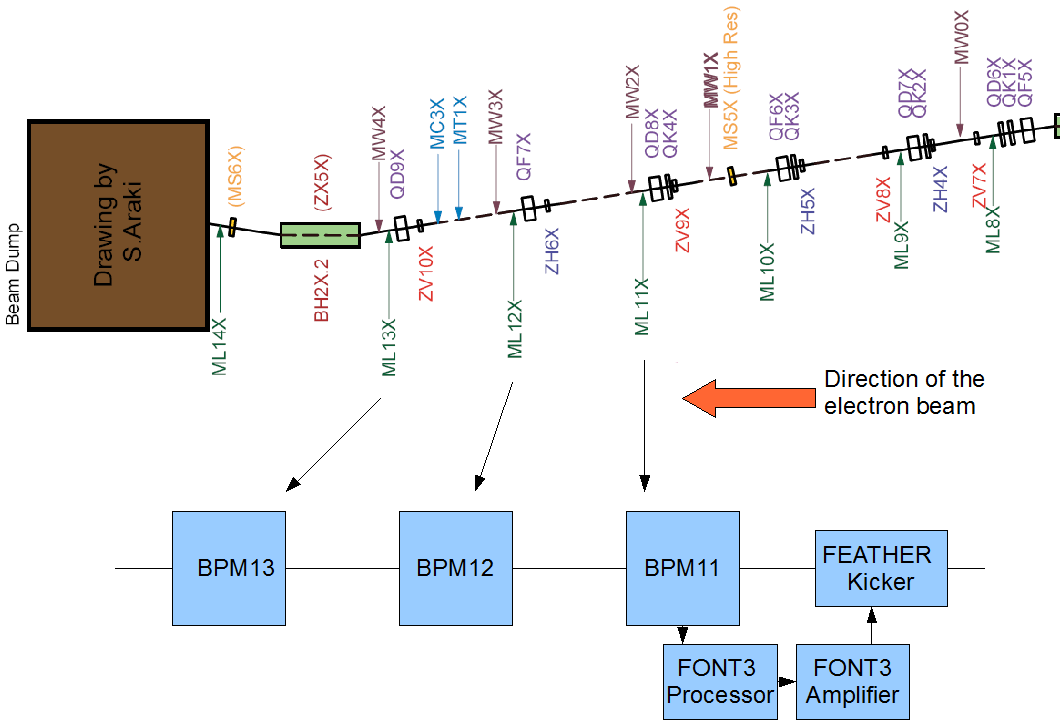

Figure 2.4: Top: ATF extraction line [53]. The prefix ML refers to stripline BPMs, QD are defocussing quadrupoles, QF are focussing quadrupoles, QK are skew quadrupoles, MW are wire scanners, ZH and ZV are correctors (for x and y respectively), MT and MC are current monitors and BH bend magnets. Bottom: Block diagram showing the components used for FONT3.

and the beamline components used for the FONT3 tests is shown in figure 2.4. There were upstream corrector dipole magnets to put offsets in the beam (ZV7X and ZV8X), a kicker (1 m upstream of ML11X) and a feedback BPM (ML11X). Two further BPMs (ML12X and ML13X) acted as witnesses downstream of the feedback loop. The BPMs used were stripline BPMs of length 12 cm which has its peak response at 625 MHz. The FONT3 processors were used with the y pickoffs on BPMs ML11X, ML12X and ML13X, called BPM11, BPM12 and BPM13 from this point forward.

2.3.2 FONT3 Processor

The processing scheme was returned to a simple difference calculation between the top and bottom BPM pickoffs. To meet the latency goal, there was no charge normalisation. With the goal of micron-level correction after two corrections, a 10% variation in charge could be tolerated. The charge profile for the bunch train at ATF was flat enough for this. The occasional bunch train with greater than 10% charge variation was removed from the data in analysis. There was a unique processor on the x pickoffs of BPM13 that outputted the sum signal for monitoring the charge and performing offline charge normalisation.

The FONT3 processor (see figure 2.5) began with two signals: the signal from the top strip and the signal from the bottom strip. At ATF, the striplines are shorted at the upstream

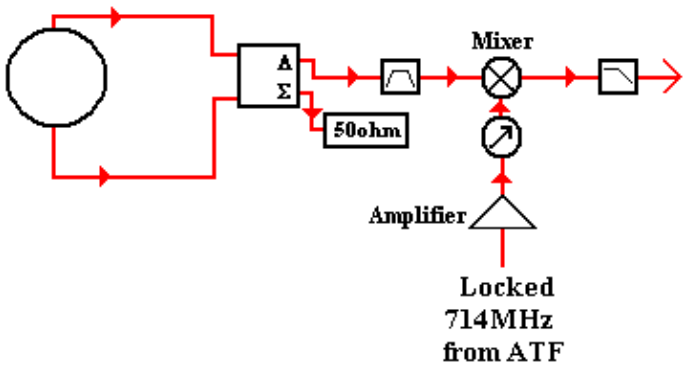

Figure 2.5: A block diagram of the FONT3 processor [49]. It takes signals from the top and bottom strips of a stripline BPM (left of diagram) and passes them through a difference hybrid (Δ). Then filters and mixers are used to produce the output to the amplifier.

end with the pickoff at the downstream end as described in section 1.5.2. At the pickoff, the BPM processor is attached. Care was used to make sure the processor was as close to the pickoffs as possible in the case of BPM11, the feedback BPM, and the cables used were the shortest possible to minimise the latency of the full feedback system.

One signal was subtracted from the other using a 180° hybrid (except for the summing processor which used a hybrid without the phase change). Exact subtraction of one signal from another when they are only picoseconds in duration requires the signal paths in the hybrids, and the cables between the striplines and the hybrids, to be well matched. However, the slightest difference between the signals in time produces a common mode signal when they are subtracted in the hybrid and in reality there is always some common mode component.

After the hybrid, the signal was downmixed to baseband to get an output that can be used to drive the kicker. It was first passed through a band-pass filter centred on 714 MHz and then passed through a mixer. The mixer required a reference signal (or local oscillator, LO) as an input. In this case, it was 714 MHz from the ATF central clock, locked to the beam. The mixer took the reference and the input from the early stages of the BPM processor (the RF signal) which after going through the bandpass filter had frequencies centred around 714 MHz. It multiplied the two signals resulting in a signal with low frequencies (under 200 MHz) and a high frequency signal around 2×714 MHz as in equation 2.1.

$$\cos(\omega_1 t)\cos(\omega_2 t) = \frac{1}{2}\left(\cos(\omega_1 + \omega_2) + \cos(\omega_1 - \omega_2)\right) \tag{2.1}$$

The LO and RF must be in phase with each other. If the phase difference between the two inputs is zero, the output is purely dependent on the beam position. If it is exactly 90° out of phase, the output is the beam position independent common mode. Most likely when the processor is first assembled, the phase difference would be some arbitrary amount. In this case, the output from the mixer depends both on position and on the phase difference. The correct phase needs to be set for the correct operation.

To adjust the relative phase between the two inputs into the mixer, the signal after the band pass filter was split two ways and sent to two mixers. The LO was also split two ways,

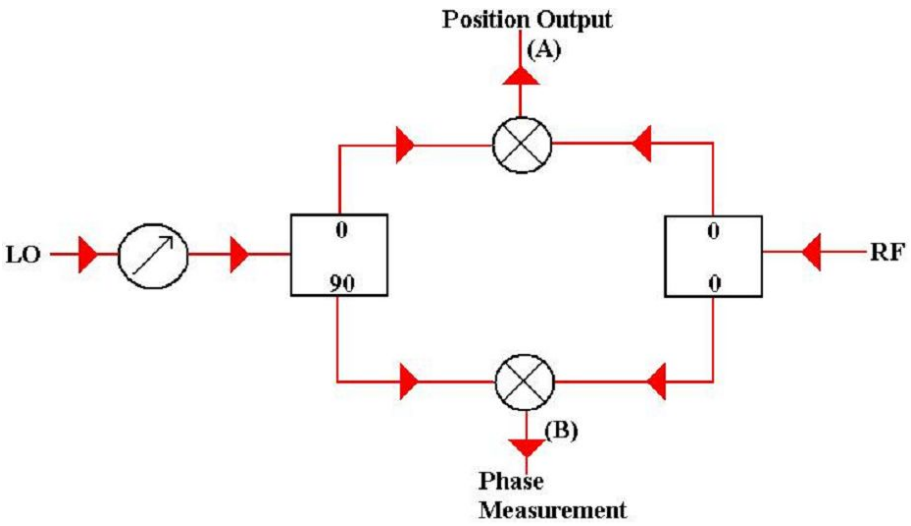

Figure 2.6: A block diagram showing the setup used to correctly phase the LO with the RF [49].

one LO path being longer than the other to introduce a 90° phase shift shown in figure 2.6. The phase of the LO was adjusted before the split and the output from the mixer with the 90°-shifted LO watched on an oscilloscope. The adjustment continued while the beam was moved by the upstream dipole magnet until the output became purely position independent. Since this common mode signal is 90° out of phase from the position signal, this method brought the LO that was not 90°-shifted to the correct phase to be mixed with the RF signal, thereby producing the purely beam position dependent output.

To remove the higher frequencies (around 2×714 MHz), and any 714 MHz leakage, from the baseband signal, the final component in the processor was a low-pass filter.

The LO phase was adjusted by variable phase shifters that could be controlled with a 0-15V power supply. They adjusted the phase of the LO from 0 to 180°.

Any jitter on the LO phase would be translated to the position signal as amplitude jitter.

This filtering scheme, using a band-pass filter before the mixer, was preferred over missing out the band-pass filter stage and just using a low pass filter to select the baseband signal as there was a strong 357 MHz signal at ATF with multi-bunch mode as this was the bunching frequency. Just a low-pass filter after the mixer would have worked if the filter had a sharp cutoff to remove the 357 MHz signal. However, a sharp cutoff compromises on speed so to keep latency low, the band pass filter was introduced to reduce the level of 357 MHz signal before the mixer.

Processor latency

The processor was modeled in SystemView [54], an RF simulation package. According to the simulation, the latency for this processor design was 4.1 ns, not including the physical size of the processor and the time for the signal to travel [49].

In practice, the latency was measured to be 4.6 ± 0.3 ns which is consistent with the predicted value assuming a signal path of ∼10 cm [49].

Processor calibration and resolution

The System View simulation of the processor predicted a resolution of 0.24 μm.

The three instrumented BPMs were calibrated using an upstream dipole magnet. Using the transfer matrix of the dipole magnet and the distance between the dipole and each BPM, the offset given to the beam by the dipole in the BPM could be calculated. The current in the dipole magnet was changed in steps, moving the beam through approximately 2 mm in each BPM.

Due to timing jitter of the oscilloscope trigger and scope noise when taking a single data point, the maximum point of the processor output was not used for calibration. Instead, normalised difference signal Y (equation 2.2) was calculated from the area under the difference signal ($V_{\text{Difference}}$) and the area under the sum signal (V_{Sum}).

$$Y = \frac{\int V_{\text{Difference}}\, dt}{\int V_{\text{Sum}}\, dt} \tag{2.2}$$

The resolution was calculated using the backslash (or "left matrix divide") operator in Matlab. This operator finds `x = A\b` using a least squares method to solve the equation `Ax = b`. Here `A` is a matrix that includes the positions of the beam in two of the three instrumented BPMs. The vector `x` uses the two BPMs to predict the third where `x` is calculated using the measured third BPM positions in the vector `b`. The resolution of the third BPM is then found by calculating the residuals, that is the difference between the predicted position and the actual position. The standard deviation of the residuals, is given as the resolution.

It was possible to run the beam at ATF in single-bunch or multi-bunch mode. The resolutions in single-bunch mode were found to be 24.5 μm, 12.2 μm and 34.3 μm (without much attention to the correct LO phasing) [49]. In multi-bunch, the presence of the 357 MHz bunching frequency put more power into 357 MHz and its harmonics (including 714 MHz). This boost in power at 714 MHz improved the resolution of the processors. The best resolution numbers achieved were 2.3 μm, 4.1 μm and 4.9 μm [49]. Shown in figure 2.7 and figure 2.8 are calibration and resolution data for one measurement of the FONT3 processor. The performance of the FONT3 processor was often not consistent between beam tests. The reliability issue was addressed in FONT4.

As shown in figure 2.7, the processors gave a linear response to the beam position over a range of ∼2 mm. The charge per bunch was approximately 0.5×10^9 electrons when this data was taken. The linearity depends on the input to the mixer [49], which cannot be above 0.25 V, and therefore the range scales with bunch charge.

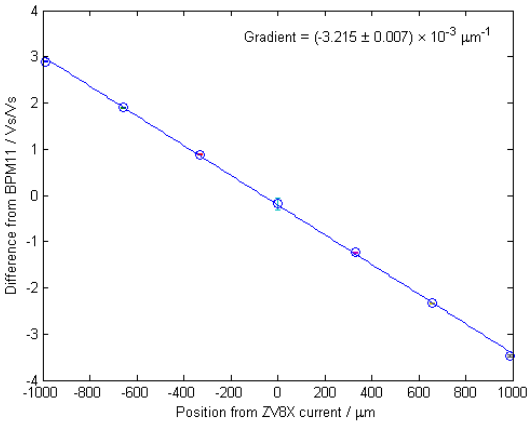

(a) BPM11 calibration

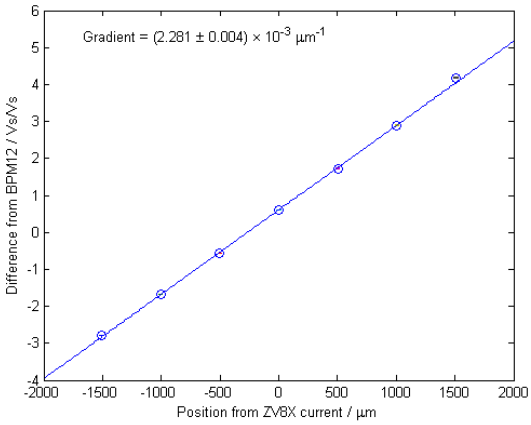

(b) BPM12 calibration

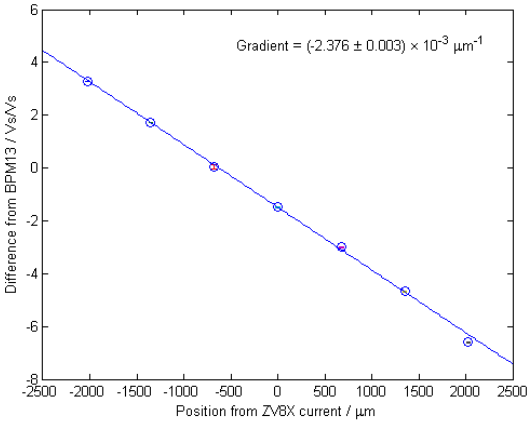

(c) BPM13 calibration

Figure 2.7: Calibration curves for three BPMs instrumented with the FONT3 analogue processor. Y (equation 2.2) versus position is shown.

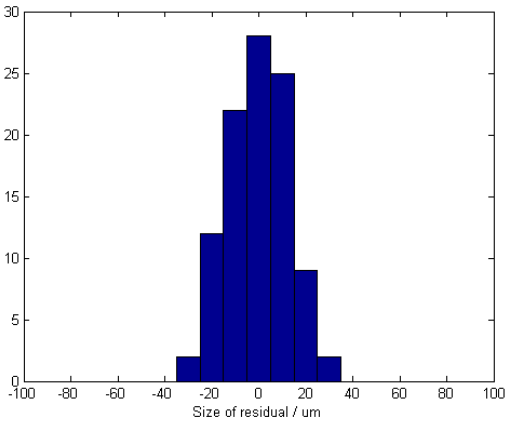

(a) BPM11 residuals showing a resolution of 12.8 μm.

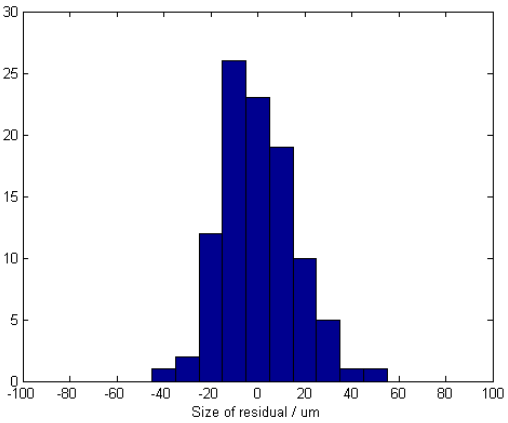

(b) BPM12 residuals showing a resolution of 15.8 μm.

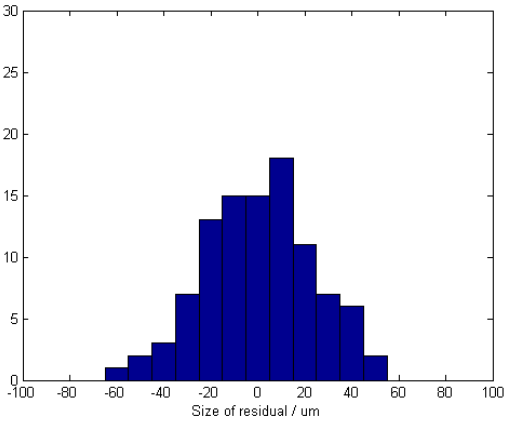

(c) BPM13 residuals showing a resolution of 23.4 μm.

Figure 2.8: The distribution of the residuals for three BPMs instrumented with the FONT3 analogue processor.

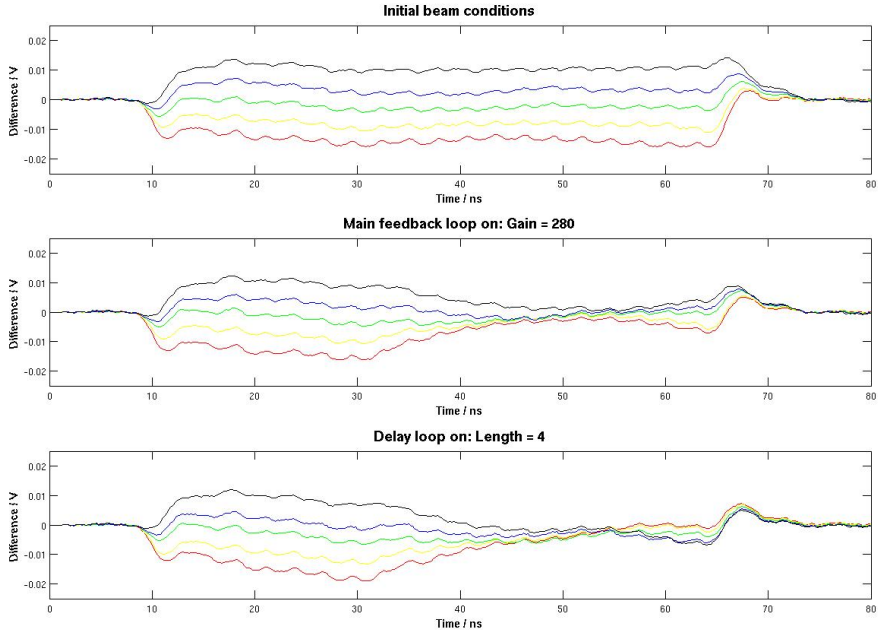

Figure 2.9: Feedback operation for FONT3 showing the signal from the difference processor on BPM11. (a) No feedback. (b) Feedback main loop on. (c) Feedback main loop plus the delay loop on [55]. Each lines shows the bunch train at a different initial position offset.

2.3.3 FONT3 Feedback Results

To perform the feedback, this processor was attached to all three stripline BPMs. The processor output from the feedback BPM was split two ways: half the signal went to the amplifier and half came out along long heliax cables to be recorded on the FONT DAQ. The lengths of cables used between the feedback BPM pickoffs and the processor, the processor and the amplifier and the amplifier and the kicker were kept to a minimum to reduce latency. There was no such latency concern with the witness BPMs so the signals from the pickoffs were carried along long heliax cables to the processors and the FONT DAQ.

A 56 ns bunch train was used, comprising 20 bunches 2.8 ns apart. The bunch train produced a signal in the striplines and was processed in the electronics. With a bunch separation of 2.8 ns, the single bunches in the train could be resolved as shown in figure 2.9(a). As with FONT1 and FONT2, an upstream dipole magnet was used to give the bunchtrain a position offset.

The feedback was turned on and the output from the processor was amplified and drove the kicker just 1.2 m upstream of the BPM. The gain on the amplifier was adjustable and chosen to bring the bunchtrain to zero in the feedback BPM. Figure 2.9(b) shows the best guess at setting the main loop gain (value 0.3106 [56]) during the tests (however, subsequent analysis of the data indicated that the gain setting was slightly too low [49]). The offsets within ± 100 μm (in blue, green and yellow) converge at zero around 48 ns in this figure. The largest offsets (in red and black) do not meet for reasons discussed in the next section. As expected with no delay loop, the correction is lost and the bunches begin to return to

Item	Value
Main Gain	0.3650
Latency / Delay length (ns)	24.0 ± 0.5
Delay Gain	0.6
Correction ratio	23:1

Table 2.6: The results from FONT3 feedback, summarised [49].

their original offsets around 55 ns in this figure.

The delay loop was of variable length and variable gain. The settings were chosen so that after the second latency period, the beam stayed corrected for the rest of the bunch train. The feedback results shown in figure 2.9(c) show the best guess at the delay loop settings during the beam tests (length 21.7 ns and gain 0.6). Subsequent analysis suggested that the delay loop length was set too low as the latency of the feedback was longer than this setting. Unlike in figure 2.9(b), the bunches do not return to their original offsets at 55 ns; instead they are given a kick that is too large and the bunches are over-corrected.

The latency of the system was measured to be 24.0 ± 0.5 ns from an analysis of the signals from when the main loop was on [49]. This was the average of two latency measurements: one where the latency was defined as the time between the signal from the very start of the bunchtrain, when it first goes above the noise level, and the point where the position falls below 90% of its maximum, and the second where the latency was defined as the time between when the signal climbed to half its maximum and the time where the signal fell to half its maximum.

Bunch trains $\sim$130 μm offset from each other were corrected to within $\sim$6 μm, a 23:1 correction.

Data were recorded with other settings and subsequent analysis indicated that the ideal settings were as shown in table 2.6.

2.3.4 Simulations of FONT3 feedback

The FONT3 feedback results shown in figure 2.9 required some investigation to be understood properly as the feedback behaviour was not ideal: figure 2.9(b) shows that the larger offsets (in red and black) do not meet and figure 2.9(c) shows that there is overcorrection in the third latency period (beginning $\sim$55 ns in the figure). These were hoped to be better understood through simulating the feedback.

Simulink [38] (a tool for modeling dynamic systems) was used to model the feedback as shown in figure 2.10. Experimental data of the beam's position in y were used as the input. The recorded difference signals from the feedback BPM, 1.2 m downstream from the kicker, were loaded at the "Beam Generator" and, using a transfer matrix, the beam was tracked back to what it would have looked like at the kicker. The kicker imparts an angle change on the beam and over the course of the 1.2 m drift space between the kicker and the BPM, the

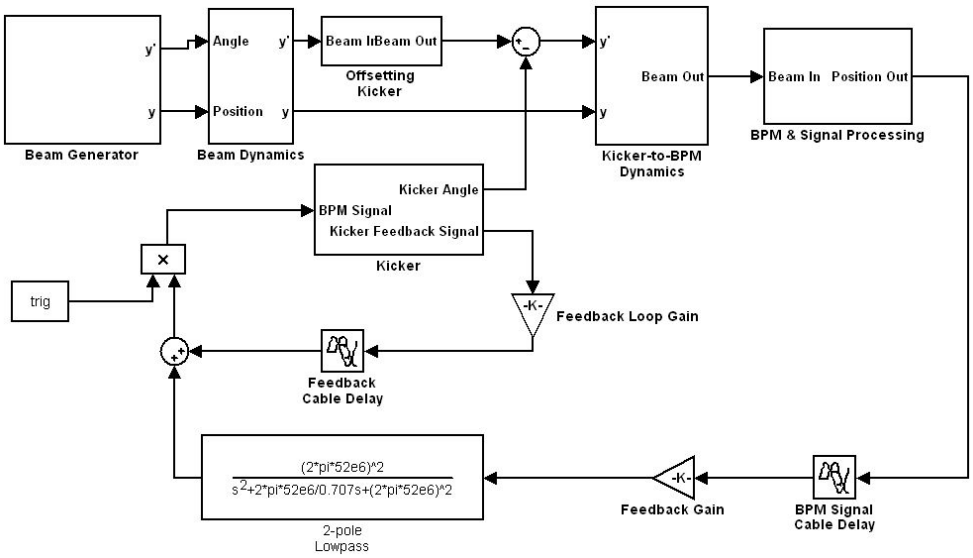

Figure 2.10: The FONT3 feedback as simulated in Simulink [57].

y position changes. As the input was already what is seen as the BPM processor output, it was not necessary to simulate the BPM processor. Instead a delay was introduced equal to that of the latency of the processor. A further delay was needed for the cabling between the processor and the amplifier. The amplifier had a bandwidth of 52 MHz and was modeled by a 2-pole Bessel function [56]. The kicker was modeled simply as an integrator with suitable delay to give a rise-time of 8 ns (which appeared to match the rise-time observed in the run at ATF) with its output affecting the beam angle. As the kicker was modeled this way rather than a full modeling of the dipole magnet and its effect on the charged beam, the amplification setting used in the feedback experiment and the gain set in this simulation bear no resemblance to each other and the gain had to be set by repeatedly running the simulation for different gains and deciding which produced the output that best matched the real feedback data. A feedback loop that takes the amplifier output through a delay equal to the latency of the feedback system, allows the correction be kept for the next latency period. The various delays used in the simulation were chosen to agree with the delays in the feedback tests at ATF.

Settings were found that gave the best feedback as shown in figure 2.11 and then parameters changed to investigate how and why the data differed. The input beams came from runs done at approximate offsets of ± 70 μm, ± 35 μm and 0 μm at the kicker. The simulation took the inputs and produced results as expected: the offset beams were corrected to zero offset at the BPM (see figure 2.11). However there was also a sharp positive signal at the end of the 56 ns bunch train. This signal appears to be from the BPM processor as it is also seen in the input to the simulation. It also appears in the data from ATF (figure 2.9) but it is more enhanced in the simulation possibly due to the amplifier bandwidth. Being after the 56 ns bunch train, it has no affect on the beam and is not a concern.

It was speculated that the amplifier may have a non-linear response for the range of initial offsets that were used. The non-linearity of the amplifier was introduced, modeled using the function shown in figure 2.12.

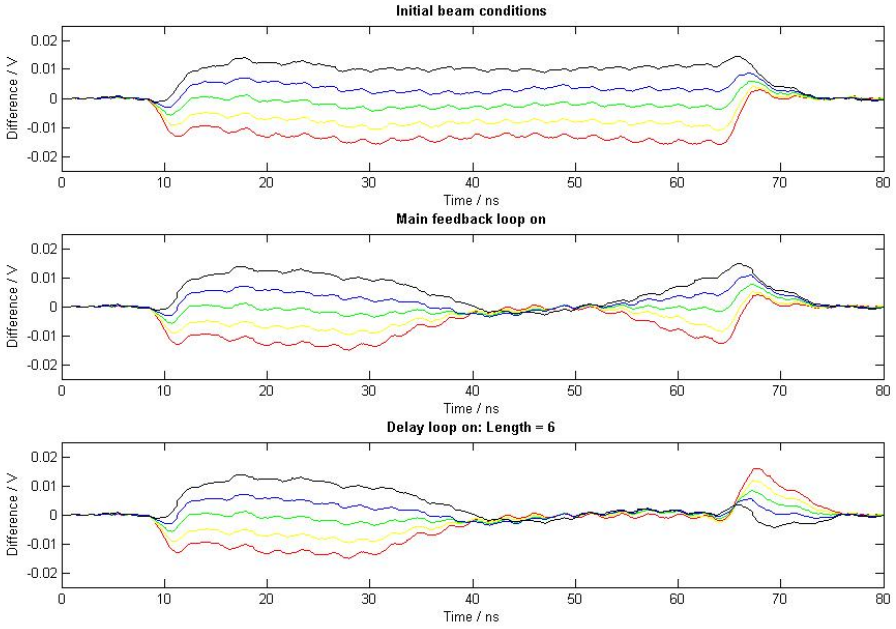

Figure 2.11: Simulation results with the signal from the difference processor versus time. Top: The average input bunch trains to the simulation. Middle: The feedback simulation with main loop on, delay loop off. Bottom: The feedback simulation with the main loop on and the delay loop on. The gain and delay loop length used here were set to produce the best feedback result possible. In each case, the five lines are the averages of 120 bunch trains.

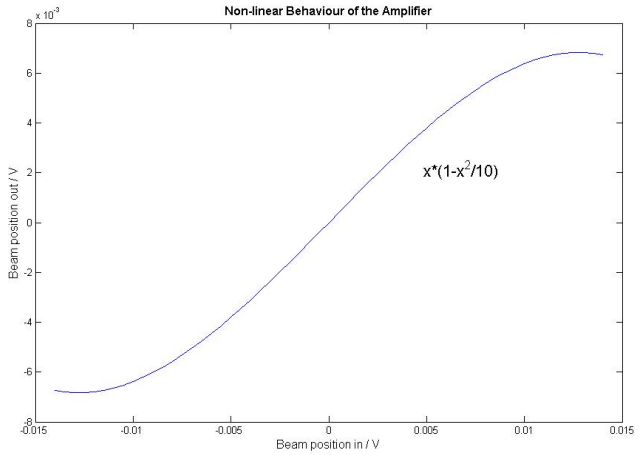

Figure 2.12: A function derived from empirical observation describing the non-linearity of the amplifier [56].

For a direct comparison to high-gain data from ATF, the simulation was run with a higher than ideal main loop gain (equivalent to a gain of 0.4655 in the FONT3 system) and the appropriate delay loop length to match the latency (24 ns). The non-linear response for the amplifier was included in this simulation. Figure 2.13(a) shows the initial beam conditions, data from ATF that was used as input to the simulation. Figure 2.13(b) shows the simulation results with a linear amplifier response. Figure 2.13(c) shows the simulation results with the non-linear amplifier response as shown in figure 2.12. Figure 2.13(d) shows the high-gain data taken during the FONT3 tests at ATF. Introducing the non-linear amplifier created a closer match to the data though it appears that the compression effect was slightly over-estimated.

Figure 2.9(c) showed overcorrection of the beams when the delay loop acted. Simulation results using a delay 2 ns shorter than the system latency (figure 2.14) confirm that there is a greater correction after the second latency period (around 55 ns) than after the first. This is because the kicker sees both the delayed signal and the offset beam signal from the BPM processor, resulting in a signal that the sum of both. The compression effect again appears to be slightly over-estimated.

The simulations demonstrated that overcorrection can occur with the delay loop set 2 ns too short and that the amplifier was non-linear so that the bunchtrains with the greatest offset were not corrected ideally.

2.4 FONT 4

With the decision to have a bunch spacing of hundreds of nanoseconds at the ILC and a train comprising thousands of pulses came the next step of making the FONT feedback a more powerful tool capable of learning and applying more complex algorithms. The extra time between bunches[2] allows the output of the super-fast BPM processor to be digitally sampled and processed by a field-programmable gate array (FPGA), applying algorithms that can predict bunch positions from an analysis of the full train.

For example, see figure 2.15. Here adjustable gains are used rather than one single main loop gain. Simulations for the TESLA design described in section 1.4.2 were used to demonstrate how using multiple gains in the feedback could lead to a lower loss of luminosity than using just one single gain.

The "train flattener" described in section 2.2 (FONT2) also demonstrates the kind of algorithm that can be applied with a digital processor. Any static bunch train profiles can be removed.

The digital processor can also have input signals from other monitors such as the luminosity monitor, using extra data to achieve the best correction possible.

This generation of FONT, called FONT4, used a new PCB version of the FONT3 analogue BPM processing scheme, a digital processor and a new amplifier. It was tested at ATF using the same setup as FONT3 with the digital processor used on the feedback BPM only.

[2]The bunch spacing for the ILC is proposed to be between 153.8 and 461.5 ns, see table 1.2.

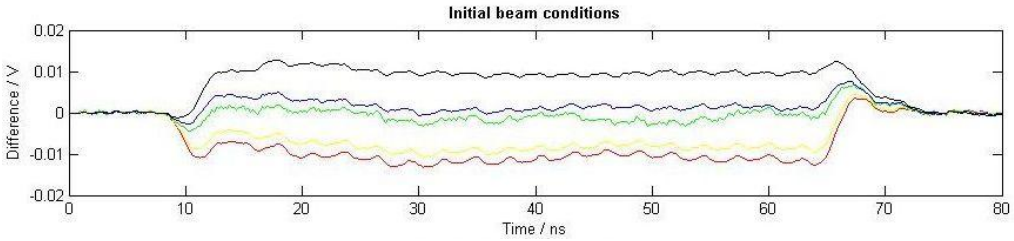

(a) Five initial beam positions at ATF (used as the input to the simulation).

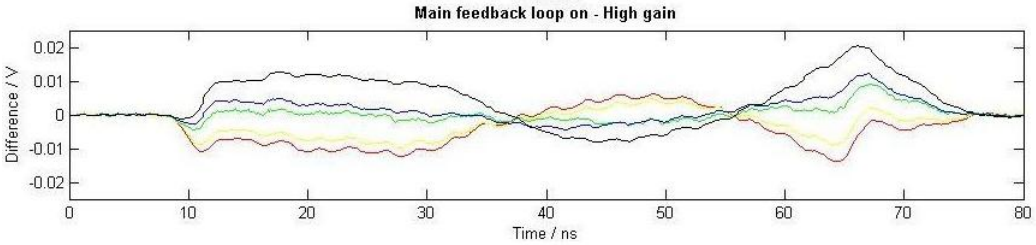

(b) The simulated feedback with the main gain set high and the delay loop off. The amplifier is linear in this simulation.

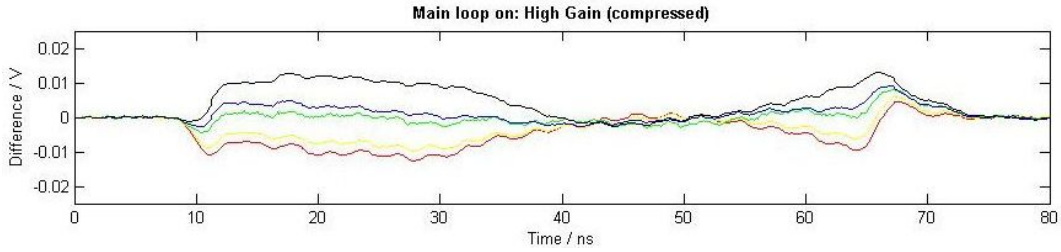

(c) The simulated feedback with a high gain setting, non-linear amplifier and no delay loop.

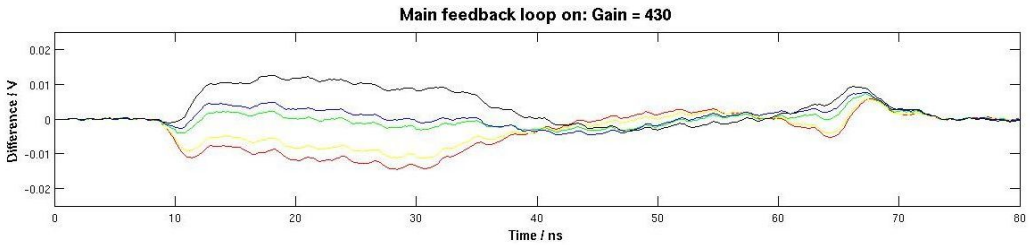

(d) Data taken at ATF with a high gain and no delay loop [55].

Figure 2.13: A comparison of simulated results and real results from ATF.

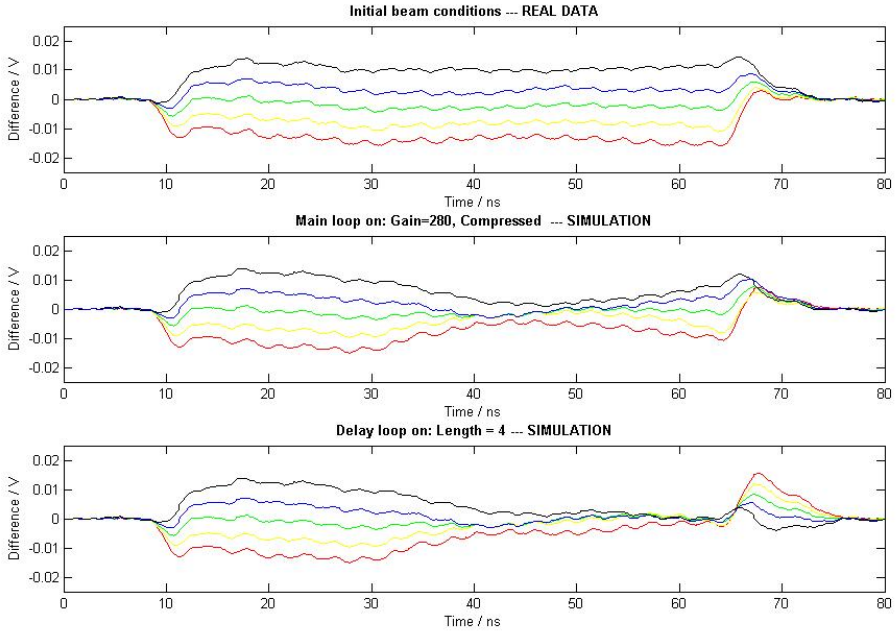

Figure 2.14: Simulation results with the signal from the difference processor versus time. Top: The average input bunch trains to the simulation. Middle: The feedback simulation with main loop on, delay loop off. Bottom: The feedback simulation with the main loop on and the delay loop on. The gain was the ideal value as in figure 2.11. The non-linear model of the amplifier was used. The delay loop length was 22 ns (2 ns short of the system latency). These are settings to model the situation in figure 2.9.

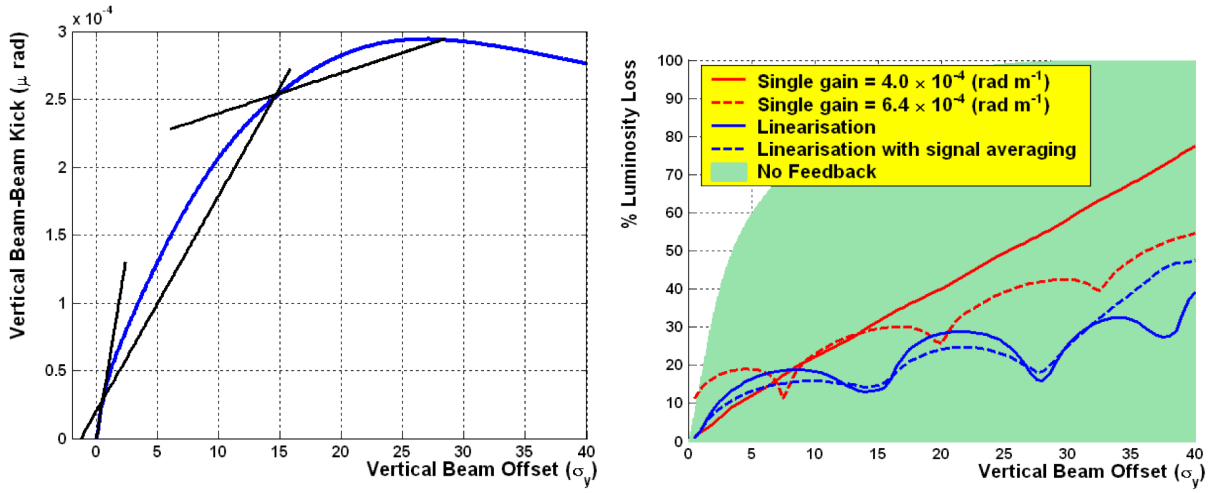

(a) The blue curve shows the kick from the beam-beam interaction at different vertical beam offsets. The black lines are examples of how this curve can be coarsely divided into linear regions.

(b) The luminosity loss in TESLA simulations of beams colliding with an offset. Without feedback, luminosity loss is shown by the green area. With feedback with a single gain setting, the luminosity loss is the area under the red lines (with the dashed red line showing a higher gain setting than the solid red line). The blue lines show feedback with multiple gains that roughly linearise the beam-beam kick relationship with offset.

Figure 2.15: Simulation results of having multiple gains depending on the offset compared to one single gain [58].

Latency is not as tight a constraint as for warm machines but it is desirable to make as many corrections as possible to ensure the best correction. Therefore the goal of FONT is to operate on a bunch to bunch basis. The smallest bunch spacing at the ILC is 153.8 ns therefore the latency budget for the FONT4 system (including time of flight and signal times) needs to be at most 150 ns. The application of sophisticated algorithms would increase the latency further.

ATF was able to provide three bunches with up to 154 ns bunch spacing. It was decided to set the FONT4 feedback latency to 140 ns as shown in table 2.7 in case it was necessary to use the smaller bunch spacing at ATF for reasons of beam quality in the ATF extraction line.

2.4.1 Analogue Processor

The FONT3 analogue processor was modified to become the front-end of the FONT4 processor. The ADC required suitably broad sum and difference signals to make sampling at the peak reliable and accurate. The width of the signals from the FONT3 processors was approximately 3.2 ns FWHM which was too narrow for sampling accurately. The bandpass and lowpass filters in the FONT3 processor were modified to give the processor a smaller bandwidth and broaden the output signal aiming for ∼10 ns. In FONT3, the lowpass filter was 170 MHz and the bandpass filter 500-900 MHz. For the simulation of a possible FONT4

		Time (ns)
Irreducible	Time of flight of bunches	4
	Signal return delay	10
Reducible	Analogue Processor	7
	Digital Processor	68
	Amplifier rise time	40
	Kicker fill time	3
	Total	132

Table 2.7: Latency prediction for FONT4 [59].

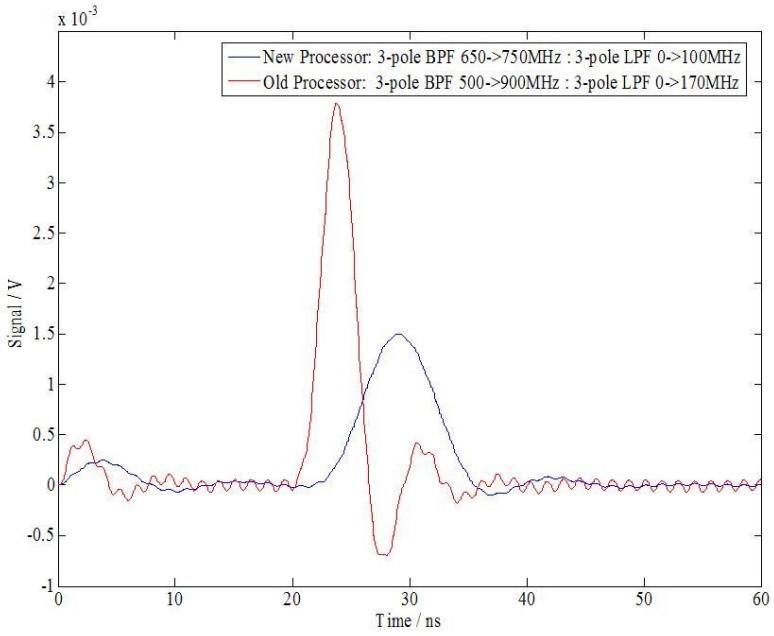

Figure 2.16: A System View simulation of the FONT3 processor output (red) and the FONT4 processor output with the revised filter values (blue) [60].

processor, the filter cutoff frequencies were assumed to be 100 MHz for the lowpass filter and 650-750 MHz for the bandpass filter. Figure 2.16 shows the simulated pulse from the FONT3 processor compared with the simulated pulse for this FONT4 analogue processor with the revised filtering scheme. The broadened pulse comes at the expense of amplitude and also latency. The actual filter scheme that was decided on for FONT4 analogue processor had a 90 MHz lowpass filter and a bandpass filter with ±130 MHz about 714 MHz.

The modified FONT3 design (figure 2.17) was mounted on a PCB and held in a rigid case. This was both more convenient (as it resulted in less set-up than the connectorised FONT3 processor) and reliable (the repeated disconnection and connection of components in the FONT3 processors created slightly different behaviour each time the processors were used). The FONT4 analogue processors also gave both sum and difference as outputs for the same pair of BPM pickoffs as shown in the schematic in figure 2.18.

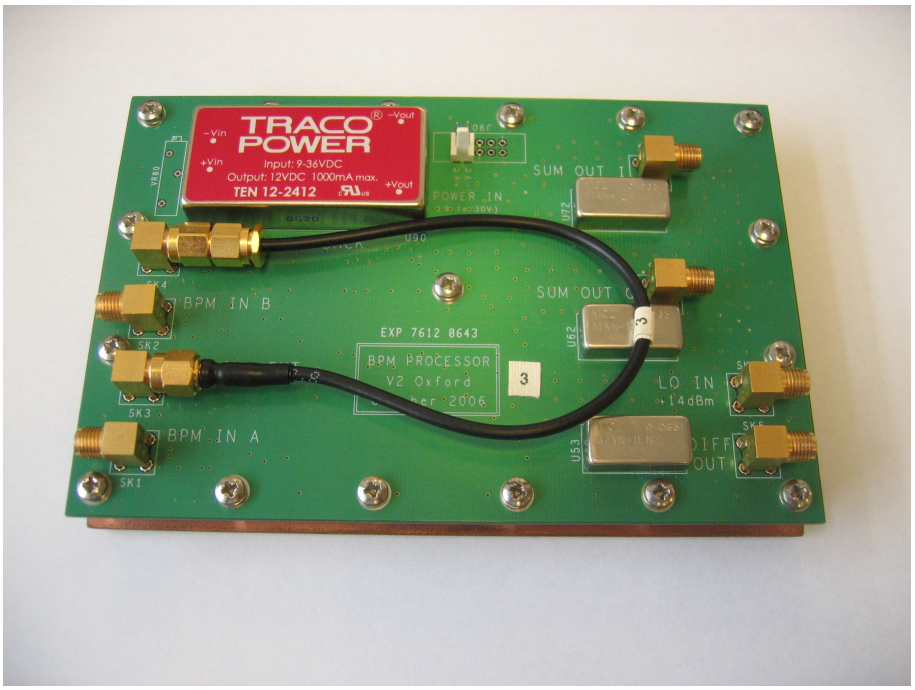

Figure 2.17: The FONT4 analogue processor [61].

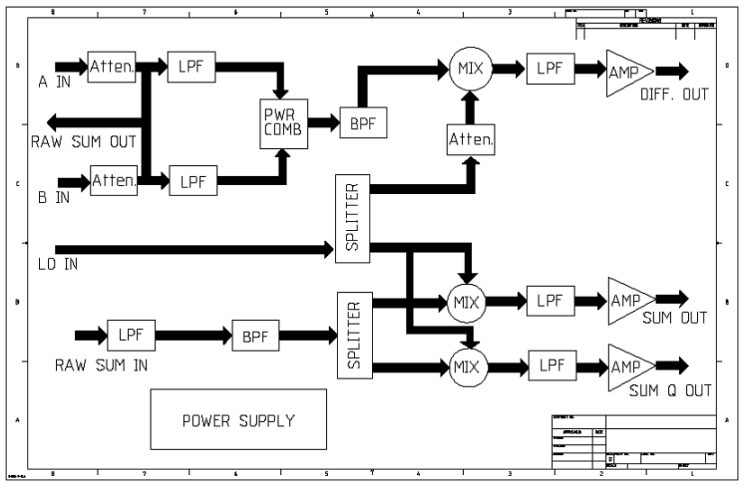

Figure 2.18: Block diagram of the FONT4 analogue processor components [61]. This is essentially the same design as the FONT3 processor (see figure 2.5) except with both the difference and the sum as output and different values for the filters.

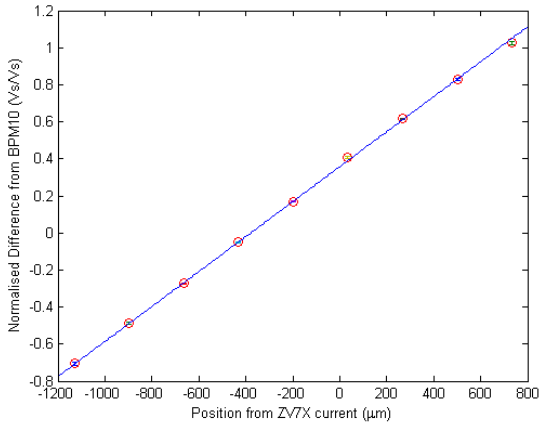

(a) BPM10 calibration

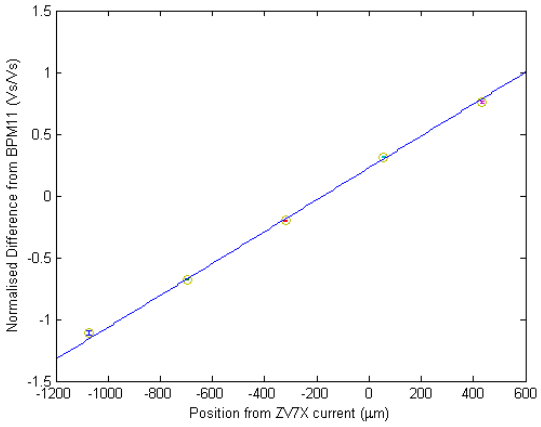

(b) BPM11 calibration

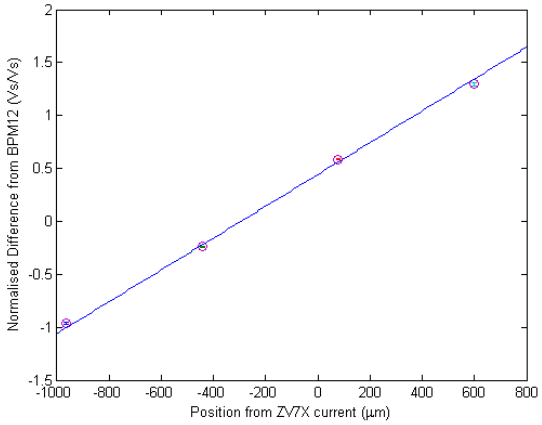

(c) BPM12 calibration

Figure 2.19: Y (equation 2.2) versus position. Calibration curves are shown for three BPMs instrumented with the FONT4 analogue processor.

The FONT4 analogue processors were calibrated using an upstream dipole magnet of known kick, exactly the same as for the FONT3 processors. The calibrations are shown in figure 2.17. As with the FONT3 processors, the resolutions were found using two BPMs to predict the third and looking at the distribution of the residuals (shown in figure 2.20). The resolutions were found to be 13.0, 7.9 and 9.9 μm.

This shows an improvement on the resolutions for the FONT3 processors (for single bunch operation), despite the smaller bandwidth of the FONT4 processor, due to the improvements in setting up the processors and phasing the LO. However, jitter on the LO of approximately 4° existed [62] and this made the resolution worse. Further improvements can still be made to reduce the common mode signal and increase the accuracy of the subtraction in the hybrid. There is ongoing work to improve the resolution of the FONT4 analogue processor.

The latency of the FONT4 analogue processor was measured using test bench equipment to generate a short pulse like half a stripline bipolar shown in figure 2.21. The latency was measured to be 10.4 ns from the peak of the input to the peak of the output. That is ∼4 ns longer than the FONT3 processor which was measured at ATF to be 6.2 ns from the peak of

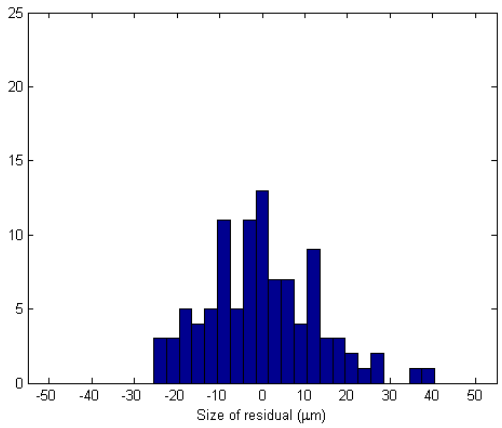

(a) BPM10 residuals

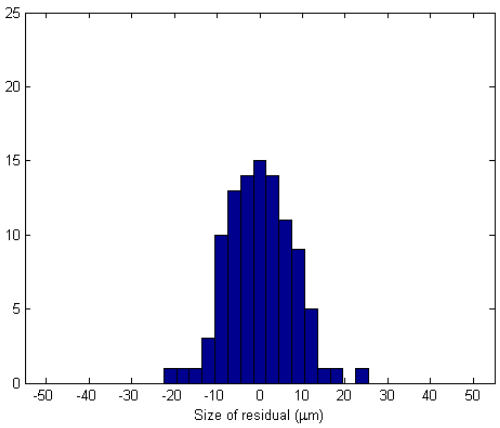

(b) BPM11 residuals

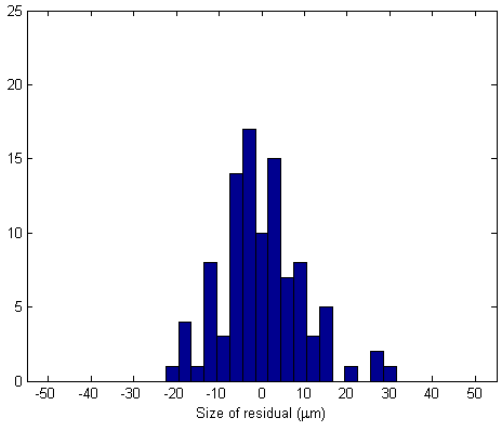

(c) BPM12 residuals

Figure 2.20: The distribution of the residuals for three BPMs instrumented with the FONT4 analogue processor.

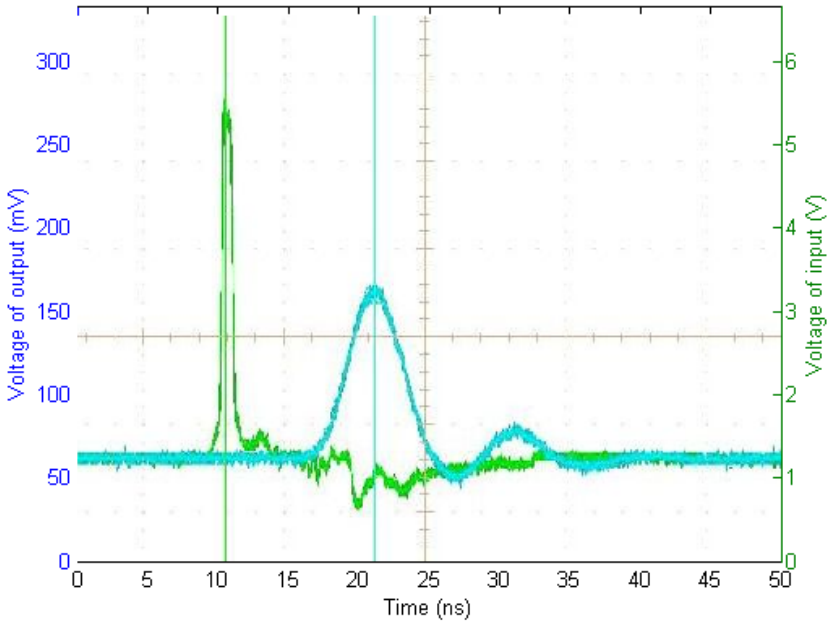

Figure 2.21: Measurement of the FONT4 analogue processor latency showing the input signal (green) and the processor output (blue) [63].

the positive-going part of the input signal to the peak of the processor output. However, the latency measurement for FONT4 included an extra low pass filter on the PCB, introduced to filter out any oscillations from the on-board amplifier which was never actually used in the tests. The low pass filter will be removed in the future FONT4 analogue processors.

The width of the FONT4 analogue processor output was 4.4 ns FWHM and approximately 10 ns full-width.

2.4.2 Digital Processor

The output from the analogue BPM processor was digitised by a 14 bit ADC capable of 105 MSPS (mega samples per second) and then processed by a Xilinx Virtex4 FPGA [64]. As the analogue processor signals were ∼10 ns wide at the maximum, this meant that only one sample per bunch was possible. It was important to make this sample at the peak of the bunch signal for the greatest sensitivity. This required a complex arrangement involving Block RAM embedded on the FPGA [65].

Sampling at the peaks of the bunches

Available at ATF was a 357 MHz (the ATF bucket spacing frequency) signal locked to the beam. This was used to clock the Block RAM (BRAM) which outputted enable bitstreams[3] for the ADC. The bitstreams were preloaded patterns for 16 different bunch spacings (from

[3]These sequences of 1s and 0s would instruct the ADC to sample or not sample.

120.4 ns to 162.4 ns in 2.8 ns steps) that mixed 357/4 MHz and 357/5 MHz clocks. By mixing the two clocks, sampling at the exact spacing between the bunches was possible whereas with only one clock the bunch spacing would need to be a multiple of the clock's time period. A bunch spacing of 154 ns, for example, with an enable bitstream based on the 357/4 MHz clock, would not have the peaks of the bunches sampled because there is a non-integer number of samples between the peaks. Based on two clocks, it is possible to have an integer number of samples in the 154 ns and therefore the sampling is in phase with the bunches. The slightly faster sampling (357/4 MHz) was used at the bunches whereas 357/5 MHz was used between the bunches.

To time the BRAM output such that the enable bitstream coincides with the bunch signals, a pre-beam trigger selected the ring-clock cycle on which the bunches were extracted. Finding the peak of the signal from the first bunch involved incrementing the address of the BRAM in 2.8 ns steps (from the 357 MHz clock) with respect to the 2.16 MHz ring frequency. Further fine tuning in case the peak of the bunch signal fell between the 2.8 ns steps was achieved using silicon delay lines on the chip.

FPGA Processing

Two methods of signal processing were developed: without charge normalisation and with charge normalisation.

Without charge normalisation was the simplest method. The difference signal from the analogue processor was sampled as above and then multiplied by a single gain number.

Charge normalisation used lookup tables to perform the normalisation and multiplication by a gain. The sum signal from the digitised analogue processor signal was inverted and multiplied by a gain via a lookup table and then this was multiplied by the digitised difference signal from the analogue processor.

The final signal after the logic was then passed to a DAC (which used the enables from the block RAM). The analogue output signal was input to the amplifier.

The delay loop is incorporated into the FPGA logic and retains the correction from one bunch to the next.

Latency

The ADC, DAC and FPGA processing were measured for latency as a function of the clocking frequency. The results, as shown in figure 2.22, suggest a latency of 70 ns at 89.25 MHz (357/4 MHz). This is the minimum latency for the digital board as the latency test does not involve processing and uses only 357/4 MHz as the system clock. It is estimated that 25 ns of the latency is from the FPGA processing, 3 ns from input and output to the FPGA and the rest from the ADC and DAC [66].

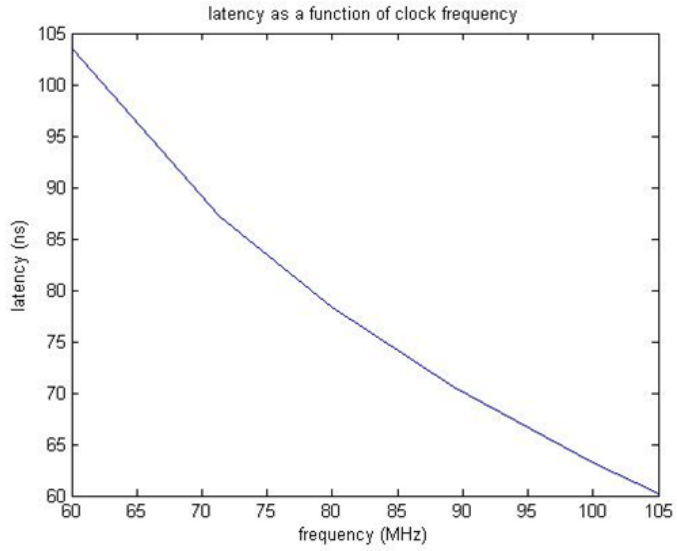

Figure 2.22: The latency of the FONT digital processor versus the frequency of the ADC and DAC [65].

2.4.3 Amplifier

The outline specification for a fast amplifier for FONT was done in Oxford and two units were manufactured by TMD Technologies [67]. It provides ±30 A to the adjustable gap kicker.

The amplifier rise time was specified to be 35 ns to 90% peak output. The specified pulse length was 10 μs to allow for use with the proposed new extraction scheme at ATF [68] which will have up to 60 bunches.

2.4.4 Method

A mode of producing three bunches at large bunch spacings was used (not to be confused with the multibunch trains with the small 2.8 ns spacing used in FONT3). Three RF buckets were filled in the damping ring with spacings a multiple of 2.8 ns. Typically, two spacings were used: 140 ns (2.8×50) and 154 ns (2.8×55). All three trains were extracted on one (∼300 ns long) kicker pulse. The charge was between 0.3 and 0.6 $\times 10^{10}$ per bunch (a little lower than the bunch charge of 1-2 $\times 10^{10}$ at the ILC).

The same setup was used as for FONT3 (described in section 2.3). The first bunch was measured in BPM11 and the FONT correction was applied to bunches 2 and 3 with the upstream kicker. Analogue processors were used on BPMs 12 and 13 to act as witness to the correction. Five different initial position offsets were given to the beams using an upstream corrector (ZV7X). The experiment was performed with and without charge normalisation. Data were recorded using the on-chip ILA (Integrated Logic Analyser) core for the feedback BPM (BPM11) and the oscilloscopes as with FONT3 for the witness BPMs.

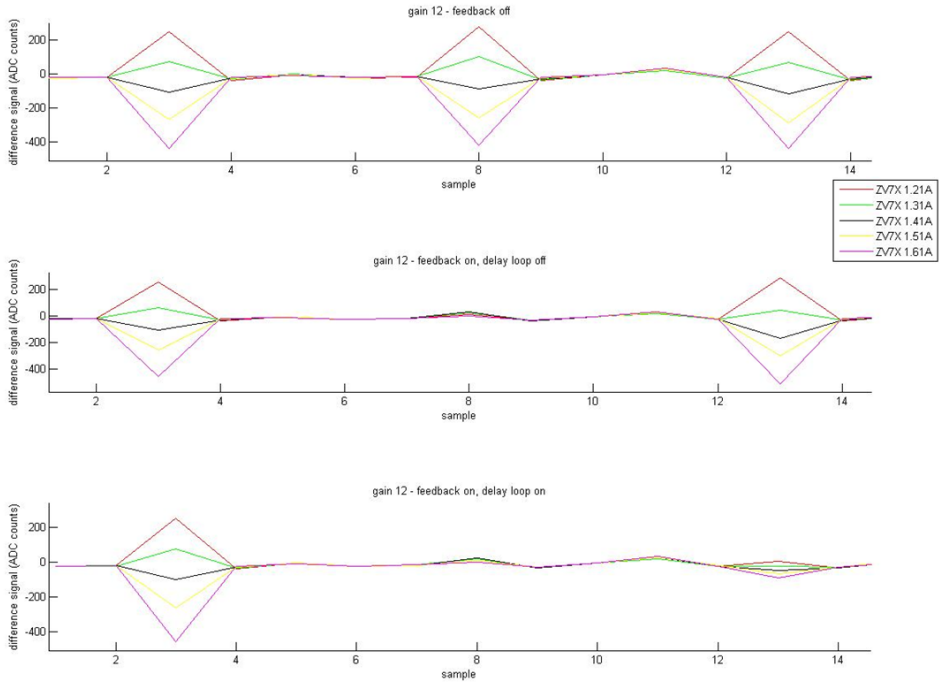

Figure 2.23: ADC counts versus sampling number. Top: the three bunches at their five initial offset positions without feedback. Middle: feedback on and delay loop off. Bottom: the feedback and delay loop on [69]. Shown are averages of 11 bunch trains.

2.4.5 Results

Figure 2.23 shows the FONT4 feedback work without charge normalisation. The five different position offsets given to the bunches using corrector ZV7X are shown as lines of different colours. As there was only one sampling point per bunch, there is not an indication of the bunch shape. Without the delay loop on, the correction is not kept for the third bunch. This shows a 7:1 correction in bunch 2.

Figure 2.24 shows the FONT4 feedback work with charge normalisation. Here, only three different position offsets were used.

Feedback with charge normalisation shows greater success in bringing the bunches to zero y offset on average. Shot by shot however, it appeared worse due to the added random error of the resolution of the charge measurement.

In both methods of signal processing, bunch 3 was not corrected as well as bunch 2. The gain was optimised for bunch 2 and the bunches did not have the same initial position offset due to variation in the amplitude of the extraction kicker pulse. This meant that bunch 3 was under-corrected if it had a larger initial offset position or over-corrected if it had a lower initial offset position. This type of behaviour where different bunches require slightly different gains can be addressed in the FPGA logic in future tests.

The latency of the FONT4 system without charge normalisation was measured by adding

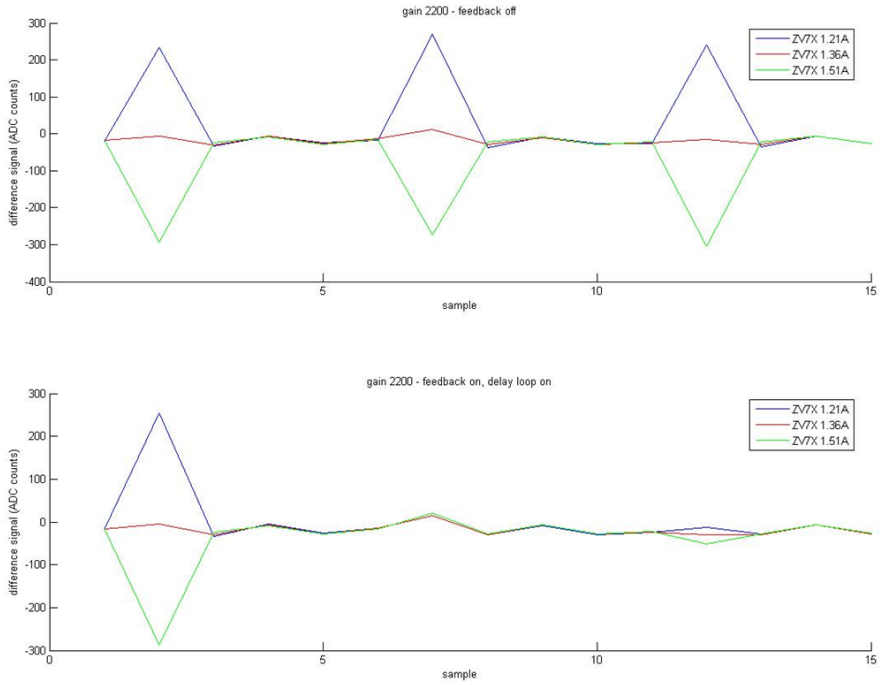

Figure 2.24: ADC counts versus sampling number. Top: the three bunches at their three initial offset positions without feedback. Bottom: the feedback and delay loop on [69]. Shown are averages of 11 bunch trains.

delay to the DAC output. The bunch spacing was set to 154 ns (the maximum available) and the feedback turned on. As long as the latency of the FONT4 system plus the additional delay was less than the bunch spacing, the second bunch was still kicked. The delay was increased until the second bunch was no longer kicked. The position of the second bunch is shown in figure 2.25 versus the additional delay. With no additional delay, the bunch is kicked to a large offset. With 40 ns of additional delay, the bunch was not kicked at all. Between 0 and 40 ns, the kick experienced by bunch 2 gradually falls as the amplifier has not reached its peak output. 90% of the full kick corresponds to approximately 15 ns of additional delay. With a bunch spacing of 154 ns, the 15 ns of slack indicates a latency for the FONT4 system of $\sim$139 ns.

Charge normalisation is expected to add 8.4 ns to the latency [66]. This brings the basic FONT4 feedback system latency to approximately 148 ns. This is below the smallest bunch spacing in the ILC accelerator parameters.

2.5 Summary

The FONT systems have been developed from low-latency analogue processors to digital processors, demonstrating their ability to correct beam offsets on test beams at NLCTA and ATF.

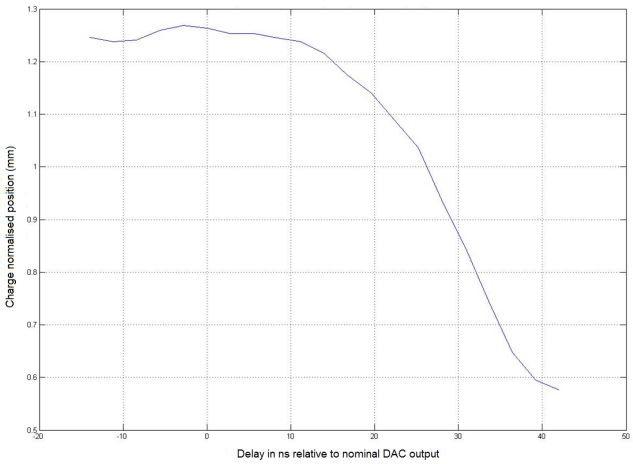

Figure 2.25: The position output of the digital FONT4 processor with delay added to the DAC output to measure the latency [69].

FONT1 successfully demonstrated how beams with different offsets could be corrected to the same trajectory within 70 ns and the correction held for the duration of the train. The correction ratio was 10:1 and a static position profile was present in each pulse that prevented all the bunches from being kicked to zero.

FONT2 improved on both latency, reducing the time to 57 ns, and effectiveness of the correction utilising a digital algorithm to remove static position offsets from the bunchtrain. The correction ratio was 14:1. FONT2 also used a solid state amplifier which was compact and a better design for the ILC.

FONT3 saw a great improvement in latency down to 24 ns and a better correction of 23:1 despite a non-linear response from the amplifier reducing its range of correction, as confirmed through simulation. These beam tests on a 1.3 GeV beam corrected the beam to 6 μm demonstrating that nanometre stability of a TeV was possible with the FONT3 feedback system.

The decision to build the ILC with superconducting cavities with large bunch spacings of 153.8 to 461.5 ns reduced the pressure on low-latency electronics allowing the use of digitisation making the feedback a more powerful tool with complex algorithms and more inputs. These digital FONT4 tests are ongoing. Current tests at ATF show full feedback without charge normalisation with a latency of 140 ns. Feedback with charge normalisation was also a success.

The future goals for FONT at ATF (and ATF2) include improving the resolution of the processor such that the natural jitter of the beam can be stabilised. The resolution of the FONT4 analogue processor, based on the FONT3 analogue processor, is $\sim$10 μm and is required to be $\sim$1 μm for micron stabilisation of the ATF beam.

Essentially, the BPM processor electronics, amplifier and delay loop have been tested without the need for an ILC-like beam. However, the conditions that the BPM is in at the test beam environments are very clean whereas a real Interaction Region (IR) is full

of backgrounds. Therefore the feedback studies were done in the absence of backgrounds. The remainder of this thesis addresses the concern of the operation of the BPM in high backgrounds.

Chapter 3

The Interaction Region at the International Linear Collider (ILC)

The FONT feedback system will be used in many places in the ILC but most prominently and essentially at the interaction point (IP) to steer the beams into collision.

The conditions at the Interaction Region (IR) of the ILC include backgrounds: mainly electrons, positrons and photons from the spent beams, pair production and beamstrahlung. These particles interact with the materials in the extraction line. To fully understand the conditions the BPM striplines will have to operate in, the forward-travelling particles and the materials they interact with need to be investigated. The goal is to understand the environment well enough to replicate it in a test-beam scenario and decide whether the current design is susceptible to the backgrounds.

3.1 Stripline susceptibility to backgrounds

The background conditions at the ILC are of interest to the FONT project because of the potential to cause noise on the striplines of the IP feedback BPM.

The resolution of the FONT BPM needs to be around a micron for nanometre stability at the IP (see section 1.4.2). This level is above the thermal noise limit and RF noise is not expected to be an issue [35], but charges hitting the striplines or being removed from the striplines also cause noise. How much noise they make and whether it degrades the resolution is the question addressed experimentally in this thesis.

3.1.1 Particle-matter interactions

Primary backgrounds at e^+e^- collisions are mainly formed from two things: e+e- pairs from the beam-beam interaction and beamstrahlung photons (see section 1.2). There is material in the IR that these background particles can interact with. As electrons, positrons and photons pass through material, they lose energy and in the process often create new

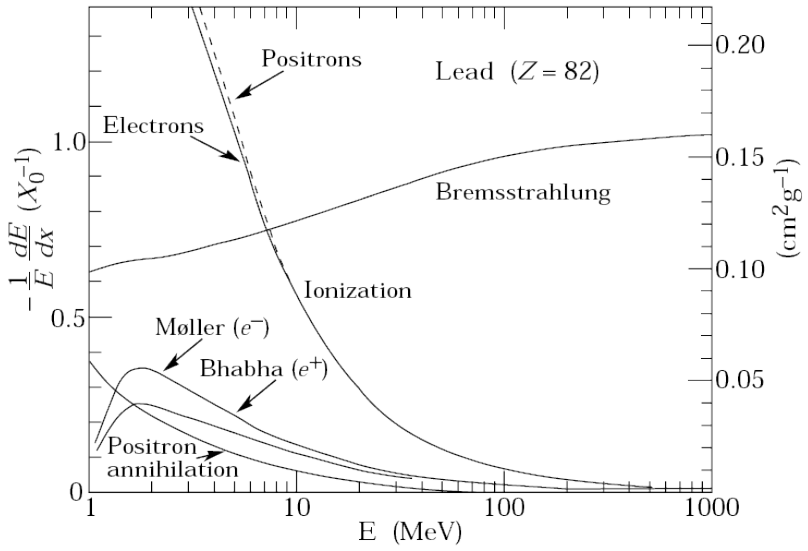

Figure 3.1: Fractional energy loss per radiation length as a function of energy for passage of electrons and positrons through lead [6].

particles. In turn, these lose energy and create new particles, forming an electromagnetic shower. This can happen metres away from the IP where the FONT BPM striplines are situated, producing secondary backgrounds and hence noise on the striplines.

The noise on the striplines could come from two sources: particles from such electromagnetic showers hitting the strips, or particles leaving the striplines due to further interactions occurring in the strips. The particles in showers are typically of low energies and composed of electrons, positrons and photons which will interact with matter and release electrons mainly through ionisation (figure 3.1) and the photoelectric effect (figure 3.2) which are the dominant methods of energy loss at low energies.

Secondary emission of electrons

This process is dominant for low energy electrons and positrons. If a material is bombarded with charged particles (referred to as primaries), electrons are emitted from the material. These electrons are called secondaries. This process is regardless of the species of primary and often the yield of secondaries to primaries is greater than 1 for low energy primaries. The secondary emission yield for lead is shown in figure 3.3. For primary electrons above $\sim$100 eV and below $\sim$1.4 keV, the yield for secondaries is greater than 1.

There are three mechanisms involved in the production of secondaries [70]. The first involves the excitation of an electron. Secondly, it needs to diffuse to the surface of the solid. Thirdly, it needs to escape the solid's surface.

A charged particle entering a solid will excite electrons into a higher energy state. This could be a "distant collision" where the incident particle creates a small perturbation in the atoms, losing only some of its energy . These create slow secondaries around 25 eV [70]. Atomic electrons can also be excited with a direct, inelastic collision. These are called delta

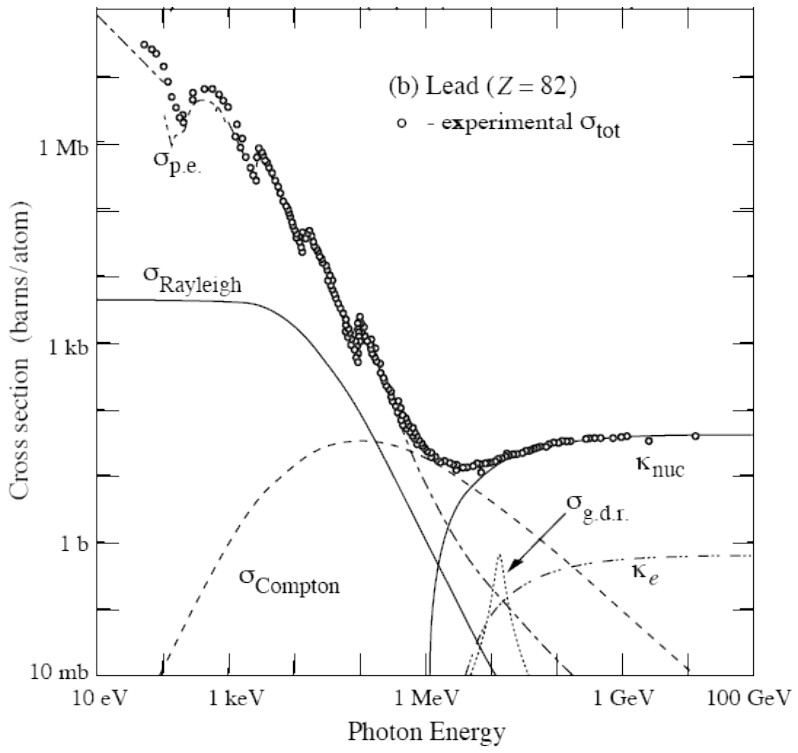

Figure 3.2: The photon total cross sections as a function of energy for passage through lead [6]. $\sigma_{\text{p.e.}}$ = Photoelectric effect, σ_{Rayleigh} = Rayleigh scattering, σ_{Compton} = Incoherent scattering, κ_{nuc} = Pair production (nuclear field), κ_{e} = Pair production (electron field), $\sigma_{\text{g.d.r.}}$ = Photonuclear interactions.

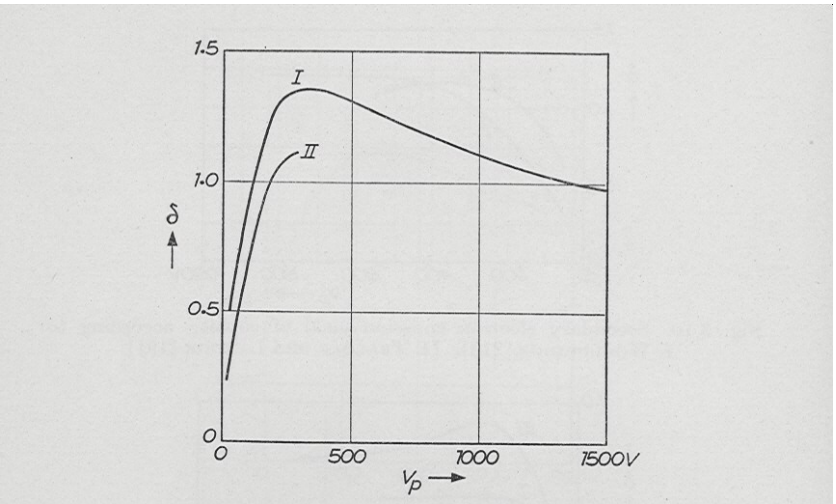

Fig. 3.13. Secondary electron emission yield of iron; according to I. Petry [44]; II. Warnecke [137]

Figure 3.3: The yield of secondary electrons from iron (δ) is plotted as a function of incident electron energy in eV [71].

rays and are relatively energetic.

After the production, the secondary electrons and the delta rays experience collisions, both inelastic (which raises the energies of other electrons, producing more secondaries in the case of the energetic delta rays) and elastic. Diffusion has been found to be a good model for how the secondaries and delta rays move from the place of production to the surface of the metal [70]. The inelastic collisions prevent the electrons from travelling very far, no more than a few atomic layers, before being absorbed. This process is material dependent. The diffusion path length in metals is usually shorter than in insulators which results in fewer electrons reaching the surface and a smaller secondary emission yield in metals [70].

If production occurs near the surface, the diffusion mean free path length may allow for the electron to reach the surface. Once there, it must have enough energy to overcome the electric fields in the surface layer (which is a component of the work function of the material) to escape. This is also material dependent, many compounds (particularly oxides) having a smaller electric potential to overcome and hence a higher yield [71].

The escaping particles therefore comprise secondary electrons, delta rays and also scattered incident particles (otherwise known as rediffused electrons [71]). Often all three types are termed secondaries as it can be hard to distinguish between them.

Since the production of secondaries mainly occurs in a very shallow layer near the surface, the incident angle affects the yield. Incident beams that graze the surface will tend to travel further within this layer (see figure 3.4).

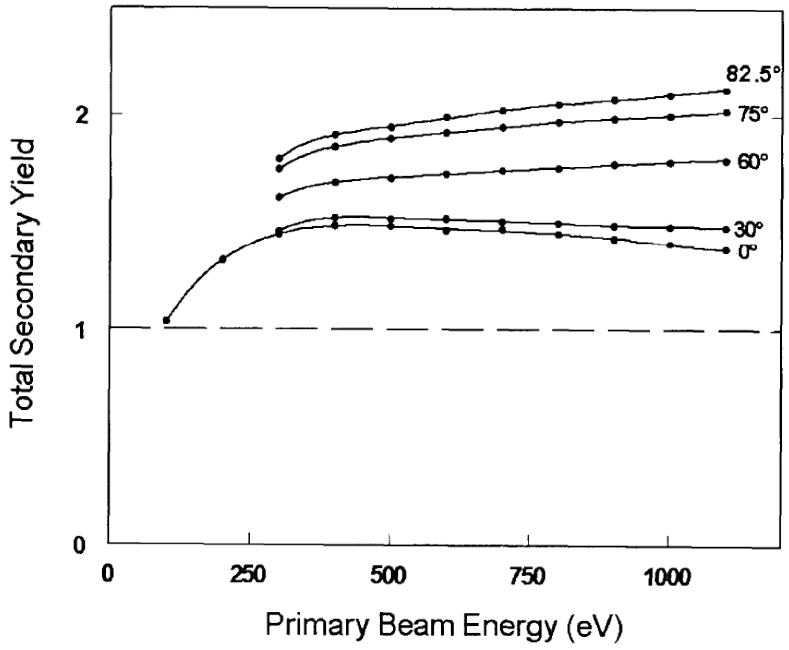

Figure 3.4: Yield of secondary electrons from a TiN/Al alloy versus energy for different angles of the incident beam of electrons [72]. The angle is measured from the normal to the alloy.

Bremsstrahlung

This is the main process in which high energy (a few tens of MeV) electrons and positrons lose energy (see figure 3.1). Bremsstrahlung is electromagnetic radiation caused by a decelerated charge. In materials, electrons and positrons are deflected by atomic fields and they radiate photons.

One radiation length (X_0) is defined as the mean distance over which an electron loses all but 1/e of its energy to bremsstrahlung [6]. It varies with material.

Photoelectric Effect

Energy loss through the photoelectric effect ($\sigma_{\text{p.e.}}$ in figure 3.2) is dominant for low energy photons. A photon strikes the surface of a material and can excite an electron and release it from the surface if the energy carried by the photon exceeds the work function of the material. The work function is the Fermi energy plus the work for moving a charge through the electric fields in the surface layer [73].

In the photoelectric effect, one photon can only cause the release of one electron. This is unlike the secondary emission of electrons where one incident particle could release many electrons.

Compton Effect

Compton scattering is a major form of energy loss for medium energy photons interacting with matter, around 1 MeV. The photon scatters off an electron, imparting some its energy to the electron, leaving at a different angle and with lower energy. Like the photoelectric effect, the electron is ejected but the lower-energy photon is also free to go on to release more electrons through further Compton scattering or the photoelectric effect.

Pair Production

Pair production (κ_{nuc} and κ_{e} in figure 3.2) is the dominant process by which photons interact with matter at high photon energies. The incident photon energy must be at least twice the electron rest mass (1.022 MeV). The process of pair production involves a photon in an external field (necessary for both energy and momentum conservation) creating an electron and a positron. The external field is usually from the atomic nuclei of the matter the photons pass through.

Usually the positron is captured by an electron and they annihilate producing two 0.511 MeV photons.

One radiation length (X_0) is 7/9 of the mean free path for pair production [6].

3.1.2 Signals of charges hitting and being emitted from striplines

A current will be induced in the BPM stripline through charges being added or removed. This current could cause errors in the position measurement if the net effect is large enough.

If an electron is added to the stripline, the current in the stripline is $q_e c F(t)$ where q_e is the charge on the electron, c the speed of light and $F(t)$ a function that describes the shape of the pulse. $F(t)$ includes a factor of $\frac{1}{2}$ since the signal is split, travelling in two directions on the stripline. The addition of an electric charge at the upstream end of the stripline is "instantaneous", therefore $F(t)$ is a delta function. However, if the hit occurs further down the stripline after an oblique approach to the stripline, there is an image charge and a flow of electrons before it actually hits the strip. Therefore $F(t)$ would have a slowly growing tail leading up to the delta function of the instantaneous deposition of the electric charge on the stripline. The voltage signal is negative.

A removed electron causes a positive voltage signal. The delta function of the initial removal of charge is followed by a small tail as the charge travels away from the stripline and its image charge decreases until the charge is fully removed.

The voltage polarity is reversed for positrons. A positron leaving the stripline creates a negative voltage and a positron being added to the stripline creates a positive voltage on the upstream pick-off. The polarities of the voltage signals are summarised in figure 3.5,

With equation 1.10, the effect caused by a charge being instantaneously added to or removed from the stripline can be estimated. This gives an upper limit for the real case. The

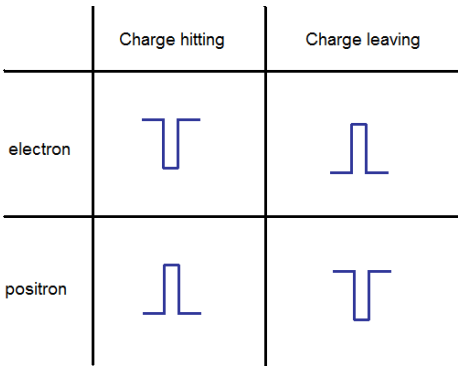

Figure 3.5: The polarities of the voltage signals caused by the addition and subtraction of electrons and positrons from a stripline.

change in I_{beam} is $\frac{1}{2}q_e c\delta(z)$ where the half comes from the signal splitting in two directions along the stripline. On a stripline that subtends an azimuthal angle of $\pi/8$ radians in a beampipe with radius (b) 2 cm, this change in current corresponds to an offset of 2 pm for a 2×10^{10} electron beam (I_{beam}). The cumulative effects of 10^6 charges will therefore correspond to an offset of $\sim$1 μm for a 2×10^{10} electron beam, which is the target resolution for the FONT BPM (section 1.4.2).

The fact that removal does not occur instantaneously means that the frequency spectrum of the noise is not flat and all particles (with their different velocities) do not deliver the same effect at the response frequency of the BPM. As a charge is removed, the image of it remains until the charge is far enough from the stripline to be considered at infinity. The striplines are, however, close to an electrically grounded wall and so any charge that crosses the short gap from the stripline to the wall is considered to be totally removed. During this period between getting knocked out and "totally removed", the signal in the stripline grows. If it takes a long time for the charge to traverse the distance from the stripline to the point of its removal (i.e. the kinetic energy of the particle is low), the signal is slow growing and low in frequency. For this reason we expect particles with low kinetic energies to fall out of the frequency range we are interested in. That is, if the signal is much slower than the normal stripline signal then it is not going to affect our position measurement and is of no interest. This limit can be estimated with an approximation of the form factor for this signal, shown in figure 3.6. The noise form factor is $\text{sinc}(\pi f T)$ (based on the assumption that the current is a top hat function) where T is the time it takes for the charge to cross the gap and f is the frequency of the 15 cm stripline (500 MHz). In this model the gap between the striplines and the wall is 4 mm and it is assumed all charges take that most direct route to the wall. The effect of charges with kinetic energy less than 100 eV is suppressed by the value on the y axis. Below 11 eV, the signal is much slower than the normal stripline signal and particles leaving the stripline below this energy do not add to the noise.

These considerations so far have not included a magnetic field. A magnetic field in this region transverse to the momentum of the charges curls the paths of the charges. In particular, the low energy charges will be curled tight and perhaps too tight to allow them to be removed from the striplines. For example, at 5 T, an electron with transverse momentum 100 eV will curl into a radius of 7 μm making the path to the wall considerably longer.

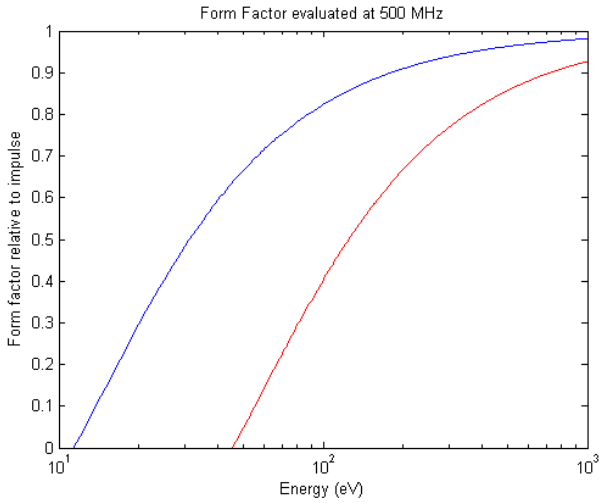

Figure 3.6: The form factor for the signal caused by charges being ejected from the striplines. Assuming 4 mm gap between stripline and wall (blue) and 8 mm gap between stripline and wall (red). It was evaluated at 500 MHz, the peak response frequency of a 15 cm stripline BPM.

Longer path lengths result in a greater suppression of the low energy particles as shown in figure 3.6 where the form factor in red considers a path twice as long as the form factor in blue.

Thus we find ourselves concerned with the particles that hit or are emitted from the striplines from a few tens of eV upwards.

3.2 The Interaction Region Components

The Reference Design Report for the ILC [11] was submitted in August 2007 after considerable work and debate. It finalises the decision to have one IR at the ILC and to have the beams at a crossing angle of 14 mrad. Prior to this, two crossing angles were in the baseline configuration: 20 mrad and 2 mrad [74]. These two crossing angles have been studied more thoroughly over the past years and some of those results are presented in this chapter on the basis that the lessons learned from these studies are also applicable to the 14 mrad design.

Currently, there are four proposed ideas for a detector at the ILC, each of which impacts the beamline near the IP: the Global Large Detector (GLD), the Large Detector Concept (LDC), the Silicon Detector (SiD) and the "4th concept" detector. The differences between the detector technologies are not a concern to the FONT project apart from the magnetic fields and the inner radii and amount of material between the IP and location of the FONT BPM. These components affect the numbers and distribution of background particles in the IR.

The IR for each detector is very similar and can be generalised by a low-Z mask, a BeamCal, a gap (suitable for the FONT BPM stripline) and a quadrupole each of which are further described in subsequent sections. Figure 3.7 shows the relative positions of these

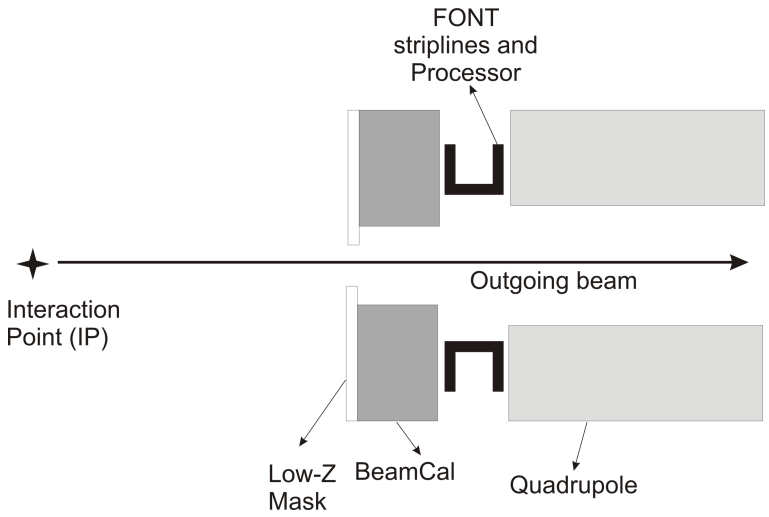

Figure 3.7: A generalised Interaction Region plan view. The main components as seen by the outgoing beam are shown and further described in the text.

objects. The z-locations, lengths and inner-radii differ between the detector concepts and the crossing angle as given in table 3.1.

The ILC will probably have two of these detectors taking turns to be installed at the IP ("push-pull" detectors) and the feedback system will operate with both of them but a detailed engineering design for this system has not yet been worked out.

3.2.1 The IR for the Silicon Detector

The Silicon Detector (SiD) [75] is well described and supported in the simulation tool package GEANT3 [76]. The investigation into IR conditions for the FONT project was based around this detector due to the maturity of its design and the GEANT3 support. Although there is some discussion of the other detector designs in the next section, the rest of this thesis only deals with the SiD case.

As is indicated by the name, the SiD is based on silicon tracking technologies. These technologies are beyond the scope of this thesis but some features of the detector are important to it. These are materials located in the "very forward region" (the forward-calorimetry components) and also the strong magnetic field of 5 T.

The detector design was considered for the three major crossing angles considered by the Global Design Effort team. In the 2 mrad case, there is no dedicated extraction line to take the outgoing beam from the IP and so the incoming and outgoing beams share the same beamline (see figure 3.8). In the 20 mrad and 14 mrad cases, there is a separate extraction line and none of the optical elements in the incoming beamline are used for the outgoing beam though they do impose space restrictions as the beamlines are so close (see figure 3.9).

In the 2 mrad crossing angle design (as shown in figure 3.8), the beampipe after the vertex of the IP expands to a radius of 8.69 cm at z = 179.5 cm. Here the tungsten mask (M1) begins and the beampipe inner radius expands to 16 cm by z = 330 cm. This wide

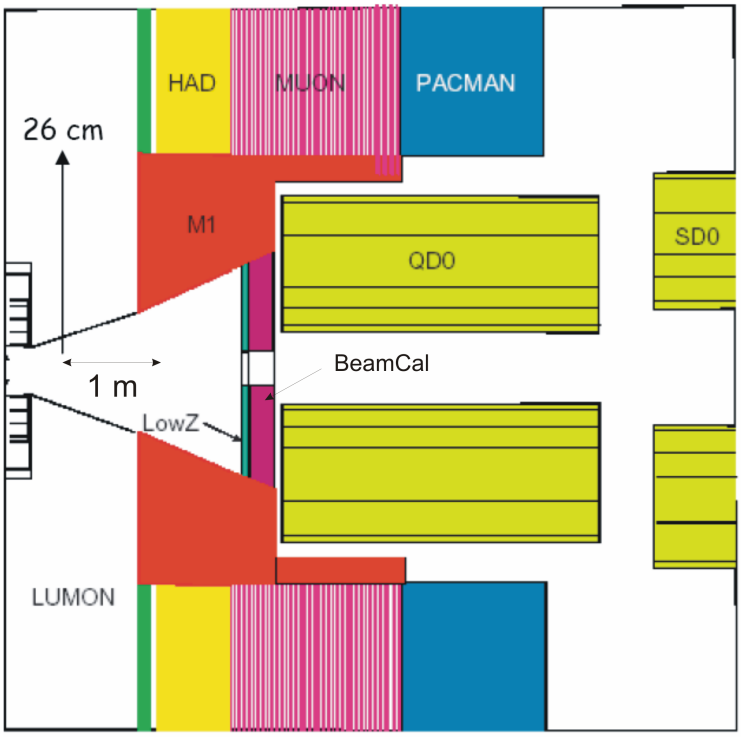

Figure 3.8: Plan view SiD IR for the 2 mrad case [75]. Showing the low-Z mask (LowZ), beam calorimeter (BeamCal), luminosity calorimeter (LUMON), instrumented Si/W mask (M1), hadron calorimeter (HAD), muon chambers (MUON), radiation shielding (PACMAN), final focus quadrupole (QD0) and strong sextupole (SD0).

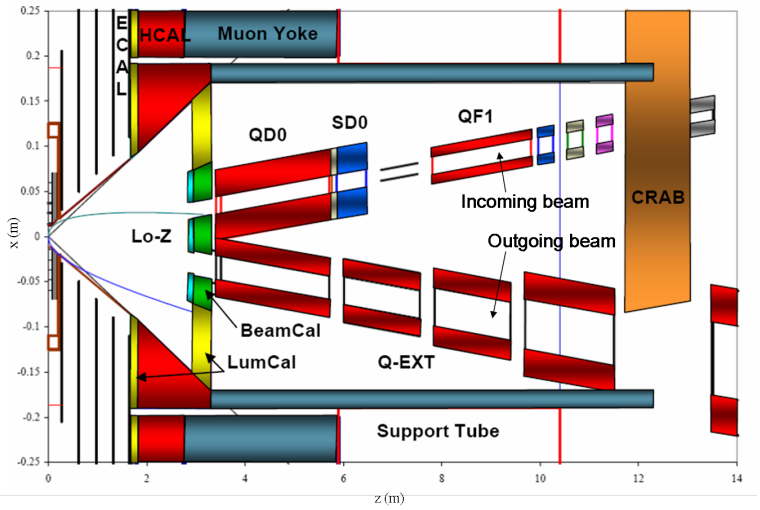

Figure 3.9: Plan view SiD IR for the 20 mrad case [75]. Showing the low-Z mask (Lo-Z), beam calorimeter (BeamCal), extraction line quadrupole (Q-EXT), electromagnetic calorimeter (ECAL), hadron calorimeter (HCAL), muon system (MUON YOKE), final focus doublet (QD0 and QF1), strong sextupole (SD0), crab cavity (CRAB) and luminosity calorimeter (LumCal).

region is immediately plugged by the low-Z[1] mask at z = 285 cm. This is most likely to be 10 cm of beryllium though carbon has also been proposed. This mask is designed to absorb the particles from the BeamCal at z = 295 cm that could otherwise cause hits on the vertex detector by being deflected back towards it [77]. Centred on the low-Z mask is an aperture for the beamline with a radius of 1.5 cm. The aforementioned BeamCal has a larger inner radius of 2.0 cm. It is made of fifty layers of tungsten, silicon and G10 and allows measurement of the instantaneous luminosity using beamstrahlung pairs. The beampipe beyond the tracking volume (z greater than 37.5 cm) is stainless steel [75] though there is discussion to make the beampipe through the BeamCal out of beryllium [77].

The 20 mrad (figure 3.9) and 14 mrad crossing angle designs are conceptually similar, except with a dedicated extraction line and also smaller apertures than the 2 mrad crossing angle design. Here, the incoming beampipe is 1.0 cm in radius and the outgoing beampipe is 1.5 cm in radius. For the 20 mrad case, the aperture through the low-Z mask is 1.2 cm in radius. For 14 mrad, it is 1.35 cm.

For all three crossing angles, there is a gap after the BeamCal and before the first extraction line quadrupole, which is also the final quadrupole doublet in the case of the 2 mrad crossing as the incoming and outgoing beams share the beam pipe. This space is highly fought after but a length of 10 cm is reserved for the IP stripline BPM.

See table 3.1 for a summary of the critical dimensions and the differences between the crossing angle schemes.

3.2.2 Other Detector Concepts

The GLD [78] and LDC [79] detectors (figures 3.10 and 3.11) are larger and based on gaseous rather than silicon tracking[2]. The solenoid fields of these detectors are lower than that of the SiD but the inner radii of the beamline elements and the materials they are made from are very similar (see table 3.1). Differences between the GLD and SiD include a Pair Monitor just upstream of the low-Z mask (which is indicated in figure 3.10) which introduces a couple of layers of silicon. There is no low-Z mask shown in figure 3.11 of the LDC IR but a carbon coating to the BeamCal/BCal is mentioned in the Detector Outline Document so again, this is a very similar IR to the SiD. Due to these similarities, no work has been done by the FONT group on the background environment created by these detectors as seen by the BPM.

The 4th Concept detector is not of the same maturity and the extraction line region is not so well defined in the Detector Outline Document currently available hence no details about its IR are given here.

[1] Here Z refers to the atomic number.

[2] The similarity of the two concepts has recently led to them combining to form the ILD detector concept [80].

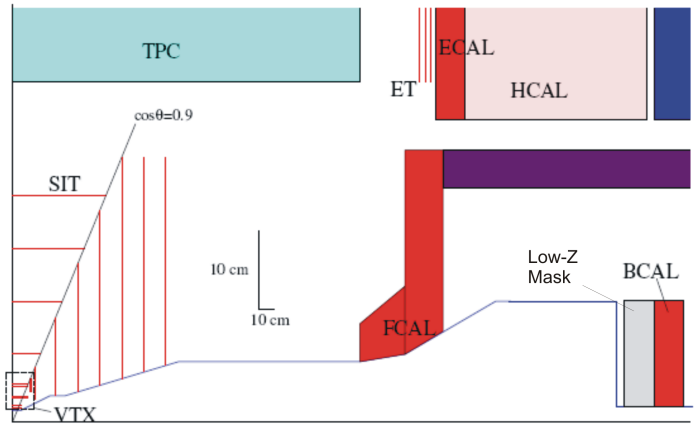

Figure 3.10: The IR of the GLD 2 mrad case [78]. Showing the low-Z mask, beamline calorimeter (BCAL), forward calorimeter (FCAL), time projection chamber (TPC), silicon inner trackers (SIT), end-cap trackers (ET), vertex detector (VTX), electromagnetic calorimeter (ECAL) and hadron calorimeter (HCAL).

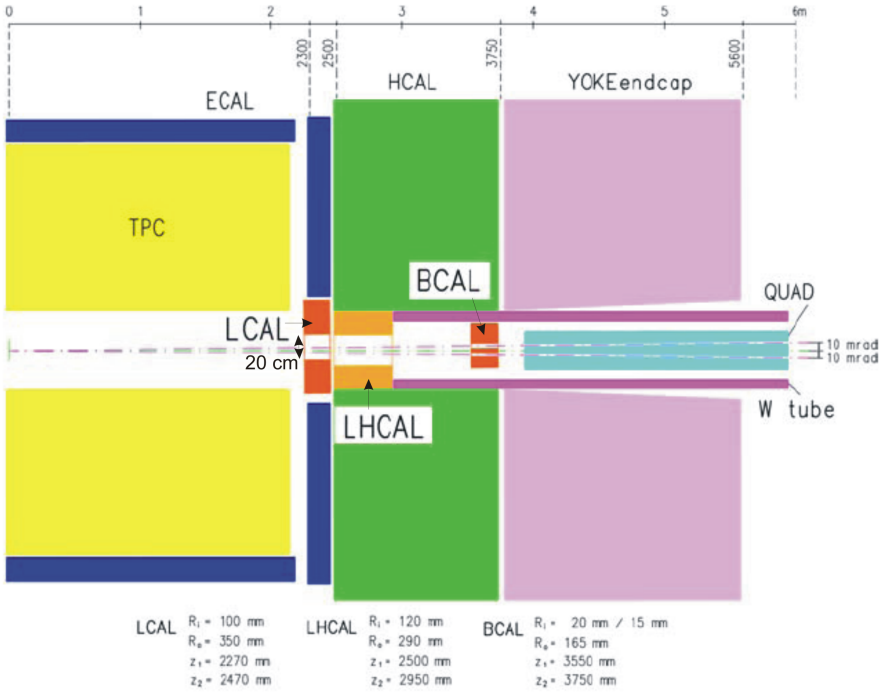

Figure 3.11: The IR of the LDC for the 20 mrad case [79]. Showing beam calorimeter (BCAL), last quadrupole of beam delivery system (QUAD), luminosity monitor (LCAL), forward hadron calorimeter (LHCAL), time projection chamber (TPC), electromagnetic calorimeter (ECAL), hadron calorimeter (HCAL), muon detector (YOKE endcap) and support for the forward calorimetry (W tube).

Detector	Crossing Angle (mrad)	Solenoid Field (T)	Low-Z z (cm)	Low-Z Inner Radius (cm)	BeamCal z (cm)	BeamCal Inner Radius (cm)	Extraction Quad z (cm)
SiD [75]	2	5	285	1.5	295	2.0	351
SiD [76]	14	5	285	1.35	295	1.5	600
SiD [75]	20	5	285	1.2	295	1.5	351
SiD [81]*	20	5	315	1.0	325	1.0	600
GLD [78]	2 and 20	3	405	2.0	430	2.0	450
LDC [79]	2	4	-	-	355	2.0	405
LDC [79]	20	4	-	-	355	1.5	405

Table 3.1: The z-location and inner radii of the low-Z mask and beam calorimeter (BeamCal) for the three proposed detectors and the crossing angles. SiD has the highest magnetic field, the lowest inner radii and z-locations nearest the IP. The very forward region has not been studied in great detail in the GLD and LDC detector concepts [80].
* The SiD model from 2005, with the default parameters as presented, was used for many studies presented in this chapter.

3.2.3 DID and anti-DID

When the beams enter with a horizontal crossing angle with respect to the solenoid field, they are given a vertical displacement. This is shown in figure 3.12 where the beam at the IP (z=0) has a vertical position offset of around 20 μm and a vertical angle offset. This needs to be compensated for as it results in synchrotron radiation which increases the beam size, thereby decreasing luminosity, and it also causes rotation of the polarisation vector leading to potentially reduced longitudinal polarisation at the IP. The case shown in figure 3.12, for example, gives an increase in the size of the beam in y by 0.31 nm. There is also a vertical angle and offset. In this example, compensation of the vertical angle using quadrupoles gives a significant increase in the size of the beam in y by 5.2 nm [82]. A detector integrated dipole (DID) field is proposed [82] where special coils wound on the detector solenoid would locally align the magnetic field lines with the incoming beam trajectory. With the aid of the final focus quadrupole doublet, the DID compensates both the angle and offset at the IP as shown in figure 3.13 where there is no vertical position or angle offset at the IP. The DID field can be optimised to reduce the beam size growth due to synchrotron radiation by an order of magnitude.

However, this has a worse effect on the outgoing beams. The transverse magnetic field that they see increases and beamstrahlung pairs are strongly affected, spiralling along the field lines and potentially striking and backscattering off the LumiCal and BeamCal. Studies for the LDC [83] showed that hits on the first layer of the vertex detector increased and backgrounds in the time projection chamber were four times higher with DID than without, as shown in figure 3.14, providing motivation to reduce the backscattering. To direct the low energy particles into the extraction line rather than hitting the material, a reverse DID field is proposed [84]. Called the “anti-DID”, this aligns the outgoing beams with the magnetic field. GEANT simulations [84] confirmed that the action of the anti-DID with the 14 mrad

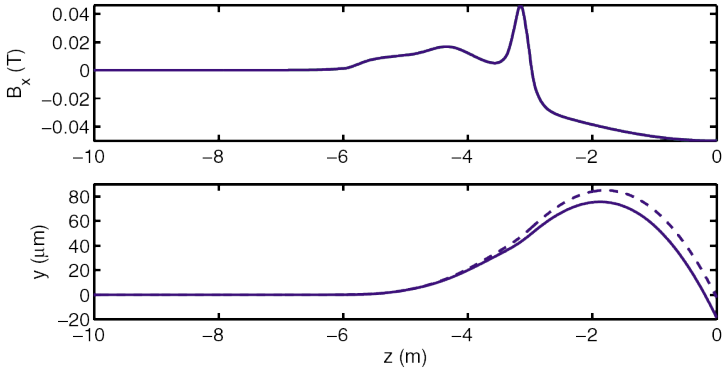

Figure 3.12: The transverse B-field experienced by the incoming beams at an IP with a crossing angle of 20 mrad is shown (top). It has the effect of giving the beam a vertical displacement (below, for two sets of focusing optics) [82].

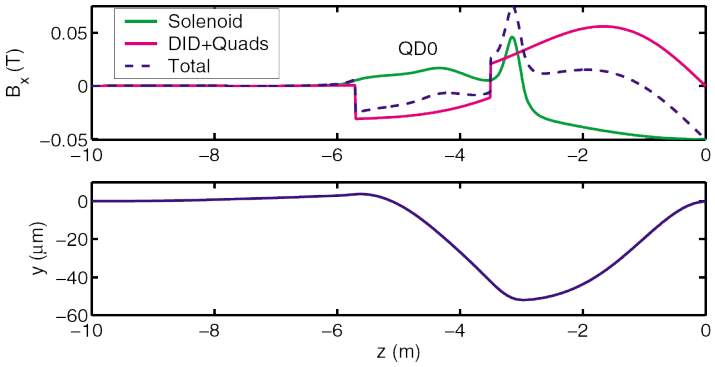

Figure 3.13: The transverse B-field experienced by the incoming beams at an IP with a crossing angle of 20 mrad is shown with just the detector solenoid (green), the DID and quadrupoles (pink) and the total transverse B-field (blue, dashed). The combined field has the effect of giving the beam a vertical displacement (below) with the vertical position offset and angle both zero at the IP (z=0) [82].

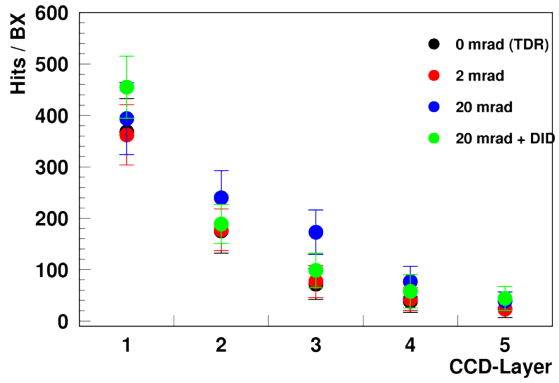

(a) Hits per bunch crossing for 0 mrad crossing angle, 2 mrad crossing angle, 20 mrad crossing angle and 20 mrad crossing angle with DID for the five CCD layers in the vertex detector.

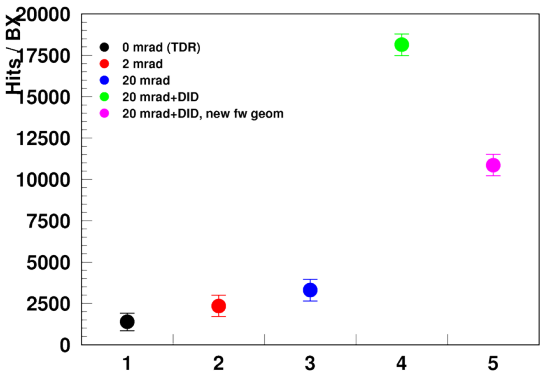

(b) Hits per bunch crossing in TPC for 0 mrad crossing angle, 2 mrad crossing angle, 20 mrad crossing angle, 20 mrad crossing angle with DID, 20 mrad crossing angle with DID and an altered, low backgrounds geometry.

Figure 3.14: The effect of DID on backgrounds at the LDC [83].

crossing angle was to decrease the number of pairs that hit the BeamCal to the same levels as for the 2 mrad crossing angle as shown in figure 3.15.

Obviously the two methods cannot be applied at once so the detector groups are considering which is the best scenario: DID or anti-DID. For the 14 mrad case, it appears that the synchrotron effects (which are related to the crossing angle θ_c as $\theta_c^{5/2}$) are small and the reduction in luminosity can be kept below 2% while directing at least 50% of the beamstrahlung pairs into the extraction line using anti-DID [84]. Therefore the anti-DID is currently in the reference design for the ILC [11].

3.3 Simulation Tools

To gain an understanding of the conditions in the IR of the ILC, it is necessary to look beyond the mechanical properties and magnetic fields of the IR and to the particles within it. The interaction at the IP is moderately clean but there are still vast numbers of photons, electrons and positrons created as the spent beams interact with the material. These need to be investigated through simulation work on computers for their distribution to be known and understood. GUINEA PIG [27], as described in section 1.3.1, simulates the beam-beam interaction that produces the primary backgrounds of the beamstrahlung photons and electron-positron pairs. GEANT [85] is a computer tool written to simulate the interaction of elementary particles with matter and so is useful in investigating the generation of secondary backgrounds in the materials of the IR.

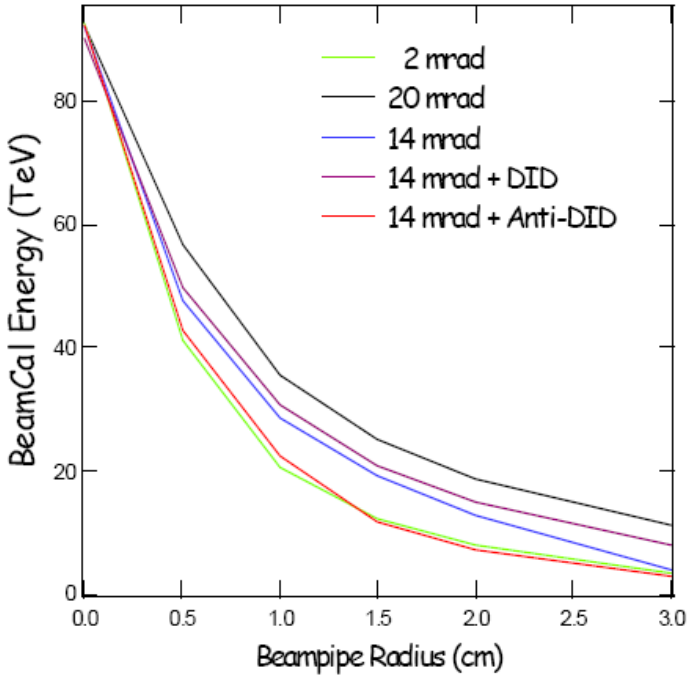

Figure 3.15: The total energy of the beamstrahlung pairs hitting the BeamCal with beampipe radius for the SiD [84]. This is shown for crossing angles 2 mrad (green), 20 mrad (black) and 14 mrad (blue) with the latter also shown with DID (purple) and with anti-DID (red).

3.3.1 GEANT Modifications

GEANT3 was developed for use in high energy physics and tracks particles in matter using Monte Carlo methods. Electromagnetic processes[3] are reproduced within a few percent, with all the dominant processes simulated for particle energies between 10 keV and 100 GeV [86].

These energies for successful tracking are above the energies of particles hitting and leaving the striplines that were found to be a concern in section 3.1.2.

GEANT3 was recoded [87] for the bremsstrahlung and Compton scattering processes using data from the French Nuclear Energy Agency [88]. The modified version follows experimental data[4] and can track these processes to the lowest energy in the data (100 eV). As figure 3.16 shows, the data has a larger bremsstrahlung cross-section than that encoded in GEANT3.

The modified GEANT3 was used throughout this project.

[3]Pair conversion, Compton collision, photoelectric effect, photo fission of heavy elements, Rayleigh effect, multiple scattering, ionisation and δ-ray production, bremsstrahlung, annihilation of positrons, generation of Cerenkov light and synchrotron radiation [86].

[4]The same method of parametrising from experimental data was used in GEANT4 [85], the c++ version of GEANT.

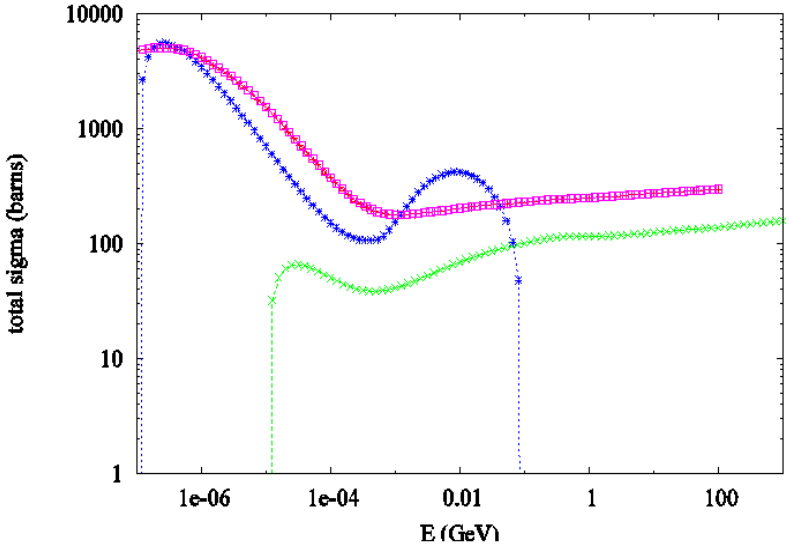

Figure 3.16: The bremsstrahlung cross-section for copper versus incident electron energy. This is shown for experimental data from the French Nuclear Energy Agency [88] (red), GEANT3 with the 10 keV hard coded lower energy limit (green), GEANT3 with the code altered to allow cross-section calculation down to 100 eV (blue) and GEANT3 recoded to follow the experimental data down to 100 eV (magenta, on top of the red experimental data).

3.4 Simulations of ILC IR conditions

The GUINEA PIG output of pairs for a head-on collision of Gaussian e^+e^- bunches was tracked using the modified GEANT3 code through a model of the SiD IR [76] from 2005 without DID (unless otherwise stated).

There were 14 accelerator parameter sets for each crossing angle (see tables 1.2 and 1.3), each producing different GUINEA PIG outputs. Each set was investigated by recording the particles hitting the IP BPM striplines. Other features of the IR were changed in the simulation and particles recorded to investigate the dependence of secondary backgrounds on features of the IR.

As described in section 1.3.1, the pair output from GUINEA PIG is the largest concern with regard to secondary backgrounds in the IR, as opposed to the photons, hadrons or spent beam. Pair production from the beam-beam interaction is at a maximum with head-on collisions [81] so these simulations are using the maximum pair backgrounds expected.

3.4.1 Number of charged particle hits

Dependence on accelerator parameter set

Varying numbers of shower particles are produced in the IR depending on the accelerator parameter set, crossing angle and position of elements in the IR [89]. The work was done

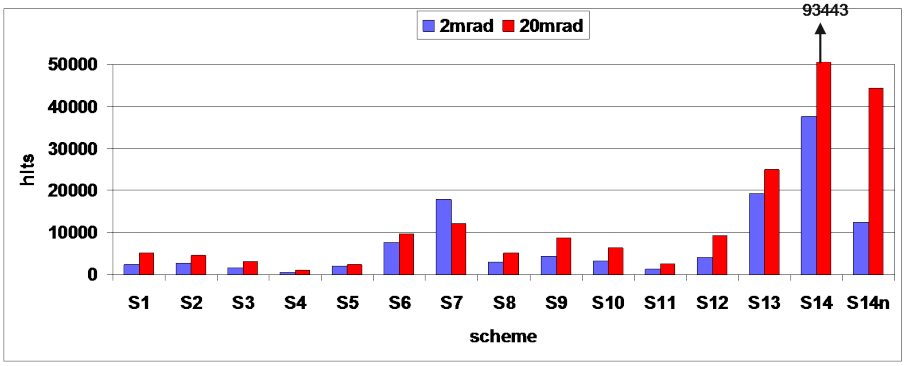

Figure 3.17: The total number of electron, positron and photon hits per stripline of a stripline BPM were counted for each parameter set at both the 2 mrad and 20 mrad crossing angles [89]. See tables 1.2 and 1.3 for the description of the schemes.

for the 2 mrad and 20 mrad crossing angles. Low beam charge schemes resulted in lower backgrounds in the IR (because there are fewer particles per bunch) and high luminosity schemes resulted in larger numbers hitting the striplines (because the beam size is small, resulting in a stronger beam-beam interaction) as shown in figure 3.17. In most cases, the 20 mrad crossing angle produces more hits on the striplines since fewer pairs hit the BeamCal in the 2 mrad crossing (figure 3.15) as they are directed down the shared incoming/outgoing beampipe and the beampipe radius is larger (see table 3.1). The scheme with the highest backgrounds was scheme 14 (described in table 1.3). In this case, $\sim 10^5$ electrons, positrons and photons hit each BPM stripline.

Dependence on z position

GUINEA PIG generated pairs were tracked through the SiD IR in GEANT3 and the origin of the particles that hit the striplines were recorded [89]. The results of the simulation (figure 3.18) showed that the sources of the particles that hit the BPM striplines were the beam calorimeter (0.72 radiation lengths of tungsten, silicon and G10) and the BPM itself, from its wall and the other striplines.

Figure 3.19(a) shows the number density of charged particles at z = 3.12 m, a location just in front of the low-Z mask in this 2005 SiD layout. The vast majority of pairs go straight down the beampipe. However, there are also a significant number that hit in between the incoming and outgoing beamlines at x = 0 cm. These are the low transverse momentum particles that are caught in the solenoid field. In figure 3.19(b), energy density is plotted at the same location. There is only a high energy density area at the extraction line (x = -3.12 cm), not at x = 0 cm, confirming that the hits at x = 0 cm are indeed all of low energies. Figure 3.20 shows the distribution of kinetic energies of the electron-positron pairs hitting the low-Z mask compared to those that both hit the low-Z mask and go on to cause hits on the striplines. It was those of mid-energies and some transverse momentum that hit the beam calorimeter and caused spray on the striplines. The selection for mid-energy particles at the low-Z mask is confirmed in this figure to depend on the solenoid field as increasing the solenoid field from 5 T to 10 T also increased the mean kinetic energy of the pairs that

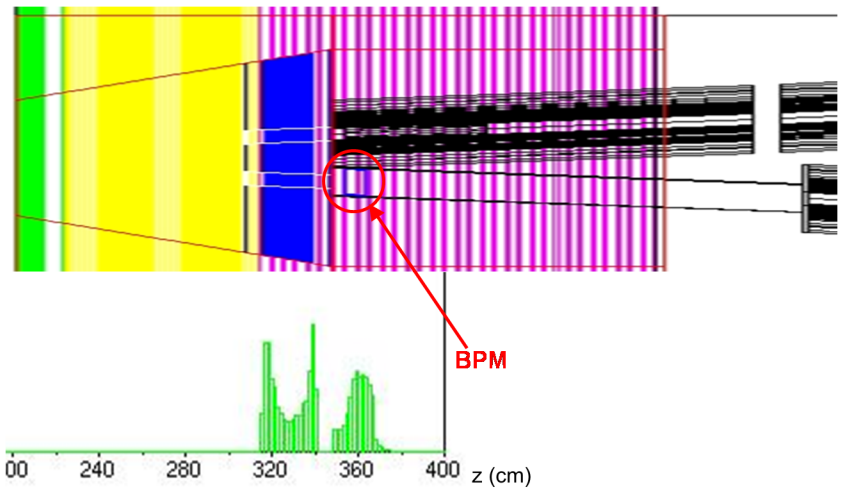

Figure 3.18: Top: the 20 mrad GEANT3 geometry. Below: (with the same horizontal scale) a histogram showing the origin of the particles hitting the striplines [89].

went on to cause hits.

Simulations for the 20 mrad crossing angle IR were also performed to investigate the effect of moving the striplines away from the source of noise (that is away from the beam calorimeter but closer to the extraction quadrupole). The simulations were performed for two accelerator parameter schemes (scheme 1 and scheme 14, see tables 1.2 and 1.3) for GEANT3 simulations with and without the low energy modification to the bremsstrahlung and Compton scattering processes. Different z locations for the stripline BPM were used between z = 350 cm (just downstream of the BeamCal) and z = 575 cm (just upstream of the extraction line quadrupole). The results of the simulations, shown in figure 3.21, indicate that the number of hits on the striplines is greatest when the striplines are placed immediately downstream of the BeamCal. At z = 525 cm, for example, the number of hits was 15% that of at z = 350 cm for scheme 14. There is a small increase of hits as the BPM is moved near the extraction line quadrupole (at z = 575 cm) but only when the striplines are very close to it as the majority of spray particles have forward-going momentum.

Dependence on BPM stripline radius

The GEANT3 simulation of the 20 mrad crossing was run with different BPM stripline radii between 0.4 cm and 1.8 cm. The number of hits increased almost linearly with the stripline radius as shown in figure 3.22 [89].

Dependence on DID

A Detector Integrated Dipole was proposed for the 20 mrad crossing angle and if implemented it would steer more particles into the BeamCal as discussed in section 3.2.3. As BeamCal hits are the major source of secondary backgrounds that hit the striplines, this is expected to create more hits on the BPM striplines. GEANT3 simulations with and without the DID

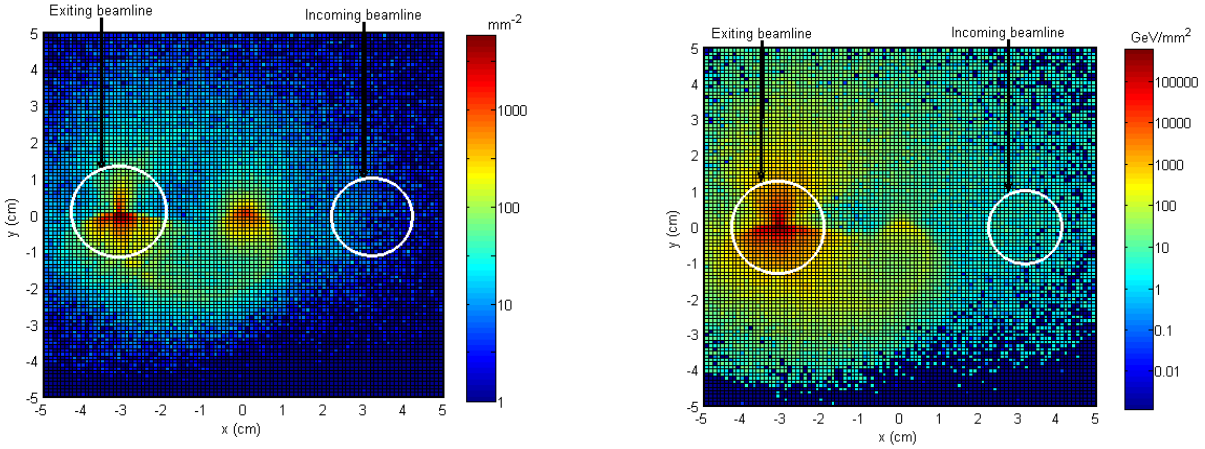

(a) The number density of electrons and positrons at location z = 3.12 m.

(b) The energy density of electrons and positrons at location z = 3.12 m.

Figure 3.19: Results from a GEANT3 simulation of background pairs interacting with the 20 mrad crossing angle for SiD (without DID). Here the low-Z mask is at z = 3.15 m. The extraction line is at x = -3.12 cm. The incoming beamline is at x = 3.12 cm.

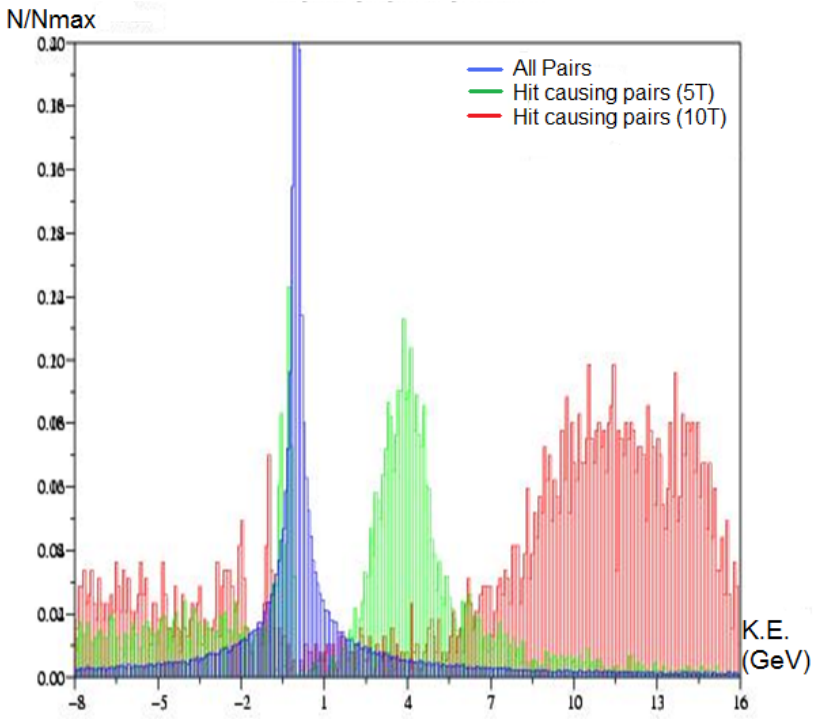

Figure 3.20: The kinetic energies of the particles that hit the low-Z mask are shown (blue) with the kinetic energies of those that cause spray on the striplines (green and red). Negative kinetic energies are positrons and positive kinetic energies are electrons. The numbers are normalised with the maximum number of particles (which occurs at very low kinetic energies). Two GEANT3 simulations were performed: one with the solenoid field at 5 T (green) and the other at 10 T (red) [89].

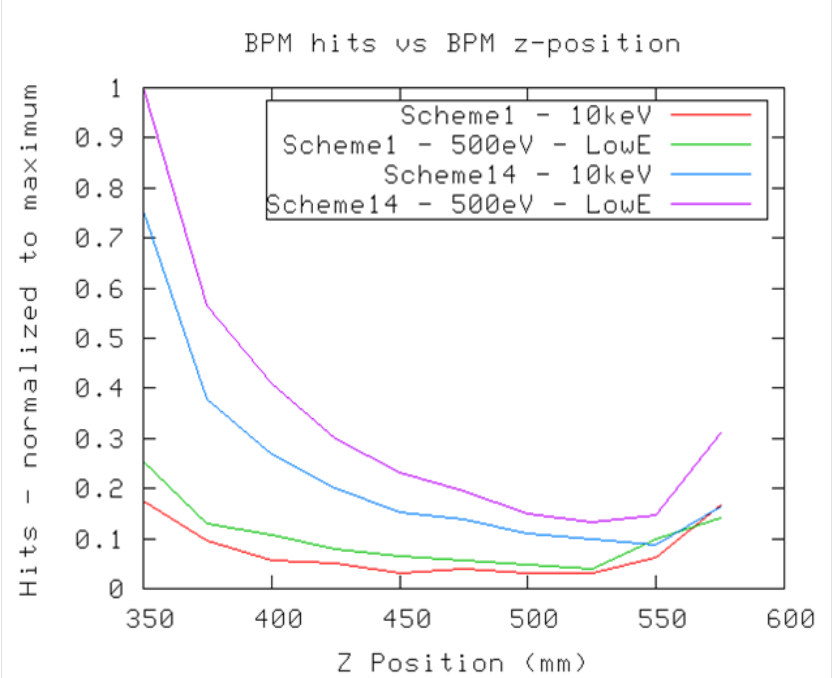

Figure 3.21: The number of hits per stripline versus the z position of the stripline BPM [89]. Results for accelerator parameter scheme 1 are shown for the unmodified GEANT3 (red) and the modified GEANT3 with a 500 eV energy cut on the bremsstrahlung and Compton scattering processes (green). Results for accelerator parameter scheme 14 are shown for the unmodified GEANT3 (blue) and the modified GEANT3 with a 500 eV energy cut (purple).

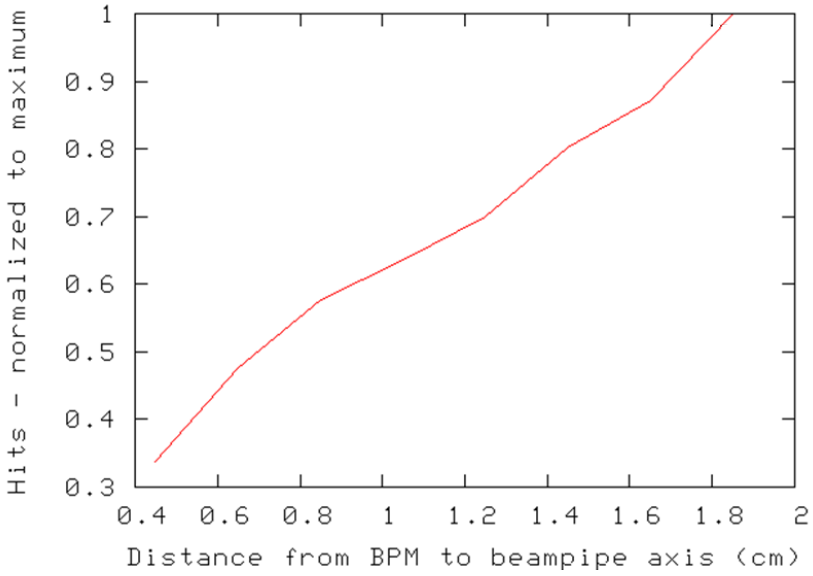

Figure 3.22: The number of hits per stripline versus the radius of the striplines of the BPM from the centre of the beampipe [89].

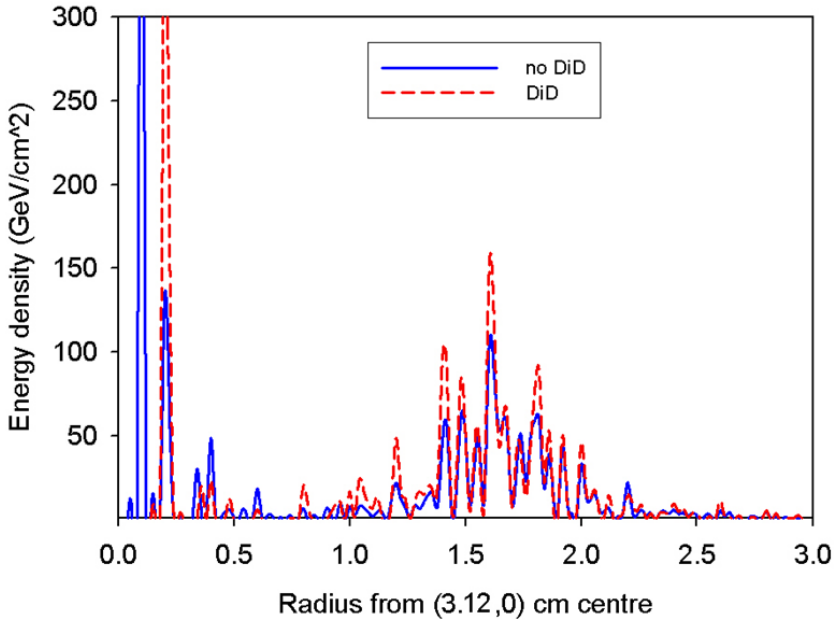

Figure 3.23: The energy density of those particles that go on to cause hits on the BPM striplines is plotted as a function of radius at z = 3.12 m (in front of the low-Z mask) [90]. The energy density for the 20 mrad crossing angle scheme 14 is shown with DID (red) and without DID (blue).

were performed and particles were recorded at z = 3.12 m, a location just in front of the low-Z mask in the model. The results of the simulations (shown in figure 3.23) confirm that the energy density of hits on the low-Z mask (of inner radius of 1.2 cm) is greater with DID than without. The figure also shows that the energy density in the clear beampipe (radius below 1.2 cm) is at a peak at a greater radius, which is due to the deflection of the pairs by the DID field.

The number of hits on the striplines was 30% greater with the DID than without. In fact, it would steer particles directly from the IP to the striplines, causing some high energy primary background particles to hit the striplines [90].

3.4.2 Distribution of charged particles

The number density of electrons, positrons and photons at the location of the IP BPM is shown in x and y in figure 3.24. The azimuthal distribution of particle hits is not symmetric. This results in the top and bottom (y) strips receiving more hits than the side (x) strips. Rotating the strips by 45 degrees would reduce the hits on the most exposed stripline by 25% as this avoids placing striplines in the noisy top and bottom regions.

This pattern is also seen in the distribution of particles that hit the low-Z mask (figure 3.25). Figure 3.25(a) shows the number distribution of the electrons and positrons that hit the low-Z mask with the lower lip of the low-Z mask having the greatest number density. It is clear from figure 3.25(b) that although the number of particles hitting the top lip of the low-Z mask is low compared to the number hitting the bottom, the particles hitting the

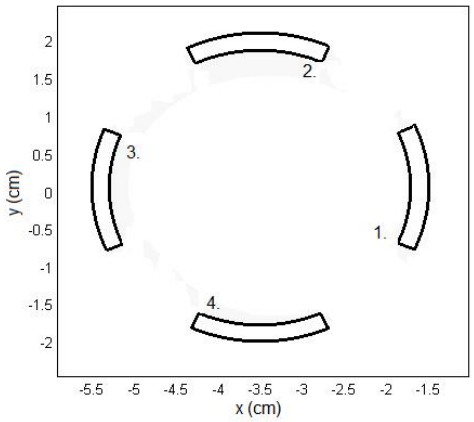

(a) The striplines for the IP feedback BPM are assumed to be arranged as above, each subtending an angle of $\frac{\pi}{4}$. The striplines are referred to in the text by the numbers shown here.

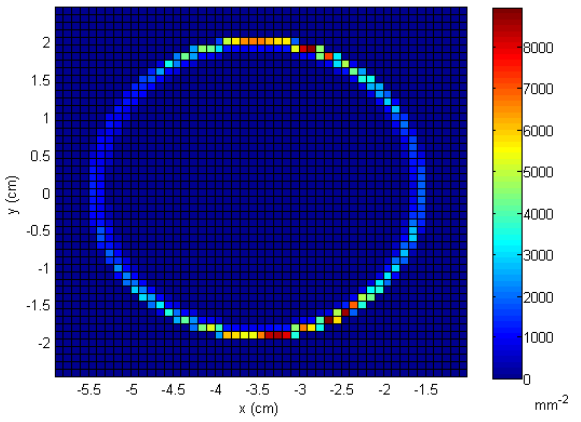

(b) The distribution of the particles at the radius and z location of the BPM striplines.

Figure 3.24: (a) The stripline labels used in this thesis for the IP feedback BPM. (b) The distribution of the particles at the location and radius of the FONT BPM striplines.

top are significant in energy. This combination of many particles hitting the lower lip of the mask and comparatively few yet more energetic particles hitting the top lip of the mask, appears to cause the asymmetric azimuthal distribution of particles hitting the striplines in figure 3.24(b).

By recording the charged particles that hit the striplines and tracking them back to the primaries that instigated the showers that created them, the sources of the hits were found. Shown in figure 3.26(a), the majority of hits on the striplines are found to be caused by particles that strike the bottom lip of the low-Z mask. Although there are comparatively few from the top lip of the mask, they are significant in energy as shown in figure 3.26(b). Also significant when energy density is considered, are the very few high-energy particles that appear in the centre of the extraction line at z = 3.12 m that, under the effects of the solenoid field, subsequently hit material and cause secondaries that hit the striplines [81].

The distribution of primary backgrounds at the low-Z mask is different for electrons and positrons. Positrons, as shown in figure 3.27(a), are spread across the whole area at z = 3.12 m whereas electrons, in figure 3.27(b), are below y = 0 cm. The defocussing of positrons is due to the beam-beam interaction [24] as the beamstrahlung positron trajectories are bent outwards from the centre of the beam by the interaction with the oncoming positron beam. The beamstrahlung electrons, being of opposite charge to the positron beam, are bent into the centre of the beam, that is, they are focussed, and they oscillate vertically.

The positron and electron distributions would be reversed for negative z values on the other side of the IP.

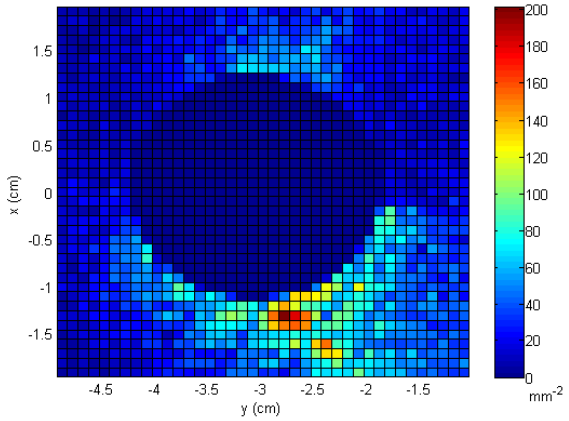

(a) The number density of electrons and positrons at location z = 3.12 m (in front of the low-Z mask). Only particles that hit the low-Z mask are shown.

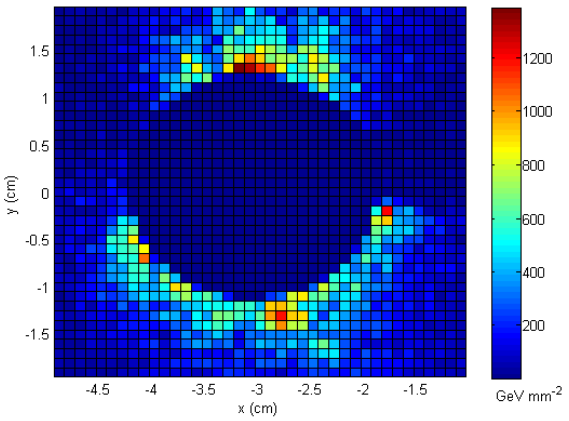

(b) The energy density of electrons and positrons at location z = 3.12 m (in front of the low-Z mask). Only particles that hit the low-Z mask are shown.

Figure 3.25: Energy and number density distributions for electrons and positrons that hit the low-Z mask. The data is from a simulation with the 20 mrad crossing angle, scheme 14 accelerator parameters set and no DID.

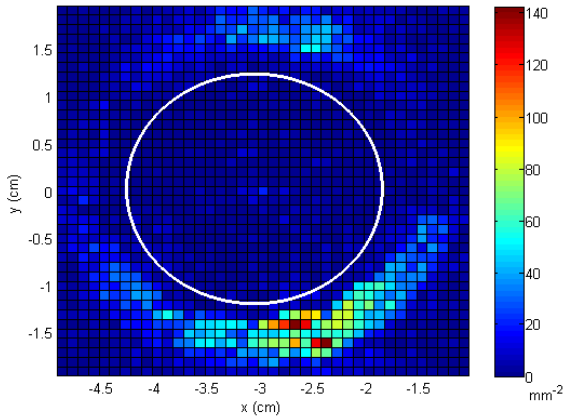

(a) The number density of electrons and positrons at location z = 3.12 m (in front of the low-Z mask). Only particles that go on to cause hits in the BPM striplines are shown.

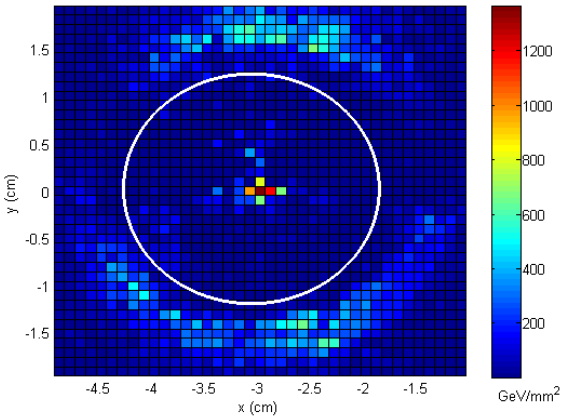

(b) The energy density of electrons and positrons at location z = 3.12 m (in front of the low-Z mask). Only particles that go on to cause hits in the BPM striplines are shown.

Figure 3.26: Energy and number density distributions for electrons and positrons near the z location of the low-Z mask. Shown are the charged particles that go on to cause hits on the striplines. The inner-radius of the low-Z mask is marked as a white circle. The data is from a simulation with the 20 mrad crossing angle, scheme 14 accelerator parameters set and no DID.

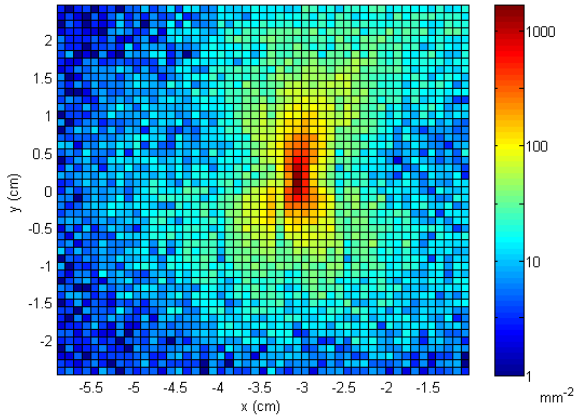

(a) The distribution of positrons at z = 3.12 m.

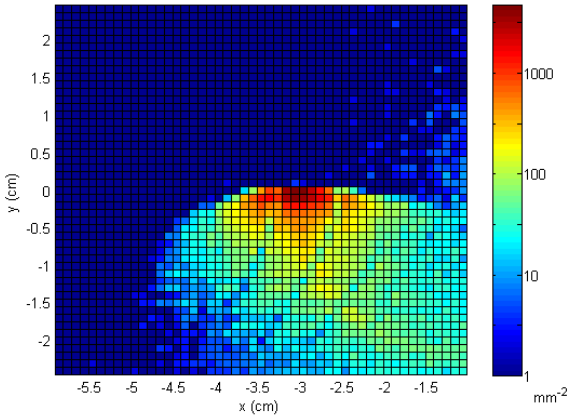

(b) The distribution of electrons at z = 3.12 m.

Figure 3.27: Particle distributions just in front of the low-Z mask (z = 3.15 m).

3.4.3 Distribution of charged particle energies

The simulation of the 20 mrad crossing angle, scheme 14 without DID was used to record the energies of the particles. The particles that enter the region where the low-Z mask sits vary greatly in energy from the minimum cut-off in the simulation to the beam energy as shown in figure 3.28(a). There are many very low energy particles, however these electrons and positrons are caught in the solenoid field and do not reach the stripline BPM region. Higher energies tend to create showers too deep in the material for the secondaries to escape. Only 30% of the electrons and positrons from the IP that hit the low-Z mask cause hits on the striplines either directly or through showering in the BeamCal. Of all charged particles recorded at z = 3.12 m, only 7% go on to cause hits on the striplines as the majority of pairs go down the extraction line beampipe without interacting with the IR material. The charged particles that do cause hits, shown in figure 3.28(b), have a mean average energy of 7.57 GeV and median of 4.84 GeV.

This peak value increases with the solenoid field (shown in figure 3.20) as charges are deflected depending on the strength of the detector solenoid field. At the higher solenoid field, charged particles with slightly higher energies are deflected onto the low-Z mask and BeamCal raising the mean energy.

This study showing the distribution of the particles in space and energy implies that the particles that cause the hits in section 3.4.1 are mainly at the top and bottom lips of the low-Z mask (figure 3.26) and of low GeV energies (figure 3.28).

3.4.4 14 mrad crossing angle simulations

The thorough investigation into the background conditions and how they varied with IR parameters was performed before the 14 mrad crossing angle was proposed. Subsequently, the 14 mrad crossing angle was modeled in GEANT3 [76] and GEANT3 simulations were performed with this crossing angle. The anti-DID field is included but it is not tuned

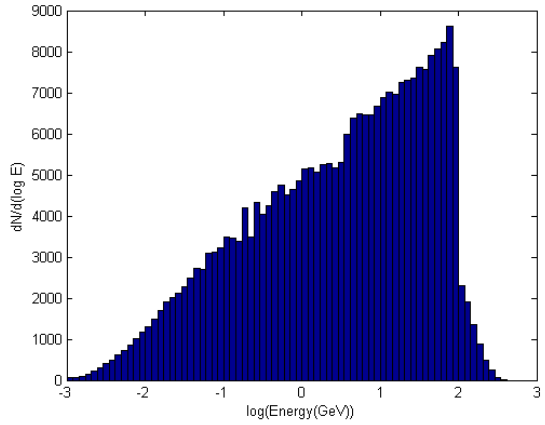

(a) Energy of all charges at z = 3.12 m.

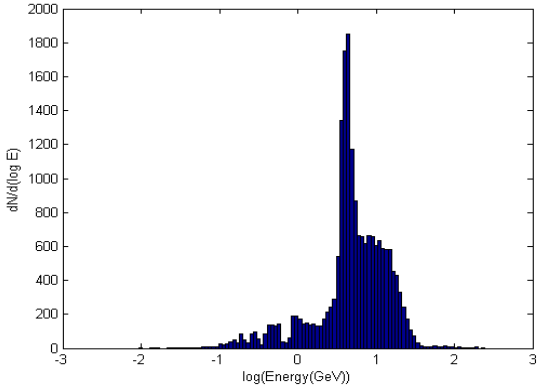

(b) Energy of charges at z = 3.12 m that cause hits on the striplines.

Figure 3.28: Comparison of energies of all charged particles at the position in front of the low-Z mask in this simulation (z = 3.15 m) and the charged particles that cause hits on the striplines.

	1	2	3	4
Electron hits	$(3.7 \pm 0.1) \times 10^4$	$(7.8 \pm 0.4) \times 10^4$	$(3.6 \pm 0.1) \times 10^4$	$(7.6 \pm 0.2) \times 10^4$
Positron hits	$(2.46 \pm 0.05) \times 10^4$	$(4.2 \pm 0.2) \times 10^4$	$(2.20 \pm 0.08) \times 10^4$	$(3.7 \pm 0.1) \times 10^4$
Photon hits	$(2.98 \pm 0.06) \times 10^5$	$(4.3 \pm 0.2) \times 10^5$	$(2.85 \pm 0.08) \times 10^5$	$(4.0 \pm 0.1) \times 10^5$

Table 3.2: The average number of particle hits on each stripline for the 14 mrad crossing, scheme 14 (anti-DID). Ten simulations with unique GUINEA PIG inputs were performed to produce the mean number of hits and the error.

correctly so does not result in lower secondary backgrounds than for without the anti-DID field (as would be expected for a correctly tuned anti-DID due to the decrease in pairs hitting the BeamCal, see figure 3.15). The average number of electron, positron and photon hits per stripline are shown in table 3.2 for ten simulations with the 14 mrad crossing angle IR. The numbers are from GEANT3 simulations using GUINEA PIG pairs inputs with the accelerator parameter scheme 14 (table 1.3).

With the untuned anti-DID and the high luminosity 1 TeV accelerator parameter scheme, these numbers represent the worst backgrounds that can be expected.

3.5 Summary

The background conditions that the IP feedback BPM is required to operate in were investigated and presented in this chapter. The interaction of primary electrons, positrons and photons with matter could cause a signal in the stripline BPM. Secondary emission through ionisation, bremsstrahlung, the photoelectric effect, the Compton effect and pair production were raised as the main processes involved with low energy backgrounds hitting

the striplines. The kind of signal this would produce in the striplines was discussed and it was concluded that a net change of approximately 10^6 charges will cause a significant signal that affects the resolution of the IP feedback BPM.

The chapter presented the materials and dimensions of the interactive region with the three proposed detectors: SiD, LDC and GLD. The very forward regions of the detectors were very similar leading to the conclusion that further studies and conclusions with just one detector could be applied to the other two. The SiD interaction region was chosen to be the layout to study further due to good support with the simulation package GEANT.

GEANT3 simulations of the SiD interaction region, primarily for the 20 mrad crossing angle design dated early 2005, were performed to investigate the effect on the level of backgrounds of changing various parameters. This included the accelerator parameter set. It was found that the high luminosity schemes (scheme 7 for 500 GeV centre of mass, scheme 14 for 1 TeV centre of mass) created the worst background conditions for the stripline BPM. The source for the particles that hit the striplines was found to be the beam calorimeter and further studies showed that the worst position for the stripline BPM in terms of number of hits on the striplines was immediately downstream of the BeamCal. The radius of the BPM was also a factor with the worst backgrounds being with the largest radius studied in the simulations (2 cm). The proposed DID for the 20 mrad crossing angle increased the number of hits on the striplines by 30%.

The GEANT3 simulations revealed an asymmetry in the backgrounds that resulted in the top and bottom striplines of the IP feedback BPM experiencing more hits than the side striplines. This was due to the primary backgrounds striking the low-Z mask with this distribution of more intensity at the top and bottom lip of the mask. The imbalance of charges hitting the striplines was low: 5×10^3 q_e for the bottom strip in the 20 mrad crossing angle, scheme 14 case. However, studies were not done for emitted particles. The total number of hits was 1×10^5 and the total yield from secondary emission and the photoelectric effect could be greater than one. This was close enough to the theoretical imbalance of 10^6 charges that would affect the BPM stripline resolution to cause concern that the backgrounds could cause problems.

The energies of the primary backgrounds can be nearly as high as the beam energy of 500 GeV (for the 1 TeV upgrade of the ILC) but the secondary backgrounds are of the order of a few GeV.

GEANT3 simulations of the 14 mrad crossing angle, scheme 14 case with an untuned anti-DID, showed ten times more hits than the 20 mrad crossing angle case.

All the work on the conditions at the IR led to an attempt to create similar conditions at a test beam (chosen to be End Station A at SLAC) described in the next four chapters.

Chapter 4

Recreating the ILC Interaction Region at End Station A

To test the robustness of striplines in ILC backgrounds, the information about the interaction region of the ILC (chapter 3) was used to build an IR mock-up.

What hits the striplines depends on the upstream material; the radiation lengths and apertures determine the energies and angles of the particles that reach the striplines. To aid in creating the distribution of particles and energies, it was decided to build a "module" replicating the important features of the ILC IR. This was installed at End Station A (ESA) at SLAC.

4.1 End Station A

The beam parameters at ESA, shown in table 4.1, match with those proposed for the ILC in terms of charge and are close in bunch length and energy spread. ESA operates with single bunches with a repetition rate of 10 Hz as opposed to the ILC which would operate with between 1000 and 5400 bunches in a pulse with a pulse repetition rate of 5 Hz [11]. However, the background studies do not require multi-bunch operation as the bunches are spaced at least 180 ns apart and the backgrounds only last for a few tens of nanoseconds. The programme at ESA ran with beam energy 28.5 GeV, although the linear accelerator at SLAC can deliver up to 50 GeV, which is almost ten times smaller than the energy of the ILC beam. However, the relatively low energy of the beam does not affect the operation of a stripline BPM (as long as the beam is relativistic, see section 1.5) and since the background particles are predominantly a few GeV in energy (figure 3.28), an ILC energy beam is not required to create them.

1.25 m of beamline was made available for the FONT module that recreated the ILC IR. There were also beam diagnostics available such as toroids, wire scanners and beam profile monitors and facilities to insert targets in the beamline. This meant ESA was ideal for this purpose as it allowed the development of unique and flexible strategies to create backgrounds (as described in chapters 5,6 and 7).

Parameter	SLAC ESA	ILC
Repetition Rate	10 Hz	5 Hz
Beam Energy	28.5 GeV	250 GeV
Bunch Charge	1 - 2 $\times 10^{10}$	$(1-2) \times 10^{10}$
Bunch Length	300 - 500 μm	300 μm
Energy Spread	0.2%	0.1%

Table 4.1: SLAC ESA beam parameters compared with those for the 500 GeV ILC [91].

4.2 The FONT Module

The module (figure 4.1) was based on the SiD design for the IR. The latest design at the time (February 2006) was used which was for the 20 mrad crossing.

The module was installed at ESA in July 2006 (figure 4.2) downstream from a wire scanner (3WS1), drift space and a profile monitor (3PR3) and upstream from a collimator (3C2).

4.2.1 The Low-Z Mask

At the ILC, the low-Z mask material will be made from either carbon or beryllium. For the FONT module, carbon was chosen as it is readily available and easier to work with than beryllium. Since the carbon had to be in a vacuum at 2×10^{-5} torr it had to be hard and non-porous[1]. It was decided to use a high-density, high-purity graphite [93].

4.2.2 The BeamCal

In the SiD design, the BeamCal is a calorimeter with 50 layers of high-Z material (tungsten), silicon, G10 and air. To match the radiation length and dimensions of the BeamCal in the module, it was assumed to be made of one high-Z material: lead, which was easy to purchase and machine. The length of lead decided upon was a close match to the radiation length of the proposed BeamCal (see table 4.2). To make it easier to move and stack around the beamline, the lead was designed as bricks with a hole machined for the beampipe to go through. The bricks were split in a staggered fashion as in figure 4.3. The beampipe was made from stainless steel and not beryllium as the choice of beampipe material is still an option between the two pending further work [77], and stainless steel represents a worse background case due to its higher density. The dimensions of the beampipe matched those most likely for the ILC.

[1]Graphite is usually pressed from powder and absorbs gases and water which would ruin a vacuum if it is used in one.

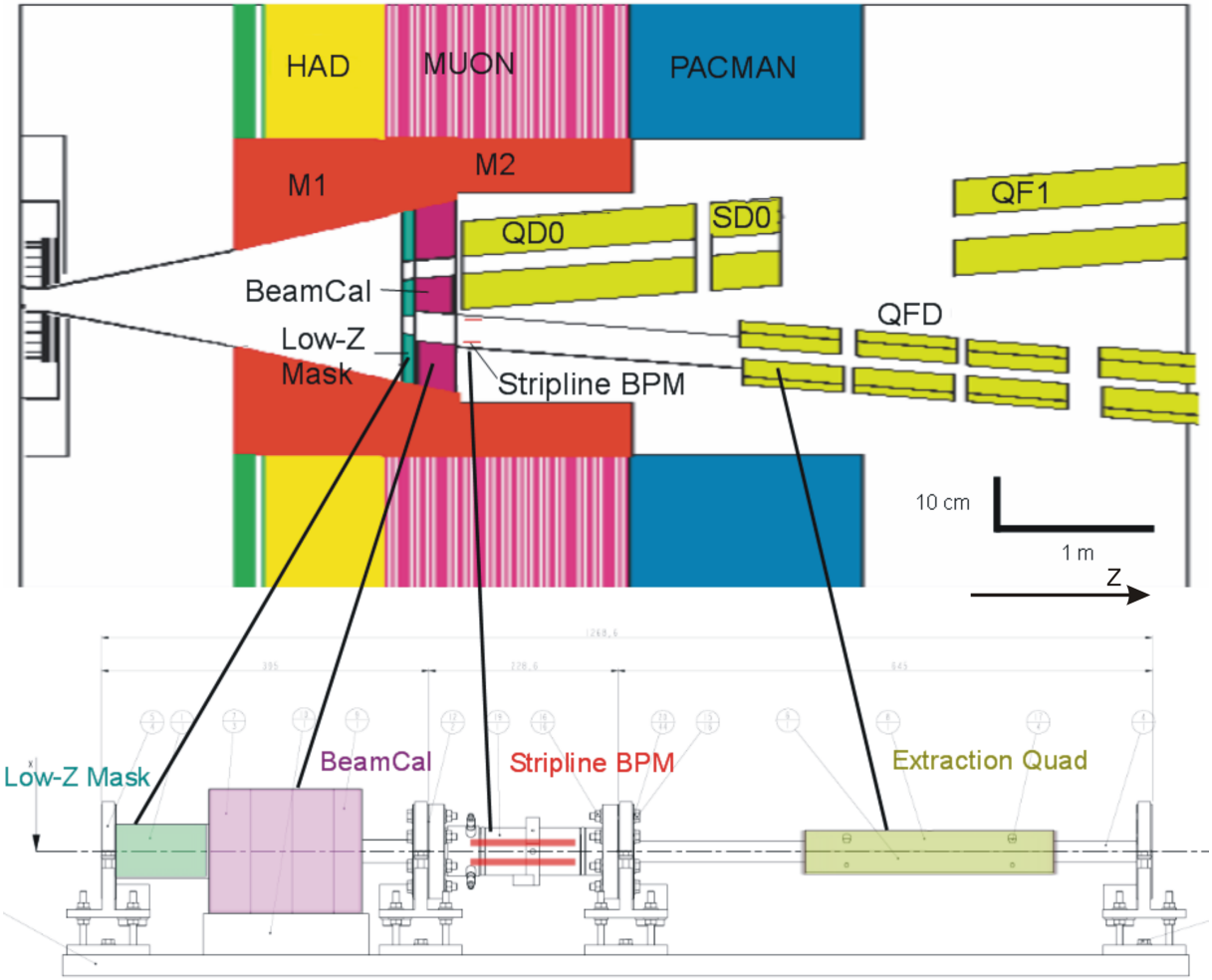

Figure 4.1: Top: Plan view of the SiD 20 mrad IR (see also figure 3.9). Below: An engineering drawing of the FONT BPM Module (side view) [92]. The beamline elements that have been mocked in the module are indicated.

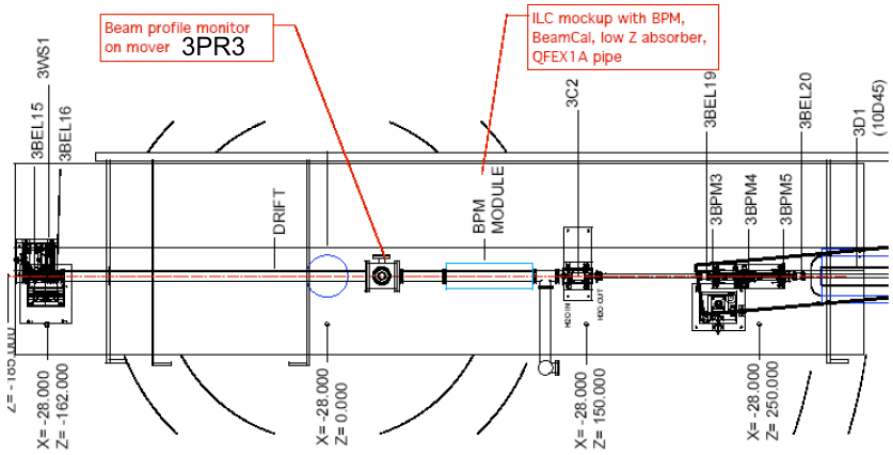

Figure 4.2: The FONT module location in ESA showing an upstream wire scanner for measuring the size of the beam in x and y (3WS1), a beam profile monitor comprising a scintillator on a mover that can be remotely inserted into the beam (3PR3) and the nearest beamline element to the module (3C2).

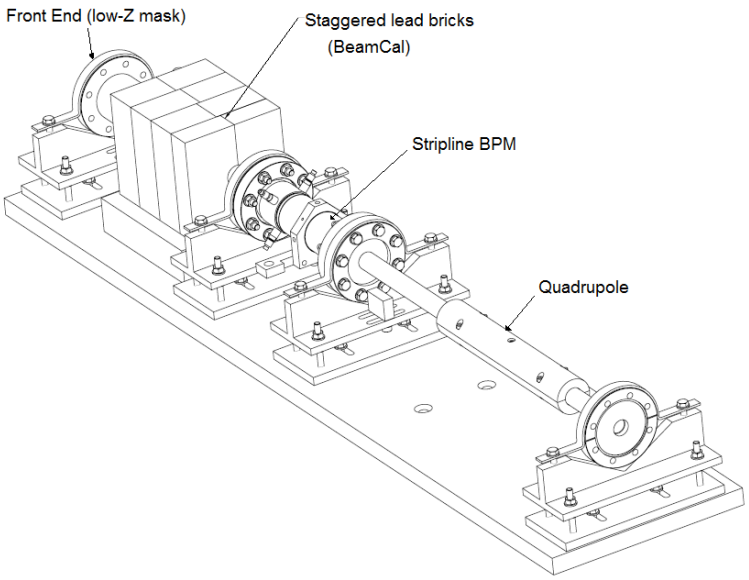

Figure 4.3: Engineering drawing showing the low-Z mask at the back, the staggered lead bricks of the "BeamCal", the stripline BPM and steel sleeve "quadrupole"[92].

Material	Radiation Length (cm)	Thickness (cm)	Thickness (Rad lengths)
Tungsten	0.35	0.25	0.7143
Silicon	9.36	0.032	0.0034
G10	19.40	0.068	0.0035
Air	30420	0.375	0.0000
	× 50 layers Total:	18.75	36.06
Lead	0.56	19.00	33.93

Table 4.2: The materials of the BeamCal are shown with the radiation length of the material and its thickness in each of the fifty layers of the BeamCal measured in centimetres and number of radiation lengths. The amount of lead in the FONT module representing the BeamCal is also shown in terms of its length in centimetres and radiation lengths in the final line of the table.

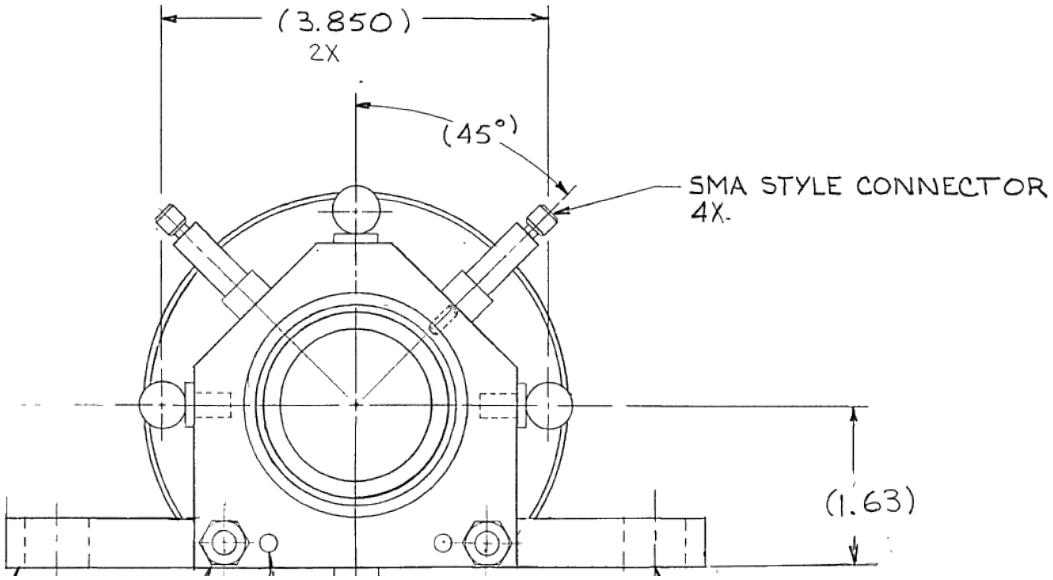

Figure 4.4: The BPM pick-offs (labeled "SMA style connector") and the striplines themselves are at 45^o to the vertical in the BPM used in the module [94].

4.2.3 The Stripline BPM

A SLAC stripline BPM was used for the feedback BPM. It was similar to those used at the final focus of the SLAC Linear Collider and the type of BPM that may be used in the ILC. The striplines were 15 cm long at a radius of 2 cm from the centre of the BPM and 4 mm from the wall of the BPM. Unlike at the ILC, the striplines were positioned at 45^o to the x and y axes (figure 4.4). The striplines were shorted on the downstream end with the pick-offs upstream. This is the most probable choice between the three options (see section 1.5.2) for the stripline at the ILC. If there does turn out to be noise, it avoids the potential noise getting doubled on its reflection, as it would in an open-ended BPM, and it avoids the potential noise being DC and saturating components in the feedback electronics, as it could in a terminated BPM.

4.2.4 The Quadrupole

The last item was the extraction line quadrupole. Since the position for this item was unfixed in the IR proposal at the time, the fake quadrupole was designed to be a sleeve of steel around the beampipe whose z position could be varied. The inner and outer radius of the steel sleeve were chosen based on drawings of the proposed superconducting quadrupoles as shown in figure 4.5 [95]. The aim was to retain the number of radiation lengths (see table 4.3) and also to keep the physical dimensions as similar as possible. The heavy material (stainless steel and the superconductive coil of 60% copper, 20% niobium and 20% titanium [76]) of the quadrupole extends to a radius of 2.4 cm and then it is mainly liquid helium with the cryostat wall at a radius of 3.6 cm. The FONT module quadrupole has an outer radius of 2.5 cm so as to be close to the dimensions of the heavy material (see table 4.3).

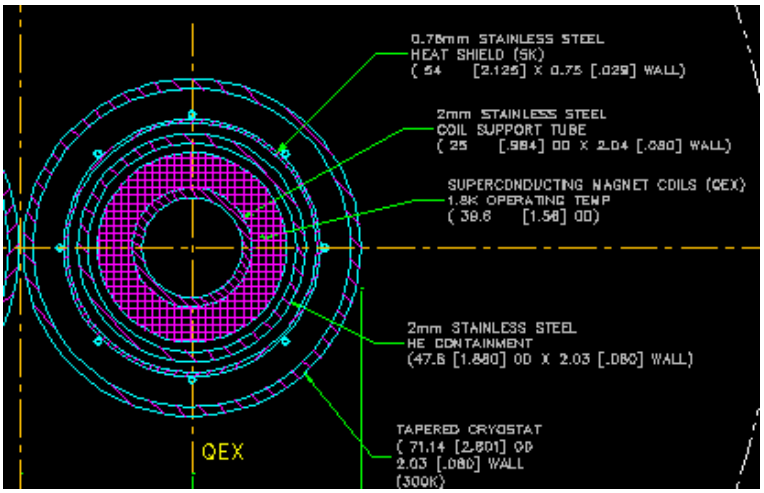

Figure 4.5: The end cross section view of the extraction line quadrupole. The design mainly consists of stainless steel (support tubes and helium containment), niobium-titanium embedded in copper (the superconducting magnetic coils) and liquid helium. [95]

Material	Radiation Length (cm)	Thickness (cm)	Thickness (Rad lengths)
Stainless Steel (SS)	1.76	0.685	0.389
Superconductor	1.58	0.730	0.463
Liquid He	756.00	1.096	0.001
	Total:	2.511	0.854
SS Beampipe	1.76	0.204	0.116
SS Sleeve	1.76	1.300	0.739
	Total:	1.504	0.855

Table 4.3: The extraction line quadrupole was recreated in stainless steel with a thickness in radiation lengths close to that of the proposed quadrupole. The overall thickness was not matched. Instead the dimensions were chosen to match the high-Z core of the quadrupole.

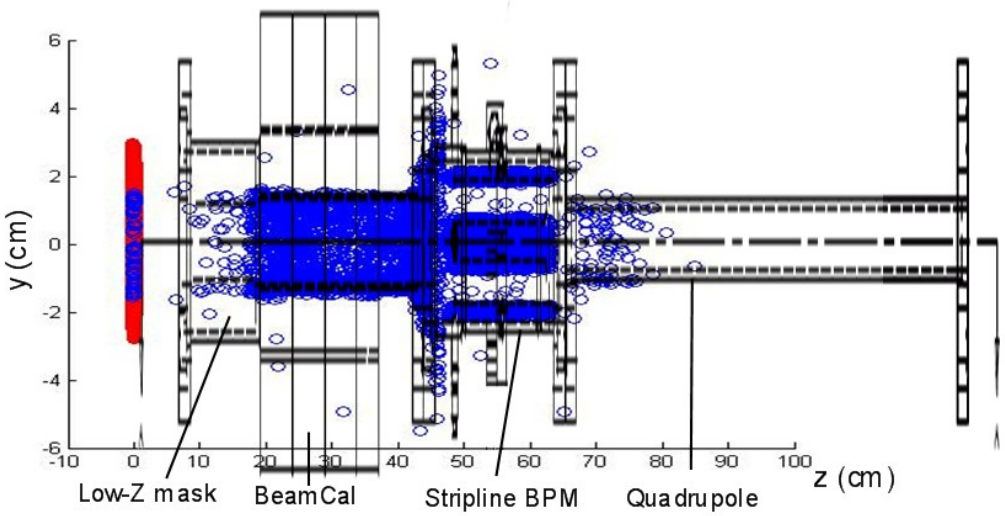

Figure 4.6: Side view of the FONT module. Blue circles represent the sources for particles that hit the striplines in a GEANT3 simulation. The input beam is shown in red.

4.2.5 Module simulations

A GEANT3 model of the module was set up. Input bunches of electrons were produced using a random number generator in Matlab in a uniform distribution out to a radius of 3 cm. They were directed along the z axis of the module. The hits on the striplines in the module's BPM were recorded in the simulation. The hits were also tracked back to their sources, i.e. where the interactions and showers took place.

In designing the module, attention was given to matching lengths and inner radii but not the outer radii (with the exception of the quadrupole) as it was assumed that mainly the inner surface of the IR elements would be involved in generating secondaries. This GEANT3 simulation was used to check this assumption before constructing the module. The hit sources were found to be in locations shown in figure 4.6. The blue circles are the source locations and are mainly gathered at the inner surface of the BeamCal and low-Z mask confirming the assumption.

This simulation also indicated that the upstream flange of the BPM is a source for many of the hits (figure 4.7). The flanges on the borrowed BPM were large and so represent a conservative case where there is no attempt to minimise the effects of backgrounds on a stripline through optimised design aimed at minimising material.

Also apparent from figure 4.7 is that the presence of an ESA collimator (3C2 as shown in figure 4.2) 230 cm downstream of the module is not a source for any hits on the striplines.

The position of the extraction line quadrupole was not precisely known at the time of designing the module so the z location of the quadrupole was adjustable. This simulation was performed with the quadrupole immediately against the stripline BPM and, as figure 4.7 shows, very few particles traveled back from it. This indicated that the contribution of the quadrupole was minimal. In addition, the fact that the length of the quadrupole mock-up did not match that of the quadrupole at the ILC was not an issue, as showers that went on

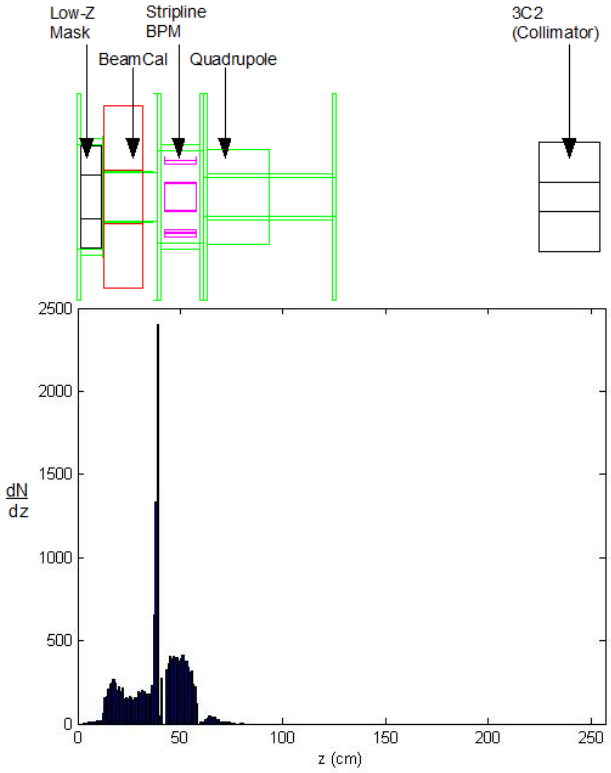

Figure 4.7: Histogram of the z location of the source of the particles that hit the striplines. A representation of the FONT module plus the downstream 3C2 collimator is shown with the same scale in z as the histogram.

the hit the striplines only occurred in the first 10 cm of its length.

It was undecided whether to make the low-Z mask from beryllium or carbon in the ILC IR. The module low-Z was made from carbon and simulation results (not shown) indicate that this produces more hits on the striplines than beryllium due to its higher Z.

4.3 Summary

The experimental investigation of the robustness of a stripline BPM to ILC IR backgrounds was carried out at End Station A (ESA) at SLAC. ESA offered similar beam charge, bunch length and energy spread to ILC and also the ability to change these parameters, if necessary, for the experiment. There were many diagnostic instruments and the beamline and operations were flexible enough for additional beamline elements and instruments to be inserted. This control and flexibility was vital for the creation of backgrounds as described in the next three chapters.

A module was built to simulate the material and inner radii of the ILC IR based on the SiD 20 mrad design. In the design, attention was paid to matching the radiation lengths and the dimensions of the low-Z mask, BeamCal and extraction line quadrupole of the ILC IR. This was used to produce secondaries through the conjunction of the module with input beams (the generation of which are described in the following three chapters) with energies and spatial distribution that matched those of the ILC at the BPM location. When there was a choice in the design, such as with the low-Z mask material and beampipe material, the decision was always with the option that gave the highest backgrounds. Simulations were used to confirm that outer-radii did not have to be matched, only the inner radii, and that the presence of a downstream collimator in ESA did not affect the backgrounds at the BPM.

Chapter 5

Methods for recreating ILC backgrounds: Introduction and Method A

5.1 Introduction to the methods for recreating ILC backgrounds

Three methods were developed to be used at ESA to test the stripline response to backgrounds.

Method A, as described in detail throughout this chapter, uses the material of the FONT module (chapter 4) to create many secondaries in the region of the BPM and study the response of the BPM to them. The ESA electron beam was moved to positions on the front face of the module, the low-Z mask. It then interacts with the material of the module, which has radiation lengths, absolute lengths and apertures closely matching those of the ILC IR, generating many secondaries. By the z location of the BPM, most of the beam comprises secondaries (only 1% of the main beam survives to this point) allowing the study of the effect of low energy particles on the raw stripline and on the processed stripline signals.

Method B, as discussed in chapter 6, uses thin foils of aluminium a few metres upstream of the module to create a halo of electrons that interact with the module and shower in the material while allowing most of the main beam to continue through the beampipe. Secondaries are therefore present in the BPM region at the same time as the main beam signal. It is therefore possible to measure the beam position in the presence of backgrounds and, by removing the foils, compare this to the beam position in a clean environment, to see if there is a degradation in resolution.

Method C, as discussed in chapter 7, creates a wide, beampipe-filling spray beam of electrons using a thick radiator in the Beam Switch Yard (BSY) at the end of the SLAC linac. A momentum bite of this beampipe-filling spray can be transported with magnets to ESA, delivering a uniform distribution of electrons to the front face of the module (the low-Z mask). Using different momentum settings and different beam charge incident on the

thick radiator, it is possible to match the average energy and number distribution of the ILC backgrounds on the low-Z mask.

These methods are summarised in table 5.1.

5.2 Methods for creating spray: A

5.2.1 Overview

In the ILC simulations, the particles that hit the BPM striplines originated from the lip of the inner radius of the low-Z mask as shown in figure 3.26. To create backgrounds at ESA, the input beam for use with the FONT module was the ESA electron beam aimed at the low-Z mask. The electron beam was positioned at different radii and locations around the mask, scanning on the $x = 0$, $y = 0$ and $x = \pm y$ lines, as shown in figure 5.1, to build up a complete picture for particles incident on all parts of the low-Z mask. The data from the stripline signals and the processed signals (using FONT4 analogue processors) were seen on a 4-channel 5 GHz oscilloscope[1] and recorded by the FONT DAQ.

This method was used at low beam charge. The ILC simulations discussed in section 3.4.2 showed that 6.4×10^4 charged particles hit the low-Z mask, delivering 3.5×10^5 GeV of energy. To deliver 3.5×10^5 GeV to the low-Z mask of the FONT module with Method A, the beam charge of the 28.5 GeV beam would have to be 1.2×10^4 electrons per bunch (3.5×10^5 GeV divided by 28.5 GeV). It was decided to use this method between 1×10^4 and 1×10^7 electrons per bunch to match and exceed ILC levels by a few orders of magnitude.

5.2.2 Simulating the experiment: Method A

Method A was simulated in GEANT3 to ensure that the secondary backgrounds it created were similar to those predicted for the IP feedback BPM at the ILC.

The existing GEANT3 model of the FONT module (from chapter 4) was used with an input of 28.5 GeV electrons (generated using a random number generator within Matlab) aimed at a radius of 1.4 cm (x = -1 cm, y = 1 cm) near stripline B. The particles that hit the four striplines were recorded. This simulation was repeated three times.

The energies of these hits for Method A were compared to those from the ILC simulations of the scheme 14, 14 mrad crossing angle with anti-DID. The energy distributions (see figure 5.2) were closely matched with the peak energies both below 1 MeV, confirming that the module combined with electrons on the low-Z mask produces similar secondary backgrounds to the ILC at the striplines.

The ratio of electron, positron and photon hits were remarkably close between the ILC case and Method A case given the difference between the primary pair backgrounds of ILC and the 28.5 GeV electron beam of ESA. The ratios are shown in table 5.2 where striplines

[1]The oscilloscope could be operated in one channel mode with a sampling frequency of 20 GHz.

	A		B		C		
	Striplines	Processors	Striplines	Processors	Striplines		Processors
					In BSY	In ESA	
Energy (GeV)	28.5	28.5	28.5	28.5	28.5	4 - 8	-
Beam Charge (electrons)	$1 \times 10^6 - 1 \times 10^7$	1.5×10^9	1.6×10^{10}	1.6×10^{10}	$4 \times 10^8 - 2 \times 10^{10}$	$1 \times 10^4 - 2 \times 10^6$	-
Beam size	2100 μm $\times$ 700 μm	1300 μm $\times$ 1000 μm	800 μm $\times$ 65 μm	800 μm $\times$ 65 μm	120 μm $\times$ 70 μm	3 cm $\times$ 3 cm	-
Beamline Components	• FONT module • Low current instrumentation		• FONT module • Aluminium foils upstream of module		• FONT module • Very low current instrumentation • Beryllium target in BSY		
General Method	Beam is moved onto low-Z mask creating secondary backgrounds.		Thin radiators are used to produce a halo of low energy particles around the main beam.		A thick radiator in the BSY is used to produce a lot of low energy particles and an energy is selected to transport to ESA.		
Pros	• Creates very large numbers of secondary particles • Can see effect of secondary particles without it being masked by a large signal from the main beam		• Can measure the position of the beam in the presence of backgrounds- a scenario like the ILC.		• Can match the average number and energy density of the ILC on the low-Z mask • Can see effect of secondary particles without it being masked by a large signal from the main beam		
Cons	• Cannot directly compare the effect from the backgrounds to the main signal • Backgrounds are not like those at the ILC in terms of relative number and energy density across the low-Z mask		• Backgrounds are very small compared to the main beam- the signal from the main beam will dominate		• Only average densities are matched, the asymmetry of the ILC backgrounds is not		

Table 5.1: Methods A, B and C for creating backgrounds at ESA are summarised. Some beam parameters are given for each method. They are different depending on whether the data being recorded is the stripline response to the backgrounds or the processor response to the backgrounds and, in the case of Method C, whether the parameters are measured in the beam switchyard (BSY) or in the end station (ESA). The beam sizes for Methods A and B were measured at ESA during the experiment. The beam size for Method C at the BSY is based on measurements by E158 [96]. The method is briefly stated with the pros and cons.

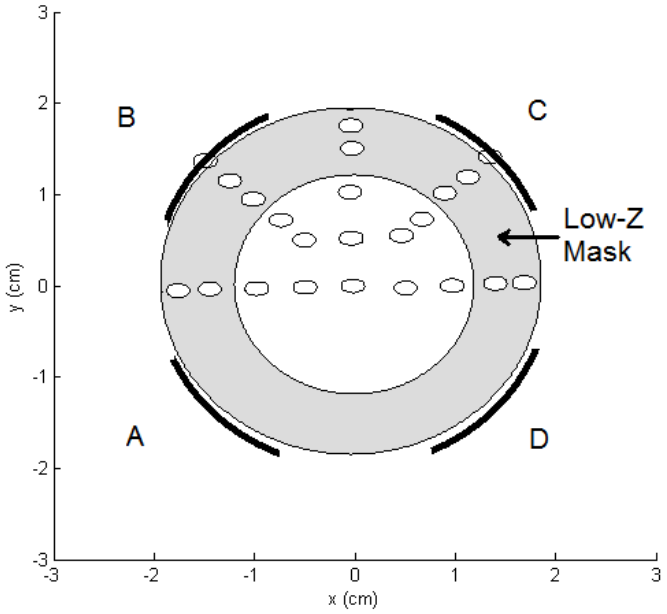

Figure 5.1: The electron beam was placed in the positions on and off the low-Z mask (shaded grey) as indicated above. The striplines are labeled A, B, C and D.

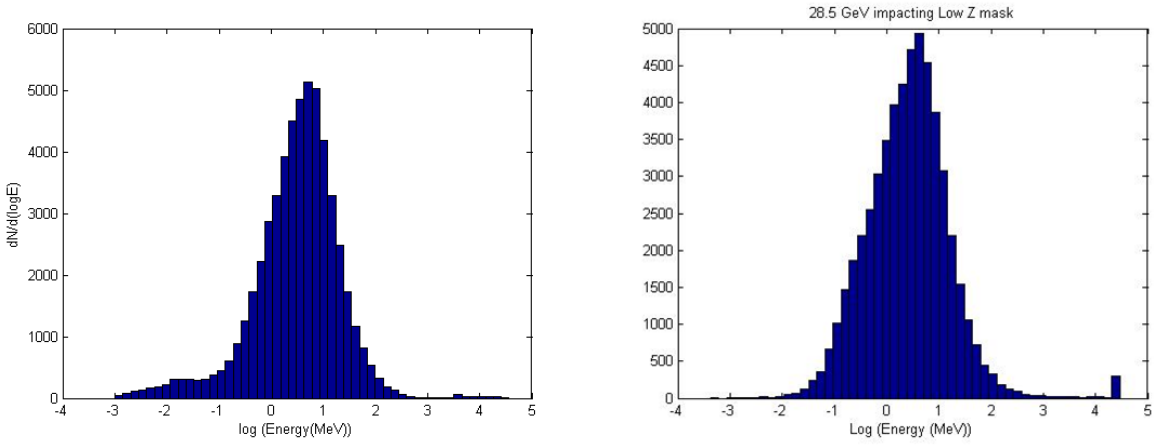

(a) ILC Scheme 14, 14 mrad crossing angle, Anti-DID. 10% of the full simulation.

(b) Method A. <1% of the full simulation.

Figure 5.2: Histograms for the energy distribution of charged particle hits on the striplines.

	ILC % of total hits				Method A % of total hits			
	1	2	3	4	A	B	C	D
Electrons	10	14	10	15	6	7	6	6
Positrons	7	8	6	7	3	4	3	4
Photons	83	78	83	78	90	89	90	90

Table 5.2: The percentage of electron, positron and photon hits on each stripline for Method A compared with the percentages for ILC feedback BPM striplines. The striplines are assigned letters as shown in figure 5.1 and numbers as shown in figure 3.24(a). The ILC simulation was for the 14 mrad crossing angle IR, anti-DID and Scheme 14 accelerator parameters.

	A	B	C	D
Electron hits	1.13 ± 0.02	1.41 ± 0.03	1.12 ± 0.01	1.72 ± 0.04
Positron hits	0.60 ± 0.01	0.82 ± 0.04	0.61 ± 0.02	1.00 ± 0.01
Photon hits	16.3 ± 0.9	16.9 ± 0.7	16.1 ± 0.5	25.2 ± 0.8

Table 5.3: The number of particle hits on each stripline for Method A per electron incident on the low-Z mask with a beam offset of r = 1.4 cm (x = -1 cm, y = 1 cm) from a GEANT simulation. The striplines are assigned letters as shown in figure 5.1.

1 and 3 of the ILC feedback BPM and stripline A of the FONT module show the closest match.

The number of electron, positron and photon hits per stripline for Method A are shown in table 5.3 (where hits are given per electron in the ESA beam). Running a beam charge of 1×10^4 electrons, the number of particle hits per stripline are similar to those at the ILC (the ILC numbers are shown in table 3.2 for the 14 mrad crossing angle IR).

5.2.3 Instrumenting the experiment: Method A

This method required instrumentation for low beam currents. Existing beam current monitors did not work below 10^8 electrons per bunch but knowledge of the beam current was required down to 10^4 electrons per bunch. It was also vital to know the position of the beam at larger offsets than the existing ESA BPMs could read so that the beam could be steered onto the low-Z mask (1.2 cm inner radius). The spot size also needed to be measured in order to reproduce the experiment in simulations.

Measuring the beam position

To aid in positioning the beam on the mask, a plastic scintillator block and CCD camera were used. A disused beam profile screen mover a metre upstream of the module (known as 3PR3) had its phosphorescent screen replaced with a block of scintillator. This scintillator

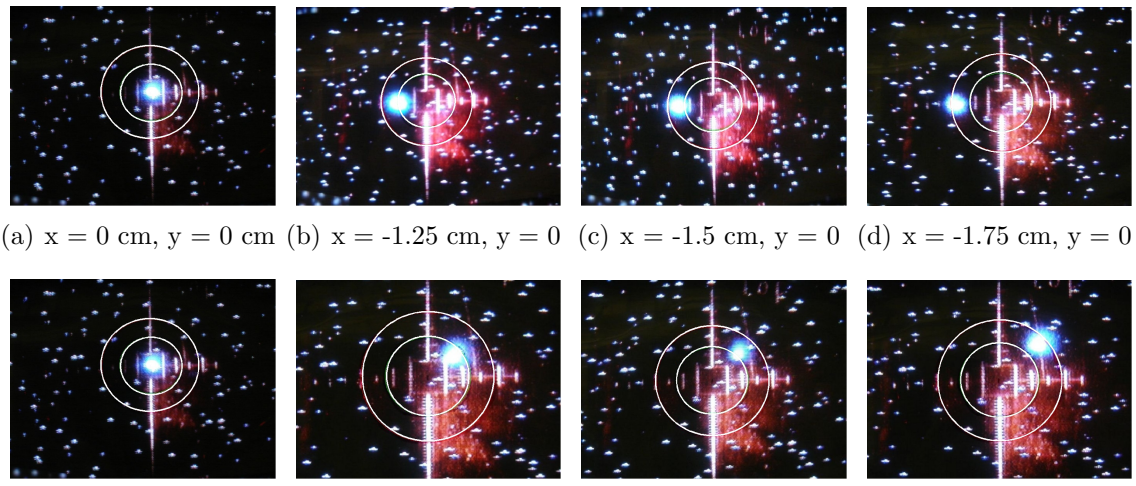

(a) x = 0 cm, y = 0 cm (b) x = -1.25 cm, y = 0 (c) x = -1.5 cm, y = 0 (d) x = -1.75 cm, y = 0

(e) x = y = 0 cm (f) x = y = 0.75 cm (g) x = y = 1 cm (h) x = y = 1.25 cm

Figure 5.3: Photographs of the CCD camera images. The inner radius of the low-Z mask (1.2 cm) is marked as a white circle (the radius is 1.2 cm). The larger white circle marks the inner radius of an upstream collimator (3C1, radius 1.95 cm). The central box in the photos is 1 square centimetre and the major tick-marks on the axes are every 0.5 cm.

produced a lot of scintillator and Cherenkov light[2] when the beam passed through it even at low charge. Mirrors in a periscope formation brought the light from the scintillator to a CCD camera housed in lead bricks about a metre below the beamline. The scintillator screen was marked with axes such that when placed in the beam, the position of the beam could be seen as a bright blue spot (see figure 5.3). The correctors that were used to give the beam a translation in x and y were upstream of a collimator (3C1). This restricted how far on the low-Z mask the beam could be moved to within the inner radius of the collimator (1.95 cm).

A huge drawback to this setup was the poor field of view that could be achieved with the camera and lenses available. Even with the best arrangement, the position of the beam could only be read to within ±0.25 cm. Another issue was that the camera was easily damaged by neutrons. The lead housing minimised this and the CCD camera was removed from the beamline when it was not in use. This made the camera lifetime sufficient for the experiment. The scintillator was susceptible to damage from high intensity beams so the scintillator was only inserted when the beam charge was below 10^7 electrons per bunch and the spot size large.

Measuring the beam spot size

The scintillator light spot was not a good indication of beam spot size so to measure this the normal wire scanners in ESA were used. Although the wire scanner signal could be amplified a little by turning up the voltage on the PMT[3], the beam spot size could not be measured

[2]Cherenkov radiation is caused by the electrons travelling faster than the speed of light in the scintillator material.

[3]Wire scanners involve passing wires across the beam and collecting secondary emission from the interaction in a photomultiplier tube (PMT).

with beam charge lower than 10^9 electrons. The current was raised to do this measurement. This should still give an adequate reading of the size of the beam spot as instabilities that could cause the size to change are only a problem at higher charges [97]. The wire scanner used was 3WS1 and can be seen in figure 4.2.

Measuring the beam charge

The beam charge was measured with three devices to span the range from 10^4 to 10^{10} electrons. An existing toroid at ESA (toroid 4140) operated above 10^8 particles. New toroid electronics were designed [98] to operate below this using a low noise FET as a voltage amplifier. The noise of the system was about 1 mV at the output restricting the operation of this toroid to currents above 1.6×10^5 electrons. The components were saturated just below 10^9 electrons. A third device, a photomultiplier tube and scintillator, was put in place to measure the beam charge below 10^5 electrons.

The low current toroid output (figure 5.4) was sampled by an ADC and read into the ESA DAQ [99] system. The ADC was easily saturated so attenuators were used to bring the signal onto the correct scale. The ADC had a pedestal of 95 counts to be removed from beam charge calculations plus there was a DC offset associated with the input of -30 counts (this was reduced in magnitude when attenuators were placed on the input) making the effective pedestal 65 without any attenuators and 92 with a 20 dB attenuator on the input to the ADC.

The low current toroid was calibrated in two ways.

The first calibration was performed against the existing calibrated toroid (4140) that operated above 10^8 electrons. The ADC window was placed in the second trough of the low current toroid signal as the first trough showed signs of saturation at the higher end of the beam charge used for calibration and the second trough did not. The calibration on toroid 4140 was 10^8 electrons per count so the resolution was poor and there was evidence of some beam charge jitter. Because of this, counts on the low current toroid and counts on the 4140 toroid were recorded over 20 pulses three times at each beam charge setting. This gave a calibration of $(3.0 \pm 0.1) \times 10^4$ electrons per count (see figure 5.5).

The low current toroid was altered in between the two experimental runs so that a calibration current equivalent to 1.35×10^8 electrons could be used to produce a signal in the toroid instead of the beam. An ADC sampled the output signal at a trough as shown in figure 5.4. The low current toroid signal caused by the actual beam current needed to be sampled at the same position in the waveform as the calibration current. According to this method, the calibration constant for sampling at the second trough was $(3.20 \pm 0.06) \times 10^4$ electrons per count. The slight difference from the previous method is due to a different ADC sampling window width. It was preferable to work at the first trough when operating at or below 1.35×10^8 electrons per bunch where there was more sensitivity. Here the calibration was $(2.232 \pm 0.008) \times 10^4$ electrons per count on the ADC.

During the experiment, it was discovered that the stripline signals were too small to be seen above the oscilloscope noise when the beam current was dropped below 10^6 electrons

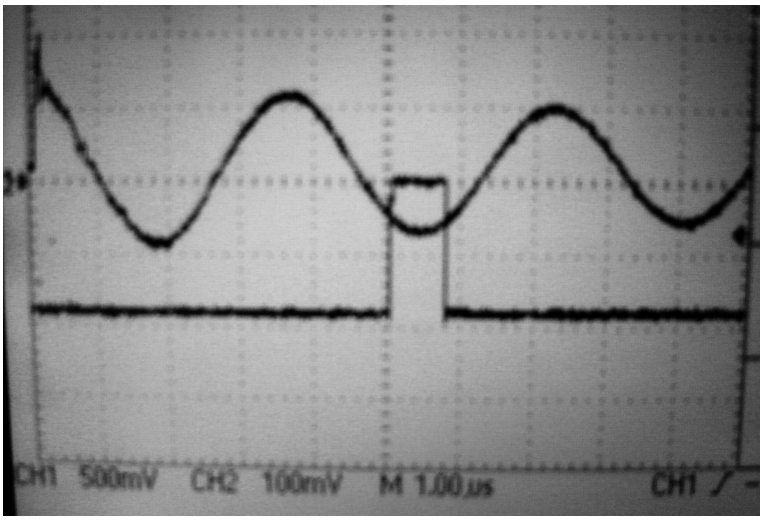

Figure 5.4: Photograph showing the signal of the low current toroid from the calibration current and the ADC window positioned at the second trough.

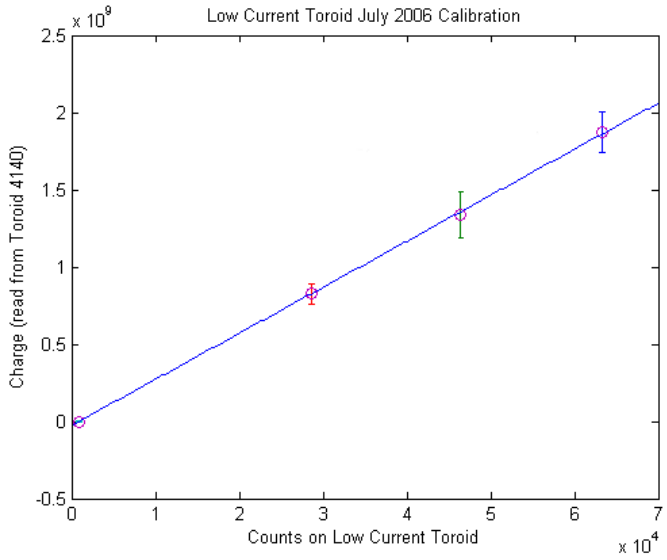

Figure 5.5: The beam charge from toroid 4140 is plotted against the number of counts on the low current toroid. The calibration is beam charge = (counts - pedestal) $\times(3.0 \pm 0.1) \times 10^4$.

per bunch. The photomultiplier, which was positioned to pick up light from the scintillator screen that was used for beam steering, was calibrated against the low current toroid but it was not required.

5.2.4 Performing the experiment: Method A

This method was used during two runs at ESA: July 2006 and March 2007. In July the raw BPM stripline signals were studied and in March the signals were recorded from the FONT4 analogue BPM processors.

Due to concern that a small beam spot would produce a beam too intense for the plastic scintillator, the optics of the standard ESA set-up were changed to make the beam spot larger. This required changing the strengths of two quadrupole magnets. Wire scans confirmed that the beam was 2100 μm in σ_x and 700 μm in σ_y for July 2006 and 1300 μm in σ_x and 1000 μm in σ_y in March 2007.

The beam was steered using upstream dipole correctors x3212 and y3313 using the scintillator and CCD camera to judge the position of the beam at the mask (as described above). The positions steered to are shown in figure 5.1. At each position, the four raw stripline signals from the BPM striplines, brought to the oscilloscope via 200 ft long cables, were recorded in batches of 20 to 100 pulses on the FONT DAQ. As the stripline signals were recorded, the beam charge was recorded through the ESA DAQ. It was necessary to make a beam charge measurement for every position as the beam charge was not stable. Repeat measurements with higher charge were performed to check the relationship between the signals and charge.

In order to see a signal from the striplines on the oscilloscope, the beam charge needed to be at least 1×10^6 electrons. Usually, a beam charge between 10^6 - 10^7 electrons was used. Higher beam charge (1.5×10^9) was required for data taking with the processors as they attenuated the signal further. This meant that the scintillator had to be removed to prevent it from being damaged and the beam had to be steered "blind". Identical magnet settings were used as for the steering with the low charge beam and it was assumed that they moved the high charge beam to the same places. After steering and taking data, the charge was lowered to 1×10^7 and the scintillator used to check the position. It appeared to be slightly low in x but within the already accepted ± 0.25 cm error in positioning the beam.

To bring the beam current down to 10^6 for operation, the method of "boot-strapping" was used whereby the current was lowered until it was half the number of counts on the low current toroid. Attenuation was then removed from the ADC input and the number of counts halved again. In this fashion, the beam current was reduced swiftly to an operating beam current below 10^7 electrons per bunch. The final number of counts was recorded and the exact beam current found with the calibration constant.

When the data with the processors were taken, the processors were set up as described in chapter 2 with a 714 MHz local oscillator. The processors were used after the 200 ft cables for easy and convenient access, not attached locally to the BPM.

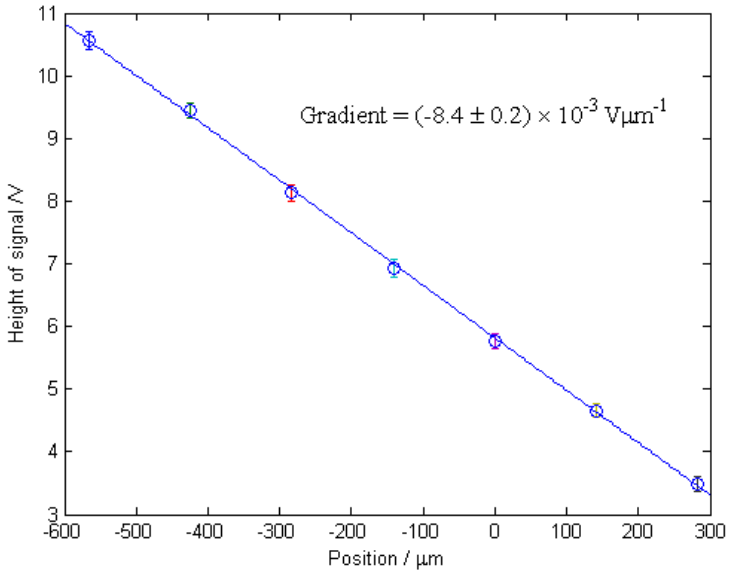

Figure 5.6: The calibration curve for paired/opposing striplines without charge normalisation.

Calibration of the processors and striplines

The stripline and processor signals were calibrated with position. The calibration was achieved using correctors to translate the entire beam in steps of 100 μm. 100 pulses were taken at each point to reduce the effect of the beam charge jitter. The beam charge was 1.5×10^{10} electrons per bunch.

The processor calibration was done using the integrated difference divided by sum as described in section 2.3.2.

The stripline calibration included Fourier interpolation being applied to the data to find the most likely values for the maximum and minimum points of the bipolar stripline signal. Then the difference between the peak to peak magnitude of two paired (i.e. opposing) striplines was calculated and plotted with the position offset to give a calibration constant of 8.4 ± 0.2 mVμm^{-1} (figure 5.6). The calibration curves for the processors and striplines normalised by charge are shown in figures 6.4 and 6.3.

5.3 Results: Method A

5.3.1 Raw stripline response

In July 2006, the stripline response was recorded with the beam positioned at several points on the low-Z mask (see figure 5.1). Due to the azimuthal symmetry of the module, many of these points were equivalent to each other. Essentially, there are two sets of data: one where the beam approaches a stripline along x = y from the centre and another where the beam is moved from the centre along y = 0.

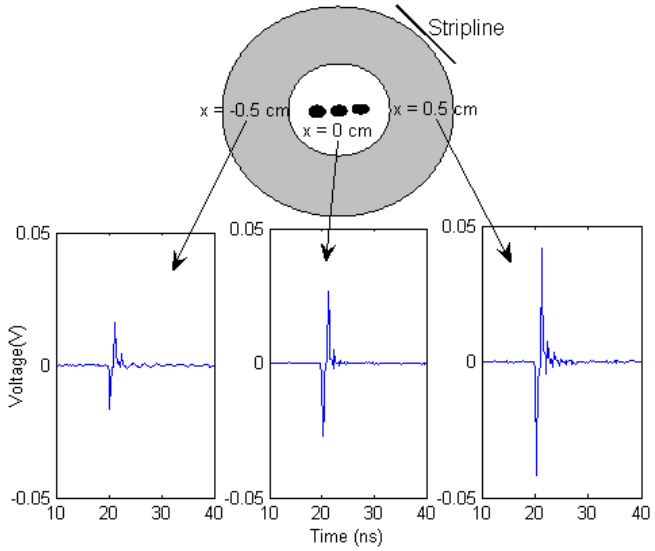

Figure 5.7: Stripline signals in volts from stripline C (see figure 5.1) at three positions on the x axis (x = -0.5 cm, x = 0 cm, x = 0.5 cm). The mean of 20 pulses is shown in each position. The beam charge for x = -0.5 cm is $(1.0 \pm 0.1) \times 10^7$ electrons, x = 0 cm is $(1.5 \pm 0.1) \times 10^7$ electrons and x = 0.5 cm is $(1.8 \pm 0.1) \times 10^7$ electrons.

The beam was moved from the centre of the beampipe to the inner radius of the low-Z mask along y = 0. The stripline response as the beam was moved within the clear beampipe was as expected; as shown in figure 5.7, the signals from the stripline grow in amplitude as the beam approaches the stripline.

Once the beam hit the low-Z mask, the signals from the striplines showed a clear difference. The striplines nearest the beam (C and D as shown in figure 5.1) showed a small change in shape with the negative-going spike of the bipolar signal being smaller in amplitude than the positive-going spike (see figure 5.8). There was a more dramatic response in the striplines on the other side of where the beam was placed (A and B). The amplitude of these signals, shown in figure 5.9, increased when the beam was at x = 1.5 cm and there is a distinct change in the shape of the response with a second negative going signal growing as the beam is moved further onto the mask as well as a DC "hump" between the negative and positive going parts of the usual stripline bipolar signal.

Charge dependence was investigated by moving the beam along y = 0 cm for a beam charge approximately five times higher than used before ($\sim 5 \times 10^7$). This is shown in figure 5.10 for two beam positions where the beam is hitting the low-Z mask. In both cases shown, the higher charge BPM signal is larger by a factor of $\sim$5 which agrees with the beam charge being larger by a factor of $\sim$5. This was true for all positions as the beam was scanned along y = 0 cm, confirming that the shape of the signals was an effect that did not change with charge and that the magnitude scaled linearly with charge.

The beam was also moved along x = $\pm$y. As the striplines of the BPM were rotated by 45°, this path moved the beam directly between one pair of striplines and perpendicular to the other pair (see figure 5.1). As the beam was moved within the clear beampipe, the striplines again behaved as expected with the pair perpendicular to the movement not

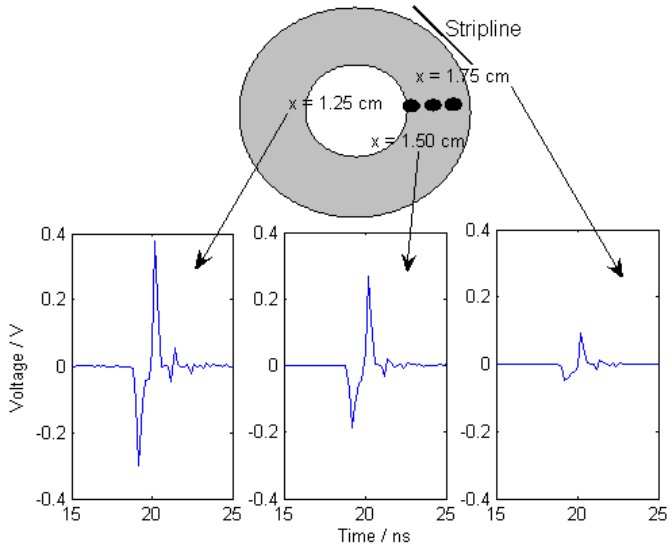

Figure 5.8: Stripline signals in volts from stripline C (see figure 5.1) at three positions on the x axis (x = 1.25 cm, x = 1.5 cm, x = 1.75 cm). The mean of 20 pulses is shown in each position. The beam charge for x = 1.25 cm is $(4.2 \pm 0.5) \times 10^7$ electrons, x = 1.5 cm is $(5.0 \pm 0.3) \times 10^7$ electrons and x = 1.75 cm is $(3.2 \pm 0.4) \times 10^7$ electrons.

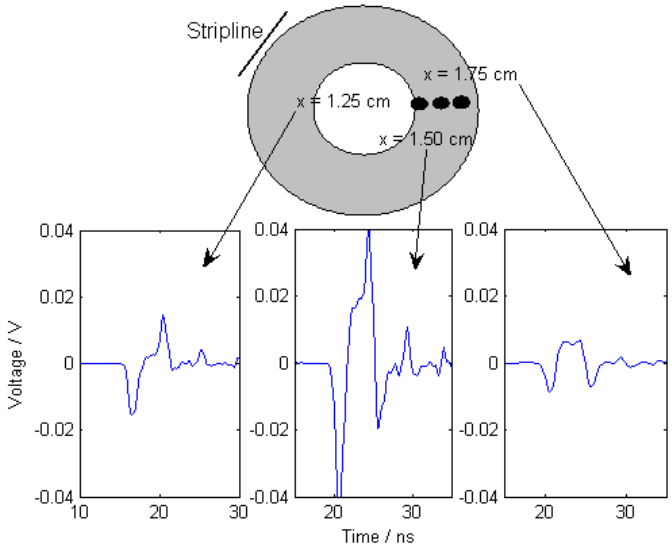

Figure 5.9: Stripline signals in volts from stripline B (see figure 5.1) at three positions on the x axis (x = 1.25 cm, x = 1.5 cm, x = 1.75 cm). The mean of 20 pulses is shown in each position. The beam charge for x = 1.25 cm is $(6.2 \pm 0.8) \times 10^6$ electrons, x = 1.5 cm is $(1.0 \pm 0.1) \times 10^7$ electrons and x = 1.75 cm is $(1.3 \pm 0.1) \times 10^7$ electrons.

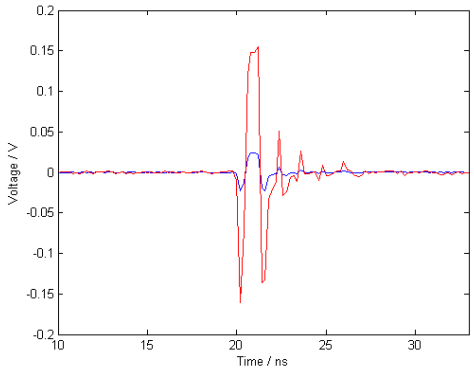

(a) Stripline B signal for the position x = 1.5 cm, y = 0 cm. In blue, the stripline signal at beam charge $(7.9 \pm 0.7) \times 10^6$. In red, the stripline signal at beam charge $(5.0 \pm 0.3) \times 10^7$.

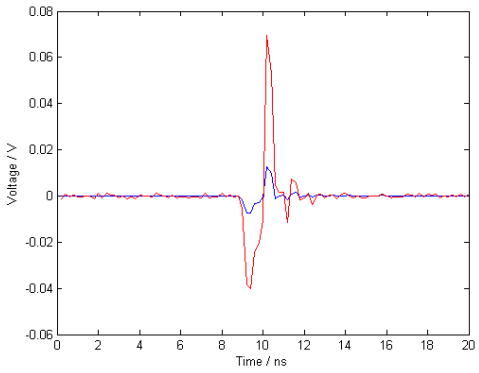

(b) Stripline C signal for the position x = 1.75 cm, y = 0 cm. In blue, the stripline signal at beam charge $(5.5 \pm 0.8) \times 10^6$. In red, the stripline signal at beam charge $(3.2 \pm 0.3) \times 10^7$.

Figure 5.10: Stripline signals at x = 1.5 cm and x = 1.75 cm with different beam charges. The mean of 20 pulses is shown at each charge.

changing, the stripline being approached gaining a larger response and the stripline opposite getting a smaller response. When the beam hit the low-Z mask, all four striplines showed a large response (figure 5.11) due to the increase of charged particle backgrounds. The signals for the perpendicular pair (striplines A and C) showed a small change in shape similar to the striplines in figure 5.8 which also had the beam moving between them rather than directly towards or away. The responses of the targeted stripline (B) and the stripline (D) on the opposite side of where the beam was placed were different: both striplines showed a new second negative-going peak and a "hump' between the first negative-going peak and the positive peak. Stripline B showed the greatest difference from the normal stripline response. The shapes changed for large offsets (see figure 5.12). Both striplines show a similar distortion, with stripline D having the larger second negative-going signal.

It was observed that the stripline signals observed in Method A could be explained qualitatively by secondary emission from the striplines superimposed on the response to charges hitting the striplines and the normal stripline response [100]. The flat positive part in the centre of the signal as seen in figure 5.12, for example, could be explained as secondary emission of electrons occurring along the length of the stripline. The construction of such signals is further discussed in chapter 8.

5.3.2 Processed difference signals

The stripline signals were processed into a difference and sum signal using the FONT4 analogue processors. The beam charge was set at 1.5×10^9 for the use of the processors. The beam was steered similar to before, along y = 0 and x = ±y.

The difference signals grew from zero as the beam was moved towards a stripline in the clear beampipe. When the mask was hit, the stripline responses all increased in amplitude so the sum signal of the processor increased. However, the difference signal did not, leading

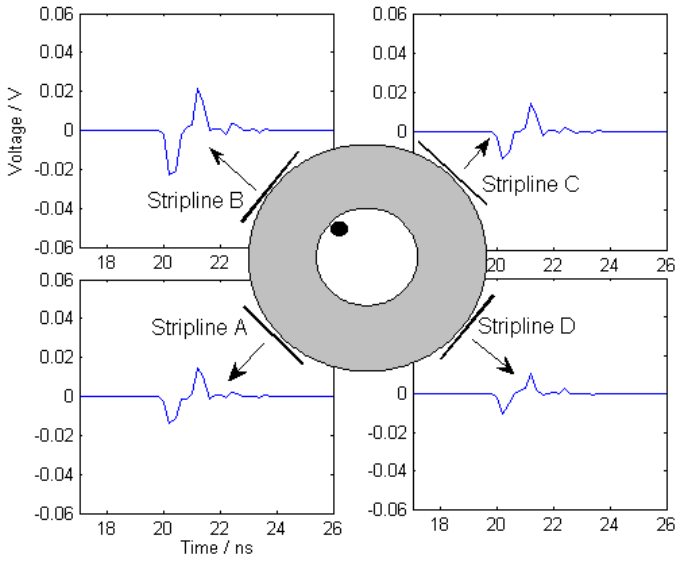

(a) Beam off mask (x = -0.75 cm, y = 0.75 cm). Beam charge is $(7 \pm 1) \times 10^6$ electrons.

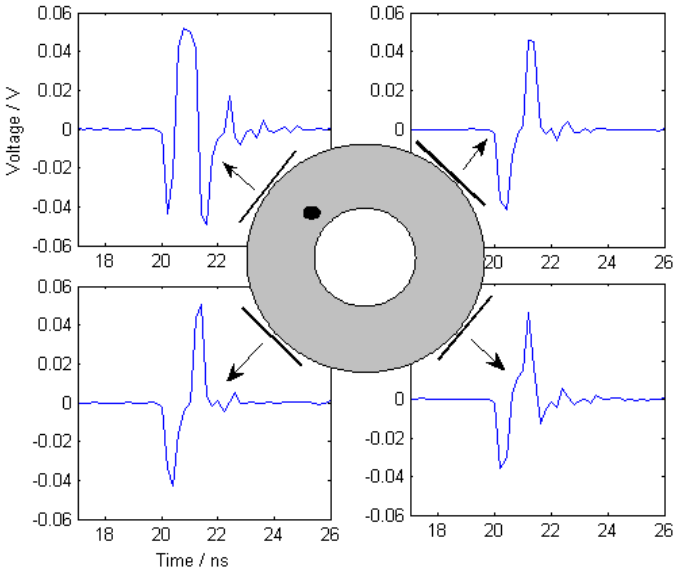

(b) Beam on mask (x = -1 cm, y = 1 cm). Beam charge is $(9 \pm 1) \times 10^6$ electrons.

Figure 5.11: The stripline responses for all four striplines before and after the beam hits the low-Z mask as it is moved along x = -y.

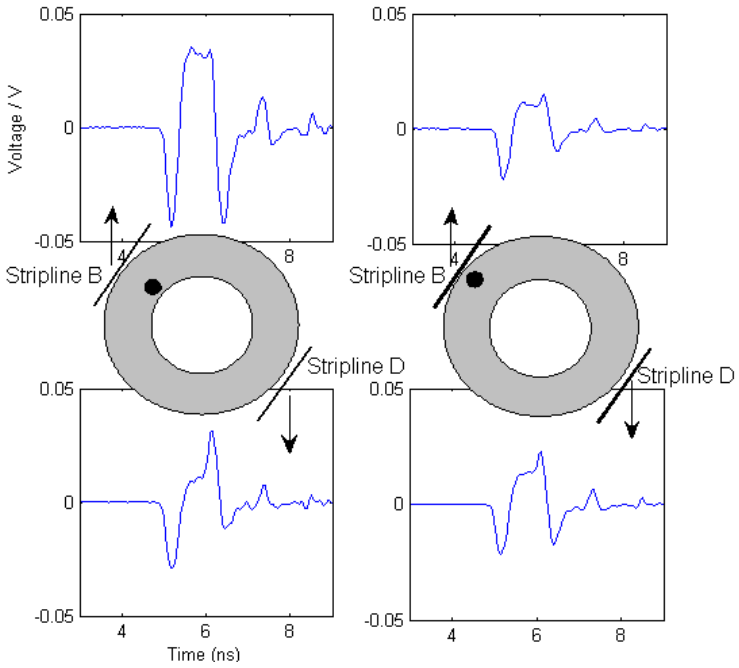

Figure 5.12: Left: Response of two striplines with the beam at x = -1 cm, y = 1 cm (on the low-Z mask) with beam charge $(9 \pm 1) \times 10^6$ electrons. Right: Response of two striplines with the beam at x = -1.25 cm, y = 1.25 cm and beam charge $(4 \pm 1) \times 10^6$ electrons.

to a smaller normalised signal. Even further on the mask, with the beam placed at r = 1.75 cm, the difference signal changed sign (see figure 5.13) showing the processor's sensitivity to the shift between the nearest stripline having the greater signal to the opposite stripline having the greater signal, as shown in figure 5.12.

5.4 ILC Prediction based on Method A

At the ILC all of the low-Z mask is illuminated by particles from the pair backgrounds (figure 3.19). Method A had illuminated spots (approximately 2 mm by 1 mm) on the low-Z mask (figure 5.1). These are two very different scenarios but assuming that the stripline signals from the results of Method A can be summed together, the effect on the striplines from charges hitting at many points around the low-Z mask can be found. For example, figure 5.14 shows two positions (R1 and R2) with the beam placed near striplines in Method A. The stripline signals recorded for the beam at R1 can be added to the stripline signals recorded for the beam in R2 to produce four stripline signals for a situation where particles hit the low-Z mask at the top and at the bottom edges of the low-Z mask.

To a first approximation, this is similar to the ILC case where the particles hitting the low-Z mask are mainly at the top and bottom (see figure 3.25).

Due to rotational symmetry, R1 is equivalent to R2 (which was confirmed in the results from Method A) and in fact only one set of results need be used. In fact, all of the Method

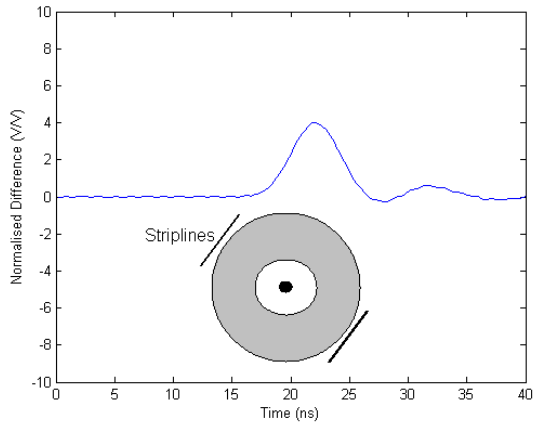

(a) x = 0 cm, y = 0 cm

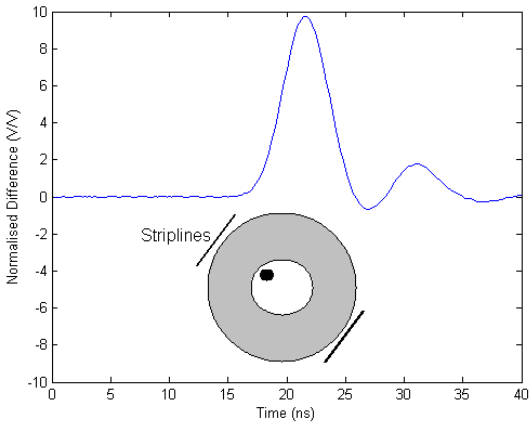

(b) x = -0.75 cm, y = 0.75 cm

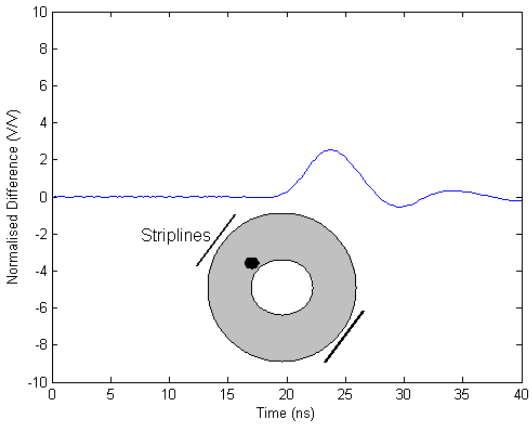

(c) x = -1 cm, y = 1 cm

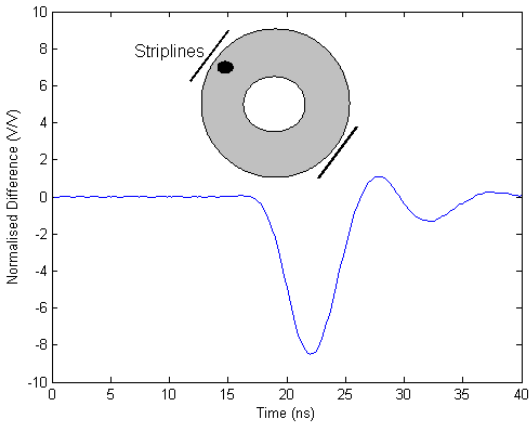

(d) x = -1.25 cm, y = 1.25 cm

Figure 5.13: The response from the FONT4 analogue processor with input signals from striplines B and D. The beam charge was 1.5×10^9 electrons.

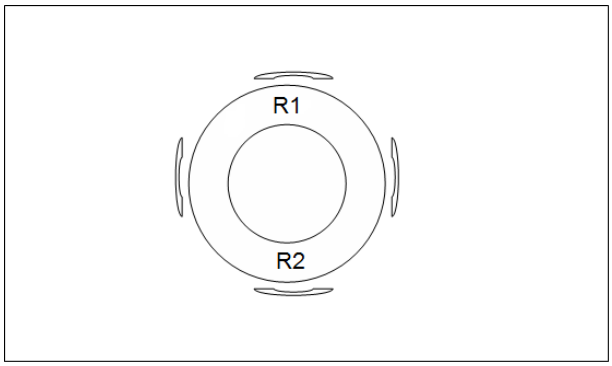

Figure 5.14: Two positions of the Method A beam (R1 and R2). These positions are on the axis between two opposing striplines.

(a) (b)

Figure 5.15: (a): Two positions of the beam (R and X) that were recorded during Method A data taking. (b): R and X extended to cover the entire front face of the module through consideration of rotational symmetry.

A data can be summarised in two positions: runs with the beam aimed along the axis of paired striplines (R) and runs with the beam aimed between two striplines (X) as shown in figure 5.15(a). By considering the rotation of the Method A stripline signals, this is expanded to eight positions (figure 5.15(b)) all of which have associated stripline signals recorded from Method A. Plus, at each R and X, signals were recorded at different radii. In this way, the stripline signals for the illumination of the entire disc of the front face of the low-Z mask can be created.

The simulation of the 14 mrad crossing angle IR with pair backgrounds for the Scheme 14 parameter set was used (section 3.4.4). Each charged electron or positron recorded at the z position of the low-Z mask (285 cm) was associated with stripline signals from R and X: a charged particle in the ILC simulation striking the plane at z = 285 cm on the axis of two opposing striplines was associated with signals from the R set of Method A data (R_{signals}) and a charged particle striking the plane at z = 285 cm on the axis between two adjacent striplines was associated with signals from the X set of Method A data (X_{signals}). Particles falling between these two sets were assumed to create a signal that is a weighted average of R and X using the azimuthal angle ϕ of the particle in the simulation. For example, with $0 < \phi < \frac{\pi}{4}$ the weighted set of signals W_{signals} is:

$$W_{\text{signals}} = \frac{(\frac{\pi}{4} - \phi)}{\frac{\pi}{4}} \times R_{\text{signals}} + \frac{\phi}{\frac{\pi}{4}} \times X_{\text{signals}} \tag{5.1}$$

Four different radii of Method A results were used: 0 cm, 1 cm, 1.5 cm and 1.75 cm. The W_{signals} for a particle was produced using the R_{signals} and X_{signals} from the data set with the radius closest to the radius at which the particle strikes the z = 285 cm plane. The Method A results were divided by the beam charge for that particular set of data so that they were stripline signals for one single charge striking the low-Z mask.

Figure 5.16(a) shows the predicted stripline signals for the ILC IP BPM using this method. Each stripline has a similar predicted signal that is clearly dominated by the pairs that go down the centre of the beampipe since they exhibit the typical bipolar signal

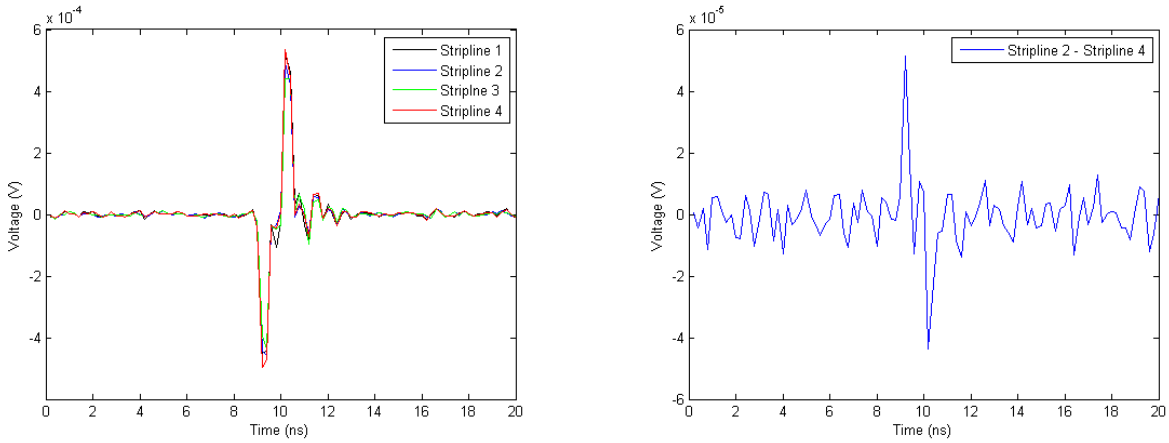

(a) Prediction for the signal on four striplines of the ILC IP feedback BPM.

(b) Prediction for the difference between the top and bottom stripline signals of the ILC feedback BPM.

Figure 5.16: The results for predicting the stripline signals for the ILC IP feedback BPM due to beam-beam pairs based on a weighted sum of Method A stripline signal results.

for charges passing in the beampipe (figure 5.7). The difference between the backgrounds-induced signal on the top stripline and the backgrounds-induced signal on the bottom stripline (stripline 2 subtracted from stripline 1) is shown in figure 5.16(b).

This peak difference of $\sim 5 \times 10^{-5}$ V between the top and bottom stripline due to pair backgrounds is the equivalent to a 6 ± 1 nm offset (from the calibration in figure 5.6). This method of predicting the stripline signals is coarse and taking the difference between two poorly known signals is therefore unreliable. As a more conservative estimate of the position error caused by the pair backgrounds at the ILC, the absolute height of one stripline can be taken ($\sim 5 \times 10^{-4}$ V) with the conclusion that the error is at the very most 60 ± 10 nm.

The main fault in this method is in treating electrons and positrons equally. Although the interactions of electrons and positrons with matter are very similar, the signals for charges passing the upstream end of the stripline are reversed (section 1.5.2). As a result, the amplitude of the predicted signal is overestimated. Given that a 60 nm error is already low enough not to impact the target resolution of 1μm, no further work was done to improve this prediction.

Improvements to this method of predicting ILC signals also include using finer steps in radius and angle. However, this method is always going to be restricted since in approximating the number distribution of charges at the low-Z mask, the energy distribution is not matched.

5.5 Summary to Method A

Method A was developed to produce a lot of secondary backgrounds by directly aiming the beam into the FONT module.

This method involved a low-charge, large-spot size beam scanning the face of the low-Z mask. This required instrumentation at ESA for low beam currents that had to make large movements in x and y.

Simulations of Method A showed a similar energy distribution of electron and positron hits on the striplines. They also showed that the ratio of electron hits to positron hits and photons hits to be close particularly in the case of Method A stripline A and ILC striplines 1 and 3. This can be attributed to the FONT module matching materials and radiation lengths and so creating similar secondary backgrounds regardless of the primary backgrounds.

The results showed raw stripline signals with distorted shapes. Essentially they can be divided into two groups: those that retain the usual bipolar doublet stripline signal (striplines C and D in figure 5.8 and striplines A and C in figure 5.11(b)) and those that show a unique shape with a flat positive central part and two negative-going peaks (striplines B and D in figure 5.12). These shapes can be qualitatively explained by the image charges of electrons passing the upstream end of the stripline and the secondary emission of electrons.

By considering a weighted superposition of the beam spots on the front face of the FONT module in various data runs of Method A, the number density of charged particles at the location of the low-Z mask in the ILC IR was approximated. The GEANT3 simulations of the 14 mrad crossing angle case with anti-DID and Scheme 14 pairs was used for this. Each position of the beam in Method A was associated with stripline signals and so the stripline signals were summed in this weighted superposition, producing a prediction for the ILC. This prediction suggested stripline signals for the IP BPM at the ILC, created by the background pairs, of <0.5 mV in amplitude. This signal produces a <60 nm error in determining position. The prediction is an overestimate due to treating electrons and positrons equally. Also when the difference of the two opposite striplines is taken it will be further reduced.

The predicted degradation in position resolution from the pair backgrounds at the IP is therefore expected to be of the order of nanometres and is not a concern for the goal of micron level resolution.

Chapter 6

Methods for recreating ILC backgrounds: Method B

Three methods of creating a beam to use in conjunction with the FONT module were developed as described in section 5.1 and table 5.1. In this chapter, Method B is discussed.

6.1 Methods for creating spray: B

6.1.1 Overview

To create a scenario where backgrounds were created in the presence of the main electron beam, Method B was developed. The BPM's measurement of the main electron beam position could be performed with and without backgrounds and the two measurements compared.

The backgrounds were created using thin foils of aluminium placed in the beamline upstream of the module. With a thin amount of material, the beam is only slightly disrupted and the position of the beam can be measured with the striplines as usual. As the electrons pass through the foils, they are deflected by the electric fields of the nuclei and electrons of the foils. Most particles are deflected at small angles and multiple times. There are also bremsstrahlung photons and electrons and positrons from pair production.

The scattered electrons, bremsstrahlung photons and some small numbers of electron-positron pairs, form a halo of particles around the main beam. Figure 6.1 shows the number density per beam charge of the particles hitting the plane with the z location of the front face of the low-Z mask in a GEANT3 simulation of Method B. In this simulation, a foil was placed 12 m upstream and the beam was 800μm in σ_x and 65μm in σ_y and going straight down the centre of the beampipe (x = 0 cm, y = 0 cm). GEANT uses the Molière Bethe formulation of multiple scattering [101] to calculate the passage of the electrons through the material of the foil. Most of the original beam remains in the centre of the beampipe (brown/red) surrounded by a low density halo (light blue). The inner radius of the low-Z mask is marked as a black circle. Those particles in the halo that hit the low-Z mask will go on to cause showers which can produce backgrounds at the location of the BPM striplines.

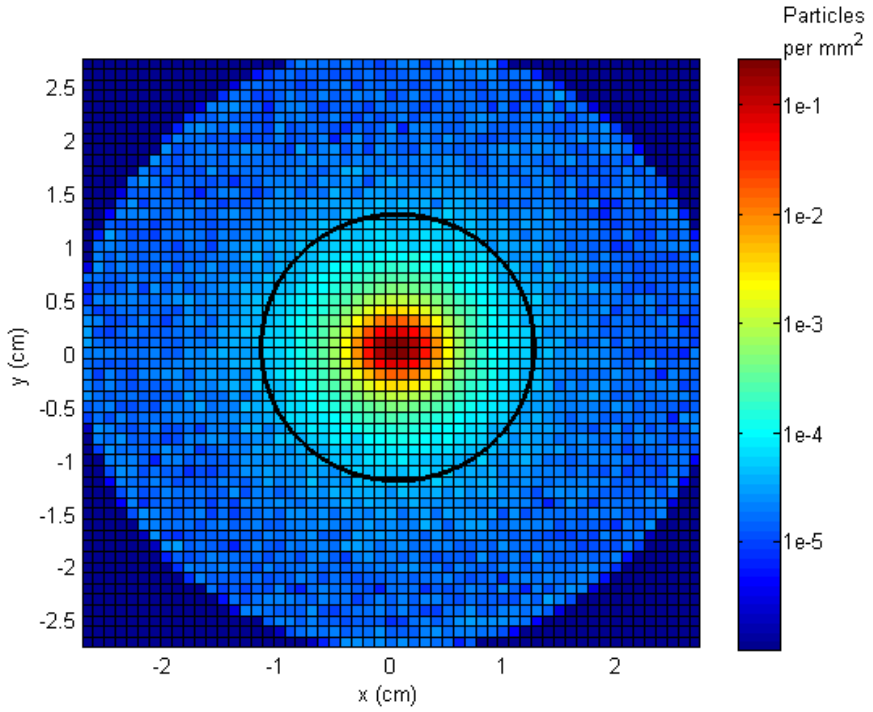

Figure 6.1: The number density of electrons, photons and positrons that hit the front face of the low-Z mask in a simulation of Method B using the 5% foil. The numbers are shown per input electron to the simulation.

6.1.2 Designing the experiment

It was important to design the Method B experiment such that enough flux was in the halo of background particles to cause secondary backgrounds at a level similar to those in Method A and those that are expected at the ILC.

To get an indication of the flux that could be expected, a beam of 1×10^6 28.5 GeV electrons hitting a thin aluminium foil was simulated in GEANT3. This investigation considered three upstream locations where a foil could be inserted into the beam: 3PR2 and 3PR3 which are profile screens and also the E158 Möller polarimeter[1] (see table 6.1). The flux was estimated between the angles subtended by the front low-Z face of the module (figure 6.2). The further upstream the foil, the higher the flux as most electrons are only scattered through small angles.

The amount of halo that hits the low-Z mask needed to be maximised to increase the secondary backgrounds. The foils were inserted in one of the more upstream positions (using the apparatus formerly used in the E158 Möller experiment) to take advantage of the greater flux of particles at the lower angles. The foil thickness was limited by radiation safety at SLAC to 5% of a radiation length. As the Möller polarimeter apparatus offered the option to use three foils, 3% and 1% radiation length foils were placed in the extra slots in case the backgrounds caused a detectable effect with the 5% foils. The main concern was to bring

[1]The E158 experiment used this device to insert foils into the beamline remotely to measure beam polarisation [102].

Source	Angle $\theta_2 - \theta_1$ (mrad)	1% Radiator flux	3% Radiator flux	5% Radiator flux
3PR2	1.74-0.76	0.23×10^{-1}	2.32×10^{-1}	7.68×10^{-1}
Möller	2.3-1.0	0.18×10^{-1}	1.85×10^{-1}	6.20×10^{-1}
3PR3	28.9-12.6	0.06×10^{-1}	0.76×10^{-1}	2.83×10^{-1}

Table 6.1: The number of hits per electron of beam charge on the low-Z mask in GEANT3 simulations. Three foils are shown (5%, 3% and 1%) at the three upstream locations (3PR2, Möller polarimeter and 3PR3) as shown in figure 6.2.

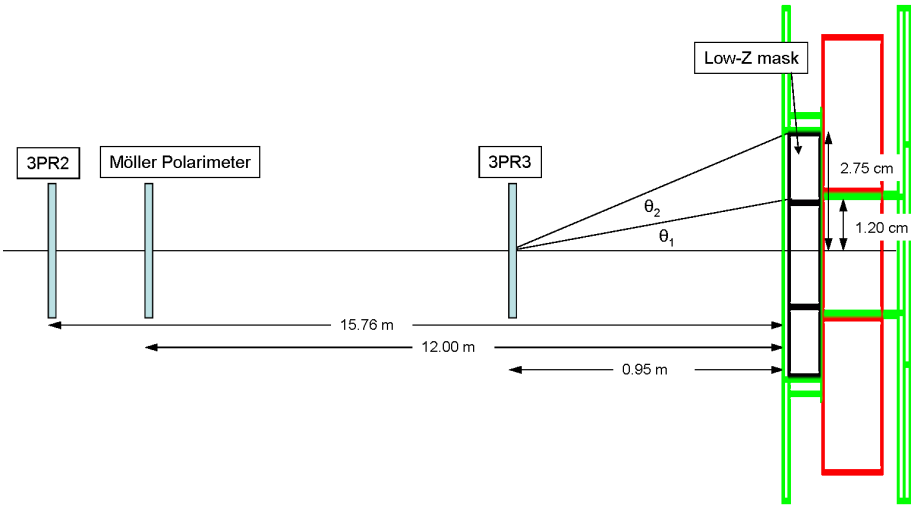

Figure 6.2: The three possible upstream foil positions [103] are shown schematically with the front end of the FONT module. The angles θ_1 and θ_2 as used in table 6.1 are defined and relevant distances given.

Experiment	Beam Charge (electrons)	Number of BPM stripline hits	Signal height (mV)
Method A (r=1.4cm)	$(9 \pm 1) \times 10^6$	$(17 \pm 2) \times 10^7$	40
1% Foil	5×10^9	$(2.91 \pm 0.05) \times 10^7$	6.8 ± 0.8
3% Foil	5×10^9	$(1.29 \pm 0.01) \times 10^8$	30 ± 3
5% Foil	5×10^9	$(2.26 \pm 0.01) \times 10^8$	53 ± 6

Table 6.2: Estimated signal heights based on a comparison of hits of the BPM striplines in GEANT3 simulations and the experimental result of Method A.

the effect of the secondary emission to a level that could be detected in the experiment given the oscilloscope resolution and the inherent jitter of the beam.

To check that this setup was capable of giving a result that could be measured on an oscilloscope with voltage resolution 4 mV, the results of Method A (section 5.3) were used with GEANT3 simulations of Method B. The Method B simulations involved a simulated ESA beam (of 28.5 GeV electrons) as an input to a GEANT3 model of a target made out of aluminium of the appropriate thickness (5%, 3% and 1% X_0) followed by 12 m of drift in vacuum and then the GEANT3 FONT module. The numbers of electrons, positrons and photons hitting each stripline in the simulations were evaluated. Comparing the number of simulated particle hits on the stripline in Method A (shown in table 5.3) to the number of simulated particle hits on the stripline in Method B (shown in table 6.2), Method B appears to create a similar level of backgrounds. Using the typical height of signals from Method A (for example, 40 mV as in figure 5.11) and the ratio of simulated particle hits on the stripline in Method A to the simulated particle hits expected on the stripline in Method B, the height of the signal expected for Method B was estimated (table 6.2). The beam charge assumed for Method B was 5×10^9 electrons because experience with Method A taught that stripline signals from higher beam charges required attenuation before the oscilloscope input.

Based on this estimate for the height of the signal caused by the backgrounds, it would be possible to see the signal due to particles hitting the striplines. However, it was not known how large the beam jitter would be. The position jitter of the beam could obscure such effects and prevent them from being seen despite them being above the resolution of the oscilloscope.

6.1.3 Performing the experiment: Method B

This method was used in the March 2007 run at ESA. The 5%, 3% and 1% X_0 aluminium foils were placed in the E158 Möller polarimeter, 12 metres upstream of the existing FONT module.

Instrumenting this method only required the standard beam diagnostics available at ESA. The normal beam charge of 1.6×10^{10} electrons per bunch was used (with attenuation before the oscilloscope input) and the standard toroid 4140 measured the charge. Special beam

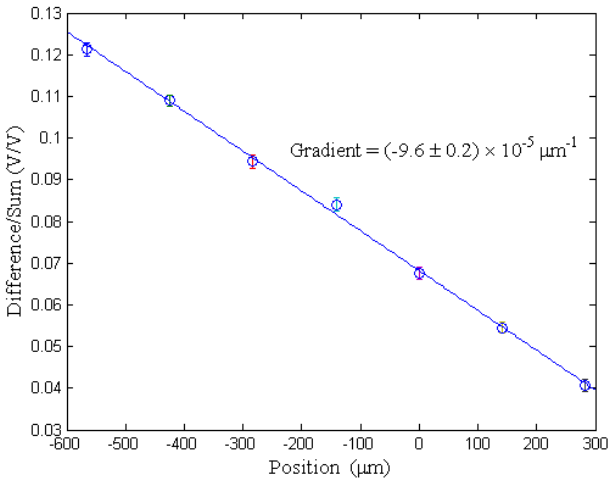

Figure 6.3: The difference between the peak-to-peak voltage of stripline A and the peak-to-peak voltage of stripline C divided by the sum as the beam was moved between the two striplines in 140 μm steps.

optics were not a concern as a diffuse beam was not required, so existing optics were used that led to a beam at the Möller location of 800μm in σ_x and 65μm in σ_y [97].

The stripline signal heights were calibrated with position[2]. The calibration was achieved by using correctors to translate the entire beam (downstream of the correctors used) in steps of 100 μm in both x and y. 100 pulses were taken at each point to reduce the effect of the beam jitter. Fourier interpolation was applied to the data to find the most likely values for the maximum and minimum points of the bipolar stripline signal before calculating the difference between two paired (i.e. opposing) striplines and dividing it by their sum. The calibration curve for striplines normalised by charge is shown in figure 6.3.

The calibration with position was also done for the position signals from the FONT4 analogue processors. The processor calibration also used full beam translation. 18 pulses were taken at each point and each difference and sum signal was integrated under (rather than taking their maxima) to remove the effects of oscilloscope trigger jitter and noise in taking a single data point [49]. The calibration curve for the processors is shown in figure 6.4.

The raw stripline signals were attenuated before the oscilloscope to reduce their voltage such that the large voltage signals from 1.6×10^{10} electrons could be seen on the oscilloscope. 1000 pulses of stripline signals were recorded using the FONT DAQ with no foil in the beam. Each foil was placed in the beam in turn and 1000 pulses taken. A final set of 1000 pulses was taken without a foil in the beam as a repeat to check for drift.

Two signals from opposite striplines (A and C) were processed using the FONT4 processors to produce difference and sum signals. 1000 pulses of processed signal were recorded for each case: no foil, 5% X_0 foil, 3% X_0 foil, 1% X_0 foil and a repeat of no foil.

With the beam on axis, the background environment for each of the four striplines in the

[2]Stripline signal heights were used, anticipating the need to relate stripline signal amplitudes to position for the background noise.

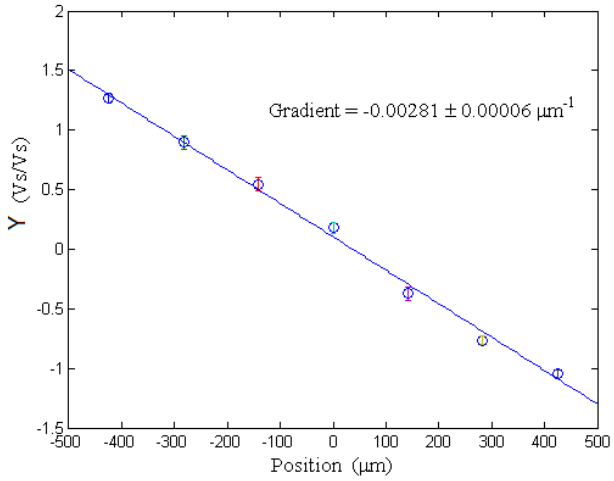

Figure 6.4: The integrated difference divided by sum signal (Y, equation 2.2) for the FONT4 analogue processors with inputs from striplines A and C as the beam was moved between the two striplines in 140 μm steps.

module is identical (by symmetry) and so by taking the difference of the signal from stripline A and stripline C, any effect from the secondary backgrounds is removed. Therefore the difference signal from the processor should be unaffected (with averaging to reduce random fluctuations) unless the subtraction of the signals is done inaccurately. To achieve a difference signal where an effect from secondary backgrounds can be seen, Method B with foils was performed at an offset of 360 μm as well as with the beam near zero. The offset could not have been too large because it needed to be within the range where the processors produced a linear output for the calibration to hold.

6.2 Results: Method B

6.2.1 Raw stripline data

By eye, no change was seen with the foils in the beam and out of the beam (figure 6.5).

The data needed to be analysed, which was done using parameters m and n, chosen to be independent of beam charge and position jitter [104]:

$$m = \frac{Q + P}{Q - P} \tag{6.1}$$

$$n = \frac{R}{Q - P} \tag{6.2}$$

Here Q refers to the maximum point of the stripline signal and P refers to the minimum point. R lies half way between the two (if Q occurs at T_Q and P occurs at T_P, R occurs at $(T_Q - T_P)/2$). This is shown in figure 6.6.

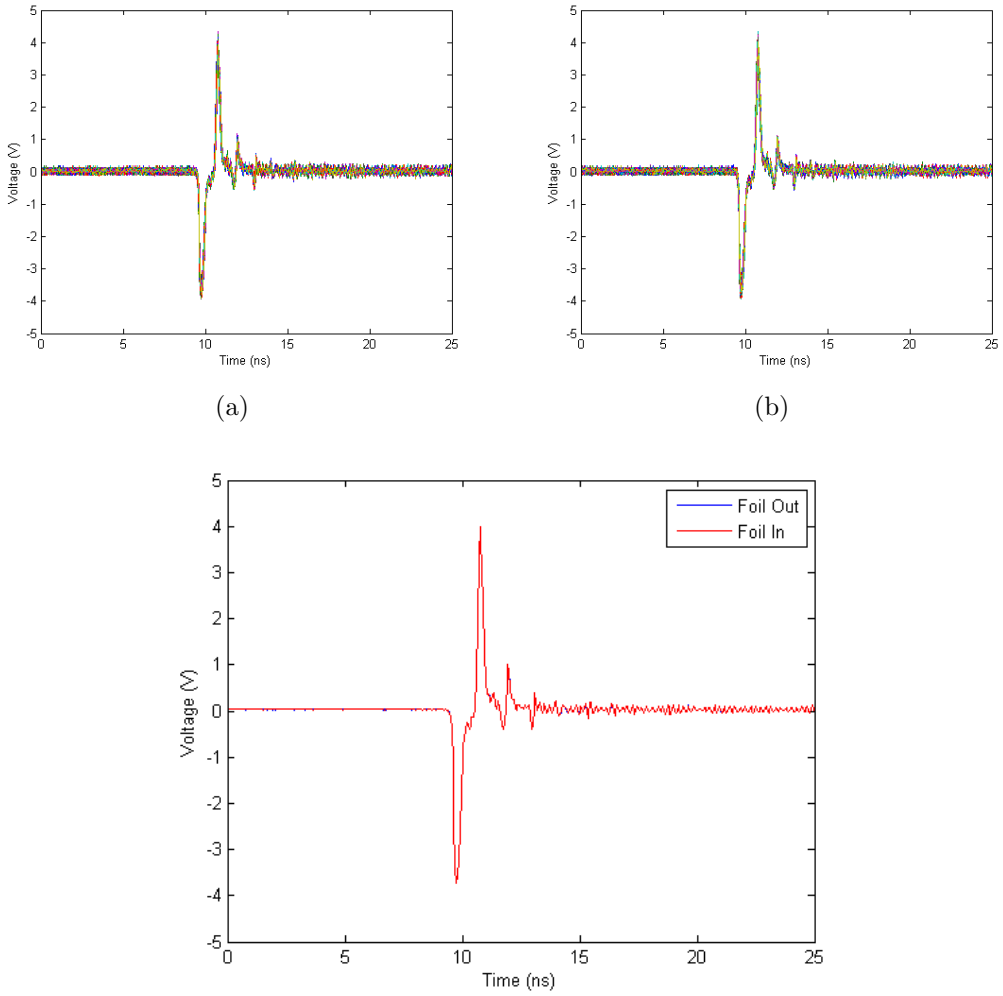

(a) (b)

(c)

Figure 6.5: The results for 1000 pulses taken with (a) no foil in the beamline and (b) the 5% foil in the beamline. The mean stripline signals are overlaid in (c) where blue is for no foil in the beamline and red is for the 5% foil in the beamline.

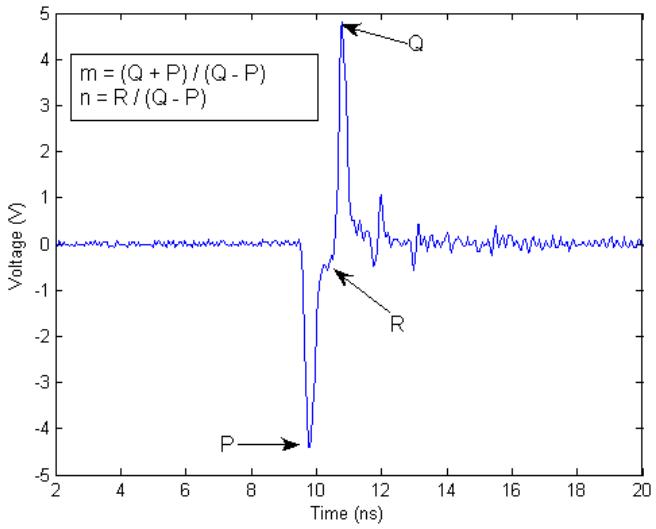

Figure 6.6: The maximum point of the stripline signal (Q), the minimum point of the stripline signal (P) and the value that occurs at a time exactly half way between those points (R).

Both parameter m and parameter n are normalised by the peak to peak height of the bipolar stripline signal ($Q - P$) which is proportional to both charge and position.

The signal from secondary particles, as seen in Method A, involves two negative polarity pulses and a flat part in between (for example figure 5.12). Parameter n_{in} (n measured with the foil in the beamline) includes the flat contribution to the stripline signal by secondary emission. Parameter m_{in} (m measured with the foil in the beamline) includes the change in the relative size of the peaks Q and P due to the negative polarity pulses. Parameter m_{out} (m measured with the foil removed from the beamline) would ideally be equal to zero as Q and P should be equal. However, with real signals this is not often the case due to capacitive and inductive effects.

m is of the most concern to this analysis as a change in stripline signal height would be mistaken as a position offset.

These parameters, m and n, were calculated for each stripline signal recorded with the foils inserted into the beamline and each stripline signal recorded with the foils removed. Fourier Interpolation was used to estimate the values that fell between sampling points to minimise the error caused by discrete sampling and the oscilloscope time sampling jitter. The means ($\bar{m}$ and $\bar{n}$) and statistical errors on the means ($s_{\bar{m}}$ and $s_{\bar{n}}$) were calculated. These are shown in table 6.3.

The difference between $\bar{m}_{\text{out}}$ and $\bar{m}_{\text{in}}$ is less than the statistical error on either mean:

$$\Delta\bar{m} = \bar{m}_{\text{out}} - \bar{m}_{\text{in}} < s_{\bar{m}} \tag{6.3}$$

The 5% foil produced the greatest secondary backgrounds but here $\Delta\bar{m} = 0.0001$ with $s_{\bar{m}} = 0.0005 (> \Delta\bar{m})$. Therefore no change in m was observed when the foils were inserted.

Foil thickness	$\bar{m}$	$s_{\bar{m}}$	$\bar{n}$	$s_{\bar{n}}$
No Foil	0.0364	4.46e-4	-0.0326	1.85e-4
5%	0.0363	4.79e-4	-0.0325	1.87e-4
3%	0.0376	4.35e-4	-0.0324	1.87e-4
1%	0.0375	4.39e-4	-0.0321	1.78e-4
No Foil (repeat)	0.0378	4.55e-4	-0.0320	1.75e-4

Table 6.3: The means of the parameters m (equation 6.1) and n (equation 6.2) as calculated for the stripline signals. The statistical errors on the means (given 1000 pulses were taken) were also calculated ($s_{\bar{m}}$ and $s_{\bar{n}}$). A repeat measurement was taken for no foil being inserted in case of drift over time. The data were taken in the order presented in the table.

The same is true for $\bar{n}_{\text{out}}$ and $\bar{n}_{\text{in}}$:

$$\Delta\bar{n} = \bar{z}_{\text{out}} - \bar{n}_{\text{in}} < s_{\bar{n}} \tag{6.4}$$

The 5% foil produced $\Delta\bar{n} = 0.0001$ with $s_{\bar{n}} = 0.0002$. Therefore no change in n was observed when the foils were inserted.

There is some drift observed between the start of this data taking run and the end so the $\bar{m}_{\text{out}}$ and $\bar{n}_{\text{out}}$ are chosen to be from the first "no foil" run, closest in time to 5% foil run.

Although no difference was observed with the foils in and the foils out, the experimental errors offer an upper limit on $\Delta\bar{m}$ and $\Delta\bar{n}$ of 0.0008 and 0.0003 respectively at the 95% confidence level. The limit on $\Delta\bar{m}$ can be used to judge the effect of the secondary backgrounds at the ILC (which is done in section 6.3.1).

6.2.2 The processed signals

Signals from the FONT4 analogue processors were examined with foils in and out of the beam. This was done twice for two beam offsets: a small offset (360 μm) and near zero (70 μm).

Figure 6.7 shows the processed signal for the initial run without foils (blue) and the runs with the foils in the beamline (red, green and cyan). In both cases, the charge normalised difference signal C (equation 6.5 with the difference signal $V_{\text{Difference}}$ and the sum signal V_{Sum}) is plotted versus time. There appeared to be a change in the processor signals when the foils were inserted. However, there was also a change between the two runs without foils (blue and black) indicating that there was drift during the course of the data. Also, the pattern in processor signals does not agree with the 1% foil causing the lowest backgrounds (and hence causing a signal similar to that of the no foil runs) and the 5% foils causing the highest backgrounds (and hence causing a signal with the greatest difference to that of the no foil runs). This is true for both beam positions: near zero (where the effect from background particles only appears in the sum and so should not cause a noticeable change in processed signal) and at 360 μm.

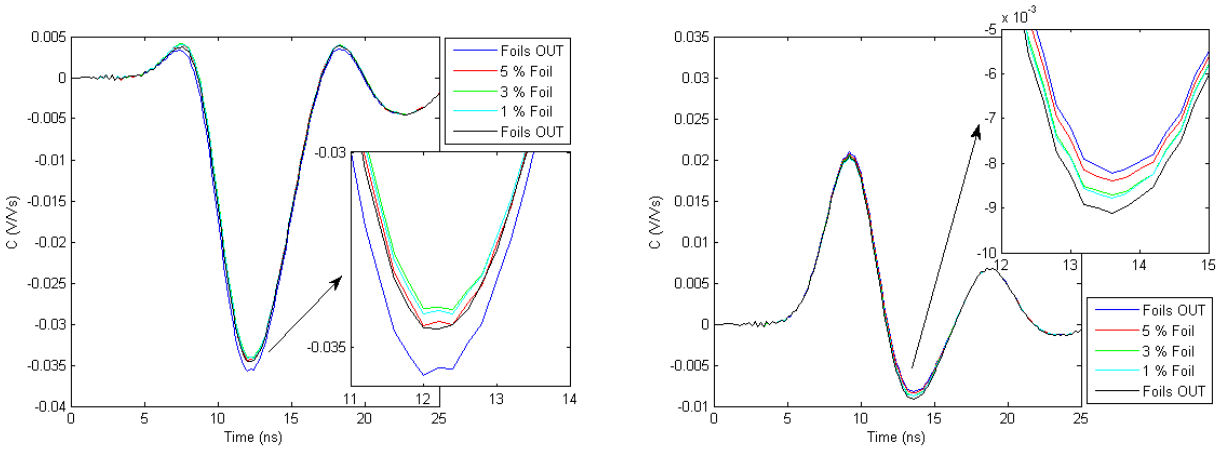

(a) Beam offset by 360 μm

(b) Beam near the beampipe centre

Figure 6.7: C (equation 6.5) versus time, averaged over 1000 pulses. The data are shown for no foils in the beamline (blue and black), the 5% foil in the beamline (red), the 3% foil in the beamline (green) and the 1% foil in the beamline (cyan). The data were taken in the order shown in the legend.

$$C = \frac{V_{\text{Difference}}}{\int V_{\text{Sum}}\, dt} \tag{6.5}$$

The processed signals were expressed as a single dimensionless value D:

$$D = \frac{\int V_{Difference}\, dt}{\int V_{Sum}\, dt} \tag{6.6}$$

This is the integrated difference divided by the sum. This removed the effect of charge jitter. It was calculated for each processed signal recorded with the foils in the beamline and for each processed signal recorded with the foils removed from the beamline. The mean ($\bar{D}$) and error on the mean ($s_{\bar{D}}$) was calculated for each foil (or no foil) case. These values are shown in table 6.4 and table 6.5.

The near zero data shown in table 6.4 shows a trend that resembles drift confirming what was seen in figure 6.7(b). Near zero, it was not expected that there would be any effect from the foils unless the stripline signals were processed in an unexpected way through the electronics. The data support that there was no effect from the foils that could be seen due to the drift between the two runs without foils. From these data, $\bar{D}$ changes by 0.035 between the first run without a foil and the final run without a foil.

With the beam at a small offset of 360 μm, there appeared to be a large difference in $\bar{D}$ of 0.053 between the data run without the foil at the start of the experiment and the data run without the foil at the end of the experiment (table 6.5). The difference between the first data run without foils and the 3% data run is largest (0.076) however this is unlikely to be due to secondary backgrounds: the pattern does not match the expected order of the 5% foil giving the largest difference followed by 3% and then 1%.

Foil thickness	$\bar{D}$	$s_{\bar{D}}$
No Foil	0.317	0.002
5%	0.307	0.002
3%	0.294	0.002
1%	0.290	0.002
No Foil (repeat)	0.281	0.003

Table 6.4: The parameter $\bar{D}$ (equation 6.6) for the processed position signals when the beam was nearly centred in the BPM. The statistical error on the mean (given 1000 pulses were taken) was also calculated. A repeat measurement was taken for no foil being inserted in case of drift over time. The data were taken in the order presented in the table.

Foil thickness	$\bar{D}$	$s_{\bar{D}}$
No Foil	-0.942	0.001
5%	-0.873	0.002
3%	-0.866	0.001
1%	-0.869	0.001
No Foil (repeat)	-0.889	0.001

Table 6.5: The parameter $\bar{D}$ (equation 6.6) was calculated for the processed position signals with the beam at a small offset of 360 μm. The statistical error on the mean (given 1000 pulses were taken) was also calculated. A repeat measurement was taken for no foil being inserted in case of drift over time. The data were taken in the order presented in the table.

No such large drift was seen in the raw stripline data. This could be a change in beam conditions during the data taking with the processors (compared to the stable beam conditions as the raw stripline data was taken) or possibly a drift within the processor, which has never been tested over extended periods of time for stability.

Due to the apparent drift, conclusions cannot be drawn from the data with the processors.

6.3 Simulating the experiment: Method B

The GEANT3 description of the module was changed to include an upstream foil to simulate this method. It included a thin foil of aluminium (with thickness that varied between 1% and 5% of a radiation length) followed by 12 m of drift as shown in figure 6.8. A Gaussian beam was generated with energy 28.5 GeV and 0.2% spread, 1000 μm in σ_x, 100 μm in σ_y and 500 μm in σ_z. 10^6 particles were used in the simulation and tracking was enabled down to 100 eV using the modified GEANT.

The outgoing beam at ESA was 28.5 GeV, well below the ILC electron energies. This does not affect the stripline signal from the main beam as the electrons are still relativistic [43] so the main stripline signal is identical to an outgoing beam signal at the ILC if beam charge is matched. The energy distribution of the scattered electrons from the foils is also many orders of magnitude low (see figure 6.9) but thanks to matching the materials in the IR,

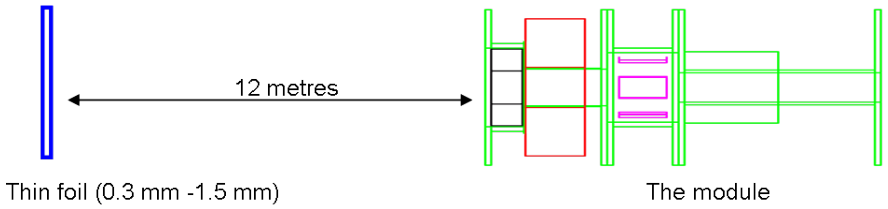

Figure 6.8: The FONT module with a thin target upstream. Green represents iron, black is carbon and red is lead. The BPM striplines are highlighted in purple and modeled to be made from iron. This is not to scale.

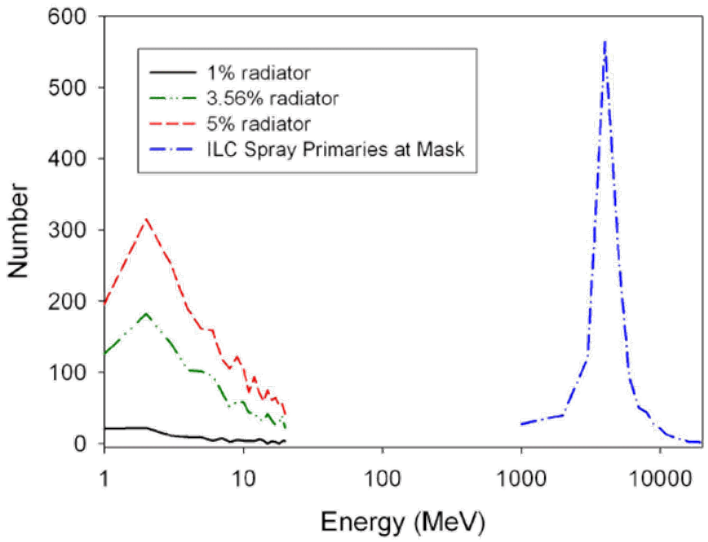

Figure 6.9: The energy spectra of the electrons in the beam halo after being passed through foils (shown in red, green and black) and the energy spectrum of the pairs from the ILC IP that hit the low-Z mask (blue) [105].

what actually hits the BPM striplines has a very similar energy distribution according to GEANT3 simulations shown in figure 6.10. The number of particles hitting the strips shown here is from a simulation with 10^6 electrons. The beam charge in Method B was 1.6×10^9, therefore the number of particles in Method B exceeds ILC numbers by approximately three orders of magnitude.

As with Method A, the percentage of hits on the striplines from photons was slightly different for Method B simulations compared with ILC simulations (table 6.6). 91% of the hits on the striplines in Method B were photons compared to ~80% for the striplines at the ILC.

6.3.1 Using GEANT3 Simulations to scale from ESA to ILC

The Method B results put limits on parameters $\Delta\bar{m}$ and $\Delta\bar{D}$. It is necessary to interpret these limits into position errors caused by noise on the striplines from backgrounds at the ILC.

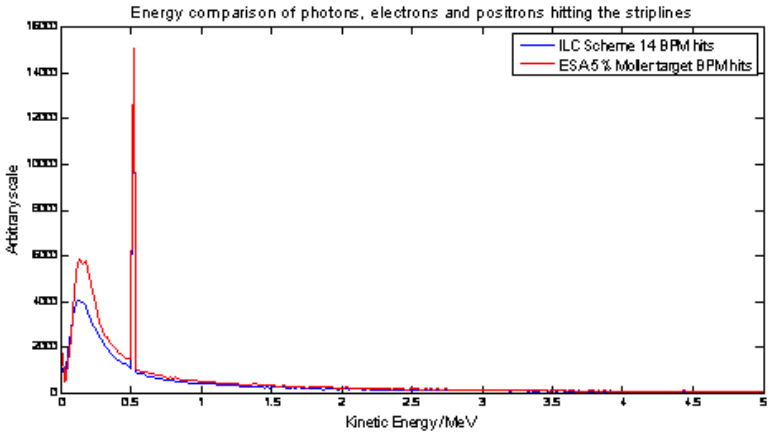

Figure 6.10: The energy distribution of the GEANT3 ILC simulation hits on the striplines (blue) and the energy distribution to the hits on the striplines with the 5% foil at ESA (red). Here electron, positron and photon hits are included, the peak at 0.511 MeV being photons from annihilation (in both curves).

	ILC % of total hits				Method B % of total hits
	1	2	3	4	A,B,C,D
Electrons	10	14	10	15	6
Positrons	7	8	6	7	3
Photons	83	78	83	78	91

Table 6.6: The percentage of electron, positron and photon hits on each stripline for Method B compared with the percentages for ILC feedback BPM striplines. Due to the symmetry of Method B, the striplines are identical. The ILC striplines are assigned numbers as shown in figure 3.24(a).

	5% foil	3% foil	1% foil
Electron hits	$(2.71 \pm 0.02) \times 10^{-3}$	$(1.39 \pm 0.01) \times 10^{-3}$	$(3.54 \pm 0.09) \times 10^{-4}$
Positron hits	$(1.51 \pm 0.01) \times 10^{-3}$	$(7.88 \pm 0.08) \times 10^{-4}$	$(1.8 \pm 0.1) \times 10^{-4}$
Photon hits	$(4.10 \pm 0.02) \times 10^{-2}$	$(2.36 \pm 0.01) \times 10^{-2}$	$(5.3 \pm 0.1) \times 10^{-3}$

Table 6.7: The number of particle hits on each stripline for Method B per electron of beam charge. Each stripline is identical due to azimuthal symmetry.

Scaling the stripline study result $\Delta\bar{m}$

$\Delta\bar{m}$ is a charge normalised parameter of the difference between a stripline with additional noise from secondary backgrounds and the same stripline without additional noise from secondary backgrounds.

Simulations were used to determine a scaling factor to relate Method B to the ILC. Through GEANT3 simulations of Method B, it is possible to express the secondary backgrounds that cause $\Delta\bar{m}$ as a number, based on the particle hits on the Method B stripline. It is also possible to do the same for the ILC 14 mrad crossing angle simulations (section 3.4.4) and then to scale the Method B results with the ratio of the secondary backgrounds in Method B to the secondary backgrounds expected at the ILC.

To proceed with scaling from ESA Method B to ILC, GEANT3 simulations were repeated with the beam parameters measured during the experiment (as stated in table 5.1). The number and energies of electrons, positrons and photons hitting the striplines were recorded as shown in table 6.7. The number of particles hitting the striplines was used as the measure of how noisy the BPM environment was in both the ESA and ILC case.

According to the 5% foil simulation, per input electron there were $(2.71 \pm 0.02) \times 10^{-3}$ electrons, $(1.51 \pm 0.01) \times 10^{-3}$ positrons and $(4.10 \pm 0.02) \times 10^{-2}$ photons hitting each stripline.

The total number of hits (electrons, positrons and photons) cannot be reliably used as an indicator for how conditions at ESA compare to ILC because the percentage of hits that are photons at ESA is greater than the percentage of hits that are photons at the ILC (as shown in table 6.6) and charged particles and photons interact with matter in different ways. Cross section data for interactions with electrons and photons were gathered from the Lawrence Livermore Evaluation Electron Data Library [106] and Evaluated Photon Data Library [107] respectively. Each particle that hit the striplines was weighted by the cross section of its interaction with iron (the material of the striplines) given its kinetic energy. The interactions with the greatest cross section at these energies was ionisation through an incident photon or electron with cross sections shown in figure 6.11. Only interactions that resulted in secondary emission and hence a signal on the stripline were considered. Interactions with all atomic sub-shells were considered plus pair production, the cross sections found through log-log interpolation and summed together to give the overall cross section. This gave each particle hit[3] a weighting that could be summed across the types of particles producing one number that could be used to compare the ILC and ESA BPM conditions and scale the results.

[3]Positrons interactions were treated using the electron interaction data.

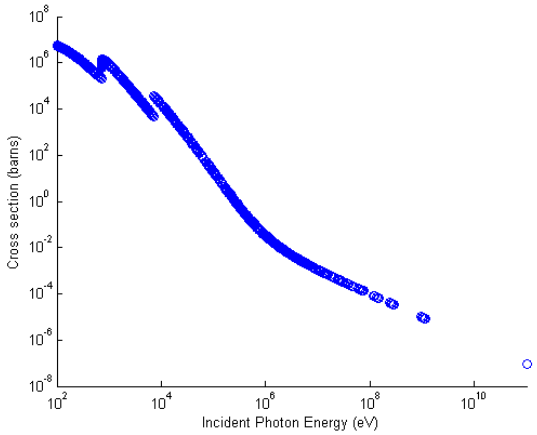

(a) Cross section for the total photoionisation of Fe with incident photon energy.

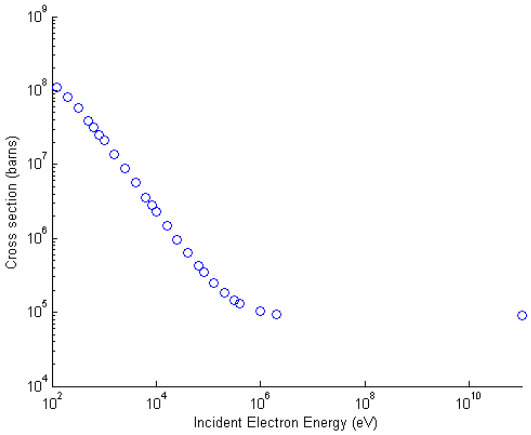

(b) Cross section for the ionisation of the Fe 4s subshell with incident electron energy.

Figure 6.11: Cross sections for particle interactions for iron from the Lawrence Livermore Evaluation Electron Data Library [106] and Evaluated Photon Data Library [107].

Using the cross section weighting to particle hits, the 5% foil case is characterised by $2.86 \pm 0.03 \times 10^3$ barns.

In the ILC 14 mrad scheme 14 simulation with anti-DID, there were different numbers of hits on each stripline (see table 3.2). Since the position is calculated using the "Difference/Sum" method, it is the imbalance between a stripline pair that is of interest, specifically the top and bottom striplines since feedback is in y. The ILC simulations indicates that per input electron, there is an imbalance between the top and bottom striplines of $(0.7 \pm 2.2) \times 10^{-7}$ electrons, $(2.2 \pm 1.1) \times 10^{-7}$ positrons and $(1.7 \pm 1.0) \times 10^{-6}$ photons. Using the cross section weighting to particle hits, the ILC case has a top strip characterised by 9 ± 1 barns and a bottom strip 7.5 ± 0.5 barns giving a maximum imbalance of 3 barns.

The 5% foil case is therefore 990 times worse in terms of particle hits.

The striplines were calibrated using the Difference/Sum method (figure 6.3). At the ILC, 1 micron resolution is required. Therefore, in Method B, since it is 990 times worse, the signal caused by hits on one of the BPM striplines needs to be less than 990 μm after the calibration is applied for this resolution to be satisfied.

$\Delta\bar{m}$ as defined in equation 6.3 is in units of dimensionless pickup radius (it is a charge normalised difference between two striplines). The measurement of $\Delta\bar{m}$ was limited by experimental errors and is therefore less than $s_{\bar{m}} = 0.0008$. Given the calibration constant in figure 6.3, this upper limit corresponds to a position of 8.5 μm. This is approximately a factor of 100 below the value that suggests a problem for the ILC stripline BPM. In ILC backgrounds, 990 times smaller than Method B backgrounds, the effect of the pair backgrounds would therefore be to create a signal on the stripline BPM that causes errors below 8.6 nm.

Scaling the processor study result $\Delta\bar{D}$

The FONT4 analogue processors use the difference between two stripline inputs and so it is not possible to look at the noise on just one stripline in the data as above.

The GEANT3 simulation with the 5% foil in place was repeated for a small beam offset of 360 μm. For each input electron there was an imbalance of hits between the stripline that was targeted and the opposite stripline. The imbalance came to $(2.0\pm0.8)\times10^2$ hits with the simulation being run four times and the results averaged. With the cross section weightings, one of the two strips used with the processor is characterised by $(2.34\pm0.06)\times10^3$ barns and the other $(2.18\pm0.02)\times10^3$ barns. This gives a maximum imbalance of 80 barns compared to the imbalance of 3 barns for the ILC.

The 5% foil case is therefore producing 28 times the imbalance on the striplines than worst imbalance in the ILC case. Thus if the position resolution of the processor is degraded by 28 μm, there is a concern for the 1 μm resolution target at the ILC.

The greatest difference observed in the parameter $\bar{D}$ ($\Delta\bar{D}$) was between the first run without foils and the run with the 3% foil. Here, $\Delta\bar{D} = 0.076$. This is a position measurement of 27 μm from the integrated difference/sum calibration (figure 6.4) and therefore only just below the 28 μm level of concern. However, the observed $\Delta\bar{D}$ is unlikely to be due to the presence of backgrounds. This would be a borderline concern if it was due to the backgrounds but the drift between the first run with the foils out and the repeat run indicates that it is not.

6.4 Summary to Method B

A method was developed to produce backgrounds at the location of the BPM in the FONT module in the presence of the main beam. This created a situation where the beam position could be measured with and without backgrounds present.

The backgrounds were created by using thin aluminium foils upstream of the module. With a foil 5% X_0 placed 12 m upstream of the module, secondary backgrounds on a stripline were ~ 990 times worse than the imbalance of secondary backgrounds between the top and bottom striplines at the ILC. The effect of the secondary backgrounds on the stripline was investigated. This study indicated that position resolution errors at the ILC due to the beam-beam pair background was less than 8.6 nm.

The investigation with the FONT4 analogue processors did not lead to any conclusions since large drift was observed in the data masking effects of the backgrounds.

Method B indicates that the backgrounds at ILC in the worst case scenario postulated (accelerator parameters scheme 14 and an untuned anti-DID) do not cause enough noise on the striplines to affect micron-level resolution.

Chapter 7

Methods for recreating ILC backgrounds: Method C

Three methods of creating a beam to use in conjunction with the FONT module were developed as described in section 5.1 and table 5.1. In this chapter, Method C is described.

7.1 Methods for creating spray: C

7.1.1 Overview

In the ILC simulations, the particles that hit the BPM striplines came from particles that hit the low-Z mask (figure 3.26) and went on to shower in the material of the BeamCal (figure 3.18). Method C was developed to reproduce the energy density and number density of particles that hit the low-Z mask in the ILC simulations at ESA.

To illuminate the whole low-Z mask with impacting particles as at the ILC, it was planned to use a beampipe-filling spray. This could be produced using a thick target in the beam switchyard (BSY) [108]. The magnets in the beamline between the BSY and ESA (called the A-line) could be tuned to deliver a momentum bite of the spray with 2% spread to ESA.

The flux of the spray beam could be controlled using adjustable slits (SL10) and the beam charge. The energy could be controlled with different momentum settings for the A-line. By adjusting these together, the average number density and energy density of particles hitting the low-Z mask in the module could be matched to the ILC conditions.

7.1.2 Thick Target Simulations

A beryllium target exists in the SLAC BSY. It is 42.7% of a radiation length thick (figure 7.1). This was modeled in GEANT3. The model for this stage was very simple: a disc of beryllium, 15.24 cm long in the beam direction. Using the random number generator incorporated in Matlab and the expected emittances [96] at the point of the target, an incident bunch of 10^5

electrons was generated. Beam energies of 7 GeV, 10 GeV, 15 GeV, 20 GeV and 30 GeV were used[1].

The particles were recorded as they left the target. Due to the creation of low energy electrons and the multiple scattering of the incident beam, the beam after the beryllium target contains particles with energies from 0 to the incident beam energy (figure 7.2).

The incident beam at the BSY is small in σ_x and σ_y (as stated in table 5.1). After the beryllium target, the beam fills the beampipe (figure 7.3).

The use of the beryllium target therefore provides a beampipe-filling spray beam of containing particles with energies from 0 to the energy of the incident beam.

7.1.3 Tracking in the A-line

The spray from the beryllium disc is produced at the end of the linac in the Beam Switch Yard and then passes through the B2 magnet which selects a certain momentum slice for transport down the A-line. Particles that are not bent by the magnet into the A-line proceed to the D10 dump (calculations indicate that the dump will be able to deal with the particle fluxes required for this experiment well within the safety margin [108]). The electrons that are bent into the A-line continue through the beam line (as described in the A-line configuration for E-158 [109]) comprising of various elements including slits (SL10) that can be opened or closed, thereby allowing variation of the flux of particles that are allowed through.

To track the electrons generated in the spray down the A-line and into the End Station, MatMerlin [110] (Merlin [111] within the Matlab environment) was used. It constructs a model of an accelerator from a MAD generated file [112] and uses MerlinC++ libraries to track particles. MatMerlin does not deal with particles hitting targets and then scattering or producing more particles, so collimation needed to be dealt with separately. The tracking was done step-by-step, initially tracking a bunch without any collimation then chopping the beam at the relevant positions and with the relevant aperture as if each collimator was a 100% absorber. Ideally the beam would be tracked to the collimator and GEANT used to find how the bunch interacts with it. The output from GEANT would be used to continue tracking. This was not performed in the preliminary investigation. Synchrotron radiation needed to be turned off as tracking with this method failed otherwise. It is not expected to affect the result as synchrotron radiation is negligible at these low energies [113].

Using the results of the spray generation from the GEANT3 model, the bunch of electrons was tracked from the position of the beryllium target to the position of the FONT module in ESA. The magnets in the beamline can be tuned within MatMerlin to transport a particular energy so only a section of the spray electrons are successfully transported; the rest are not deflected along the beamline and are removed via the 100% collimation routine. The spray beam, once it is transported to the final position, is a couple of centimetres wide and would fill the beam pipe at the ILC (see figure 7.4). The rectangular shape of the spray beam in figure 7.4 is due to upstream collimation at the rectangular entrance (D10) to ESA. This

[1]The SLAC linac can deliver up to 50 GeV beams.

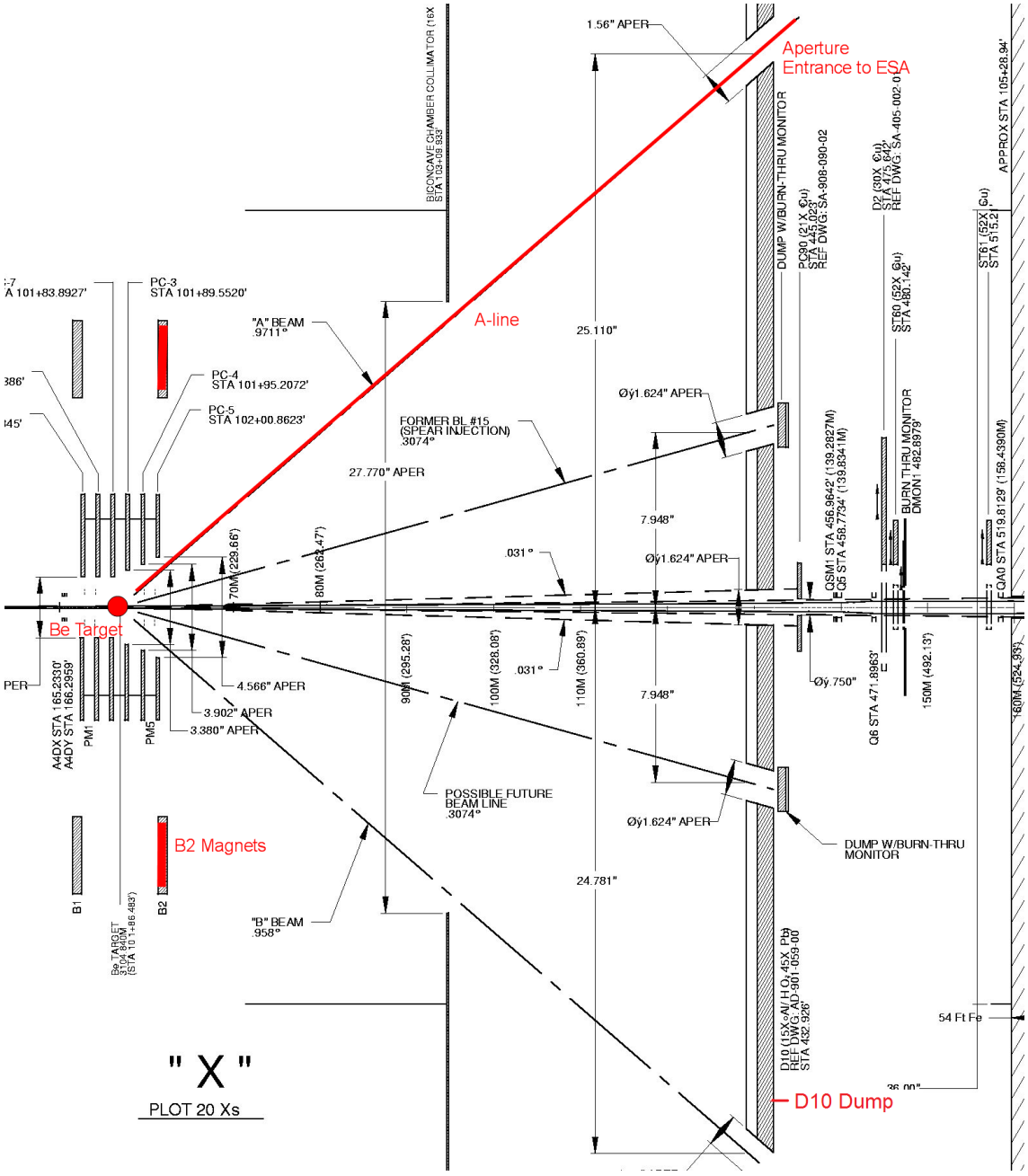

Figure 7.1: Layout of the Beam Switch Yard (BSY) and A-line [108]. The beryllium target is shown (labeled Be Target) and also magnets (labeled B2 Magnets) to deflect the beam from the linac to the A or B line. The entrance to the End Station is a 1.56 inch rectangular aperture (labeled Aperture) in the D10 dump.

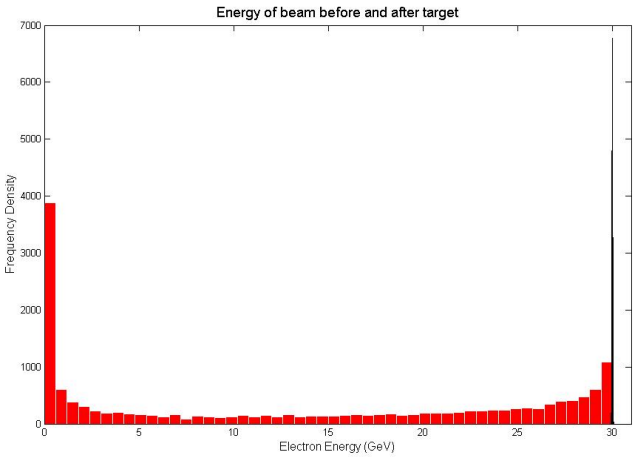

Figure 7.2: The electron energy distribution for a 30 GeV beam (±0.2% energy spread) incident on the beryllium target (black) and the electron energy distribution of the beam after the beryllium target (red).

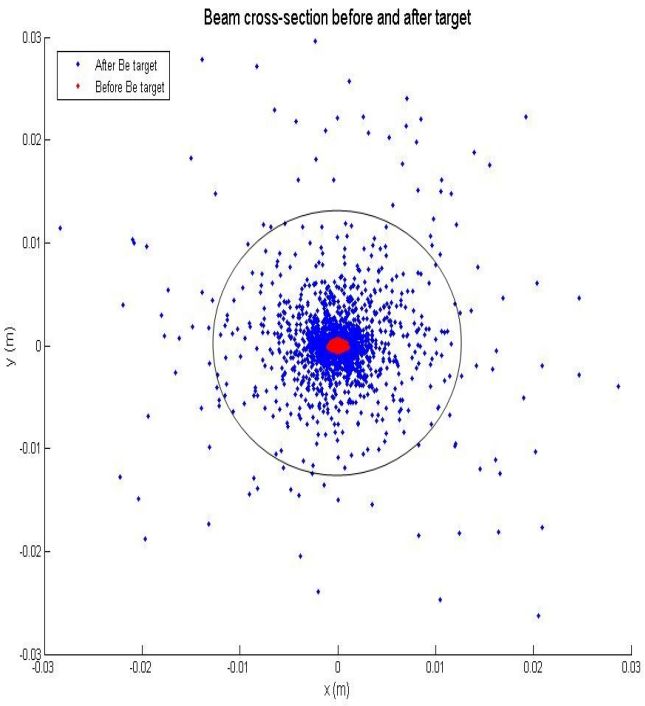

Figure 7.3: The x-y distribution of the incident beam of 30 GeV electrons (red) and the spray generated from the target (blue).

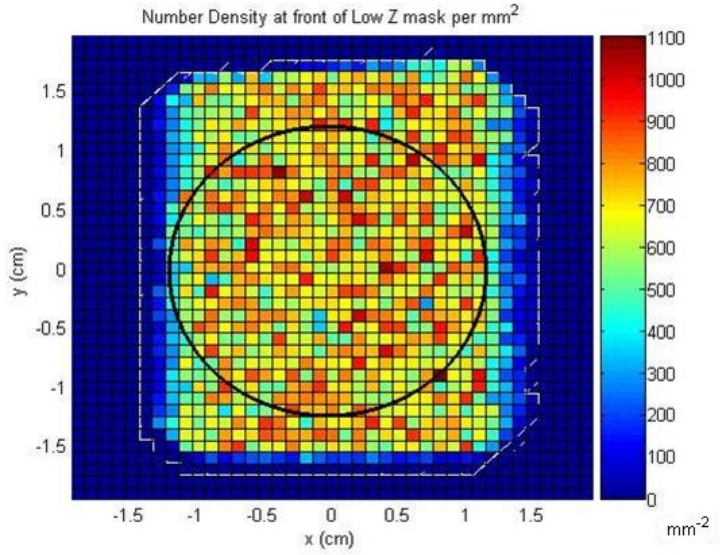

Figure 7.4: The number density (per mm^2) of the spray at the position of the FONT module. The inner radius of the low-Z mask is marked as a black circle.

wide spray beam is a closer match to the spatial distribution at the ILC of the low energy background pairs on the low-Z mask (see figure 3.25) than Method A (see figure 5.1) or Method B (see figure 6.1).

The tracking from the target to ESA was repeated with the beamline tuned to various acceptance energies and also for different incident beam energies hitting the target. The fraction of electrons that survive to the position of the FONT module was recorded and plotted against the momentum setting of the A-line for different energies of the electrons incident on the beryllium target (figure 7.5). This graph allows estimation to be made of the fluxes expected at ESA given the energy at which the linac is running, the momentum setting of the A-line and the beam charge.

7.2 Simulating the experiment: Method C

As before, it was checked through simulations that these conditions were not dissimilar to those at the ILC with regards to the hits on the BPM striplines. 1×10^6 28.5 GeV electrons were used as the beam incident on the beryllium target. The A-line momentum was set at 4 GeV/c. The output from the A-line tracking was used as input to a GEANT3 simulation of the module. The energies of the charges that hit the striplines were recorded. Figure 7.6 shows both the energy distribution from the ILC GEANT3 simulations [87] and this Method C simulation. The distributions are similar as anticipated as the module materials match the IR materials.

Such simulations were repeated with different tuned momentum selection in the A-line with different beam charges to demonstrate that for a fixed linac energy (in these simulations, 28.5 GeV) any ILC scheme could be matched in both energy and number density of charged particle hits on the low-Z mask. The results are shown in figure 7.7. In this figure, data

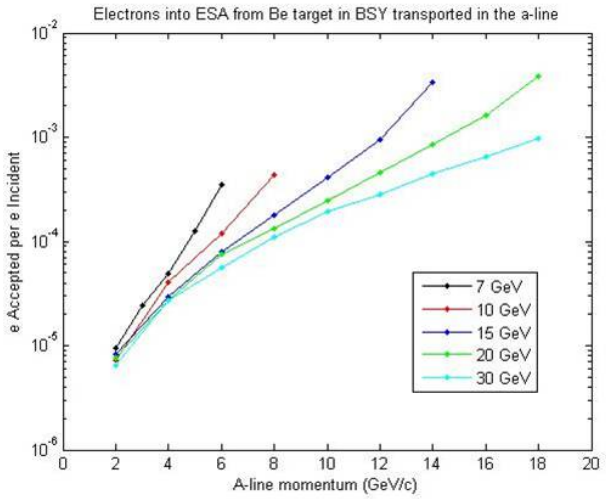

Figure 7.5: The number of electrons per electron incident on the beryllium target that reach the FONT module depending on the momentum setting of the A-line (x axis) for different linac energies (7 GeV in black, 10 GeV in red, 15 GeV in blue, 20 GeV in green and 30 GeV in cyan).

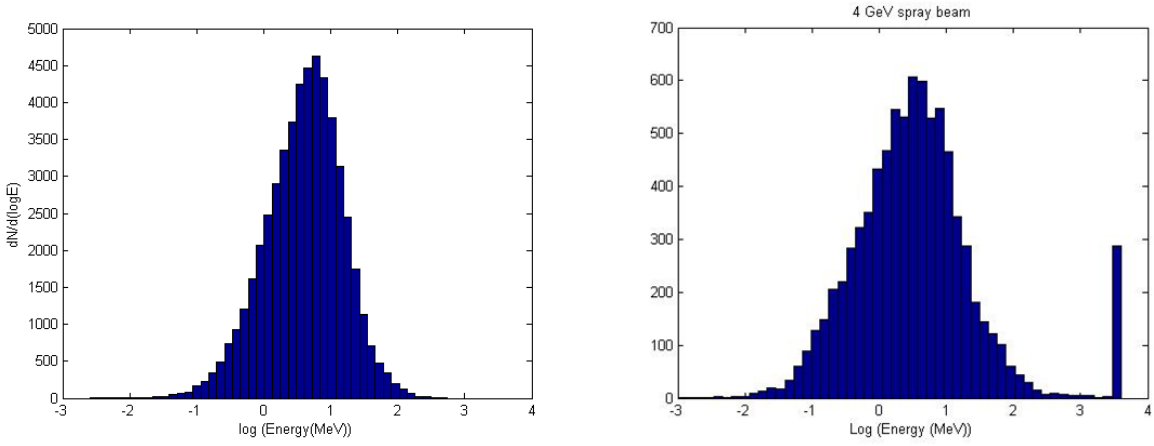

(a) ILC Scheme 14, 14 mrad crossing angle. 10% of the full simulation.

(b) Method C (as described in the text).

Figure 7.6: The energy distribution of particles that hit the striplines in GEANT3 simulations.

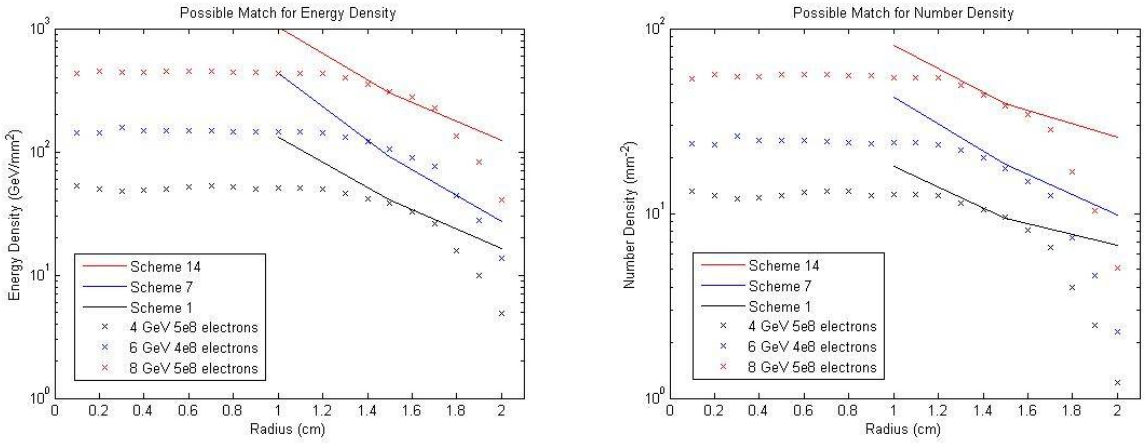

(a) Energy density

(b) Number density

Figure 7.7: The average energy and number density of the particles versus radius. ILC schemes (full lines) are compared to the average energy and number density of the particles in Method C (crosses).

are shown from simulations of the ILC with the 20 mrad crossing angle and pairs from the beam-beam interaction of three schemes: 14, 7 and 1 (that is, the 1 TeV high luminosity scheme, the 500 GeV high luminosity scheme and the 500 GeV TESLA scheme as described in tables 1.2 and 1.3). The number density and energy density of the charged particles hitting a plane at z = 3.12 m, just in front of the low-Z mask, are shown as lines. These densities are the values to be matched at ESA since previous studies (figure 3.26) indicated that the particles that hit the low-Z mask are the ones to cause hits on the striplines. The figure shows the Method C produced background densities that are close to matching those of the ILC schemes. For example, 5×10^8 electrons of energy 28.5 GeV incident on the beryllium target and an A-line momentum setting of 8 GeV can match the number and energy densities of the charged particles hitting the low-Z mask at the ILC with the scheme 14 accelerator parameter set.

It seems unlikely from the results of the other methods that this method would produce any signal at all on the striplines unless the ILC conditions were exceeded rather than matched. By using the maximum beam charge at ESA of 2×10^{10}, the Method C set-up with the incident 28.5 GeV electrons on the beryllium target and the A-line momentum setting 8 GeV exceeds ILC Scheme 14 conditions by a factor of 40.

7.3 Summary to Method C

Method C was developed to more closely match the number and energy density of particles hitting the low-Z mask, previously shown to be the sources for showers in the BeamCal that create the backgrounds at the stripline location. This method involves creating a spray beam of electrons that fills the beampipe. The existing beryllium target in the beam switch yard at SLAC is suitable for this purpose and produces a wide beam of energies from 0 to the incident beam energy. The energy to be transported to the end station can be selected

by tuning the magnets of the A-line to transport a momentum bite of this spray, the rest going to a dump. By carefully choosing the initial beam energy, the initial beam charge and the momentum setting for the A-line, simulations using a combination of GEANT3 and MatMerlin show that both the energy and number density of primaries on the low-Z mask can be matched between ILC and ESA. Increasing the beam charge could make the conditions worse.

This method requires instrumentation capable of measuring very low beam charge (see also Method A section 5.2.3). Matching ILC conditions for ILC accelerator scheme 1 requires 5×10^8 28.5 GeV electrons incident on the beryllium target and a 4 GeV/c A-line momentum setting (figure 7.7). The studies of the A-line acceptance (figure 7.5) indicate that the beam charge in the end of the A-line will be $\sim 10^4$ electrons per bunch.

Methods A and B were easier to implement in terms of the instrumentation equipment required and commissioning for radiation safety. The results from Methods A and B indicated that Method C, which is capable of producing backgrounds only 40 times worse than scheme 14 ILC backgrounds, would not have seen any effect on the striplines. Method A produced backgrounds ∼800 times worse and Method B, ∼1000 times worse, with only very small effects from the secondary backgrounds. Therefore, Method C was not used.

Chapter 8

GEANT3-based simulations of stripline signals

8.1 Simulating stripline signals

8.1.1 Overview

Based on the premise that the stripline signals are the sum of three signals (emission of charges, impaction of charges and the normal stripline response caused from charges passing the upstream end of the stripline as proposed in section 1.5.2 and section 3.1), a set of tools was developed to predict the stripline signal.

The first stage is a GEANT3 simulation of a stripline BPM in background conditions. The charged particles hitting the striplines, leaving the striplines and passing the plane at the z position of the upstream end of the stripline are recorded. The next stage is to create the normal stripline response, the response from emission and the response from impaction, given the information from the recorded particles.

The simulation of stripline signals was tested against the Method A results before being used with ILC GEANT3 simulations to predict the stripline signals of the IP feedback BPM.

8.1.2 Using GEANT3 results to produce the normal stripline response

The normal stripline response was calculated using results from the GEANT3 simulation by recording the x-y position of each particle and the time as it passed the upstream end of the stripline BPM.

As described in section 1.5.2, an electron produces a negative voltage pulse as it passes the upstream end of a stripline[1], the magnitude of which is related to its distance from

[1]The type of stripline used here has a shorted downstream end and the signals picked off at the upstream end.

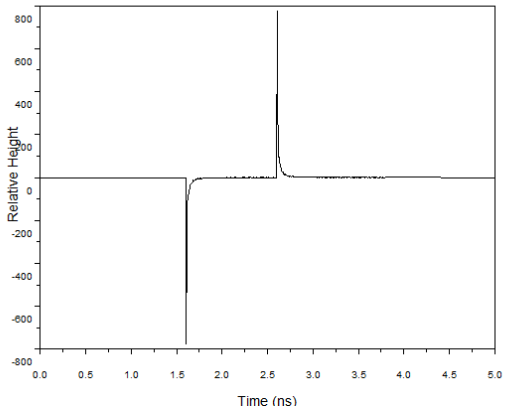

(a) The stripline response as created from simulation results.

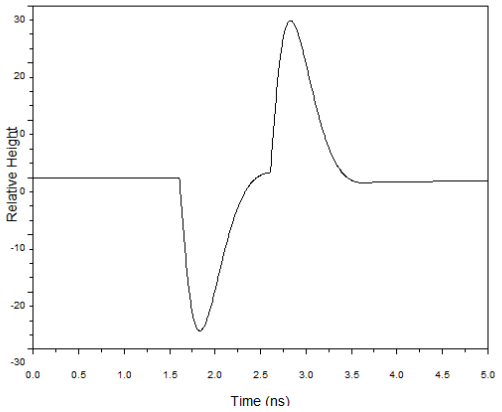

(b) The stripline response passed through a 2nd order 900 MHz Butterworth low pass filter to reproduce the effects of the cables from the stripline to the oscilloscope.

Figure 8.1: The stripline response to charges passing its upstream end, created as described in the text from a GEANT3 simulation of Method A with the beam positioned at a radius of 1.55 cm.

the striplines. For each charged particle recorded as going past the upstream end of the stripline, a weighting was calculated per stripline based on its distance from each stripline (and therefore the angle it subtends) and the direction of the response of the stripline. For example, if the electron was at the centre of the beampipe, the weighting was -1/8th for each stripline as each stripline intercepts an eighth of the induced charge (subtending an angle of $\frac{\pi}{4}$), and a negative voltage is produced.

The times of arrival of the electrons at the upstream end of the stripline (from the time of flight parameter in GEANT) were binned in a histogram with the weightings as calculated for each stripline. This signal was inverted and shifted in time by $2L/c$ and superimposed with the original signal, this being the signal reflected off the downstream end of the shorted stripline. Together, the first signal and its reflection produce a bipolar doublet as shown in figure 8.1(a).

The experimental setup included 200 feet long cables with 3.9 dB attenuation per 100 feet at 900 MHz [113] and the signals were recorded with an oscilloscope with an input bandwidth of 1.5 GHz [49]. To make the simulation results match the data, a low pass filter was applied digitally within Scilab [114] to the simulation results as shown in figure 8.1(b). The type of digital filter was chosen purely because the results looked similar to the experimental data.

8.1.3 Response from emission

The emission of charges occurs along the length of the stripline. As a charge is emitted, it causes a signal (in figure 8.2, an electron and the associated positive signal is shown). The signal splits and travels two ways: upstream and downstream. The upstream-travelling

signals essentially appear as a DC offset if there is uniform charge emission along the stripline, as the signals from charges emitted along the stripline arrive at the upstream pick-off over a period of time. The time of arrival at the upstream end can be calculated from the time the charge was emitted from the stripline (this is the time of flight t_{tof} parameter in GEANT) and its position on the stripline (with the assumption that the electric signal in the stripline travels at the speed of light c). That is, the upstream-travelling signal arrives at $t_1 = l/c + t_{tof}$. The difference between the time of arrival of the first charge being emitted (that is a charge at the upstream end) and the time of arrival of the last charge being emitted is approximately $2L/c$ (where L is the length of the stripline, in this case 15 cm) since the maximum distance the signal has to travel in the striplines is L and this emission would be caused by a particle that has to travel approximately an extra L from the upstream end before hitting the stripline.

Each emission also causes a downstream-travelling signal in the stripline which is reflected (and inverted) at the downstream end of this shorted stripline. It arrives at $t_2 = (2L\text{-}l)/c + t_{tof}$. The reflected signals from all charges being emitted from the stripline tend to arrive at the upstream pick-off at the same time since t_{tof} measured with respect to the first strike of a secondary background particle on the upstream end of the stripline is approximately l/c (approximating the velocity of the secondary background particles to be along the z direction at the speed of light). This causes one large spike $2L/c$ after the start of the signal.

Figure 8.3 shows the type of signal that can be constructed using this treatment of simulation data. In this figure, the electrons and positrons that were flagged by the simulation as exiting the stripline were recorded. The signal for each electron leaving has been assigned to be +1 and each positron leaving -1 (according to section 3.1.2) with the assumption made that as soon as the charge is emitted it is removed to infinity. The timing of the signal is the time of flight from the simulation (t_{tof}) plus the time it takes for a signal to travel from the position where the particle was emitted to the upstream end of the stripline (t_1). This was produced as a histogram and added to a histogram similarly created but with the signal timing for the downstream-going part that gets reflected at the shorted end of the stripline (t_2).

The assumption that as a charge was emitted it was removed to infinity was improved upon. It does not hold for particles that go down the beampipe, that is particles that are not quickly removed by hitting the beampipe wall. The improvement involved assigning a weighting between 0 and ± 1 (+ for electrons and - for positrons) depending on its angle and z-position of emission [81]. If the position and angle of ejection resulted in the charged particle travelling alongside a stripline within the beampipe, then the signal it causes is not due to a net change in charge of the full electron or positron. This is because some induced charge remains on the stripline as the charge passes the end of the stripline. The signal corresponds to 1 minus the fraction of induced charge on the stripline as the charge passes the end. Therefore, the weighting is not ± 1 but $\pm(1 - \alpha/2\pi)$ where α is the angle subtended by the charged particle on the stripline as it passes the stripline's end.

Charges that did not pass down the beampipe and instead hit the beampipe wall or another stripline were automatically given the weighting ± 1.

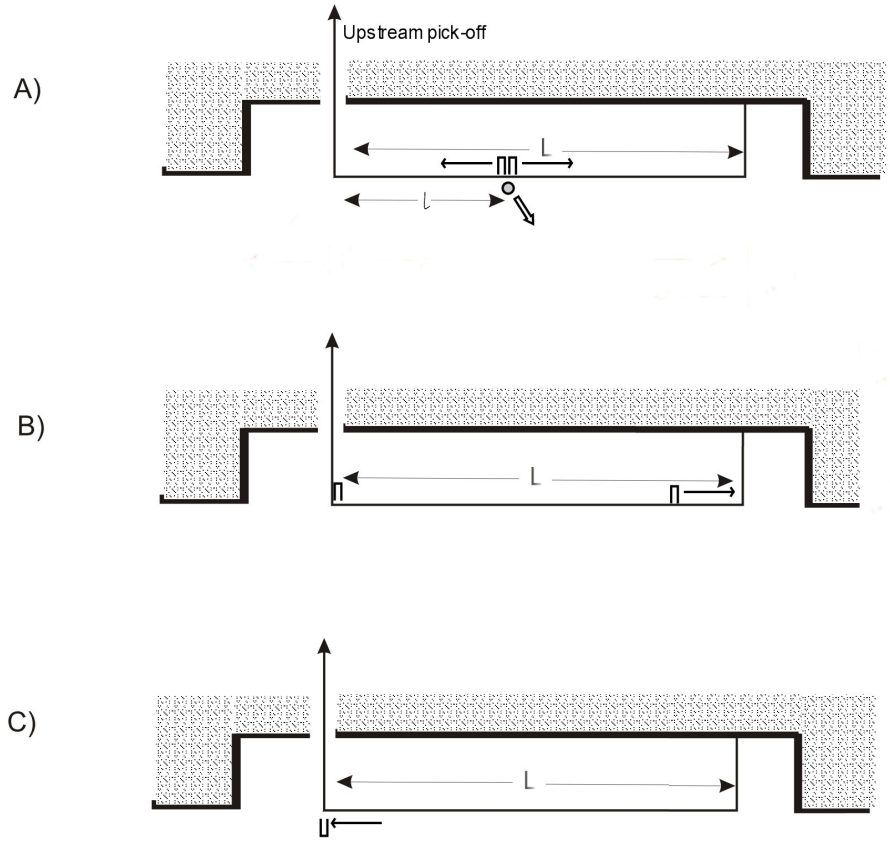

Figure 8.2: A shorted stripline of length L with an electron emitted a distance l along the stripline. The associated signal is positive and travels upstream and downstream as described in the text. A shows $t = t_{tof}$. B shows $t = t_1 = t_{tof} + \frac{l}{c}$. C shows $t = t_2 = t_{tof} + \frac{2L-l}{c}$.

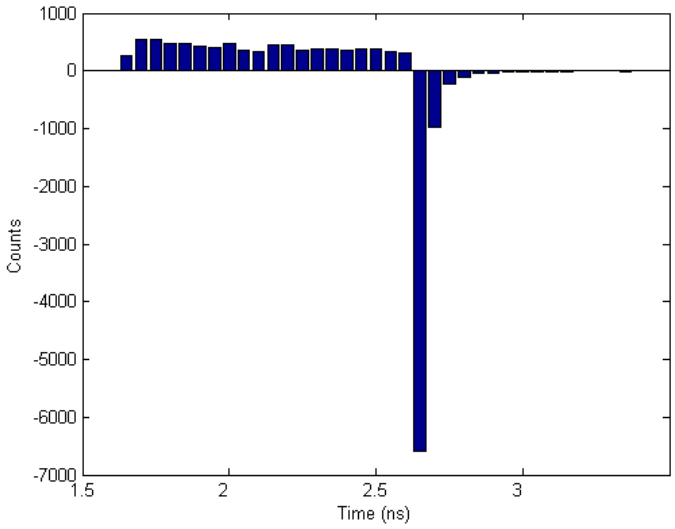

Figure 8.3: The signal caused by charged particles leaving the striplines shown as a histogram. This is based on simulations and created from the treatment described in the text with the approximation that all charged particles leaving give the same amplitude of signal (± 1).

A full electromagnetic solution of this would be ideal as the emitted charges are not relativistic. Therefore the associated electric field is not a "pancake" (as described in section 1.5.2) making the calculation of the amplitude of the induced charge (and its approximation as a delta function) incorrect.

Also, not all the signal on the stripline occurs at t_{tof}, only $\pm\frac{1}{2}$, with the rest of the $\pm(1 - \alpha/2\pi)$ occurring after as the charge moves away from the stripline and the induced charge decreases in magnitude. This suggests that the estimate for the signal due to an emitted charge based on this method will be slightly higher in amplitude and shorter in time than the true signal.

The signal created for the emission (and its reflection off the shorted downstream end of the stripline) was passed through the low pass filter as described for the normal stripline response signal. The result is shown in figure 8.4.

8.1.4 Response from impaction

A first approximation for the response from impacting charged particles is to assign a weighting of ± 1 to each hit (with the sign as given in figure 3.5). However, just as with the emission response, this was improved upon.

The hits on the striplines are predominantly at low angles as shown in figure 8.5 and spend much time close to the striplines before they impact. Therefore, assuming that they come from infinity and immediately impact the stripline is a bad approximation. Figure 8.6 shows three stages where some signal is caused on the stripline. The majority of charges that hit are also included in the normal BPM stripline signal response as they come from

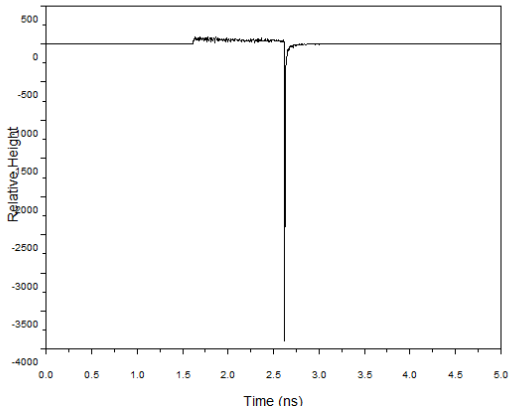

(a) The signal caused by charged particles leaving the striplines.

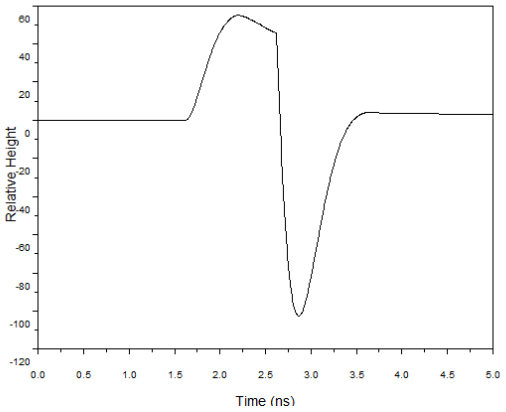

(b) The signal caused by charged particles leaving the striplines after being passed through a 2nd order 900 MHz Butterworth low pass filter.

Figure 8.4: The signal caused by charged particles leaving the striplines based on simulations and created from the treatment described in the text with consideration given to the fact that not all charges are removed to infinity.

upstream and pass the upstream end of the stripline before they hit. This is stage 1 in figure 8.6. Here, the signal height is related to the angle the charged particle subtends from the stripline ($\alpha/2\pi$) as described above for the normal stripline response. This is a fraction of the signal from the net change of a whole electron or positron charge. The rest of the signal (1 - $\alpha/2\pi$) is deposited as the charge approaches the stripline (stage 2) and when it impacts (stage 3). It is assumed for simplicity that all the remaining signal occurs at the moment of impact (stage 3).

Charges that hit the striplines can also come from emissions from other striplines or the wall of the beampipe. In fact, these made up approximately 50% of the hits. These were assigned weights of ± 1 delivering all of the particle charge when it impacts.

The weights are therefore calculated in the same manner as with the emitted charges but with the sign of the signals reversed as described in figure 3.5. The time for arrival of the signal and its reflection at the upstream end of the stripline are also calculated as they were for the emitted charges.

The resulting signal for charges hitting the striplines was passed through the low pass filter (as with the normal stripline signal) to replicate the effects of the cable and oscilloscope. The results are shown in figure 8.7.

8.2 Simulation of Method A Results

This method of recreating the stripline response based on a GEANT3 simulation was tested and calibrated against the results from Method A.

The existing GEANT3 model of the FONT module was used with an input beam from a

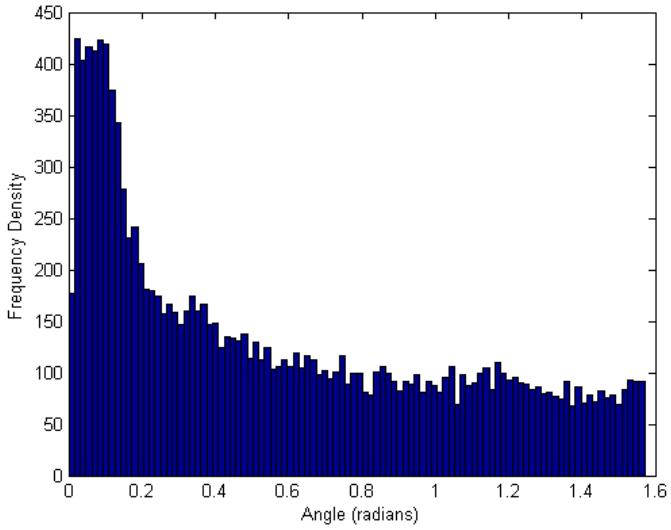

Figure 8.5: The angle of approach of electrons that hit the striplines (measured with respect to the stripline surface). Many approach at low angles and so are near the stripline for relatively long amounts of time.

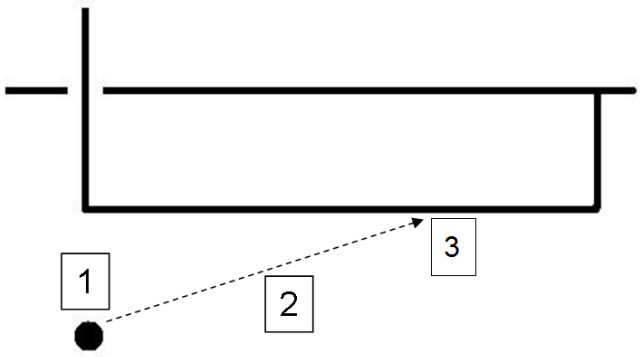

Figure 8.6: 1. Particles that pass the upstream end of the stripline contribute to the signal described in section 8.1.2. 2. The charged particle approaches the stripline. 3. The charged particle hits the stripline.

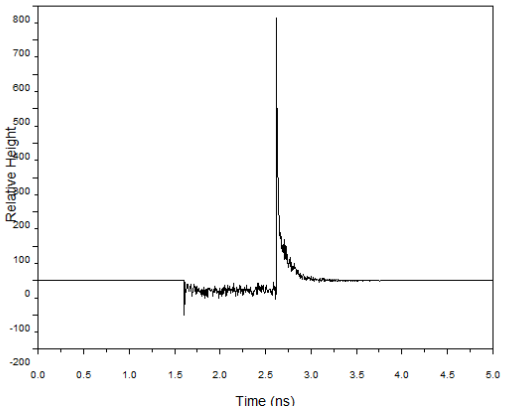

(a) The signal caused by charged particles hitting the striplines.

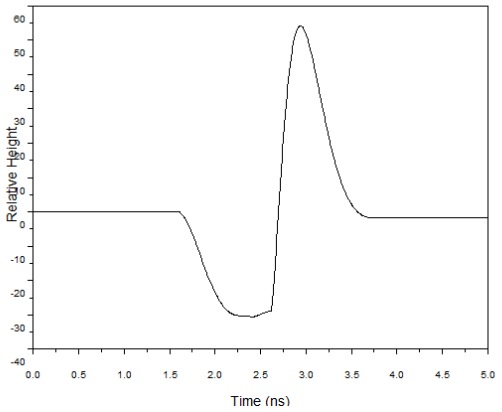

(b) The signal caused by charged particles hitting the striplines after being passed through a 2nd order 900 MHz Butterworth low pass filter.

Figure 8.7: The signal caused by charged particles hitting the striplines based on simulations and created from the treatment described in the text.

random number generator within Matlab with parameters matching those used at ESA with Method A. The electrons and positrons crossing the stripline volumes were recorded and flagged depending on whether they were entering or exiting. The charged particles passing the upstream end of the stripline were also recorded. These data were used as described in section 8.1 to simulate the three signals (emission, impaction and the normal stripline response) and sum them together in an attempt to replicate the data observed in the run in July 2006.

By considering the addition of the normal stripline signal (figure 8.8(a)) to the proposed response for emitted charges (figure 8.8(b)) and impacting charges (figure 8.8(c)), the total stripline response was calculated from simulation only. This result is shown in figure 8.8(d) which was then passed through a digital low-pass filter (figure 8.8(e)).

Shown in figure 8.9 are the results for three positions: x = -1 cm y = 1 cm, x = -1.1 cm y = 1.1 cm and x = -1.25 cm y = 1.25 cm. These can be compared to the Method A results in figures 5.11 and 5.12 (where the beam position is known to ±0.25 cm). The stripline signal observed in the results of Method A striplines B and D with two negative peaks and a flat, positive region in between, is predicted in the simulations. However, A and C also show this shape in the simulated response (though reduced in amplitude) but in the Method A results, striplines A and C have a negative peak followed by a positive peak with no flat, positive region.

It appears that the amount of hits is the principal cause of the difference between the Method A results and the simulated signals. By increasing the signal from impaction by a factor of 1.3, a set of simulated signals that were a closer match to the Method A results were produced (figure 8.10). Here, the simulation results shown are for the beam position of x = -1.1 cm y = 1.1 cm since this simulation produced results closest to the signals seen in Method A with the beam at x = -1 ±0.25 cm y = 1 ±0.25 cm. To achieve an even closer

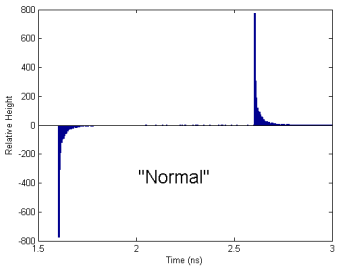

(a)

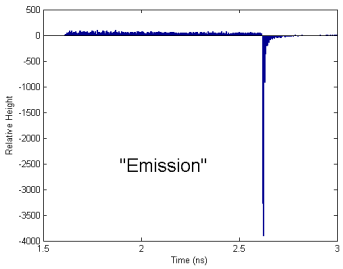

(b)

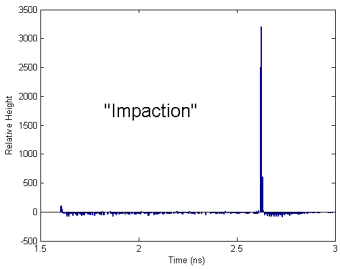

(c)

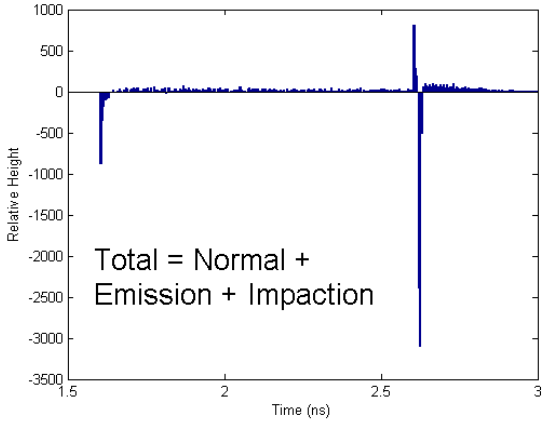

(d) The sum of the three simulated signals.

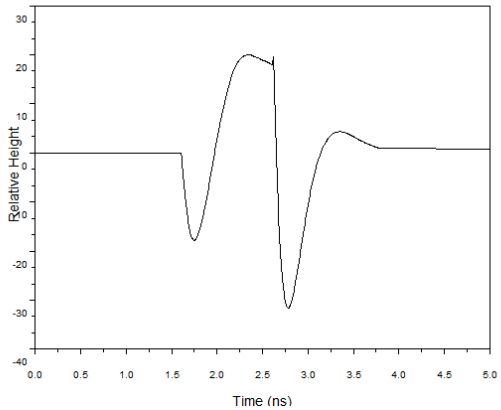

(e) The sum of the three simulated signals after being passed through a 2nd order 900 MHz Butterworth low pass filter.

Figure 8.8: The signal caused by charged particles passing the upstream end of the striplines, leaving the striplines and hitting the striplines based on simulations. This shows the simulated stripline response associated with stripline B with the beam at x = -1 cm, y = 1 cm.

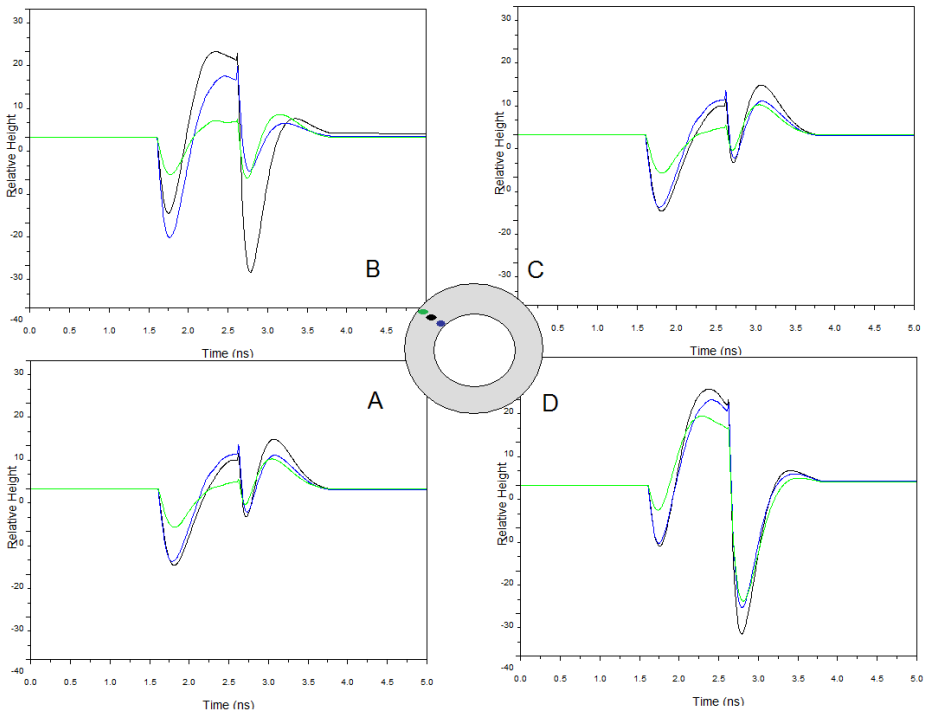

Figure 8.9: The simulated stripline signals predicted for Method A. Shown are the results of the simulations with the beam at position x = -1 cm y = 1 cm (blue), x = -1.1 cm y = 1.1 cm (black) and x = -1.25 cm y = 1.25 cm (green). The simulations are for a beam charge of 1×10^4 electrons.

match would require each stripline to be treated differently, i.e. the prediction for stripline B would require a greater contribution from the emission component and the prediction for stripline D would require a lower contribution from the emission component.

This change in contribution could indicate the need for a revision to the weightings system or a GEANT3 simulation with lower energy cuts for all processes.

The partial success of the simulations as opposed to total success is not unexpected. The signal shapes are extremely sensitive to many factors including the digital filter used and the precision in time the additions and subtractions of signals were performed. The electrical signals in the striplines were assumed to travel at the speed of light and the particles were assumed to be relativistic. The end result is extremely sensitive to the amplitude and the weightings used were approximated as described. Most importantly though, the processes expected to dominate at the low energies of secondary backgrounds were not simulated at all below 10 keV (the photoelectric effect, ionisation, diffusion of low momentum electrons etc.).

Achieving qualitatively similar signals was reassuring in that the tools required for predicting signals have been developed sufficiently for estimates of magnitude.

The Method A signals were used to calibrate the simulation. The simulations had been done for a bunch charge of 10^4 electrons. These were scaled up to 9×10^6 electrons to match the beam charge used at ESA. The simulated signal for stripline B for position x = -1.1 cm y = 1.1 cm and bunch charge 9×10^6 electrons is shown in figure 8.11(a). The Method A

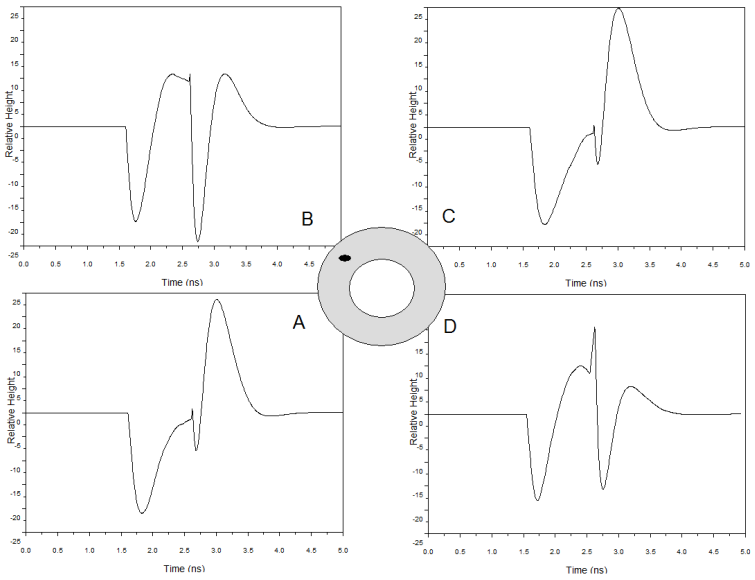

(a) x = -1.1 cm, y = 1.1 cm, 1.3 times hits. Beam charge is 1×10^4 electrons.

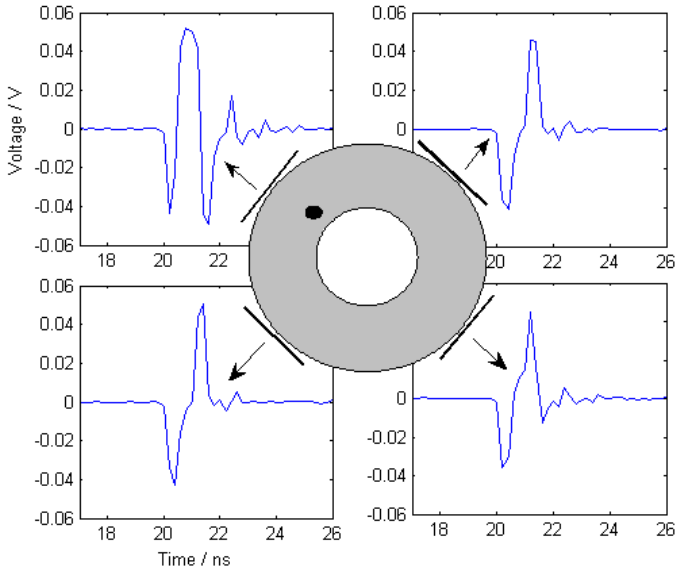

(b) Beam on mask (x = -1 cm, y = 1 cm). Beam charge is $(9 \pm 1) \times 10^6$ electrons.

Figure 8.10: The stripline responses for all four striplines before and after the beam hits the low-Z mask as it is moved along x = -y. (a) Simulation (b) Method A data.

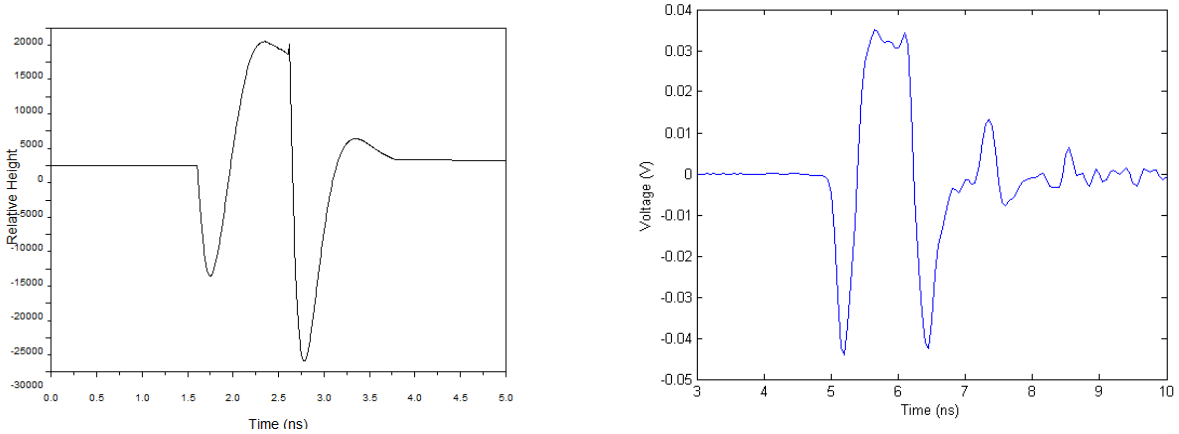

(a) Prediction of a Method A stripline signal based on the method of simulating signals as described in the text.

(b) Stripline data from the Method A ESA experiment.

Figure 8.11: Stripline B signals with the beam at x = -1 cm, y = 1 cm.

ESA data for stripline B for position x = -1 ±0.25 cm y = 1 ±0.25 cm and bunch charge $9 \pm 1 \times 10^6$ electrons is shown in figure 8.11(b). Comparing the simulation to the data, there are $(45 \pm 5) \times 10^4$ counts per volt (where the error is from the uncertainty in charge).

8.3 Prediction for the ILC

GUINEA-PIG

For the simulation of Method A signals, an input beam was generated with parameters from beam measurements at ESA during the experiment. For similar simulated signals for the ILC case, it is necessary to start with an input from GUINEA-PIG.

The input chosen was from a GUINEA-PIG simulation of the beam-beam interaction for the scheme 14 accelerator parameter set. The scheme 14 backgrounds were considered for this purpose because it is by far a worse case scenario (see section 3.4.1). This scheme refers to a 1 TeV centre of mass energy and a high beam charge (see table 1.3).

The pairs output from the beam-beam interaction was selected. The photons were not of interest as they went straight down the beampipe without causing secondary backgrounds (see section 1.3.1). The number of pairs produced is at a maximum when the beams collide head-on (i.e. there is no offset) and so to create the worst case scenario for secondary backgrounds, the GUINEA-PIG pairs were used from a simulation of a head-on collision.

GEANT

The GUINEA-PIG pairs input was used with a GEANT3 model of the 14 mrad crossing angle IR [76] adapted to include a 10 cm long stripline BPM downstream of the BeamCal.

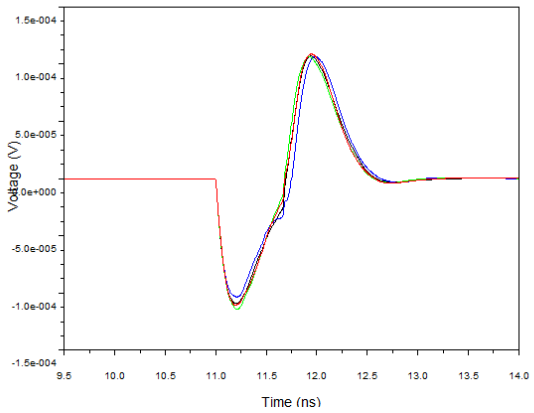

Figure 8.12: Prediction of the ILC IP BPM stripline signals from the secondary background particles caused by pairs from the beam-beam interaction (stripline 1: black, stripline 2: blue, stripline 3: green, stripline 4: red). The scale is in volts, set by the comparison between predicted stripline signals and the data from ESA.

The same modified GEANT3 code (see section 3.3.1) was used for this as has been used throughout this thesis. See section 3.4.4 for details on the GEANT3 simulation of the 14 mrad crossing angle layout.

Electrons and positrons were recorded as they entered the stripline volumes, left the stripline volumes or passed the upstream end of the stripline.

Signal creation

The output from the GEANT stage was manipulated within Matlab to sum the net signals from charges leaving, hitting and passing the striplines. The signals this created were passed though a 2nd order Butterworth digital filter in Scilab [114] with a discrete low pass cut-off frequency at 900 MHz.

The same simulation method was applied to the ILC GEANT data as was applied to Method A. Therefore the height of the resulting signals are directly comparable and the calibration to voltage found in section 8.2 was applied to the result as shown in figure 8.12.

To decrease CPU time to a manageable level, the ILC GEANT simulation was only a 10% simulation of all the input pairs. The final signals were scaled appropriately such that they show the predictions for all pairs from a single bunch crossing.

These signals of 0.11 ± 0.01 mV in amplitude correspond to a position of 13 ± 1 nm using the calibration of the striplines without normalisation by charge (figure 5.6).

With the FONT4 processing electronics, the difference of two striplines is taken. If the two striplines have identical signals from the pair backgrounds, then by taking the difference the issue of the background signal causing a position error is removed (assuming exact subtraction in the processor). Therefore, this estimate of 13 nm error is an upper limit as if none of the pair background signal was removed in the subtraction. Should the noise signals

on paired striplines be of opposite sign from each other, the subtraction could make the magnitude of the noise signal worse by a factor of two. However, the ILC simulated signals showed the signals on all four striplines to be of very similar shape and polarity.

8.4 Summary

Simulations were constructed to recreate the stripline signals based on the premise that all the voltage on the stripline came from three sources: charges passing the upstream end, charges leaving the stripline and charges hitting the stripline.

The tool was used to predict the stripline signals for Method A and then compared with the data as recorded at ESA. There was success in reproducing the shapes such as that shown in figure 8.11. Striplines A and C were slightly less successfully reproduced and required a 30% increase in the signal from impacting charges to produce the bipolar doublet as seen in Method A (figure 8.10).

Despite the uncertainty in the signal shape due to the many assumptions made in the simulations (filter, speeds of charges and signals, EM fields and charge interactions) the reasoning behind the simulated signals seemed firm as the shapes could be reproduced and understood. Using the experimental data for a Method A test with the beam hitting the low-Z mask at a radius of 1.4 cm, the simulated signals were calibrated from the arbitrary counts of the simulation to a signal voltage.

The stripline signals for the IP feedback BPM of the ILC were constructed using the 14 mrad crossing angle SiD IR, untuned anti-DID and accelerator parameter scheme 14. The signal due to the beam-beam pair backgrounds (and the secondary backgrounds they created by interacting with the material in the IR) on one stripline was 13 ± 1 nm, representing an upper limit on the position resolution degradation, assuming that none of the signal is removed on taking the difference of two striplines.

A full electromagnetic solution of charges passing, hitting and being emitted from the striplines would improve the prediction for stripline signals but there is no reason to believe it would greatly affect the stripline signal amplitudes. Therefore the method presented in this chapter is sufficient to draw the conclusion that the backgrounds at ILC in the worst case scenario for beam-beam pair backgrounds do not cause enough noise on the striplines to affect micron-level resolution.

Chapter 9

Summary and Conclusions

9.1 Summary

The development of a feedback system for y position offset correction at the ILC interaction point has been successful both in test beams demonstrating the position correction and in electromagnetic background tests. In order to test the robustness of the system in backgrounds, ILC backgrounds were studied and reproduced using different methods at the ESA facility at SLAC. The response of a stripline to the backgrounds was analysed.

9.1.1 Feedback tests of the full FONT system

The feedback system for position correction at the IP has been tested at NLCTA and ATF and the ability to correct offsets on the required timescales has been demonstrated. The development of a digital component to the feedback system is ongoing. The tests performed to date and their results are summarised in table 9.1.

The initial FONT experiments (FONT1, section 2.1, and FONT2, section 2.2) were at NLCTA used a bunch train of 2000 bunches, lasting 177 ns. To demonstrate the full feedback system of not only correcting beam offsets but also retaining that correction after a latency period, the latency needed to be under 80 ns. This was achieved (FONT1 feedback latency was 70 ns and FONT2 feedback latency was 57 ns). A correction for position offsets given to the beam was observed when feedback was on and it was retained over the full bunchtrain with the delay loop on (figure 2.2 and figure 2.3) The addition of beam flattening using an AWG plus charge normalisation on the same pulse made FONT2 a remarkable success with a 14:1 correction of the beam.

FONT3 moved the experiment to ATF and used a much shorted bunch train of 20 bunches lasting 56 ns. This required a much lower latency, ∼20 ns, to demonstrate the full feedback system. It was, however, a beam with low position jitter and a flat profile in both charge and position (when well-tuned) making it possible to achieve better corrections. Plus, the beam energy of ∼1 GeV meant that demonstrating micron-level correction at ATF corresponded to nanometre-level correction at ∼1 TeV with the same feedback system.

	FONT1	FONT2	FONT3	FONT4
Components	• 1 button BPM • Analogue Processor • Charge normalisation with one pulse delay using AWG • Valve Amplifier	• 3 button BPMs (one feedback and two witness BPMs) • Analogue Processor • Charge normalisation using logarithmic amplifiers • AWG used as a beam flattener • Solid-state amplifier	• 3 stripline BPMs (one feedback and two witness BPMs) • Analogue Processor • No charge normalisation • Solid-state amplifier	• 3 stripline BPMs (one feedback and two witness BPMs) • Analogue Processor • Digital processor (able to implement charge normalisation) • Solid-state amplifier
Test Beam	NLCTA	NLCTA	ATF	ATF
Beam Energy (GeV)	0.065	0.065	1.28	1.28
Latency (ns)	70	57	24	140
Resolution (μm)	-	10.9	12.2 single bunch, 2.3 multibunch	7.9
Correction Ratio	10:1	14:1	23:1	7:1

Table 9.1: A summary of FONT test beam results from NLCTA and ATF.

Feedback was successfully demonstrated (as shown in figure 2.9) though it appeared from subsequent simulations that the amplifier was non-linear and the delay loop length was too short. However, with a 23:1 correction of the beam, 2.3 μm resolution and a latency of 24 ns, it was undoubtedly a great achievement.

FONT4 continued at ATF with a train of three bunches separated by between 140 and 154 ns. To demonstrate the full feedback system, the latency of the system had to be ∼140 ns. As the bunch spacing at the ILC is, at the smallest, 153.8 ns, this also met the ideal conditions for being able to do bunch-to-bunch feedback at the ILC. With the comparatively long time available between bunches, the feedback system was made more powerful by introducing digital processing. The analogue processor provided difference and sum signals that could be sampled by an ADC. The digital processor, an FPGA, was used with two methods: one was to apply a gain and the other to charge normalise. In both cases, correction of the second and third bunch was demonstrated within a latency of ∼140 ns.

The future of FONT4 development is two-fold. There is a drive to improve the front-end analogue processor to micron resolution. The dependence on an external reference (the 714 MHz local oscillator) is a potential source of resolution degradation as the phase of the signal drifts with time. A correlation with temperature has been found and there are plans to improve its stability. However, a processing scheme that is independent of an external reference could be necessary.

The main development however is with the FPGA logic as FONT exploits its power. Algorithms in the future can be produced to remove static bunch train profiles, apply variable gains and involve other inputs.

9.1.2 Background tests of a stripline BPM

A module was built that could be inserted into the beamline at ESA, replicating the important materials, lengths and inner radii of the ILC IR (as described in chapter 4). This meant that no matter how different the beam at ESA from the pair backgrounds at ILC, the background distributions at the FONT module striplines were close to the background distributions at the ILC IP BPM striplines (figures 5.2, 6.10 and 7.6 show the energy distribution of particle hits on the striplines and tables 5.2 and 6.6 show the percentages of hits that are electrons, positrons and photons).

Method A (chapter 5) was developed and then put into effect during July 2006 and March 2007. It used a low charge electron beam at ESA to scan the front face of the FONT module (the low-Z mask), recording the signals from the striplines at different locations. The positions at the front face of the module illuminated by the beam were summed together using weightings from simulations of the 14 mrad crossing angle ILC case (with worst case pair backgrounds from Scheme 14) such that it approximated the pairs number density at the low-Z mask (z = 285 cm). The stripline signals associated with these positions in Method A were likewise summed together producing likely stripline signals for the IP feedback BPM as shown in figure 5.16. The prediction for ILC indicated that the effect on the striplines of the beam-beam pair backgrounds and the secondary backgrounds produced an error in

position measurement of less than 60 nm.

Method B (chapter 6) was developed and then put into effect in March 2007. It used a thin radiator (up to 5% X_0 aluminium) to create a halo of scattered electrons (plus some photons and positrons) around the main beam. The halo interacted with the material of the module (the low-Z and the BeamCal) to produce secondary backgrounds at the location of the stripline BPM. No difference was seen in the stripline signals with these secondary backgrounds present. The experimental errors allow an upper limit to be placed on the size of the effect on the striplines from secondary backgrounds. Using a scaling factor based on the particle hits on the striplines weighted by the cross-section of the particle interaction, the upper limit for the effect of the secondary backgrounds at the ILC was found to be 8.6 nm (95% confidence level). The processed position signals were also investigated but the results were dominated by drift possibly from the reference signal used in the processor to downmix the stripline signal. The processed results were, however, able to confirm that any effect will be below a micron.

Method C (chapter 7) was developed but not put into effect due to the results of the previous two methods, which were easier to implement and produced worse backgrounds. It would have been able to produce, at ESA, a secondary beam of electrons that matched the number density and energy density of the ILC pairs at the location of the low-Z mask. It could exceed the density at the ILC by a factor of forty. A thick radiator (42.7% X_0 beryllium) located in the beam switchyard would have produced primary backgrounds in a broad range of energies. The A-line could be tuned to transport one particular momenta (with a 2% momentum spread) to ESA with the spatial distribution of the transported spray beam set by the collimators in the A-line (mainly the entrance to the D10 dump). The results are expected to be similar to those of Method A but for an entirely illuminated low-Z mask (removing the need to sum the results of illuminated spots).

The observation of shapes such as those shown in the results for Method A (figures 5.11 and 5.12) that could be qualitatively explained through signals caused by charge particle hits and emissions along the length of the stripline, spurred on the development of tools based on GEANT3 simulations that could predict stripline signals in any background environment. The method created for constructing the expected stripline signals (as described in section 8.1) was tested and calibrated against the Method A signals. It was found to be able to recreate the stripline signal shapes that were observed with only minor tweaks being necessary. It was applied to the results of a GEANT3 ILC simulation (for 14 mrad crossing angle, scheme 14 accelerator parameter set and an untuned anti-DID). It predicted a position error below 13 nm.

These methods and results are summarised in table 9.2.

9.2 Outlook

The FONT prototype R&D is ongoing with successful demonstrations of feedback correcting position offsets at NLCTA (FONT1 and FONT2) and ATF (FONT3 and the continuing

	Method A	Method B	Method C	Simulation
Method	Target low charge beam at low-Z mask to create secondary backgrounds.	Use a thin radiator to create a halo around the beam that interacts with the module to create secondary backgrounds.	Use a thick radiator to create a wide spray beam that can be transported to ESA. This interacts with the module to create secondary backgrounds.	Simulations only.
Components	FONT Module. Low beam charge instrumentation.	FONT module. Aluminium foils.	FONT module. Beryllium target. Very low beam charge instrumentation.	GUINEA-PIG and GEANT3 simulations.
Times worse than ILC	~ 800	990 (striplines) 28 (processors)	40	-
Analysis	Matching number density of charged particles hitting the plane at the low-Z position in Method A to the ILC 14 mrad crossing angle IR (according to simulation).	Comparing the number of particle hits on the striplines in Method B to the ILC 14 mrad crossing angle IR (according to simulation) weighted by cross-section of the particle interaction.	By matching number density and energy density, a direct result is achieved such that Method C stripline signals are good approximations already to ILC stripline signals.	Analytical consideration of what signals are caused and how using time of flight and position data from GEANT3 simulations.
Prediction for position error on ILC IP BPM	< 60 nm	< 8.6 nm	-	< 13 nm

Table 9.2: A summary of EM background methods and results for stripline tests.

development of FONT4). The main concerns currently are to improve the resolution of the analogue front-end to the processor and to demonstrate the power of the FPGA in producing good corrections even with bunch trains with irregular charge or position profiles.

The placement of the IP feedback BPM in the proposed location of the IR, downstream of the BeamCal, is in an environment with high secondary backgrounds but the results for estimating the errors such backgrounds would create indicate that this is unlikely to be a concern. The primary and secondary backgrounds from the beam-beam interaction and the subsequent interactions of electron-positron pairs with IR material, will not decrease the sensitivity of the micron resolution IP feedback BPM in measuring position. Indeed, even for the worse case with a 1 TeV centre of mass energy and high luminosity accelerator parameter set plus an untuned anti-DID, the effect appears to be below 8.6 nm.

Although these studies into the stripline signals due to backgrounds are complete, further investigation into them could be achieved using a stripline with the downstream end terminated through 50 Ω (the characteristic impedance of the stripline) instead of being shorted (as shown in figure 1.15). Here, the only signal off the downstream end of the stripline would be the signal from impacting and emitted charges since the "normal" stripline response is mainly cancelled from the signal as the image charge hops from the stripline to the beampipe wall (as described in section 1.5.2). Some "normal" stripline response would appear on the downstream end of the stripline as termination is rarely perfect, the velocities of the beam and signal in the striplines are not an exact match and there are often discontinuities in the stripline [39]. However, this could help confirm and perfect the understanding of the emission and impaction signals as described in chapter 8 if better understanding is required. In these studies, the small predicted effect on the striplines due to ILC pair backgrounds does not motivate further investigation.

The simulations in chapter 8 could also be improved with a full electromagnetic simulation of the striplines in charged particle backgrounds. There does not appear to be any existing electromagnetic simulation software that models both fields and the addition and subtraction of charges [81], so such a simulation would require more work than the method used in this thesis. Again, there is no reason to suspect this will change the result of the predictions in this thesis by much, if at all, and since the effect on the striplines is predicted to be so small, there is no motivation to investigate it further.

The performance of the stripline BPM over time was not investigated. The difference between the mechanical and the electrical centres of a stripline BPM can change by the order of microns over a time period of up to one week [115]. Frequent calibration is therefore necessary. The background studies could be performed over long periods of time in case these have an effect on the frequency of calibration. They may also be some other drift of position reading with time in the processor that needs to be investigated, possibly with temperature.

Bibliography

[1] Lillian Hoddeson, Laurie Brown, Michael Riordan & Max Dresden, editors. "The Rise of the Standard Model: A History of Particle Physics from 1964 to 1979". Cambridge University Press (1997).

[2] See for example B. Povh, K. Rith, C. Scholz & F. Zetsche. "Particles and Nuclei". Springer (2002).

[3] See for example Francis Halzen & Alan D. Martin. "Quarks & Leptons: An Introductory Course in Modern Particle Physics". John Wiley and Sons (1984).

[4] See for example the unpublished lecture series by M.A. Parker. "Frontiers of Particle Physics" (2004). Cambridge University.

[5] Stefano Moretti. "Selected topics in Phenomenology". In "Proceedings of the School for Experimental High Energy Physics Students", CCLRC (2005). RAL-TR-2006-002.

[6] W.-M. Yao *et al.*. "Review of Particle Physics". Journal of Physics G, **33** (2006). `http://pdg.lbl.gov`

[7] Fermilab Press Release. "Tevatron collider yields new results on subatomic matter, forces" (2007). `http://www.fnal.gov/pub/presspass/press_releases/tevatronresults.html`

[8] DOE/NSF High Energy Physics Advisory Panel. "Discovering the Quantum Universe: The role of particle colliders" (2005). `http://interactions.org/quantumuniverse/dqu.pdf`

[9] D. N. Spergel *et al.*. "Wilkinson Microwave Anisotropy Probe (WMAP) Three Year Results: Implications for Cosmology" (2006). `http://map.gsfc.nasa.gov/`

[10] Michael E. Peskin. "Dark Matter and Particle Physics". SLAC-PUB 12493 (2007).

[11] "International Linear Collider Reference Design Report" (August 7, 2007). `http://www.linearcollider.org/cms/?pid=1000437`

[12] Jean-Eudes Augustin, Jonathan Bagger, Barry Barish (chair), Giorgio Bellettini, Paul Grannis, Norbert Holtkamp, George Kalmus, G. S. Lee, Akira Masaike, Katsunobu Oide, Volker Soergel & Hirotaka Sugawara. "Final International Technology Recommendation Panel Report" (2004). `http://www.ligo.caltech.edu/~BCBAct/ITRP_home.htm`

[13] Graphic courtesy of ILC / form one visual communication. http://www.interactions.org/imagebank/

[14] Tor Raubenheimer. "Suggested ILC Beam Parameter Range" (February 2005). http://www-project.slac.stanford.edu/ilc/acceldev/beampar/Suggested%20ILC%20Beam%20Parameter%20Space.pdf

[15] F. Richard, J. R. Schneider, D. Trines & A. Wagner (Editors). "TESLA Technical Design Report" (March 2001). http://tesla.desy.de/new_pages/TDR_CD/start.html

[16] United States Linear Collider Steering Group. "U.S. Linear Collider Technology Options Study" (2004). http://www.slac.stanford.edu/xorg/accelops/

[17] H. Wiedemann. "Particle Accelerator Physics", volume II. Springer, 2nd edition (1994).

[18] R. Aßmann, M. Lamont & S. Myers. "A Brief History of the LEP Collider". Nuclear Physics B - Proceedings Supplements, **109**, 2 (2002).

[19] A. De Roeck (Editor). "CMS Physics Technical Design Report". Technical report, CERN (2006). CERN/LHCC 2006-021. http://cmsdoc.cern.ch/cms/cpt/tdr/

[20] Kyle S. Cranmer. "Potential for Higgs Physics at the LHC and SuperLHC". arXiv:hep-ph/0512154v1 (2005). Invited talk at 2005 International Linear Collider Physics and Detector Workshop and Second ILC Accelerator Workshop, Snowmass.

[21] The LHC / LC Study Group. "Physics Interplay of the LHC and the ILC". Phys.Rept., **426**, 47-358 (2006).

[22] Rohini M. Godbole. "LHC-ILC Synergy". Acta Physics Polonica, **B37**, IISc-CHEP-2/06 (2006). ArXiv:hep-ph/0604230v1.

[23] The NLC Design Group. "Zeroth Order Design Report for the Next Linear Collider". LBNL-5424,SLAC-474,UCRL-ID-124161,UC-414 (1996).

[24] D. Schulte. "Study of Electromagnetic and Hadronic Background in the Interaction Region of the TESLA Collider". Ph.D. thesis, Universität Hamburg (1996).

[25] Tony Hartin. "Polarization and nonlinear effects in the beam-beam interaction" (October 2007). Talk given at CLIC Workshop.

[26] S.S. Hertzbach, T.W. Markiewicz, T. Maruyama & R. Messner. "Backgrounds at the Next Linear Collider". In the Proceedings of 1996 DPF / DPB Summer Study on New Directions for High-Energy Physics (Snowmass 96), Snowmass, Colorado, 25 Jun - 12 Jul 1996, pp ACC021.

[27] Daniel Schulte. "GUINEA PIG: an e+e- beam beam simulation program". http://www-sldnt.slac.stanford.edu/nlc/programs/guinea_pig/gp_index.html

[28] Juhao Wu, T.O. Raubenheimer, A.W. Chao, A. Seryi & C.K. Sramek. "Luminosity Loss due to Beam Distortion and the Beam-Beam Instability". SLAC-PUB-11272 (2005). In Proceedings of the Particle Accelerator Conference, 2005.

[29] D. Schulte. "An Update on the Banana Effect". 26th Advanced ICFA Beam Dynamics Workshop on Nanometre-Size Colliding Beams, Lausanne, Switzerland (2-6 September 2002). CERN-AB-2003-009-ABP, CLIC-NOTE-560.

[30] Kaoru Yokoya & Pisin Chen. "Beam-beam Phenomena in Linear Colliders". Lecture at US/CERN School on Particle Accelerators (1990). `http://www.linearcollider.org/wiki/doku.php?id=bcd:dec2005version`

[31] K. Yokoya. "CAIN simulation code". `http://acc-physics.kek.jp/Yokoya/default.html`

[32] G. White & N. Walker. "Design and Simulation of the ILC Intra-train Orbit and Luminosity Feedback Systems". EUROTeV-Report, 088 (2006).

[33] I.-A. Melzer-Pellmann. "Study of beam-beam effects with offset and angle scans". EUROTeV-Report, 021 (2007).

[34] A. Seryi. "Shaky Road to Subnanometer Beams. NLC Ground Motion, Vibration and Stabilization Studies". SLAC-PUB, 8825 (May 2001). `http://www.slac.stanford.edu/cgi-wrap/getdoc/slac-pub-8825.pdf`

[35] Stephen R. Smith. "Design of an NLC Intrapulse Feedback System". Linear Collider Collaboration Tech Notes, 0056 (2001).

[36] Javier Resta Lopez. "Placet based start-to-end simulations for the ILC with Intra-train FB system" (2007). Talk given at ILC-LET meeting.

[37] D. Schulte, A. Latina, N. Leros, P. Eliasson & E. DAmico. "The Tracking Code PLACET". `https://savannah.cern.ch/projects/placet/`

[38] The MathWorks. "MATLAB and Simulink for Technical Computing". `http://www.mathworks.com/`

[39] D.P.McGinnis. "The Design of Beam Pickup and Kickers". Extract from Beam Instrumentation Workshop, Vancouver, Canada (1994). In AIP Conference Proceedings Vol. 333 Issue 1.

[40] Stephen R. Smith. "Beam Position Monitor Engineering". SLAC-PUB, 7244 (1996).

[41] M. Minty. "Beam Diagnostics I". In "CERN Accelerator School", (2004).

[42] Steve Smith. Private Communication.

[43] V. Sargsyan. "Comparison of Stripline and Cavity Beam Position Monitors". DESY-TESLA-2004-03.

[44] M. Ross *et al.*. "Resolution of a High Performance Cavity Beam Position Monitor System". EUROTEV-Report, 037 (2007).

[45] "Next Linear Collider Test Accelerator (NLCTA) at the Stanford Linear Accelerator Center (SLAC)" (2006). `http://www-project.slac.stanford.edu/lc/local/Projects/NLCTA/nlcta.htm`

[46] "Accelerator Test Facility (ATF)" (2007). `http://atf.kek.jp/`

[47] "Accelerator Test Facility (ATF) 2" (2007). `http://lcdev.kek.jp/ATF2/`

[48] "Zeroth order design report for the Next Linear Collider" (1996). SLAC-R-0474-VOL-1.

[49] Stephen Molloy. "A Fast Feedback System Designed to Maintain Luminosity at a Linear Collider". Ph.D. thesis, Queen Mary, University of London (2006).

[50] Simon Jolly. "An Intra-pulse Fast Feedback System for a Future Linear Collider". Ph.D. thesis, Oxford University (2003).

[51] Glen White. "FONT SEPUI compliant interface". Private Communication.

[52] S. Araki *et al.*. "Proposal for the Next Incarnation of Accelerator Test Facility at KEK for the International Linear Collider". In Proceedings of the Particle Accelerator Conference, Knoxville, Tennessee, RPPP003 (2005).

[53] S. Araki. "ATF layout".

[54] Agilent EEsof EDA. "SystemVue (formerly SystemView)". `http://eesof.tm.agilent.com/products/systemvue/`

[55] Steve Molloy. Private Communication.

[56] Colin Perry. Private Communication.

[57] Glen White. "Simulink Model for FONT3". Private Communication.

[58] Glen White. "Feedback On Nano-Second Timescales: Fast Feedback Simulations". In "Proceedings for Nanobeams Workshop in Lausanne, Switzerland", (2002). `http://icfa-nanobeam.web.cern.ch/icfa-nanobeam/slides2.htm`

[59] P.N. Burrows, G. Christian, C. Clarke, B. Constance, H. Dabiri Khah, T. Hartin, C. Perry, C. Swinson, A. Kalinin, S. Molloy & G.R. White. "The FONT4 ILC Intra-train beam-based digital feedback system prototype". In "Proceedings of PAC07, Albuquerque, New Mexico, USA", (2007). MOPAN108.

[60] Steve Molloy. "Reminder of work done on the FONT4 Processor" (2005). Internal FONT note.

[61] Hamid Dabiri-Khah. Private Communication.

[62] Y. Honda. "Feedback Signal From IP-BPM" (2007). Talk given at ATF2 Meeting. http://atf.kek.jp/collab/md/projects/project_frame.php?project_page=2

[63] Christina Swinson. "BPM processor latency measurements" (September 2007). Internal FONT note.

[64] Xilinx Virtex-4 Multi-Platform FPGA. http://www.xilinx.com/products/silicon_solutions/fpgas/virtex/virtex4/index.htm

[65] Glenn Christian. "FONT4 Status Report" (2007). Talk given at Linear Collider: Accelerator and Beam Delivery Plenary Meeting. http://www.hep.man.ac.uk/lc-abd/lc_abd_Apr07/lcabd-apr07_gchristian.ppt

[66] Glenn Christian. Private Communication.

[67] TMD Technologies. http://www.tmd.co.uk/

[68] Marc Ross. "Experiments at ATF2-KEK" (2007). Talk given at ILC Detector Test Beam Workshop.

[69] Glenn Christian. "FONT4 May Run Analysis" (2007). Internal FONT note.

[70] E.J. Sternglass. "Theory of Secondary Electron Emission by High Speed Ions". Physical Review, **108** 1–12 (1957).

[71] H. Bruining. "Physics and Applications of Secondary Electron Emission". Pergamon Press (1954).

[72] Robert E. Kirby & Frank K. King. "Secondary Electron Emission from Accelerator Materials". SLAC-PUB, 8380 (February 2000).

[73] Neil W. Ashcroft & N. David Mermin. "Solid State Physics". Thomson Learning (1976).

[74] ILC Global Design Effort. "Baseline Configuration Document". **"Frascati BCD"** (December, 2005). http://www.linearcollider.org/wiki/doku.php?id=bcd:dec2005version

[75] SiD Design Study. "SiD Detector Outline Document" (May 19 2006). http://www-sid.slac.stanford.edu/

[76] Takashi Maruyama. "GEANT3 model for the SiD IR of the ILC". Private Communication.

[77] William Morse. "LumiCal and BeamCal" (July 11, 2007). Private Communication.

[78] GLD Concept Study Group. "GLD Detector Outline Document". **Version 1.2.1** (October 5, 2006). http://ilcphys.kek.jp/gld/

[79] LDC Working Group. "Detector Outline Document for the Large Detector Concept" (July 2006). http://www.ilcldc.org/

[80] Mark Thomson. "Possibilities for UK involvement in the GLDC detector concept" (2007). Private Communication.

[81] Tony Hartin. Private Communication.

[82] Brett Parker & Andrei Seryi. "Compensation of the effects of a detector solenoid on the vertical beam orbit in a linear collider". Phys. Rev. ST Accel. Beams, **8**, 041001 (2005).

[83] C. Grah & K. Buesser. "Backgrounds and Forward Region". FCAL Collaboration Workshop (September 2005).

[84] Andrei Seryi, Takashi Maruyama & Brett Parker. "IR Optimization, DID and Anti-DID". SLAC-PUB 11662 (January 2006).

[85] "GEANT - Detector Description and Simulation Tool". `http://wwwasd.web.cern.ch/wwwasd/geant/`

[86] "GEANT3 Manual" (March 1995). `http://wwwasdoc.web.cern.ch/wwwasdoc/geanthtml3/geantall.html`

[87] Tony Hartin. "Geant3 modification". `http://www-pnp.physics.ox.ac.uk/~hartin/FONT.html`

[88] Nuclear Energy Agency. `http://www.nea.fr/`

[89] Tony Hartin. "Feedback BPM background environment and BDS design". In "Proceedings of the 2005 International Linear Collider Physics and Detector Workshop and 2nd ILC Accelerator Workshop (Snowmass 2005)", Number ILCAW0531. `http://www.slac.stanford.edu/econf/C0508141/`

[90] Tony Hartin. "DID and Direct Hits". Meeting (February 17 2006). Internal FONT note.

[91] Mike Woods. "ILC Beam Tests in End Station A" (January 2007). Talk given at ILC Detector Test Beam Workshop, Fermilab.

[92] Brian Todd. Daresbury Laboratory, UK.

[93] Le Carbone graphite & carbon manufacturing. `http://www.lecarbone-gb.co.uk/`

[94] SLAC Mechanical Design drawing. SLAC assembly drawing number SA2365035002.

[95] Brett Parker. "Update on SC Quads Design for 20 mrad IR" (April 2005). Talk given at Beam Delivery Meeting.

[96] P. Bosted. "Study of E158 Beam Spot Size". E158 Experiment Documents (2001). `http://www.slac.stanford.edu/~bosted/e158/aline.txt`

[97] Frank Jackson. Private Communication.

[98] Bob Simmons. Private Communication.

[99] Zen Szalata. "ESA Data Acquisition Software". Documentation. http://www-project.slac.stanford.edu/ilc/testfac/ESA/files/DAQ/

[100] Alexander Kalinin. "Effects of Secondary Emission Electrons in the ESA ILC Mock-up Pickup" (2006). Internal FONT note.

[101] H.A. Bethe. "Moliére's Theory of Multiple Scattering". Physical Review, **89**, 6 1256–1266 (March 15, 1953).

[102] Imran Younus. "First Observation of the Parity Violating Asymmetry in Moller Scattering". Ph.D. thesis, Syracuse University (2003).

[103] Ray Arnold. Private Communication.

[104] Alexander Kalinin. Private Communication.

[105] Tony Hartin. "Thin Radiator" (January 5 2007). Internal FONT note.

[106] S.T. Perkins, D.E. Cullen & S.M.Seltzer. "Tables and Graphs of Electron-Interaction Cross Sections Derived from the LLNL Evaluated Electron Data Library (EEDL), Z = 1 - 100". **31** (1991).

[107] D. Cullen, J.H. Hubbell & L. Kissel. "The Evaluated Photon Data Library". **Vol.6**, Rev.5 ('97 version).

[108] R. Arnold & T. Fieguth. "Spray Electron Beam for Tests of Linear Colider Forward Calorimeter Detectors in SLAC End Station A". IPBI-TN-2004-5 (2004). http://www.slac.stanford.edu/xorg/lcd/ipbi/notes/tn_beamcalspray.pdf

[109] "A-line" (2002). Configured for E-158. http://www-project.slac.stanford.edu/ilc/testfac/ESA/files/Beam_Optics/ALine_E158-R009.pdf

[110] Nick Walker. "MATMERLIN particle tracker". EUROTeV-Memo-2005-002-1 (2005). http://www.eurotev.org/e158/e1364/e1391/e1393/EUROTeV-Memo-2005-002-1.pdf

[111] Nick Walker. "Merlin: A C++ Class Library for performing Charged Particle Accelerator Simulations". http://www.desy.de/~merlin/

[112] Mark Woodley. "A-line Optics MAD Deck". Private Communication.

[113] Mike Woods. Private Communication.

[114] Copyright 1989-2007. INRIA ENPC. "Scilab". http://www.scilab.org/

[115] P. Tenenbaum. "Studies of Beam Position Monitor Stability". In "Beam Interactions Workshop", (1998). http://www.slac.stanford.edu/pubs/confproc/biw98/tenenbaum.pdf